Predictive multiscale computational modeling of nanoparticles in flame reactors

by

Maulik Mehta

A dissertation submitted to the graduate faculty

in partial fulfillment of the requirements for the degree of

DOCTOR OF PHILOSOPHY

Major: Chemical Engineering

Program of Study Committee:
Rodney O. Fox, Major Professor
R. Dennis Vigil
Monica H. Lamm
Mark S. Gordon
Theresa Windus

Iowa State University

Ames, Iowa

2012

TABLE OF CONTENTS

LIST OF TABLES

LIST OF FIGURES

ABSTRACT

This dissertation details a predictive computational approach for modeling titanium dioxide nanoparticles in flame reactors. The industrial production of these nanoparticles is done using the chloride process, i.e. titanium tetrachloride ($TiCl_4$) is oxidized in a flame to form titanium dioxide (TiO_2) particles:

$$TiCl_4(g) + O_2(g) \longrightarrow TiO_2(s) + 2Cl_2(g).$$

In absence of thermochemical data most previous works used the one-step reaction mechanism given above. But this problem was alleviated recently by West et al. (2009) [R.H. West, R.A. Shirley, M. Kraft, C.F. Goldsmith, W.H. Green, Combust. Flame 156(2009) 1764-1770], by proposing a detailed mechanism for this oxidation process, which includes 30 species and 66 reactions. As the oxidation of $TiCl_4$ happens in a flame, this detailed mechanism becomes more complex with interactions of the hydrocarbons with oxidizer as well as chlorine. Hence, the proposed detailed mechanism in this work extends to 107 species and 501 reactions. Comparisons are made between the one-step and detailed mechanism to show that different models would result in very different product properties.

A bivariate population balance model was proposed to evaluate the size distribution of nanoparticles in the flame reactor. This model tracks both the area and volume distributions and accounts for nucleation, surface growth, aggregation and sintering of the nanoparticles. The results from this model are used to evaluate the particle size and shape for the two chemical mechanisms, which in turn are compared to experimental results. Also explored are the roles of gas-phase and surface phase reactions.

Accurate models for the nanoparticles involve developing a detailed chemical mechanism and modeling the transport process. This is especially true in the case of flame reactors where

the flow structure and turbulence are of major importance. Computational fluid dynamics based techniques can be used to understand and implement this coupling between transport processes and chemical reactions. But due to the large number of species and reactions involved, coupling this detailed chemistry with flow solvers is computationally very expensive. Thus, to represent the correct chemistry while making the problem computationally viable reduction of the detailed mechanism is carried out.

Finally, discussed are the results from the successful application of the models and techniques refined during the dissertation work to an industrial system. The findings show that the developed models can accurately track particle evolution in an industrial reactor.

In summary, this work uses detailed chemistry and bivariate distribution to present a predictive multiphysics computational model for TiO_2 nanoparticle synthesis in flame reactors, that can be employed to optimize operating conditions based on desired product particle size distribution.

CHAPTER 1. Introduction and Background

"Nanoscale titanium dioxide (nano-TiO_2) has a much greater surface area of a given mass or volume of nanoparticles compared to an equivalent mass or volume of conventional TiO_2 particles, affording greater potential for properties such as catalytic activity and UV absorption at certain wavelengths.

These properties have led to the exploitation of nano-TiO_2 for a wide variety of applications, including self-cleaning surface coatings, UV-resistant coatings and paints, solar cells, disinfectant sprays, and water treatment agents and topical sunscreens. Market revenues for titanium dioxide nanopowders in 2009 were US $360 million, rising to US $1465 million in annual revenues by 2017." The World Market for Titanium Dioxide Nanopowders, Future Markets, Inc., July 2010 (24).

1.1 Motivation

Nanoparticles have numerous applications in drug delivery, catalysis, energy and semiconductors. Flame synthesis represents a viable technique for large scale production of such valuable inorganic nanoparticles due to its cost effectiveness, scalability, and relatively simple single step process with no mechanically moving parts compared to wet chemical processes (31). Because of these advantages, about 90% of commercial nanoparticles by volume and value are made by gas-phase flame synthesis currently (7).

Although widely used in industry, the process is not well understood and process optimization is based mostly on experiments, which are hard to perform due to the harsh conditions and short time-scales, so a computational modelling approach is very beneficial. Thus, gaining fundamental insight into flame reactors will lead to the manufacturing of nanoparticles with more tightly controlled product properties and minimal variability. The aim of this report is to

develop a highly detailed model for one such inorganic nanoparticle, titanium dioxide (TiO_2, also called titania), which could increase our understanding of this complex process.

1.2 Titanium Dioxide

Titanium dioxide nanoparticles are traditionally used as white pigments but have found use in diverse areas like photocatalysis (4), reducing nitrogen oxide emissions (94), catalyst supports (70), photo catalysts (86), ultra-violet filtering materials (91), surface treatments like antifog coating (14)) and cosmetic applications (76). They are thus, an industrially important compound, with more than 4 million metric tonnes of titania being produced annually. Around 60% is used in paints or coatings, 20% in plastics, 12% in paper and 8% in a wide range of smaller applications.

Titanium dioxide occurs in nature as minerals rutile, anatase and brookite. The most common form in these is rutile, which also is the most stable form. Both anatase and brookite upon heating convert into rutile. Similar to most other ores, the rutile ore extracted from the ground is too impure to be used directly as a pigment and must be processed before being used in titania production.

1.3 Production of Titanium Dioxide

Titanium dioxide is produced mainly through two routes; the sulfate process and the chloride process. In the sulfate process the titanium ore, usually ilmenite ($FeTiO_3$), is digested into sulfuric acid (H_2SO_4) and $FeSO_4.7H_2O$ is crystallized out. After hydrolysis, filtration and washing dilute H_2SO_4 is removed and after this calcination is performed to produce titania pigment.

The dominant process for the production though is the chloride process. In the chloride process the ore, usually natural or synthetic rutile, is chlorinated with coke to form titanium tetrachloride ($TiCl_4$).

$$TiO_2(\text{rutile}) + 2Cl_2 + C \longrightarrow TiCl_4 + CO_2. \tag{1.1}$$

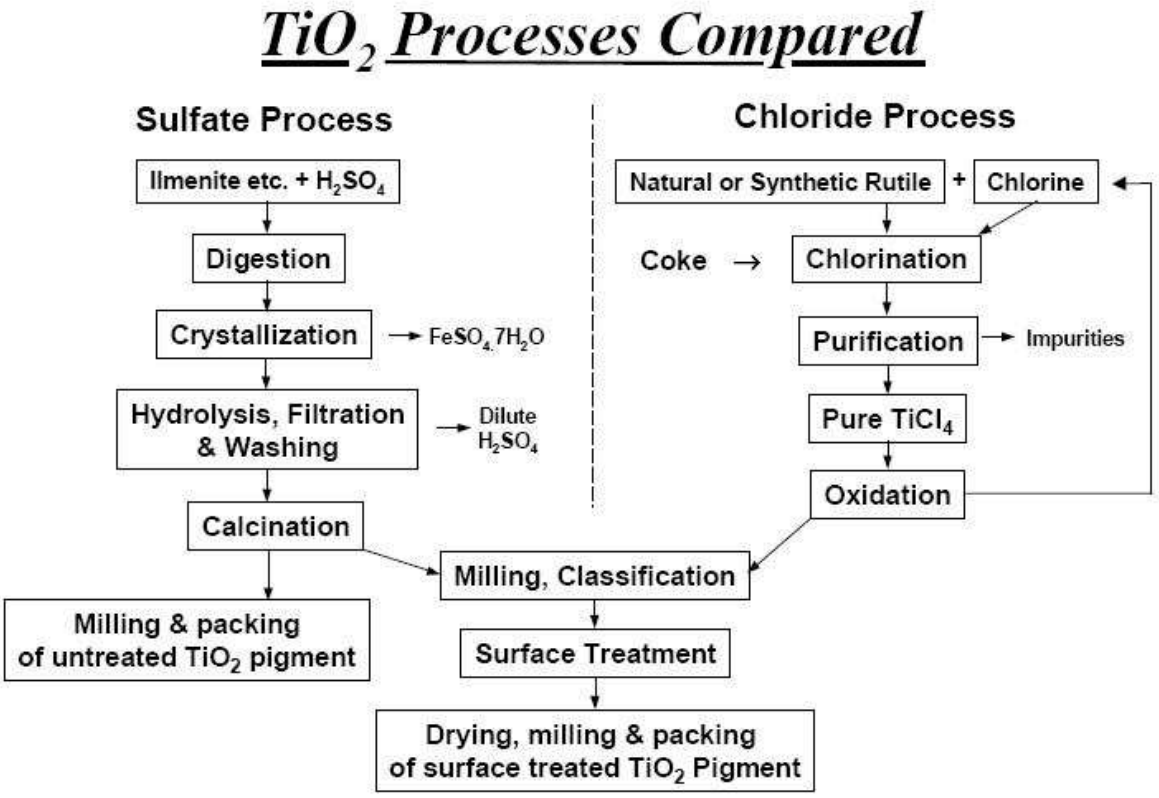

Figure 1.1 Comparison of the two routes to TiO_2 production.

The $TiCl_4$ produced is then purified using distillation and then oxidized at high temperatures (1100-2000 K) (17; 8) and moderate, near atmospheric pressures (2-3 bar) (78) to produce TiO_2 pigments.

$$TiCl_4 + O_2 \longrightarrow TiO_2 + 2Cl_2. \tag{1.2}$$

1.4 Experimental work

Most early attempts to understand the chloride process were done using the flow-tube experiments. These consist of a tubular reactor heated with external heating elements or a furnace (see Figure 1.2). Varying ratios of the reactants, oxygen and precursor ($TiCl_4$), usually diluted with argon are fed at one end and the titania particles were collected on the other end. The reactants are relatively cold when they enter the reactor at one end,

although some variations allow pre-heating of reactants (26). Pratsinis et al. (1990) (68) used such an apparatus to measure the overall reaction rate for titanium dioxide oxidation. For determining the reaction rate, the concentration of $TiCl_4$ is measured using Fourier transform infrared spectroscopy (FTIR) and then fit into an Arrhenius plot to determine the activation energy and the pre-exponential factor. The oxidation rate of $TiCl_4$ was measured between 973–1273 °K.

Ghoshtagore studied the kinetics of rutile (TiO2) thin film deposition from the reaction (16)

$$TiCl_4 + O_2 \longrightarrow TiO_2 + 2Cl_2. \tag{1.3}$$

in a horizontal flow system with a rf-heated susceptor. Based on these experiments he developed a reaction rate for surface reaction on TiO_2 for temperatures between 673 - 1120 K. The surface reaction rates of $TiCl_4$ is based on this expression.

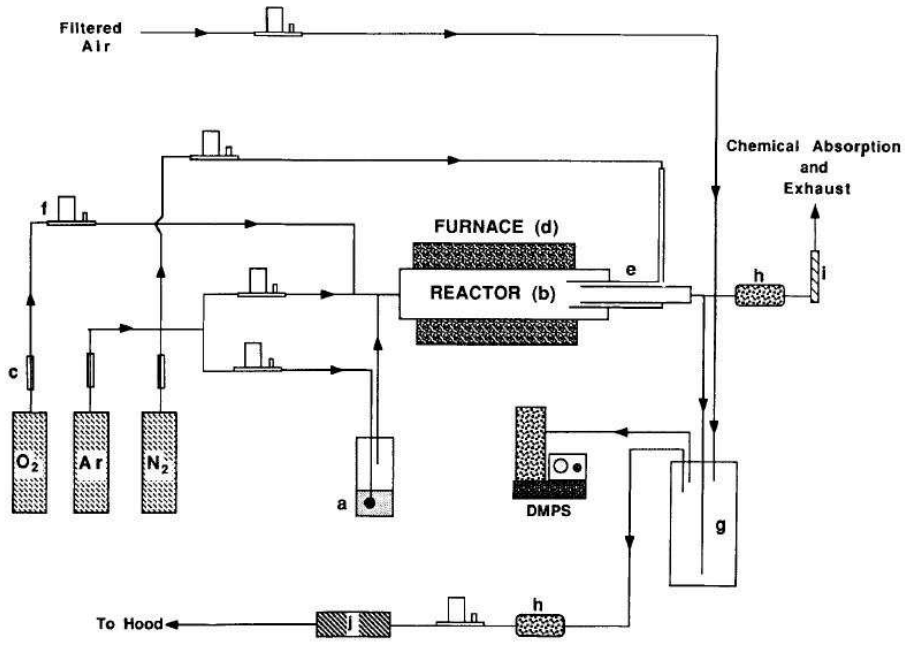

Figure 1.2 Flow tube experimental apparatus used to produce titania particles from vapor-phase oxidation of titanium tetrachloride from Akhtar et al. (1991) (1).

As well as flow-tube experiments, titania formation has been studied in a laminar diffusion flame with both $TiCl_4$ (70) and titanium tetraisopropoxide (TTIP) (96) as precursors (see Fig-

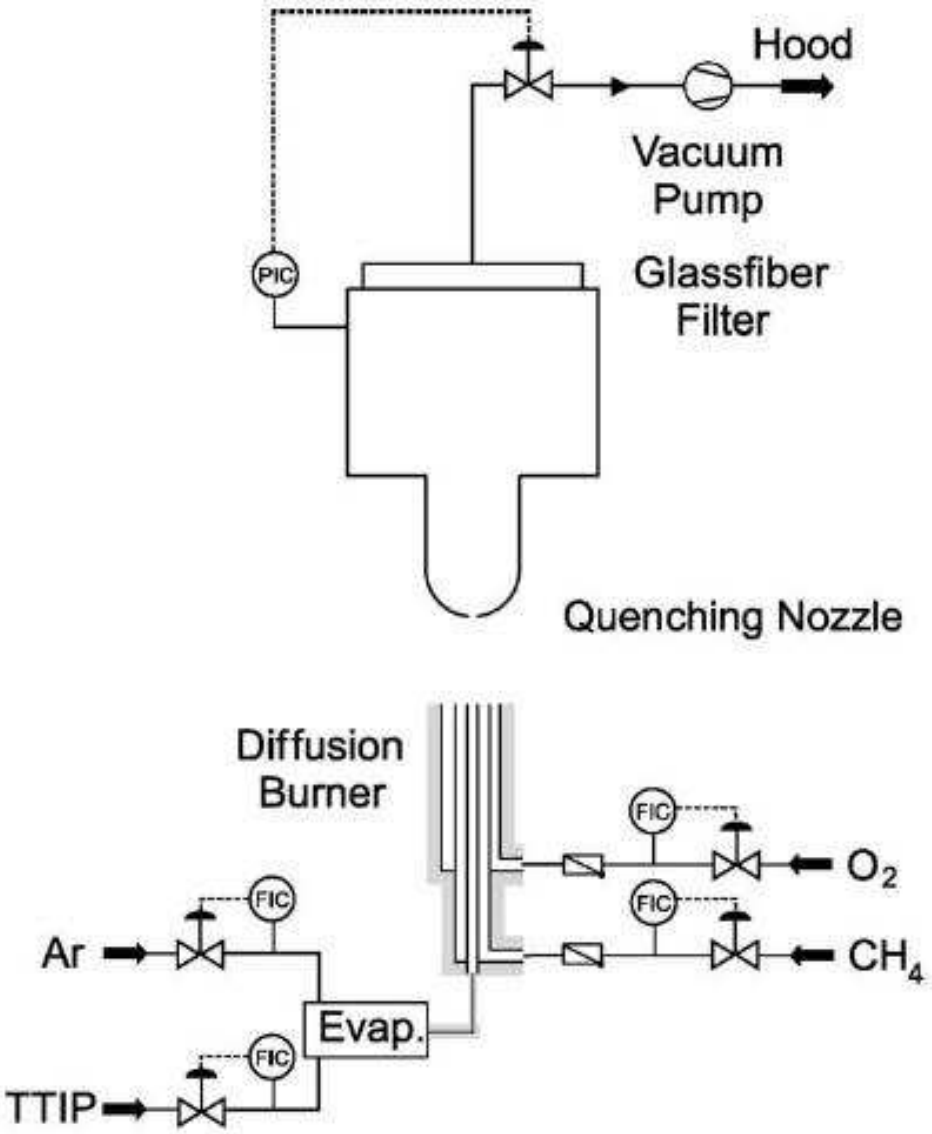

Figure 1.3 Schematic of the experimental set-up in diffusion flames from Wegner et al. (2002) (96).

ure 1.3). As these experiments occur in diffusion flames, they are very good approximation of the industrial flame reactors and serve as framework for modelling this process. The apparatus consist of a multi-nozzle flame reactor with oxygen, fuel (usually methane), argon and precursor coming from different nozzles. Different flame configurations (fuel and oxidant flow rate and position) are used to get nanoparticles of different size and morphology (70). The diffusion flame experiments are used to discuss the size and specific surface area of the nanoparticles but unlike the flow-tube experiments no comments on the reaction rates are made on these systems.

Primary particle sizes are usually measured by analyzing the images from scanning electron microscopy (SEM) (1) or transmission electron microscopy (TEM) (2; 10). The specific surface area was measured by BET nitrogen absorption, from which primary particle size can be estimated (29).

1.5 Flame reactors

Although there are variety of ways to fabricated nanoparticles (74), the combustion-based synthesis has been one of most successful techniques for industrial level production of commercial grade nanoparticles (95). Flame synthesis provides high purity nanoparticles with a good production scalability (75) while utilizing a relatively simple process without involving a large quantity of wet chemicals. Besides, the high temperatures in combustion-based methods are able to provide the driving energy for the precursor conversion process without requiring additional energy sources (e.g. heaters (97), plasma (18), electricity (30), or lasers (15)). Combustion-based methods are favorable for the mass production of metal oxide nanoparticles because a flame is one of the most economical and readily accessible sources for fast metal oxidation processes, making the flame synthesis a more economically competitive route over competing methods for high-rate synthesis. Therefore, it is not surprising that most commercial nanoparticles are manufactured by combustion based processes (7).

A general schematic of the flame synthesis process can be seen in Figure 1.4 of nanoparticles. In flame synthesis the fuel (usually CH_4) is mixed with precursor ($TiCl_4$) and sprayed into a pre-existing flame. The fuel evaporates and combusts, exposing the precursors to the high

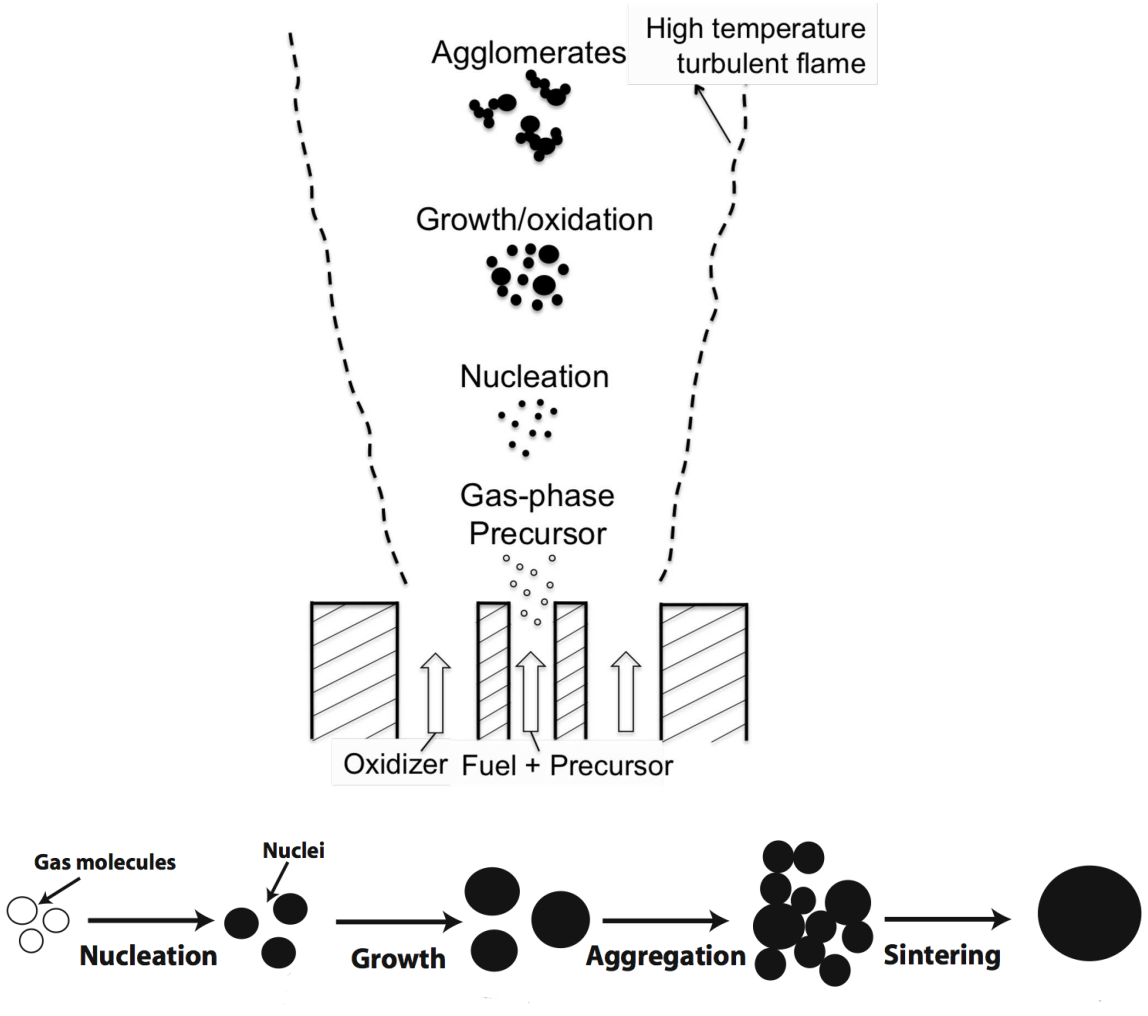

Figure 1.4 Flame synthesis of nanoparticles.

temperature flame. Here, the chemical reaction mechanism and particle growth mechanisms take over leading to nucleation, growth and further evolution of nanoparticles. The production of these nanoparticles is tightly coupled to turbulent combustion with different size nanoparticles being obtained at different flame heights. Flow configuration (fuel and oxidant flow rate and position) have also been found to effect the final product particles giving particles with different sizes and morphologies (70).

1.6 Chemical mechanisms

The chloride process, even though being the most widely used method for titanium dioxide production, is not well understood and the kinetics for this process remain incomplete (32). Experiments have been carried out (as discussed in the previous section) but the lack of thermochemical data has prevented the development of a detailed thermodynamically consistent mechanism. The chemical kinetics of $TiCl_4$ oxidation can be represented by chemical mechanisms with different degrees of complexity; one-step and detailed gas-phase mechanism.

Despite its commercial appeal, the kinetics of titania formation are not widely studied in the literature and most of the modeling work has been done with a global rate based on a one-step Ti oxidation reaction. The one-step model does not consider any Ti intermediates and thus, ignores the role intermediates could play in the gas-phase synthesis of nanoparticles. For a more detailed look at Ti oxidation, (100) have proposed a detailed mechanism. Even though the major purpose of the flame is to provide energy for TiO_2 formation, its presence complicates the already complex Ti oxidation chemistry. Fuel combustion is essentially a hydrocarbon oxidation reaction and this leads to competition between the fuel and the precursor for the oxygen present. Hence, the use of a comprehensive chemical mechanism would also lead to the accurate representation of interactions between the fuel and precursor.

1.6.1 One-step gas-phase mechanism

Pratsinis et al. (1990) (68) investigated the oxidation of $TiCl_4$ vapor between 973 °–1273 °K and reported the overall oxidation kinetics of $TiCl_4$ as a one-step reaction:

$$TiCl_4(g) + O_2(g) \longrightarrow TiO_2(s) + 2Cl_2(g). \tag{1.4}$$

The rate is first order with respect to $TiCl_4$ and nearly zero order for O_2 up to a ten-fold oxygen excess. This rate has been the basis of many numerical studies of TiO_2 nanoparticle formation (69; 82; 90; 55; 20; 21). However, the experiments used to develop the kinetic expression were performed at much lower temperatures than those encountered in flame reactors; hence, the use of one-step kinetics at higher temperatures should be done with caution. Also, the experiments done by Pratsinis et al. (68) are for $TiCl_4$:O_2 concentration ratios from 1:1 to 1:20 but in a flame reactor there could exist regions where these ratios are below 1:1. Thus, the use of the rate found by these experiments could lead to over-estimation of TiO_2 nanoparticle formation for these regions. The rate expression has a first-order dependence on $TiCl_4$ and zero-order dependence on O_2 up to a 10-fold excess. For higher O_2 concentrations, the rate is half order with respect to O_2. The reactions on the surface have also been modeled assuming the single-step reaction and the rate for surface reaction are found from experiments done by (16) in the temperature range of 400 ° – 850 ° C. (The chemkin mechanism file for one-step mechanism can be found in Appendix A.)

1.6.2 Detailed gas-phase mechanism

In has been argued (100) that the accurate modeling of nanoparticle formation in a flame reactor requires a detailed chemical mechanism that can properly represent the complex chemistry encountered in flames. In the past, the absence of thermochemical data prevented any simulations using detailed chemistry. West et al. (2007a) (98) performed DFT-based quantum calculations to determine the necessary thermochemical data and proposed the first thermodynamically consistent mechanism for $TiCl_4$ oxidation containing 25 species and 51 reactions (99), and recently extended it to 30 species and 66 reactions (100). Thermodynamic equilibrium studies based on the mechanism of West et al. (2007a) (98) suggest that at temperatures

above 600 K the critical nucleus size contains at least five Ti atoms. However, this mechanism does not include any species involving more than three Ti atoms, and in absence of molecules with more Ti atoms, West et al. (2007b) considered the collision of two molecules with two or more Ti atoms as a particle inception event. This transition from reversible gas-phase reactions to irreversible particle formation is considered to be premature and the nucleation rate computed by this assumption is expected to be an overestimate.

Therefore, this mechanism must be augmented with additional reactions before it can be used to predict nanoparticle nucleation. Following the suggestion of West et al. (2007b) (99), three collision-limited reactions to represent nanoparticle nucleation in this work are added to the mechanism of West et al. (2009) (100) :

$$Ti_2O_2Cl_4(g) + Ti_3O_4Cl_4(g) \longrightarrow Ti_5O_6Cl_8(s),$$

$$Ti_2O_2Cl_5(g) + Ti_3O_4Cl_4(g) \longrightarrow Ti_5O_6Cl_8(s) + Cl(g),$$

$$Ti_2O_2Cl_6(g) + Ti_3O_4Cl_4(g) \longrightarrow Ti_5O_6Cl_8(s) + Cl_2(g).$$

As mentioned before, in a flame the Ti-oxidation process is even more complex with flame chemistry becoming very important. The main purpose of the flame is to provide heat so that the Ti-oxidation reactions can take place as the initial $TiCl_4$ decomposition reactions are endothermic (refer to R1, R2, R3 in Table 1 of (98)) and require heat for their occurrence. As combustion of the fuel occurs, heat is provided for decomposition reactions to proceed, which starts the chain of reactions leading to the formation of Ti oxides. As fuel combustion is also an oxidation reaction, both hydrocarbon and Ti intermediates compete for oxygen in the flame. Because carbon lies higher than titanium in the oxygen reactivity series and also due to the fact that the initial $TiCl_4$ decomposition is endothermic, fuel combustion is initially the preferred reaction.

The fuel usually used is methane (CH_4) and hence, to take into account methane combustion chemistry GRI-Mech 2.11 (Bowman et al.) is included to model Ti oxidation in flames. The oxidation of $TiCl_4$ to form TiO_2 leads to the formation of chlorine gas (Cl_2). The presence of Cl_2 can lead to hydrocarbon chlorination, hence, methane chlorination chemistry as described in (79) is also added to the kinetics. The resulting detailed Ti oxidation mechanism, along with GRI-Mech 2.11 for methane combustion (Bowman et al.) and methane chlorination (79),

containing a total of 107 species and 500 reactions, is hereinafter referred as the detailed kinetic mechanism.

In summary, the chemical mechanism used in this work contains 86 species and 431 reactions for one-step Ti oxidation, and 107 species and 501 reactions for detailed Ti oxidation. The chemkin mechanism file for detailed mechanism can be found in Appendix A.

1.7 Modeling approaches

Prediction of particle properties in a flame reactor is a complex process involving chemical reactions, particle growth mechanism and turbulence. Thus, the computational model for nanoparticle production needs to provide not only the accurate expressions for these process, but also describe the interactions between them.

The evolution of particles in the flame reactor has been tracked through a population balance equation (PBE), which models the population of particles undergoing processes such as nucleation (creation), surface growth, aggregation (a collision which results in particles sticking together), and sintering (in which aggregates try to becomes more spherical). The effects of nucleation from the gas phase, aggregation and surface growth can be tracked using just one variable (usually volume). But to model sintering, in which particles tend to become more spherical and lose surface area, an additional variable (surface area) is required. Titania production has been modelled in literature with various combinations of the above stated particle evolution events. Table 1.1 provides a brief survey of the particle evolution events and methods used to solve the PBE previously.

Monodisperse models are the simplest and track just the average properties of particles. Hence, they are used to track a single property typically volume, or size (69). An extension to the monodisperse model is to allow each volume (or size) of particle to have a variable, but single, second parameter, such as average surface area (89) or number of primary particles (58). Although these models track two variables, a full population balance equations is not solved for the second variable. Thus, for example in Tsantilis and Pratsinis (2000) (89) particles of a certain size cannot have a distribution of surface areas, only an average. Models have been developed where two independent variables, like volume and surface area (106) or volume and

Table 1.1 Titania population balance models in literature

Article	**Chemistry**	**nucleation**	**surface growth**	**aggregation**	**sintering**	**PBE model**
Akhtar et al. ‘91 (1)	One-step	✓	×	✓	×	Sectional
Xiong and Pratsinis ‘91 (105)	One-step	✓	×	✓	×	Sectional and moments
Xiong and Pratsinis ‘93 (106)	One-step	✓	×	✓	✓	Sectional
Pratsinis and Spicer ‘98 (69)	One-step	✓	✓	✓	×	Monodisperse
Tsantilis and Pratsinis ‘00 (89)	One-step	✓	×	✓	✓	Sectional
Nakaso et al. ‘01 (57)	One-step	✓	×	✓	✓	Sectional
Mühlenweg et al. ‘02 (56)	One-step	✓	×	✓	✓	Sectional
Spicer et al. ‘02 (82)	One-step	✓	✓	✓	×	Moving sectional
Tsantilis et al. ‘02 (88)	One-step	✓	✓	✓	✓	Moving sectional
Moody and Collins ‘03 (53)	One-step	✓	×	✓	×	Moments
Jeong and Choi ‘03 (27)	One-step	✓	×	✓	✓	Sectional
Park and Rogak ‘03 (58)	One-step	✓	✓	✓	✓	Sectional
Tsantilis and Pratsinis ‘04 (90)	One-step	✓	✓	✓	×	Moving sectional
Morgan et al. ‘05 (54)	One-step	✓	✓	✓	✓	Stochastic
Heine and Pratsinis ‘07a (20)	One-step	✓	×	✓	✓	Sectional
Heine and Pratsinis ‘07b (21)	One-step	✓	×	✓	✓	Monodisperse
West et al. ‘07 (99)	Detailed	✓	✓	✓	✓	Stochastic
West et al. ‘09 (100)	Detailed	✓	✓	✓	✓	Stochastic
Mehta et al. ‘10 (51)	Detailed	✓	×	✓	×	Moments
Jethro et al. ‘11 (3)	Detailed	✓	✓	✓	✓	Moments
Sung et al. ‘11 (84)	Detailed	✓	×	✓	×	Moments
Sung et al. ‘12 (83)	Detailed	✓	×	✓	✓	Moments
Mehta et al. ‘12 (49)	Detailed	✓	✓	✓	✓	Moments

primary-particle volume (21) are tracked.

Sectional techniques divide the distribution into sections, and track the particle properties in each section. For each section an ordinary differential equation (ODE) is solved which is coupled to the neighboring sections based on a discretization scheme. But these schemes suffer from numerical diffusion (82). Numerical diffusion can be minimized by using a large number of sections but this adds to the computational cost. To alleviate these problems moving sectional techniques are used (39), which allow the boundaries between the sections to move. Sectional techniques are easy to solve with any common solvers for ODEs (22), but the computational cost of solving for every section is very high and the introduction of new variables to track more properties would lead to even higher computational cost.

Stochastic techniques have also been used to study this process (54; 99; 100). Stochastic techniques solve for the full multivariate particle population density, and, unlike sectional methods do not suffer from the numerical diffusion. In these methods the solution of population balance equation is approximated by an ensemble of N particles. This a major disadvantage of stochastic techniques, as to reduce statistical errors a large ensemble is required for the simulations. This leads to additional computational time being required for the solution.

Because of the high computational time required, both, sectional and stochastic methods, are not computationally viable for computational fluid dynamics (CFD) methods. The method of moments (MOM) remains computationally the most efficient approach to solve population balance equations for CFD applications. In these methods the first few moments of the size distribution are tracked and can be solved quickly with an ODE solver (47; 45). In moment methods, the population balance equations are replaced by transport equations for moments. Hence, by providing closures for these moment equations the particle size distribution is approximated. Even though moment methods do not solve for the full PBE, the lower order moments can be used to track all the useful information about the particle properties. Computational competitiveness and the presence of appropriate information in the lower moments, have led to the use of method of moments technique for modeling nanoparticle evolution process (51).

1.8 Need for modeling

As discussed above titania is an inorganic nanoparticle with ubiquitous uses in important areas. Majority of titania is produced by the chloride process and although this process has been used in the industry for decades (102), extensive research has not been carried out to understand its production in flame reactors.

In a flame reactor, the precursor is transported by a turbulent flow field, and encounters spatially varying gas composition and temperature fields, depending on the precursor injection configuration. Both precursor transport and reaction history affect particle evolution (such as nucleation and surface growth) and determine the final properties of the nanoparticles (e.g., relative surface area). The flow structure and turbulence are of major importance as they determine species and thermal energy transport and reactant mixing, flame quenching by air entrainment, and particle properties such as polydispersity, morphology, homogeneity, and crystallinity (19). Thus, in order to predict the particle properties produced by a turbulent flame reactor, it is necessary to have a detailed multiscale model that can capture all of the relevant processes. The gas-phase oxidation kinetics play a key role in the overall model because they determine the rate of nanoparticle nucleation and surface growth. In turn, these kinetics are strongly coupled the combustion kinetics through the temperature-dependent rate constants (i.e., the rate of nanoparticle nucleation is enhanced at higher temperatures).

Most of the models in the literature have used a over-simplified one-step chemistry (refer Table 1.1) which does not account for the complex Ti oxidation kinetics, methane combustion and chlorination as well as the coupling between these mechanisms. Even in the recent work by West (99; 100), which develops detailed chemistry, the nanoparticle nucleation event is an over-estimate and the mechanism doesn't study the effects of fuel combustion on Ti oxidation. Also, overlooked in previous works is the very important coupling of chemical kinetics with turbulence and mixing effects.

The evolution of the particle volume and surface area in the flame reactor can be tracked through a bivariate population balance equation (PBE), which models the evolution of particles undergoing processes such as nucleation, surface growth, aggregation, and sintering. In the

production of nanoparticles, it is found that reactors pass through different zones where only certain source terms of the population balance are dominant (9). Initially, mixing and kinetics are very important, which leads to the consumption of the precursor. Precursor consumption leads to the introduction of particles in the system and both the nucleation and growth term account for this increase in particle mass. After the precursor is consumed the evolution of product particles is generally governed by aggregation and sintering (i.e., loss of surface area at constant volume). Hence, the relative position in the flame where these particle evolution events occur determine the effect each event will have on the product properties.

The accurate modeling of combustion-based systems requires a comprehensive mechanism that captures the complex gas-phase chemical reactions leading to the production of the particles. This mechanism should precisely capture nanoparticle oxidation, as well as all of the hydrocarbon oxidation reactions taking place in the flame. Also needed is a correct description of the transition from the gas-phase species to the particulate phase and of further particle evolution (i.e., nucleation and surface growth). In flame synthesis, both fuel and nanoparticle precursor are sprayed into a pre-existing flame. The fuel evaporates and combusts, exposing the precursor to the high-temperature flame. Here, the chemical reaction mechanisms and particle growth mechanisms take over, leading to nucleation, growth and further evolution of nanoparticles. The production of these nanoparticles is tightly coupled to turbulent flames, with different size nanoparticles being obtained for different flame configurations (70). The prediction of particle properties in a flame reactor is complex, involving chemical reactions, particle growth mechanism and flame dynamics. Hence, a computational model for nanoparticle production needs to provide not only accurate expressions for the aforementioned processes, but also describe the interaction between them. This work aims to use the most detailed chemistry, represent all the particle evolution events and have a proper representation of flow fields, to give a detailed and comprehensive model for titania synthesis in flame reactors.

1.9 Layout of the report

Chapter 1 introduces the problem statement, builds background on titanium dioxide, and discusses the previous work done in the field and the reasons to improve and add to them.

Chapters 2-6 talk about the work done in course of this dissertation.

Chapter 2 explains population balance modeling methods and how they can be used to derive meaningful information for the nanoparticle synthesis. It also details how the source terms involved in the population balance equation are modeled for this system. Chapter 3 looks at the effect different chemical mechanisms have on prediction of particle properties. Chapter 4 describes the mechanism reduction carried which would facilitate the use detailed mechanism with complex flow solvers. Chapter 5 discuss the application of the population balance model into an industrial system.

Chapter 6 summarizes the progress made and draws conclusions from the results. It also details the future avenues of work which would be undertaken for completion of this dissertation. Additional information is provided in the Appendices. A bibliography concludes this dissertation.

CHAPTER 2. Population Balance Modeling

In which an overview of population balance modeling is presented. The quadrature method of moments for univariate case is explained. A bivariate distribution is proposed for our system and is then closed by using the conditional quadrature method of moments. The source terms used to solve the population balance equations are introduced and modeled for both one-step and detailed gas-phase mechanism. A new surface growth model is introduced for the detailed gas-phase mechanism.

2.1 Overview

The evolution of nanoparticles in a turbulent flame reactor can be described by a bivariate volume, surface-area population balance equation (PBE) containing terms for (1) nucleation, (2) surface growth, (3) aggregation, and (4) sintering (54). In the nucleation step, nuclei with a given volume and surface area are formed from the gas-phase species, with the formation of nuclei, surface reactions occur leading to growth in both volume and surface area of the particles. Aggregation occurs when two (or more) particles collide to form a single particle. As these agglomerates pass through high-temperature region of the flame, they tend to decrease their surface area by becoming more spherical. This process is known as sintering. The various evolution events lead to corresponding source terms appearing in the PBE.

Nucleation is the process by which gas phase molecules are transferred to the solid phase through the formation of nuclei and this leads to the addition of mass (or volume) into the particle phase in the form of nuclei. Surface reactions lead to further growth of the nuclei and they also add mass to the particle phase. Aggregation is a collisional growth process occurring due to particle-particle collisions. This leads to the formation of an agglomerate, which is an ensemble of primary particles attached by only point contacts.

Finally, when these agglomerates pass through high-temperature regions, the ensemble tries to minimize its surface area by undergoing temperature-dependent surface-relaxation processes wherein the agglomerate with a given volume tends towards a spherical shape, a process which is know as sintering. This leads to the formation of aggregates that are an ensemble of subparticles partially coalesced with each other. In contrast with an agglomerate, in the aggregate the particles have started to fuse into each other. It is important to note that coalescence (or sintering) cannot happen without collision (or aggregation). Only after the formation of an agglomerate, coalescence leads to the formation of aggregates and results in an increase in primary particle size. Full coalescence leads to a new primary particle while partial coalescence leads to the formation of aggregates.

The collision products start as agglomerates that, with solid-state sintering, may become aggregates and, given sufficient time and temperature, ultimately become larger primary particles. This complete transformation occurs in the high-temperature region of the flame. If the high-temperature region is relatively narrow, the transformation is arrested short of full coalescence into new primaries and as a result aggregates are formed. At lower temperatures where coalescence is negligible, these aggregates may start to collide with each other leading to the further formation of agglomerates.

Distinction between nuclei and primaries is important to understand, nuclei are formed after the phase change reactions and are the smallest solid phase entity introduced into the system. After the introduction of nuclei other particle evolution events result in the increase in the size of the introduced nuclei leading to the formation of primaries. Nucleation and aggregation do not have a direct effect in increasing primary sizes. Whereas, both surface growth and sintering lead to an increase in the primary size. Hence, after particle evolution in the flame, a primary particle is the smallest quantity present in the system.

In summary, nucleation leads to particle creation, and surface reactions lead to the growth of primary particles. Both surface growth and aggregation also lead to an increase in agglomerate size. Sintering is, however, different as when it occurs the agglomerate looses surface area and as the primary particles begin to coalesce some individual primaries in the agglomerate are eliminated resulting in larger primary size for the agglomerate. Sintering thus, leads to an effect

on both primary particle size as well as the aggregate surface area. The effects of nucleation from the gas phase, aggregation and surface growth can be tracked using just one variable (usually volume). But to model sintering, which leads to loss of surface area, an additional variable (surface area) will be required.

The predictive modeling of nanoparticles in flame reactors requires detailed chemical kinetics and particle evolution models as well as a correct description of the turbulent flame structure. Using computational fluid dynamics (CFD) to model nanoparticle synthesis in flame reactors has proven to be an important tool for understanding and implementing coupling between transport processes and chemical reactions (11). But the use of CFD with detailed models for chemistry, particle evolution and transport results in a new challenge, namely excessive computational time. The use of CFD techniques to model a turbulent flame would require the solution of the PBE at every grid point. Thus, the accurate solution of the PBE, while being computationally viable, is essential in the multiscale modeling of flame reactors.

Many different methods can be used to track the PBE such as sectional methods (106), moving sectional methods (82; 104), stochastic techniques (99) and moment methods (51). Sectional techniques divide the distribution into sections, and track the particle properties in each section. For each section an ordinary differential equation (ODE) is solved which is coupled to the neighboring sections based on a discretization scheme. But sectional schemes suffer from numerical diffusion in phase space, which can be minimized by using a large number of sections but this adds to the computational cost (82). To alleviate these problems moving sectional techniques are used (39), which allow the boundaries between the sections to move. Sectional techniques are easy to solve with any common solvers for ODEs (22), but the computational cost of solving for every section in a CFD solver would be intractable, and the introduction of new variables to track more properties would lead to even higher computational cost.

Stochastic techniques have also been used to study flame synthesis of nanoparticles (54; 99; 100). Stochastic techniques approximate the full multivariate particle population density, and, unlike sectional methods do not suffer from the numerical diffusion in phase space. In these methods the solution of population balance equation is approximated by an ensemble of N particles. This a major disadvantage of stochastic techniques, as to reduce statistical errors

a very large ensemble is required for the simulations. This leads to additional computational time being required for the solution, making them unsuitable for coupling with a CFD solver.

Because of the high computational time required, both sectional and stochastic methods, are not computationally viable for coupling with CFD solvers. The method of moments (MOM) remains computationally the most efficient approach to solve population balance equations for CFD applications. In these methods the first few moments of the size distribution are tracked and can be solved quickly with an ODE solver (47; 45). In moment methods, the population balance equations are replaced by transport equations for moments. Hence, by providing closures for these moment equations the particle size distribution is approximated. Even though moment methods do not solve for the full PBE, the lower-order moments can be used to track most of the useful information about the particle properties, such as total particle concentrations and primary sizes. Computational competitiveness and the presence of appropriate information in the lower moments have led to the use of moment methods for modeling nanoparticle evolution process in the context of CFD and titania synthesis has been successfully modeled in CFD simulations with the help of moment methods (51; 84).

A particular class of moment methods called the quadrature method of moments (QMOM) has found popularity when the PBE can be represented by only one internal coordinate (45; 52). QMOM can be thought of as a presumed PSD method with the PSD represented by weighted delta functions. The closure problem that arises by this representation is solved by finding out the weights and abscissas using the quadrature approximation (47). These methods are especially useful for CFD applications as they require the solution of a relatively small number of scalars (moments) at each grid point. Thus, QMOM provides us with an attractive alternative to solve the PBE while being computationally viable. Recently, Cheng et al. (2010) (6) introduced a conditional QMOM (CQMOM) which can be used to solve PBEs represented by two internal coordinates making the QMOM applicable for the cases where sintering is considered in the PBE as well.

2.2 Univariate distribution

The evolution of nanoparticles in a turbulent flame reactor can be described by a volume-surface PBE containing terms for nucleation, surface growth, aggregation, and sintering (106). As noted above the presence of sintering requires the consideration of an additional coordinate surface area. But as a first approximation sintering is neglected, hence the PBE can be written in terms of only the volume coordinate.

The corresponding univariate PBE is given by

$$\frac{\partial n(v)}{\partial t} + \frac{\partial G_v(v) n(v)}{\partial v} = J(T,\phi)\delta(v - v_0) + \frac{1}{2}\int_0^v n(v-u)n(u)q(v-u,u)du - n(v)\int_0^\infty n(u)q(v,u)du \quad (2.1)$$

where $n(v)$ $(\#/m^3)$ is the number density function (NDF) of nanoparticles with volume v, ϕ denotes the gas-phase species molar concentrations, v_0 is the volume of a nuclei, $q(v,u)$ is the aggregation kernel and repeated Roman indices imply summation. $J(T,\phi)$ is the nucleation rate and G_v is the growth rate.

2.3 QMOM

The direct solution of the PBE in a turbulent flow solver is intractable and unnecessary. Instead, using a MOM, the volume moments are defined by

$$m_k = \int_0^\infty v^k\, n(v)dv. \quad (2.2)$$

These moments have physical significance and can be compared to experimental data. For example, the zero-order moment m_0 is the particle number density (or particle concentration), and m_1 is the particle volume density (which is directly proportional to the mass concentration since the density of the solid is constant).

Thus, the univariate PBE in Eqn. (2.1) can then be replaced by the transport equations for the volume moments:

$$\frac{\partial m_k}{\partial t} = J(T,\phi)v_0^k - \int_0^\infty k v^{k-1} a^l G_v(v) f(v) dv + \int_0^\infty v^k \left(\frac{1}{2}\int_0^v n(v-u)n(u)q(v-u,u)du - n(v)\int_0^\infty n(u)q(v,u)du\right)dv, \quad (2.3)$$

where growth and the aggregation term are not closed. For univariate PBE, these terms are closed using the quadrature method of moments (QMOM) (47; 46).

The derivation for the moments equations and their representation in terms of weights and abscissas is done below for a more complex case of bivariate PBE (Section 2.5). Hence, these derivations are not repeated here.

2.3.1 Accuracy of QMQM

As noted earlier TiO_2 synthesis with simultaneous nucleation, surface growth, aggregation and sintering has been modeled using sectional methods (106; 82) where the full PBE is solved. To validate the use of moment methods, the accuracy of the QMOM approximation is checked by plotting the moments found by QMOM against those found by solving the full PBE. The solution to the full PBE (Eqn. 2.1), considering nucleation, growth and aggregation of particles, is found by the discretization method described by Kumar and Ramkrishna (38). Here, nucleation only depends on v and is given by

$$J(v) = (N_{0,n})/(v_{0,n}) \exp(-v/v_{0,n}) \tag{2.4}$$

where $N_{0,n} = 1$ and $v_{0,n} = 10^{-3}$. A constant growth ($G_v = 1$) and aggregation ($q(v,u) = 1000$) are used.

QMOM was implemented using three weights and three abscissas so this requires the first six moments of the PBE to be tracked. The definition of moments is as given in Eqn. 2.2. QMOM was found to track the first six moments quite accurately (see figure 2.1) with significant reduction in computing time.

Thus, the moment methods like QMOM are a useful way to solve the PBE. These methods contain adequate information about the PSD while being computationally viable.

2.4 Bivariate distribution

Including the sintering event, the PBE assume a bivariate form $f(v,a)$, which depends on two internal coordinates, volume (v) and surface area (a). The equation by which this

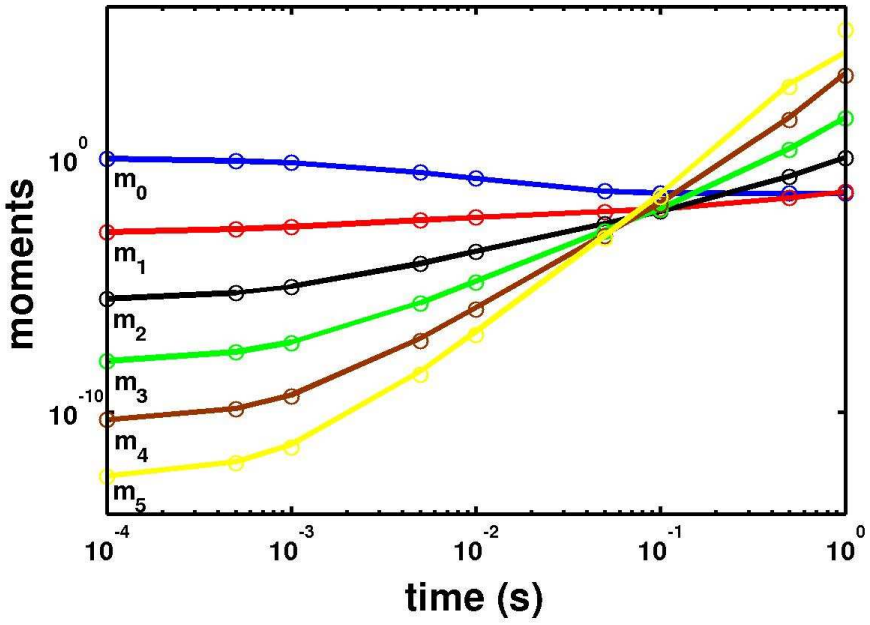

Figure 2.1 Comparison of the moments computed by full solution to the PBE (lines) and QMOM (symbols).

distribution function evolves in time can be written as

$$\frac{\partial f(v,a)}{\partial t} + \frac{\partial G_v(v,a) f(v,a)}{\partial v} + \frac{\partial G_a(v,a) f(v,a)}{\partial a} - \frac{\partial S_a(v,a) f(v,a)}{\partial a} = J(T,\phi)\delta(v-v_0)\delta(a-a_0) + B(v,a) - D(v,a) \quad (2.5)$$

where G_v and G_a are the growth rates of volume and surface area, respectively, due to surface growth, S_a is the rate of change of surface area due to sintering, J is the nucleation rate of particles from the gas phase, and

$$\begin{aligned} B &= \frac{1}{2}\int_0^a \int_0^v \beta(v-v^*, v^*, a-a^*, a^*) f(v-v^*, a-a^*) f(v^*, a^*) dv^* da^* \\ D &= \int_0^\infty \int_0^\infty \beta(v, v^*, a, a^*) f(v,a) f(v^*, a^*) dv^* da^* \end{aligned} \quad (2.6)$$

are the birth and death rates, respectively, due to aggregation. In the nucleation term, T is the gas-phase temperature, ϕ denotes the gas-phase chemical species, and it is assumed that nuclei have volume v_0 and surface area a_0.

2.5 Moment equations

The moments of the bivariate distribution function are defined by

$$m_{k,l} = \int_0^\infty \int_0^\infty a^l v^k f(v,a) dv da. \tag{2.7}$$

A transport equation for the moment $m_{k,l}$ can be found from Eqn. (2.5) by using

$$\int_0^\infty \int_0^\infty a^l v^k [\text{Eqn. (2.5)}] dv da \tag{2.8}$$

Given below is the derivation of each term separately.

The first term in Eqn. (2.8) is

$$\int_0^\infty \int_0^\infty a^l v^k \frac{\partial f(v,a)}{\partial t} dv da = \frac{d}{dt} \int_0^\infty \int_0^\infty a^l v^k f(v,a) dv da = \frac{dm_{k,l}}{dt}. \tag{2.9}$$

Using integration by parts, the volume growth term yields

$$\int_0^\infty \left(\int_0^\infty v^k \frac{\partial}{\partial v} [G_v(v,a) f(v,a)] dv \right) a^l da$$
$$= \int_0^\infty \left[v^k G_v(v,a) f(v,a) \Big|_0^\infty - \int_0^\infty k v^{k-1} G_v(v,a) f(v,a) dv \right] a^l da, \tag{2.10}$$

which, for $0 \leq G_v$,[1] reduces to

$$\int_0^\infty \int_0^\infty v^k a^l \frac{\partial}{\partial v} [G_v(v,a) f(v,a)] dv da = - \int_0^\infty \int_0^\infty k v^{k-1} a^l G_v(v,a) f(v,a) dv da. \tag{2.11}$$

Similarly, the area growth leads to

$$\int_0^\infty \left(\int_0^\infty a^l \frac{\partial}{\partial a} [G_a(v,a) f(v,a)] da \right) v^k dv$$
$$= \int_0^\infty \left[a^l G_a(v,a) f(v,a) \Big|_0^\infty - \int_0^\infty l a^{l-1} G_a(v,a) f(v,a) dv \right] v^k da, \tag{2.12}$$

which reduces to

$$\int_0^\infty \int_0^\infty v^k a^l \frac{\partial}{\partial a} [G_a(v,a) f(v,a)] dv da = - \int_0^\infty \int_0^\infty l v^k a^{l-1} G_a(v,a) f(v,a) dv da. \tag{2.13}$$

The sintering term yields

$$\int_0^\infty \left(\int_0^\infty a^l \frac{\partial}{\partial a} [S_a(v,a) f(v,a)] da \right) v^k dv$$
$$= \int_0^\infty \left[a^l S_a(v,a) f(v,a) \Big|_0^\infty - \int_0^\infty l a^{l-1} S_a(v,a) f(v,a) dv \right] v^k da \tag{2.14}$$

[1] For systems with negative growth (e.g. oxidation of soot) an additional term results for $m_{0,0}$ due to loss of particles

which reduces to

$$\int_0^\infty \int_0^\infty v^k a^l \frac{\partial}{\partial a}[S_a(v,a)f(v,a)]dvda \\ = -\int_0^\infty \int_0^\infty l v^k a^{l-1} S_a(v,a) f(v,a) dvda. \quad (2.15)$$

The nucleation term yields

$$\int_0^\infty \int_0^\infty J(T,\phi)\delta(v-v_0)\delta(a-a_0)a^l v^k dvda = J(T,\phi)v_0^k a_0^l. \quad (2.16)$$

Now, changing the order of integration and also changing the variables for the birth term due to aggregation in Eqn. (2.6) results in:

$$\int_0^\infty \int_0^\infty v^k a^l B(v,a)dvda \\ = \frac{1}{2}\int_0^\infty a^l \int_0^a \left[\int_0^\infty \left(\int_0^v \beta(v-v^*, v^*, a-a^*, a^*) f(v-v^*, a-a^*) f(v^*, a^*) dv^*\right) v^k dv\right] da^* da \quad (2.17)$$

and can be changed from Eqn. (2.17) by change in order of integration

$$= \frac{1}{2}\int_0^\infty a^l \int_0^a \left[\int_0^\infty \left(\int_{v^*}^\infty \beta(v-v^*, v^*, a-a^*, a^*) f(v-v^*, a-a^*) v^k dv\right) f(v^*, a^*) dv^*\right] da^* da \quad (2.18)$$

and by change in variables Eqn. (2.18) can be written as

$$= \frac{1}{2}\int_0^\infty a^l \int_0^a \left[\int_0^\infty \left(\int_0^\infty \beta(v', v^*, a-a^*, a^*) f(v', a-a^*)(v'+v^*)^k dv'\right) f(v^*, a^*) dv^*\right] da^* da \quad (2.19)$$

Performing the same operations with respect to a as well would lead to

$$= \frac{1}{2}\int_0^\infty \int_0^\infty \int_0^\infty \int_0^\infty (v'+v^*)^k (a'+a^*)^l \beta(v', v^*, a', a^*) f(v', a') f(v^*, a^*) dv^* da^* dv' da', \quad (2.20)$$

which can be finally written as

$$\int_0^\infty \int_0^\infty v^k a^l B(v,a)dvda = \frac{1}{2}\int_0^\infty \int_0^\infty \int_0^\infty \int_0^\infty (v+v^*)^k (a+a^*)^l \\ \beta(v, v^*, a, a^*) f(v,a) f(v^*, a^*) dv^* da^* dvda. \quad (2.21)$$

Using the symmetry of the aggregation kernel ($\beta(v,v^*,a,a^*)=\beta(v^*,v,a^*,a)$), the death term can be written as

$$\int_0^\infty\int_0^\infty v^k a^l D(v,a)dvda = \frac{1}{2}\int_0^\infty\int_0^\infty\int_0^\infty\int_0^\infty \left(v^k a^l + v^{*k}a^{*l}\right) \beta(v,v^*,a,a^*)f(v,a)f(v^*,a^*)dv^*da^*dvda. \quad (2.22)$$

Collecting all of the terms in Eqn. (2.8) yields the unclosed moment equation:

$$\begin{aligned}\frac{dm_{k,l}}{dt} = J(T,\phi)v_0^k a_0^l &- \int_0^\infty\int_0^\infty kv^{k-1}a^l G_v(v,a)f(v,a)dvda \\ &- \int_0^\infty\int_0^\infty lv^k a^{l-1}\left[G_a(v,a)-S_a(v,a)\right]f(v,a)dvda \\ &+ \frac{1}{2}\int_0^\infty\int_0^\infty\int_0^\infty\int_0^\infty \left[(v+v^*)^k(a+a^*)^l - v^k a^l - v^{*k}a^{*l}\right] \\ &\beta(v,v^*,a,a^*)f(v,a)f(v^*,a^*)dv^*da^*dvda. \quad (2.23)\end{aligned}$$

Because of the nonlinearities present in the growth and aggregation kernels, the right-hand side of this equation is not closed in terms of the moments. In order to proceed, a closure approximation is needed to represent the distribution function. As described in Sec. 2.6, the unclosed terms will be closed using the conditional quadrature method of moments (CQMOM).

2.6 CQMOM

For univariate cases quadrature method of moment (QMOM) can be used to solve the PBE accurately and efficiently (46). However, in a bivariate system, a method is needed that can reconstruct the distribution function in terms two internal coordinates. Thus, to solve for multivariate cases, the conditional quadrature method of moments (CQMOM) proposed by Cheng et al. (2010) (6) is used. CQMOM is similar to QMOM in the sense that the moment equations are represented by a set of weights and abscissas. For N-point accuracy, N sets of weights and abscissas are needed, which can be found by inversion of $2N$ moments.

The basic idea behind CQMOM is that the weights and abscissas of the second internal coordinate can be conditioned on the first, and the third on the second, and so on. For this case, first the weights and abscissas are found in the volume direction (obtaining w_i and v_i) and

then for each w_i and v_i, the weights ($w_{i,j}$) and abscissas ($a_{i,j}$) are found in the area direction to construct the bivariate moment-based PBE.

Using CQMOM, the distribution function is approximated by

$$f(v,a) = \sum_{i=1}^{N_v}\sum_{j=1}^{N_a} w_i w_{i,j}\delta(v-v_i)\delta(a-a_{i,j}). \tag{2.24}$$

Thus the CQMOM approximation for the moments is

$$m_{k,l} = \sum_{i=1}^{N_v}\sum_{j=1}^{N_a} w_i w_{i,j} v_i^k a_{i,j}^l. \tag{2.25}$$

Applying CQMOM to Eqn. (2.11) yields

$$\int_0^\infty\int_0^\infty k v^{k-1}a^l G_v(v,a)f(v,a)dvda = \sum_{i=1}^{N_v}\sum_{j=1}^{N_a} k w_i w_{i,j} v_i^{k-1} a_{i,j}^l G_v(v_i,a_{i,j}). \tag{2.26}$$

Similarly, the area growth and sintering lead to

$$\begin{aligned}\int_0^\infty\int_0^\infty l v^k a^{l-1}\left[G_a(v,a)-S_a(v,a)\right]f(v,a)dvda \\ = \sum_{i=1}^{N_v}\sum_{j=1}^{N_a} l w_i w_{i,j} v_i^k a_{i,j}^{l-1}\left[G_a(v_i,a_{i,j})-S_a(v_i,a_{i,j})\right].\end{aligned} \tag{2.27}$$

Applying quadrature, the aggregation terms become

$$\begin{aligned}\int_0^\infty\int_0^\infty v^k a^l\left[B(v,a)-D(v,a)\right]dvda \\ = \frac{1}{2}\sum_{i=1}^{N_v}\sum_{j=1}^{N_a}\sum_{m=1}^{N_v}\sum_{n=1}^{N_a} w_i w_{i,j} w_m w_{m,n}\beta(v_i,a_{i,j},v_m,a_{m,n}) \\ \left[(v_i+v_m)^k(a_{i,j}+a_{m,n})^l - v_i^k a_{i,j}^l - v_m^k a_{m,n}^l\right].\end{aligned} \tag{2.28}$$

Collecting all of the terms, the closed moment equation can be obtained:

$$\begin{aligned}\frac{dm(k,l)}{dt} = J(T,\phi)v_0^k a_0^l + \sum_{i=1}^{N_v}\sum_{j=1}^{N_a} k w_i w_{i,j} v_i^{k-1} a_{i,j}^l G_v(v_i,a_{i,j}) \\ + \sum_{i=1}^{N_v}\sum_{j=1}^{N_a} l w_i w_{i,j} v_i^k a_{i,j}^{l-1}\left[G_a(v_i,a_{i,j})-S_a(v_i,a_{i,j})\right] \\ + \frac{1}{2}\sum_{i=1}^{N_v}\sum_{j=1}^{N_a}\sum_{m=1}^{N_v}\sum_{n=1}^{N_a} w_i w_{i,j} w_m w_{m,n}\beta(v_i,a_{i,j},v_m,a_{m,n}) \\ \left[(v_i+v_m)^k(a_{i,j}+a_{m,n})^l - v_i^k a_{i,j}^l - v_m^k a_{m,n}^l\right].\end{aligned} \tag{2.29}$$

The solution of Eq. (2.29) requires an algorithm to find the weights (w_i and $w_{i,j}$) and abscissas (v_i and $a_{i,j}$) from the moments. N_v and N_a weights and abscissas are used in the volume and surface-area directions, respectively. Typically, $N = 3$ nodes provides accurate predictions.

To find the weights and abscissas from the moments using CQMOM, the following steps are performed (6):

1. Given $m_{k,0} = \langle v^k \rangle$ for $k = 0, \ldots, 2N_\mathrm{v} - 1$, use the Wheeler algorithm (101) to find $\{w_i, v_i\}$ for $i = 1, \ldots, N_\mathrm{v}$.

2. For each $l = 1, \ldots, 2N_\mathrm{a} - 1$, solve for $\langle a^l \rangle_i$ using a linear system derived from $m_{k,l} = \langle v^k a^l \rangle = \sum_{p=1}^{N_\mathrm{v}} w_i v_i^k \langle a^l \rangle_i$ for $k = 0, \ldots, N_\mathrm{v} - 1$. For example with $l = 1$, $m_{k,1} = \sum_{i=1}^{N_\mathrm{v}} w_i v_i^k \langle a \rangle_i$ generates a linear system with a Vandermonde matrix:

$$\begin{bmatrix} 1 & 1 & 1 \\ v_1 & v_2 & v_3 \\ v_1^2 & v_2^2 & v_3^2 \end{bmatrix} \begin{bmatrix} w_1 & & \\ & w_2 & \\ & & w_3 \end{bmatrix} \begin{bmatrix} \langle a \rangle_1 \\ \langle a \rangle_2 \\ \langle a \rangle_3 \end{bmatrix} = \begin{bmatrix} m_{0,1} \\ m_{1,1} \\ m_{2,1} \end{bmatrix},$$

   which is solved to find $\langle a \rangle_i$:

$$\begin{bmatrix} \langle a \rangle_1 \\ \langle a \rangle_2 \\ \langle a \rangle_3 \end{bmatrix} = \begin{bmatrix} 1/w_1 & & \\ & 1/w_2 & \\ & & 1/w_3 \end{bmatrix} \begin{bmatrix} 1 & 1 & 1 \\ v_1 & v_2 & v_3 \\ v_1^2 & v_2^2 & v_3^2 \end{bmatrix}^{-1} \begin{bmatrix} m_{0,1} \\ m_{1,1} \\ m_{2,1} \end{bmatrix}.$$

3. For each i, use the Wheeler algorithm to invert the moments $\langle a^l \rangle_i$ for $l = 0, \ldots, 2N_\mathrm{a} - 1$ to find $\{w_{i,j}, a_{i,j}\}$.

The moments needed to solve the bivariate case used in this work are given in Table 2.1 for $N_\mathrm{v} = N_\mathrm{a} = 3$.

The bivariate PBE is finally closed by the help of CQMOM with the weights and abscissas of the defined moments.

2.7 Models for the PBE source terms

The evolution of nanoparticles can be tracked by the population balance equation (PBE). This PBE is written in terms of source terms, for nucleation, growth, aggregation and sintering.

Table 2.1 Moment list for bivariate-CQMOM case with $N_{\mathrm{v}} = N_{\mathrm{a}} = 3$.

$m_{0,0}$	$m_{0,1}$	$m_{0,2}$	$m_{0,3}$	$m_{0,4}$	$m_{0,5}$	
$m_{1,0}$	$m_{1,1}$	$m_{1,2}$	$m_{1,3}$	$m_{1,4}$	$m_{1,5}$	
$m_{2,0}$	$m_{2,1}$	$m_{2,2}$	$m_{2,3}$	$m_{2,4}$	$m_{2,5}$	
$m_{3,0}$	$\downarrow$	$\downarrow$	$\downarrow$	$\downarrow$	$\downarrow$	
$m_{4,0}$	$\langle a \rangle_1$	$\langle a^2 \rangle_1$	$\langle a^3 \rangle_1$	$\langle a^4 \rangle_1$	$\langle a^5 \rangle_1$	$\rightarrow \{w_{1,j}, a_{1,j}\}$
$m_{5,0}$	$\langle a \rangle_2$	$\langle a^2 \rangle_2$	$\langle a^3 \rangle_2$	$\langle a^4 \rangle_2$	$\langle a^5 \rangle_2$	$\rightarrow \{w_{2,j}, a_{2,j}\}$
$\downarrow$	$\langle a \rangle_3$	$\langle a^2 \rangle_3$	$\langle a^3 \rangle_3$	$\langle a^4 \rangle_3$	$\langle a^5 \rangle_3$	$\rightarrow \{w_{3,j}, a_{3,j}\}$
$\{w_i, v_i\}$						

After using the method of moments, the source terms of the PBE can be written in terms of its weights and abscissas. Providing models for these source expressions, in terms of these weights and abscissas, the PBE equation can be closed and solved to provide valuable information about the system. This section provides the source terms for these particle evolution expressions. The source terms below are derived for a bivariate PBE.

2.7.1 Nucleation

Particle nucleation is a very important first step that leads to further particle evolution events. In the nucleation step, nuclei with a given volume and surface area are formed from the gas-phase species. As this inception depends on creation of particles from the gas phase by reactions involving intermediates, the rates of nucleation are based on the concentration of these intermediates involved. As the two chemical mechanism studied have very different reactions and intermediates the nucleation expression for both are quite different.

2.7.1.1 One-step model

For one-step chemistry, the single step reaction Eqn. (1.2) leads to nucleation. Each TiO_2 molecule with $v_0 = 3.32 \times 10^{-29}$ m^3 and $a_0 = 5 \times 10^{-19}$ m^2 is treated as nuclei. The nucleation rate is found by remembering that the single step reaction leads to both nucleation and surface growth (82).

$$J(T, \phi) = \max(0, k_{\mathrm{total}} - k_{\mathrm{s}} A) N_{\mathrm{av}} [\mathrm{TiCl_4}] \tag{2.30}$$

where $k_{\text{total}} = 8.26{\times}10^4 \exp(-10681/T)$ (1/s) is the total oxidation constant, $k_{\text{s}} = 49 \exp(-8993/T)$ (m/s) is the surface oxidation rate, $A = m_{0,1}$ (m^2/m^3) is the particle surface area concentration, N_{av} is Avogadro's number.

2.7.1.2 Detailed model

To take into account the effect of the intermediate species encountered in a flame reactor on the nucleation event (Eqn. 1.6.2), for the detailed mechanism the postulated reactions leading to the formation of $Ti_5O_6Cl_8$ is treated as a nucleation event with each $Ti_5O_6Cl_8$ molecule treated as a nuclei (51). Note that the $Ti_5O_6Cl_8$ is assumed to undergo an instantaneous surface oxidation reaction to replace the Cl atoms by O atoms:

$$Ti_5O_6Cl_8(s) + 2O_2(g) \longrightarrow Ti_5O_{10}(s) + 4Cl_2(g)$$

so that the final composition of the nuclei is Ti_5O_{10} with $v_0 = 16.60 \times 10^{-29}$ m^3 and $a_0 = 14.6 \times 10^{-19}$ m^2. Thus, in comparison to the one-step reaction, the detailed mechanism will produce a nuclei that is five times larger. These assumptions result in a nucleation rate defined as (51)

$$J(T, \phi) = k_{\text{nucl}} N_{\text{av}} [Ti_5O_6Cl_8][O_2]^2 \tag{2.31}$$

where the gas-phase chemical concentrations appearing on the right-hand side are found from the detailed kinetic model. This reaction is assumed to be diffusion limited and irreversible so that the pre-exponential factor is $k_{\text{nucl}} = 10^{25}$ [$\text{cm}^6/(\text{mol}^2\text{s})$] and the activation energy in the exothermic direction is zero.

2.7.2 Surface Growth

As TiO_2 nuclei are formed, they may undergo surface reactions that leads to deposition of titania from gas phase. The mechanism by which gas-phase species oxidize directly on the nanoparticle surface instead of forming nuclei has been examined both by experiments (81) and through computational methods (25; 99). However, due to lack of progress in obtaining kinetic data for this surface growth process, this study, like other population balance models before it (69; 82; 90; 55; 99), uses the rate expression based on experiments done by Ghoshtagore (16).

The deposition of titania on the surface, leads to both the increase in volume and area. Hence, two separate expressions for growth, one for growth in volume and the other for area are given.

For volume growth rate is modeled by

$$G_v(v,a) = k_{\mathrm{s}}[\mathrm{TiCl_4}]N_{\mathrm{av}}v_0 a. \tag{2.32}$$

The surface growth is related to volume growth by (59)

$$G_a(v,a) = G_v(v,a)\frac{da}{dv} = G_v(v,a)\frac{2}{r}, \tag{2.33}$$

which can be written in terms of a using the effective radius $r = \sqrt{a/4\pi}$ (59):

$$G_a(v,a) = 4\left(\frac{\pi}{a}\right)^{1/2} G_v(v,a) = 4k_{\mathrm{s}}[\mathrm{TiCl_4}]N_{\mathrm{av}}v_0\sqrt{\pi a}. \tag{2.34}$$

Note that other definitions of r are also possible (59). These growth expression are referred in the following text as the *simple* growth expressions.

As stated earlier, the fundamentals of Ti oxidation are not well understood as both chemical reactions and particle evolution events happen extremely rapidly. Competition between gas-phase and surface reactions during the particle formation process is critical to particle properties (69). Based on their studies, (69) found that at high $TiCl_4$ concentrations result in high concentrations of TiO_2 nuclei, that have enough surface area to consume $TiCl_4$ by surface reactions and effectively quench gas-phase oxidation of $TiCl_4$. At the other extreme, low $TiCl_4$ concentrations produce a low concentration of TiO_2 nuclei which results in not enough area being available for surface reactions to compete with gas-phase oxidation. In addition, additives used to control the size of titania particles (107) will likely have an impact on surface growth rates and hence detailed investigation of the surface growth events is of major importance. In the absence of kinetic data, estimation for growth rate has been primarily modeled using the simple expression (Eq. 2.32). Recently, (80) have given a expression for surface growth of titania. They assume that initial decomposition of $TiCl_4$ is slow such that, in their reactor simulations, over 99% of Ti atoms in gaseous phase are contained in $TiCl_4$ at all times (80). Thus, $TiCl_4$ is the most important gaseous intermediate and the proposed rate is based on an Eley-Rideal model that consists first of $TiCl_4$ adsorption followed by reaction with O_2.

The high temperatures encountered in the flame reactor result in fast $TiCl_4$ decomposition and hence other gaseous intermediates are also expected to play an important role in surface reactions. The elaborate description of the Ti-oxidation process in the detailed mechanism with a large number of intermediates, leads us to propose a different description of surface growth. Precursor decomposition leads to the formation of a large number of intermediates and as discussed above intermediates and reactions leading to $Ti_5O_6Cl_8$ determine the nucleation event. For the new growth expression, it is assumed that intermediates after decomposition contribute both to nucleation and the surface growth process based on the specified rates. Following this assumption, all intermediates (except $Ti_5O_6Cl_8$) undergo surface reactions leading to deposition of titania on the surface of the nuclei. The rate expressions describing the surface reactions for different intermediates are assumed to be the same as described by Ghoshtagore (16). Following this assumption the volume growth rate for detailed mechanism is given by

$$G_{\mathrm{v}} = k_{\mathrm{s}} \sum [\mathrm{Ti}_x\mathrm{O}_y\mathrm{Cl}_z] N_{\mathrm{av}} v_0 a \tag{2.35}$$

where $\sum[\mathrm{Ti}_x\mathrm{O}_y\mathrm{Cl}_z]$ is the sum of all gaseous Ti species in the system except $Ti_5O_6Cl_8$. Here, $k_{\mathrm{s}} = 49\exp(-8993/T)$ (m/s) is the surface oxidation rate (16). The surface growth is related to volume growth by relation discussed above and hence the surface growth rate is

$$G_{\mathrm{a}} = 4\left(\frac{\pi}{a}\right)^{1/2} G_{\mathrm{v}} = 4k_{\mathrm{s}} \sum [\mathrm{Ti}_x\mathrm{O}_y\mathrm{Cl}_z] N_{\mathrm{av}} v_0 \sqrt{\pi a}. \tag{2.36}$$

These new growth expressions are referred as *detailed* growth expressions in the rest of the text.

2.7.3 Aggregation

Collision between nanoparticles is an important process that is responsible for the formation of structured particle clusters, such as aggregates and agglomerates. The aggregation step proceeds through particle-particle collisions, the frequencies of which depend on the nanoparticle volumes and gas-phase properties (e.g. temperature and viscosity). As more particle are nucleated in the system the probability of their collision rises, which leads to the formation of large aggregates.

The model for the aggregation kernel is (13)

$$\beta(v, v^*, a, a^*) = \frac{2RT}{3\mu N_{\text{av}}} \left(\frac{1}{v^{1/d_{\text{f}}}} + \frac{1}{(v^*)^{1/d_{\text{f}}^*}} \right) \left(v^{1/d_{\text{f}}} + (v^*)^{1/d_{\text{f}}^*} \right) \tag{2.37}$$

where R is the gas constant, and μ the gas viscosity. In this work the fractal dimension is taken to be 2.5 assuming diffusion-limited aggregation. Note the aggregation rate (Eqn. 2.37) increases quadratically with number density and linearly with temperature.

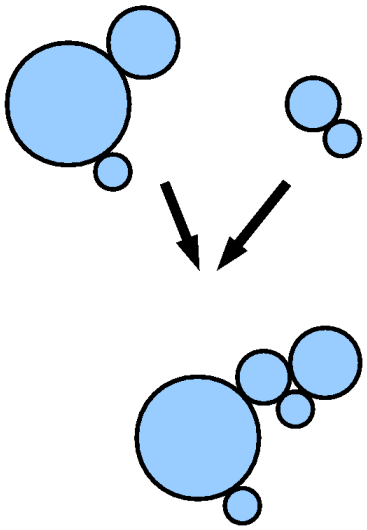

Figure 2.2 Aggregation event occurs by particle particle collision.

2.7.3.1 Fractal dimension

Fractals are an excellent model to characterize the morphology of clusters of particles formed by aggregation. The fractal dimensions provide the indication of the compactness of aggregates. The fractal dimension can be found from the moment information assuming $d_{\text{f}} = 3$ when $a = a_{\text{min}}$, $d_{\text{f}} = 1.7$ when $a = a_{\text{max}}$ and doing a linear interpolation for the values of a in between. $a_{\text{min}}(v, a)$ is the same as a_{s} and a_{p} described below and $a_{\text{max}}(v) = a_0(v/v_0)$. This

leads to the expression of $d_{\mathrm{f}}(v,a)$ as:

$$d_{\mathrm{f}}(v,a) = \frac{1.3a + 1.7a_{\min}(v,a) - 3a_{\max}(v)}{a_{\min}(v,a) - a_{\max}(v)}. \tag{2.38}$$

It should be noted that for each $\beta(v,a,v^*,a^*)$, two d_{f} are used: $d_{\mathrm{f}} = d_{\mathrm{f}}(v,a)$ and $d_{\mathrm{f}}^* = d_{\mathrm{f}}^*(v^*,a^*)$.

2.7.4 Sintering

The sintering step is modeled as a temperature-dependent surface-relaxation process wherein a particle with a fixed volume tends towards a spherical shape. Sintering occurs after particle nucleation and aggregation, and is much faster at high temperatures such as inside the flame. Hence, the relative amount of sintering will depend strongly on whether the particles are formed before or after the flame surface.

The rate of sintering of a particle, consisting initially of two separate, spherical particles contacting each other, can be approximately described by Koch and Friedlander (36)

$$S_a(v,a) = \frac{1}{\tau_{\mathrm{f}}}(a - a_{\mathrm{s}}) \tag{2.39}$$

where a is the surface area, v the volume of the particle and a_{s} is the surface area of a solid sphere with volume v.

Several attempts have been done to extend Eqn. (2.39) for more complicated shapes (37; 12; 92; 41). The points-of-contact (POC) model introduced by Johannessen (28) is used in this work:

$$S_a(v,a) = \begin{cases} \frac{(a-a_{\mathrm{s}})}{\tau_{\mathrm{f}}(d_{\mathrm{p}}^*)} & \text{if } n_{\mathrm{p}} \leq 2 \\ (n_{\mathrm{p}} - 1)\left(\frac{0.41 a_{\mathrm{p}}}{\tau_{\mathrm{f}}(d_{\mathrm{p}})}\right) & \text{if } n_{\mathrm{p}} > 2 \end{cases} \tag{2.40}$$

where $a_{\mathrm{s}} = (36\pi v^2)^{1/3}$, $d_{\mathrm{p}}^* = (3v/\pi)^{1/3}$, $d_{\mathrm{p}} = 6v/a$, $a_{\mathrm{p}} = 36\pi v^2/a^2$ and $n_{\mathrm{p}} = a^3/(36\pi v^2)$. The sintering time τ_{f} is found by

$$\tau_{\mathrm{f}}(x) = k_0 x^m \frac{T}{T_0} \exp\left[\frac{E_{\mathrm{a}}}{R}\left(\frac{1}{T} - \frac{1}{T_0}\right)\right] \tag{2.41}$$

where $k_0 = 1 \times 10^{28}$ m^{-4}, $T_0 = 1400$ K, $m = 4$, R is the gas constant and $E_{\mathrm{a}} = 1.5 \times 10^5$ J/mol (108).

When $n_{\mathrm{p}} < 2$, the rate of sintering is proportional to the excess surface, $(a - a_{\mathrm{s}})$, and follows Eqn. (2.39). But when $n_{\mathrm{p}} > 2$, the sintering rate at each point of contact is proportional to an

excess surface area of $(2a_{\mathrm{p}} - a_{2.\mathrm{p,s}})$ with sintering diameter d_{p} and $a_{2.\mathrm{p,s}} = 2^{2/3}a_{\mathrm{p}}$ the surface area of a sphere with volume $2v_{\mathrm{p}}$. The number of contact points is assumed to be $n_{\mathrm{p}} - 1$.

Sintering only leads to the decrease in area and has no effect on the volume of the aggregates. As mentioned before, all the other particle evolution events: nucleation, growth and aggregation lead to an increase in the surface area of our system. The only exception being sintering, which due to its tendency of making irregular particles more spherical leads to a decrease in surface area.

2.8 Chapter Summary

A nonlinear integro-differential equation for the evolution of the size distribution of nanoparticles in a flame reactor called the population balance equation (PBE) was introduced in this chapter. Also introduced was an efficient method for the solution of these equations in the univarite case, using the quadrature method of moments (QMOM) approach. These equations become bivariate, when sintering is also involved in the model. Hence, conditional quadrature method of moments (CQMOM) for solution of these equations is used and the closure for moment equations in terms of weights and abscissas of the distribution function are provided.

Also introduced were models for nucleation, growth, aggregation and sintering by which the PBEs evolve. We can now solve for nanoparticle particle size distribution in flame reactors accurately with this complete PBE model.

CHAPTER 3. Effect of Chemical Mechanism

In which the effect of chemical mechanism on the nucleation event is investigated for one-step and detailed mechanism using plug flow and partially stirred reactor model. The effect of the chemical mechanisms on different flow configurations is studied. It is found that the location of maximum nucleation depends on the choice of mechanism used. Also explored are the roles of gas-phase and surface phase reactions.

3.1 Introduction

Ti oxidation chemistry can be described by two gas-phase mechanisms; one-step and detailed chemistry. Most models for titania production use the one-step chemistry for modeling. But with the introduction of detailed kinetics by West et al. (2009) (100), now detailed chemistry can be also be used to model this process. In this chapter first, the effect of different chemical mechanisms (i.e., one-step, detailed, flamelet) on the prediction of nanoparticle nucleation is investigated using a plug-flow reactor (PFR) and a partially stirred tank reactor (PaSR) to model the flow field. These simulations demonstrate that particle nucleation occurs much later in the flame with detailed titanium oxidation chemistry as compared to one-step chemistry. It has also been shown that the use of different flow configurations leads to products with distinct properties (70). Thus, the effect of chemical mechanisms on flow configurations is also explored by developing a full population balance model with nucleation, growth, aggregation and sintering.

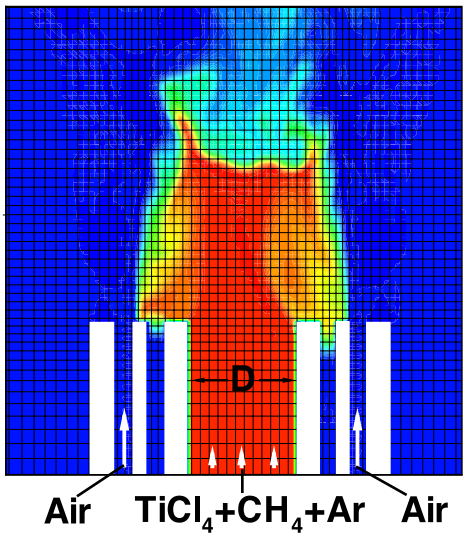

Figure 3.1 Configuration of inlets for flame reactor corresponding to the experiment.

3.2 Effect of chemical mechanism on nucleation

For titanium dioxide nanoparticles manufactured in flame reactors, the precursor is injected into a pre-existing flame exposing it to a high-temperature gas phase, leading to nucleation and particle growth. Predictive modeling of this chemical process requires simultaneous development of detailed chemical mechanisms describing gas-phase combustion and particle evolution as well as advanced computational tools for describing the turbulent flow field and its interactions with the chemical processes. To facilitate this interaction, a flamelet model representing detailed chemistry for particle nucleation is proposed. The effect of different chemical mechanisms (i.e., one-step, detailed, flamelet) on the prediction of nanoparticle nucleation is investigated using a plug-flow reactor (PFR) and a partially stirred tank reactor (PaSR) to model the flow field. These simulations demonstrate that particle nucleation occurs much later in the flame with detailed titanium oxidation chemistry as compared to one-step chemistry. For the three different mechanisms GRI-Mech 2.11 (Bowman et al.) was used for methane combustion. Titanium chemistry was modeled either using one-step or detailed titania oxidation.

3.2.1 Model Description

Since this section aims to look at only the effect of the chemical mechanism on nucleation events, a univariate PBE accounting for the nucleation and aggregation events is solved using quadrature method of moments (QMOM) (Section 2.3). The corresponding univariate PBE is given by

$$\frac{\partial n(v)}{\partial t} = S_v(T,\phi)\delta(v-v_0) + \frac{1}{2}\int_0^v n(v-u)n(u)q(v-u,u)du - n(v)\int_0^\infty n(u)q(v,u)du \quad (3.1)$$

where $n(v)$ $(\#/m^3)$ is the number density function (NDF) of nanoparticles with volume v, ϕ denotes the gas-phase species molar concentrations, v_0 is the volume of a nuclei and $q(v,u)$ is the aggregation kernel. For the one-step reaction, the nucleation rate is given by

$$S_v(T,\phi) = \max(0, k_{\text{total}} - k_s A) N_{\text{av}}[\text{TiCl}_4] \quad (3.2)$$

where N_{av} is Avogadro's number, the surface reaction rate constant is

$$k_s(T) = 49\exp(-8993/T) \quad (\text{m/s}), \quad (3.3)$$

and $A = \pi m_0 (6m_1/(\pi m_0))^{2/3}$ (m^2/m^3) is the particle surface area concentration and m_0 and m_1 are moments of the PBE. Note that for the one-step reaction, each TiO_2 molecule is treated as a nuclei with $v_0 = 3.32 \times 10^{-29}$ m^3, and thus (in the absence of aggregation where $m_1/m_0 = v_0$) the one-step reaction will produce a larger number of nanoparticles. The nucleation expression for detailed mechanism remains the same as listed in Eqn. (2.31). Assuming the particle collisions are generated by Brownian motion, aggregation is given by Eqn. (2.37).

The PBE in Eqn. (3.1) can then be replaced by the transport equations for the volume moments:

$$\frac{\partial m_k}{\partial t} = S_v(T,\phi)v_0^k + \int_0^\infty v^k \left(\frac{1}{2}\int_0^v n(v-u)n(u)q(v-u,u)du - n(v)\int_0^\infty n(u)q(v,u)du\right)dv, \quad (3.4)$$

where the aggregation term is closed using QMOM. The PBE is represented by six moment transport equations based on volume (Eqn. (3.4) with $k = 0, 1, \ldots, 5$). Comparison of the lower-order moments between different chemical mechanisms will give us an idea about the effect of the chemical mechanism on nucleation.

3.2.2 Scaling of moments

The moments of the PBE evolve based on chemistry, as reactions occur nanoparticles nucleate and then aggregation proceeds. As this evolution depends on chemical time-scales, moments m_k can vary over many orders of magnitude in a short period of time. Hence, these moments equations are inherently stiff. A log scaled version of the moments equations is used to tackle the stiffness of the original set of equations. Following log scaling the moments are transformed into:

$$m_k^* = \ln(m_k), \tag{3.5}$$

which results in the the moment equations (Eqn. (3.4)) transforming into

$$\frac{dm_k^*}{dt} = \exp^{-m_k^*} S\left(m_k\right) \tag{3.6}$$

where, $S\left(m_k\right)$ is the RHS of the moment equation computed with moment m_k (Eqn. (3.4)).

The logarithmic scaling of the moment set has proven to reduce the stiffness of the problem, making the computation efficient. Log-scaled moments are used in the remainder of this work.

3.2.3 Flamelet tables

To model gas phase chemistry three different models are used; one-step, detailed and flamelet tables. The flamelet model parametrizes the thermochemical composition of the gas phase using the mixture fraction, which is a conserved scalar (63). The steady-flamelet assumption has been used successfully to model a wide-range of flame configurations (66; 72; 33; 87; 63). In the steady-flamelet model, one-dimensional flamelet equations are solved *a priori* and the results stored in a look-up table. Essentially, the one-dimensional equations correspond to a counter-diffusion flame (63). Any gas-phase composition, ϕ, can be retrieved as:

$$\phi = \mathcal{H}(\xi, \chi), \tag{3.7}$$

where $\mathcal{H}$ is the flamelet mapping, ξ is mixture fraction, and χ is the stoichiometric mixture fraction dissipation rate. Here, the scalar dissipation rate is fixed at 80.0 s^{-1} . This high value is intended to model the high shear region immediately downstream of the nozzle, where most of the nucleation occurs. In the PaSR simulations described below, mixture fraction is evolved as a scalar and the gas-phase composition obtained using the above relation. The flamelet tables are constructed using the FlameMaster code (65). The mixture-fraction dimension in the look-up table is discretized using 1000 points. Note that using a single mixture fraction restricts the applicability of the flamelet table to a reactor with two inlet streams (11).

In summary, while using a flamelet model a look-up table is constructed based on the chemistry before the start of the simulation. This flamelet table is parametrized by mixture fraction (mixture fraction dissipation rate remains constant in this work). Thus, during the course of the simulation the gas-phase properties like temperature and concentration of species can be found by looking up the previously generated table, using the current mixture fraction values.

3.2.4 PFR model

The flame reactor is first modeled as a partially-premixed jet of precursor/fuel/air entraining the surrounding air. The plug-flow assumption allows us compare the evolution of the volume moments of the NDF for each chemical mechanism under idealized conditions (i.e., no back mixing of fluid). Initial conditions for the PFR are found from the mass flow rates of CH_4 (fuel), $TiCl_4$ (precursor), Ar (inert gas) and air (oxidant) for Flame 11 in Pratsinis et al. (1996) (70). Since the temperature and concentrations in a PFR evolve with time due to chemical reactions and entrainment of air, the flamelet assumption is not directly applicable (11). Therefore, only the one-step and the detailed mechanisms are compared in the PFR.

The partially-premixed PFR is modeled assuming a two-environment micromixing model (11), where a round jet of precursor/fuel/air issuing from the central nozzle (environment 1) entrains the surrounding air (environment 2). The evolution of composition variables in

environment 1 ($\langle\phi\rangle_1$) can be represented by

$$\begin{aligned} \frac{dp_1}{d\tau} &= \gamma(1-p_1)p_1, \\ \frac{d\langle\phi\rangle_1}{d\tau} &= \gamma(1-p_1)(\langle\phi\rangle_2 - \langle\phi\rangle_1) + \frac{d_{\text{jet}}}{v_{\text{jet}}} S(\langle\phi\rangle_1), \end{aligned} \tag{3.8}$$

where $\tau = tv_{\text{jet}}/d_{\text{jet}}$ is dimensionless time from which the fluid left the nozzle, v_{jet} is the inlet velocity of the jet, d_{jet} is the inlet diameter of the jet, p_1 is the mass fraction of environment 1, $\langle\phi\rangle_i$ is the composition vector of the ith environment, $\gamma = 0.0094$ is the spreading rate of a turbulent round jet (67), and S represents the composition source term due to chemical reactions. It is assumed that no reactions take place in environment 2, and thus $\langle\phi\rangle_2$ is constant (i.e., found from the conditions of the surrounding air). The initial condition for p_1 is set to 1.415×10^{-5}, and that for $\langle\phi\rangle_1$ are discussed below. Note that p_1 grows monotonically towards unity, representing the entrainment of surrounding air.

3.2.5 PaSR model

In order to relax the highly idealized mixing assumptions used in the PFR, a PaSR is also used to model the flame reactor under partially stirred conditions. PaSR models, which are essentially the application of a stochastic Monte-Carlo process to approximate the solution of the transport equation for the joint probability density function (PDF) of all reactive species (77), can be used to model well-macromixed turbulent reacting flows. In the modeling of turbulent reacting flows based on PDF methods, the fluid composition changes by both reaction source terms and by mixing (11). The change in composition due to reaction is treated exactly, while molecular mixing has to be modeled. Modeling mixing in a PaSR involves prescribing the evolution of stochastic particles in such a way that they mimic the change in composition of a fluid particle due to mixing in a turbulent reactive flow (73). In the PaSR, the residence time distribution is assumed to be exponential, corresponding to a well-macromixed reactor (11). Thus, in comparison to the PFR with no back mixing between fluid particles, the PaSR has maximum back mixing of the fluid.

In this work, the stochastic simulation of the PaSR uses 1000 particles (n). Each particle carries information about its mixture fraction, enthalpy, species mass fractions (ϕ) and six

volume moments. The PaSR is fed with two inlet streams, one stream injecting $TiCl_4$, mixed with CH_4 and Ar and the other stream injecting air with mass flow rates corresponding to Flame 11 (70). The mean residence time for each particle in the PaSR is 15.4×10^{-2} s. The modified Curl's approach (73) is used to model molecular mixing in the PaSR with a characteristic mixing time of 1.25×10^{-2} s. The initial conditions are set to ensure that combustion occurs, and the simulation is allowed to reach steady state (approximated three mean residence times) before data are collected. The code for the PaSR model can be found in Appendix B.

3.2.6 PFR results

The PFR model is used for both the one-step and the detailed nucleation mechanisms with the initial conditions given in Table 3.1. For the PFR results, only nucleation is considered and particle aggregation is disabled in the models. The temperature profiles for both cases evolve similarly (see Figure 3.2). The maximum flame temperature occurs at about $\tau = 80$, but the evolution of number density (m_0) follows a different pattern for each case. For the one-step mechanism (see Figure 3.2(a)), $TiCl_4$ is consumed very rapidly at temperatures above 1000 K so that all of the nucleation occurs by $\tau = 15$, after which the number density decreases as the jet is diluted with air. In comparison, the detailed nucleation model (see Figure 3.2(b)) produces a relatively small number particles at approximately $\tau = 30$ followed by a much larger number after $\tau = 100$ (i.e. after the flame surface).

Table 3.1 Initial conditions for PFR

Parameter	Environment 1	Environment 2
Temperature (K)	1080	333
Ar (mass fraction)	0.332	0
CH_4 (mass fraction)	0.166	0
N_2 (mass fraction)	0.309	0.767
O_2 (mass fraction)	0.094	0.233
$TiCl_4$ (mass fraction)	0.099	0

With the detailed nucleation mechanism, the maximum nucleation rate occurs in the tem-

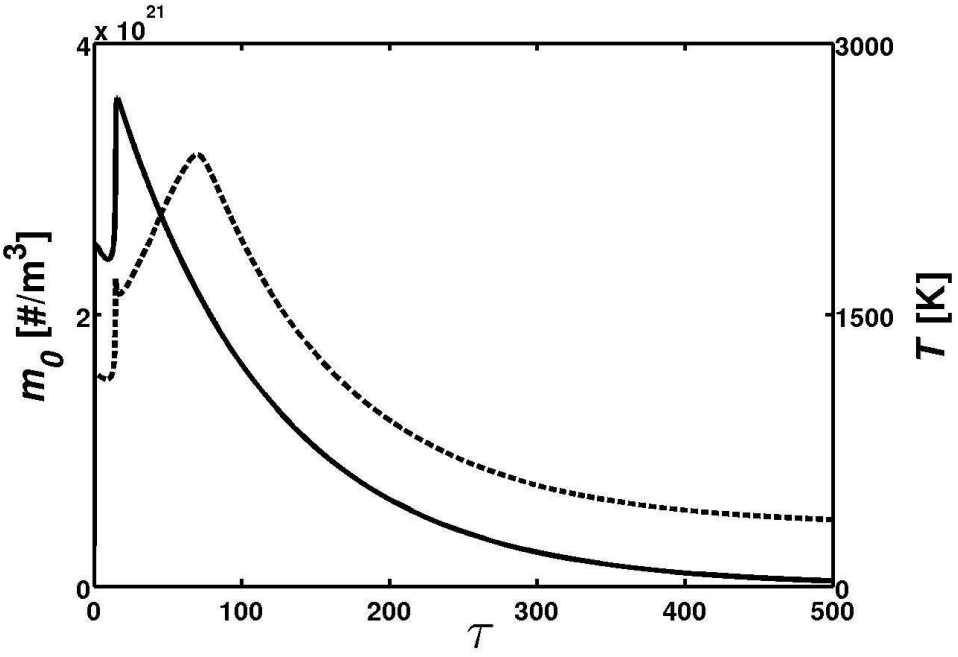

(a) One-step nucleation

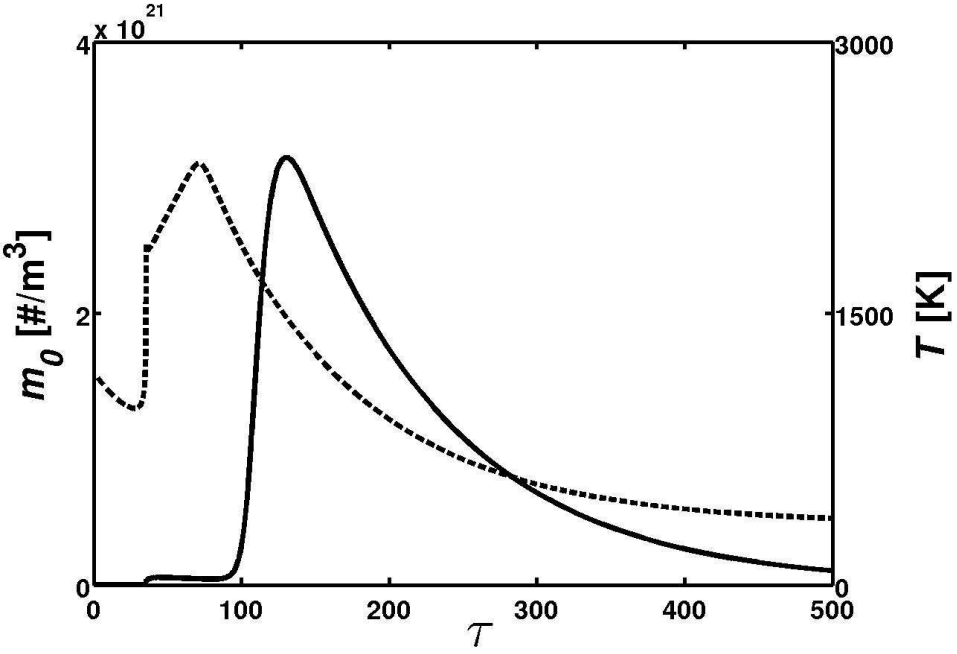

(b) Detailed nucleation

Figure 3.2 Evolution of number density (solid) and temperature (dashed) in PFR.

perature range $T = 1500$–1800 K, while outside this range nucleation is negligible. Since in the PFR the flame temperature passes through this range on both the rich side ($\tau < 90$) and the lean side ($\tau > 90$) of the flame, two bursts of nucleation are observed. In contrast, for the one-step nucleation mechanism, the precursor is completely reacted once the temperature reaches 1600 K for the first time ($\tau < 30$). These observations imply that for the one-step reaction all of the particles will be formed upstream of the flame surface, and then will subsequently pass through the high-temperature region of the flame where particle sintering can take place. In contrast, for the detailed mechanism most of the particles are formed downstream from the high-temperature flame surface and, hence, would be less susceptible to sintering. We can thus conclude that the choice of the nucleation model will have a strong effect on the predicted particle properties (e.g. sintered vs. non-sintered) since the two models predict very different locations in the flame for particle nucleation.

3.2.7 Evolution of Ti species in detailed mechanism

As noted earlier the detailed mechanism has a preferential temperature range of $T = 1500$–1800 K for production of nuclei. Hence, the evolution of the important Ti species in the detailed mechanism is studied to have a closer look at the kinetics of the nucleation event.

Observing the concentration plots for Ti species evolution, it is noted that, initially the rise in temperature ($\tau \sim 30$) leads to production of $TiOCl_2$, Ti dimers ($Ti_2O_2Cl_4$, $Ti_2O_2Cl_5$, $Ti_2O_2Cl_6$) and higher Ti molecules ($Ti_3O_4Cl_4$, $Ti_5O_6Cl_8$) (Figure 3.3). It is seen with increase in temperature most Ti prefers to remain in $TiOCl_2$ (from $\tau = 30$ till $\tau = 90$). But as temperature decreases $TiOCl_2$ dimerizes to $Ti_2O_2Cl_4$, which remains the most preferred intermediate during the rest of the simulation. The temperature goes down with further progression in the flame and it is found that at lower temperatures (below $T = 750$ K), Ti also has an affinity to exist as another stable dimer $Ti_2O_2Cl_6$. The dimer $Ti_2O_2Cl_5$ exists in very low concentrations compared to the other dimers and is not expected to play a significant role in the nucleation process. Hence, it is found that the concentration of $Ti_2O_2Cl_4$ increase with decrease in temperature and below a temperature of $T = 1400$ K it holds constant (the slow decrease seen in figure 3.3 is due to dilution by the entraining air). The concentration of $Ti_2O_2Cl_6$ increase at

even lower temperatures (from $T = 600$–750 K) and after this holds steady.

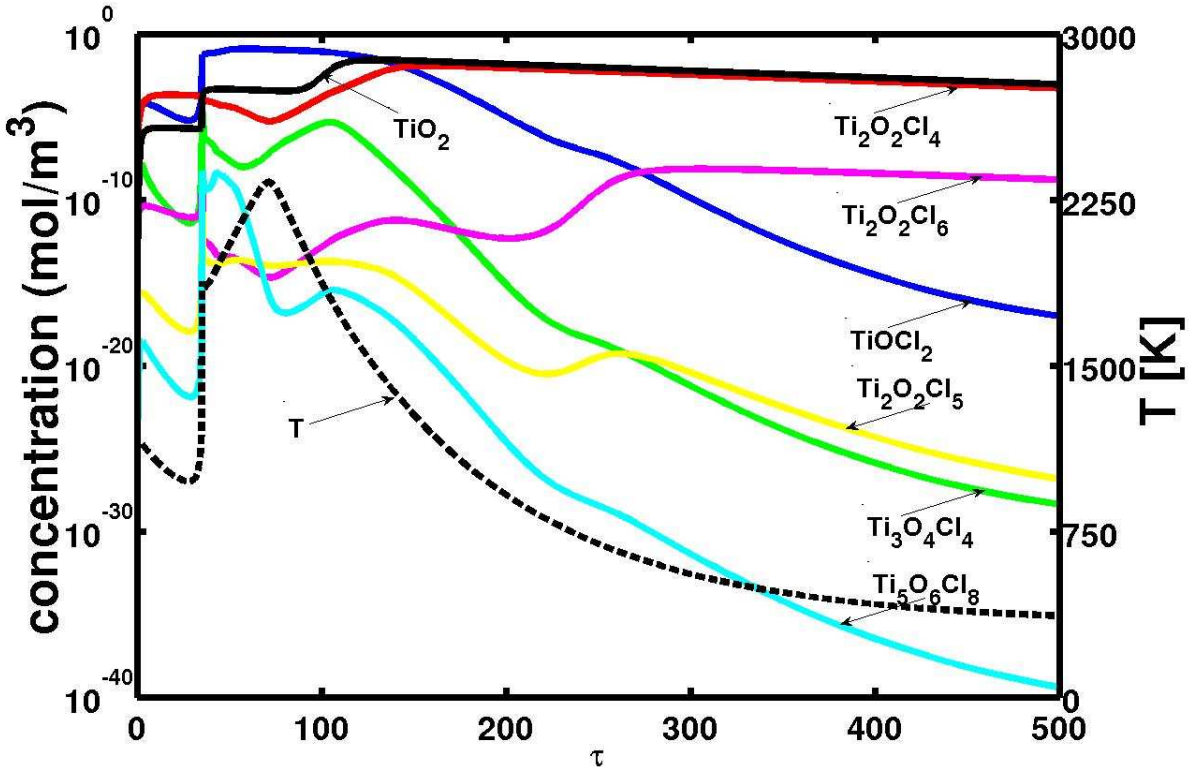

Figure 3.3 Evolution of Ti species with temperature for detailed mechanism.

It should be remembered that both Ti oxidation and CH_4 combustion are competing for oxygen. Initially, most of the O_2 is consumed by CH_4 and this leads to the combustion and rise in temperature. With the rise in temperature the Ti oxidation rates increase and higher Ti molecules are formed. The rapid combustion also leads to CH_4 consumption and hence, more oxygen is present to form higher Ti molecules. The concentration of high Ti molecules first increase with (up till $\tau = 110$) but with enough oxygen present these molecules are converted into TiO_2, which leads to decrease in their concentrations at later times.

Due to the fact that the PFR model evolves only by nucleation, the plot for TiO_2 concentrations have a direct collaboration with evolution of number density (compare Figures 3.2(b) and 3.4(a)). Looking at plots for detailed mechanism it is found (as stated earlier) that location for maximum nucleation is in temperature range of $T = 1500$–1800 K (from $\tau = 100$

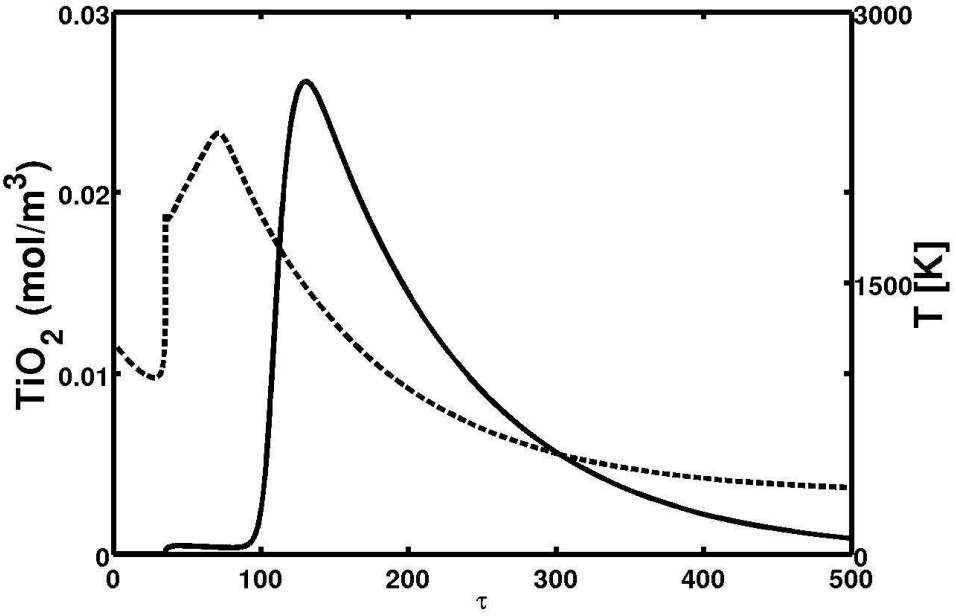

(a) Profile for TiO_2 production

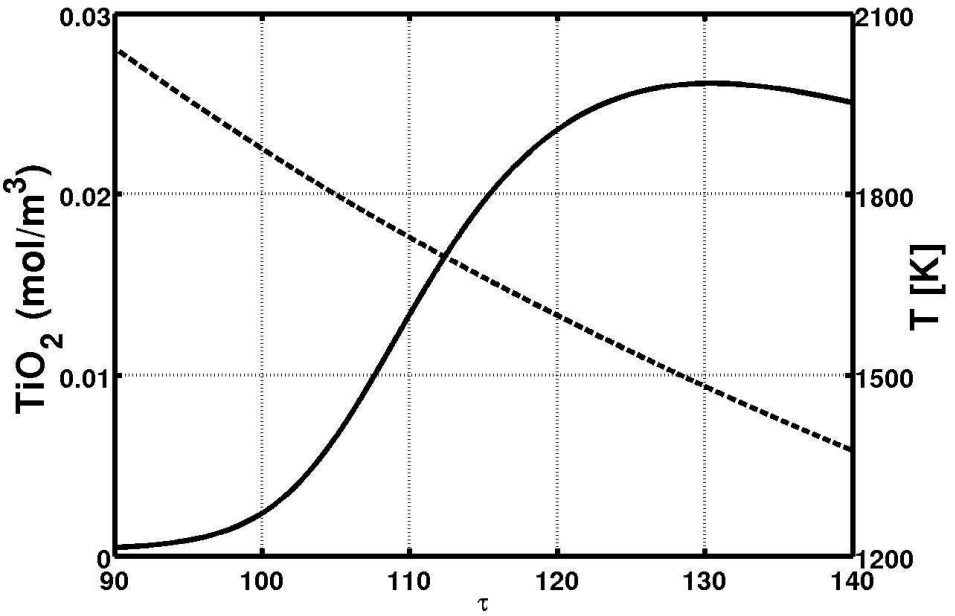

(b) Location of maximum TiO_2 formation

Figure 3.4 Evolution of TiO_2 (solid) and temperature (dashed) in PFR.

till $\tau = 130$). The concentration of TiO_2 is the highest at $\tau = 130$ when the temperature is $T = 1500$ K.

In summary, it is concluded that the detailed mechanism for Ti oxidation prefers to form $Ti_5O_6Cl_8$ (the molecule whose oxidation leads to TiO_2) in a temperature range of $T = 1500$–1800 K in the flame. For other temperatures, Ti molecules in the system either prefer to be in $TiOCl_2$ (at high temperatures) or in its dimer, $Ti_2O_2Cl_4$. Consequently, based on the kinetics and the given model most of the nucleation for the detailed mechanism would occur in the temperature range of $T = 1500$–1800 K.

3.2.8 PaSR results

The PaSR model with the inlet conditions given in Table 3.2 is used to run the six different cases listed in Table 3.3. The combustion chemistry is treated either by using the detailed kinetic mechanism or by using a flamelet approximation. The nucleation chemistry is treated either by using one-step or detailed chemistry. In the two "all flamelet" cases, the combustion and nucleation chemistry are tabulated into one flamelet table.

Neglecting surface growth we find that each particle cluster contains a collection of primary particles. The total number of primary particles N_p in an agglomerate is related to the particle diameter d_p through a power-law expression based on the fractal dimension (13)

$$N_\mathrm{p} = A \left(\frac{d_p}{d_\mathrm{po}} \right)^{d_f}, \tag{3.9}$$

where d_po is the diameter of monodispersed primary particle, found from the respective v_o. For one-step $d_\mathrm{po} = 3.98 \times 10^{-10}$ m and for the detailed nucleation $d_\mathrm{po} = 6.82 \times 10^{-10}$ m. The value of A varies with different values of d_f but if Eqn. (3.9) holds for $d_p \to d_{po}$ ($N_\mathrm{p} \to 1$), then A has a value of unity. The total volume of the cluster can then be calculated by multiplying N_p by the primary particle volume v_0. The total volume of the cluster can also be found by dividing the first volume moment (m_1) by the zeroth volume moment (m_0). This leads to

$$N_\mathrm{p} v_o = \left(\frac{m_1}{m_0} \right) \tag{3.10}$$

Then using the expression for N_p from Eqn. (3.9), we can find the particle diameter d_p by

$$d_\mathrm{p} = d_\mathrm{po} \left(\frac{m_1}{m_0 v_o} \right)^{1/d_f}. \tag{3.11}$$

The results reported in Table 3.3 were averaged over all n particles used in the PaSR. Thus,

$$\langle T \rangle = \frac{\sum_{i=0}^{n} T(i)}{n}, \quad \langle m_0 \rangle = \frac{\sum_{i=0}^{n} m_0(i)}{n}, \quad \langle d_\mathrm{p} \rangle = \frac{\sum_{i=0}^{n} d_\mathrm{p}(i)}{n}, \tag{3.12}$$

give us the average value of T, m_0 and d_p, respectively.

Table 3.2 Inlet conditions for PaSR

Parameter	Initial	Stream 1	Stream 2
Mass Flow Rates (mg/s)	–	97.08	10.92
Temperature (K)	1400	333	333
Ar (mass fraction)	0	0	0.555
CH_4 (mass fraction)	0	0	0.278
N_2 (mass fraction)	0.767	0.767	0
O_2 (mass fraction)	0.233	0.233	0
$TiCl_4$ (mass fraction)	0	0	0.167

The high air flow rates used in the experiments lead to immediate combustion and consumption of the precursor at the entrance of the jet. This leads to the production of nuclei immediately upstream of the jet. As this paper aims to look at the effect of the chemical mechanisms on nucleation, the residence time of the PaSR was chosen so as to predict the nucleation of particles in the upstream regions of the jet. Shorter residence times would ensure that nucleation dominates and the effect of using different mechanisms on the particle inception process can be studied. The scalar dissipation was fixed at 80.0 s^{-1} for the PaSR simulation. This high value is intended to model the high shear region immediately downstream of the nozzle, where most of the nucleation takes place.

The plots shown in Figure 3.5(a) for both the detailed flame, one-step nucleation and the detailed flame, detailed nucleation reach the same temperature distribution at steady state. This tells us that the Ti-oxidation chemistry has no effect on the flame temperature for either the one-step or detailed nucleation. The predictions of temperature for all the cases involving flamelets depend on the mixture fraction and mixture-fraction dissipation rate. As the same mixing time and the mixture-fraction dissipation rate are used for all the cases involving flamelets, the temperature evolution and the steady-state temperature are the same for all

cases involving flamelets (Figure 3.5(b)).

The one-step nucleation produces more nuclei ($\langle m_0 \rangle = 7.26 \times 10^{18}$ 1/m^3) than detailed chemistry ($\langle m_0 \rangle = 1.06 \times 10^{18}$ 1/m^3). This is expected as the nuclei size for one-step chemistry is five times smaller than for detailed chemistry, and thus it produces about five times more nuclei than the detailed mechanism. Because of the high air flow rates, most of the precursor is consumed on the lean side of the flame (here $\xi_{\text{air}} = 0$ and $\xi_{\text{fuel}} = 1$). Thus we see that most of the nucleation happens near the mean mixture fraction at steady state ($\xi = 0.1$) for all the models (Figure 3.6). Similar to the PFR, the nucleation as predicted by the one-step mechanism occurs on the lean side of the flame ($\xi < 0.1$). In contrast, for the detailed mechanism nucleation occurs both on the lean ($\xi < 0.1$) and on the rich side ($\xi > 0.1$) of the flame. We also see from these figures that the flamelet assumption can be used to represent the chemistry with reasonable accuracy (see Figures 3.6(b) and 3.6(f)); however, it does tend to over-predict the nucleation rate on the lean side of the flame (compare Figures 3.7(b) and 3.7(f)).

As the particles are formed immediately upstream of the jet in the PaSR, the mean particle sizes predicted by all mechanisms are on the order of 10 nm (see Table 3.3). Both the back mixing in the PaSR and the high air flow rates ensure that the particles are distributed very close to mean mixture fraction. The PaSR simulations look at the region very close to the jet exit. Thus, we observe that the particles have just started aggregating after nucleation in the PaSR, but the aggregation event has not started to dominate nucleation, which would result in larger particles.

Table 3.3 Average temperature, number density, and cluster diameter in PaSR

Case	$\langle T \rangle$, K	$\langle m_0 \rangle$, #/m^3	$\langle d_p \rangle$, nm
Detailed flame chemistry, one-step nucleation	1440	7.26×10^{18}	6.92
Detailed flame chemistry, detailed nucleation	1408	1.06×10^{18}	5.48
Flamelet, one-step nucleation	1305	1.76×10^{19}	8.38
Flamelet, detailed nucleation	1328	4.54×10^{17}	3.47
All flamelet with one-step nucleation	1303	1.78×10^{19}	8.46
All flamelet with detailed nucleation	1316	2.04×10^{18}	5.86

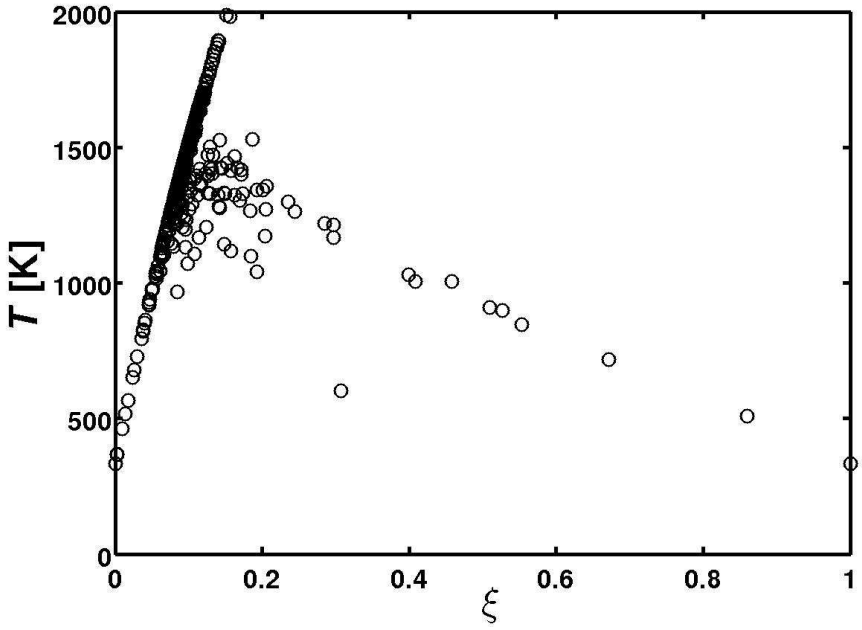

(a) Detailed flame chemistry

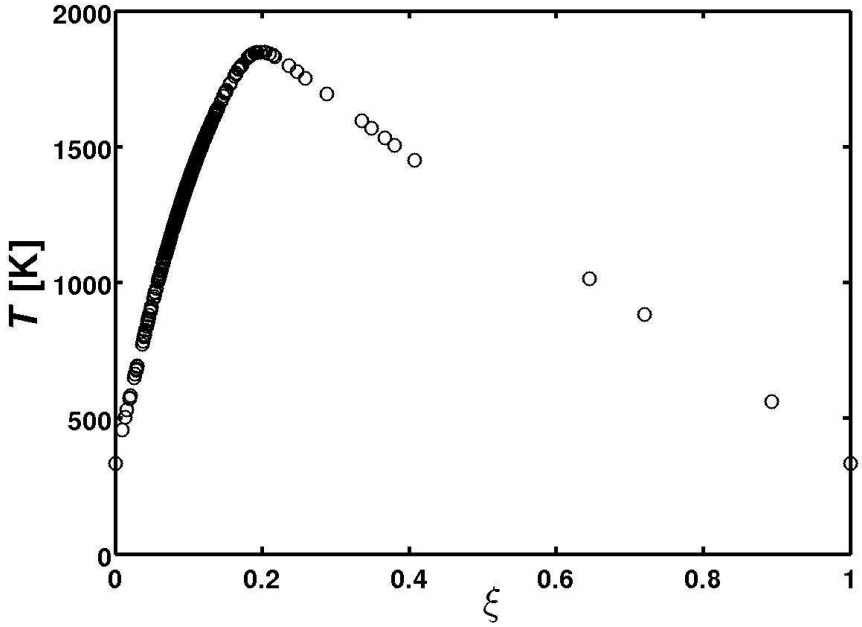

(b) Flamelet chemistry

Figure 3.5 Scatter plots of temperature (T) versus mixture fraction (ξ) in PaSR.

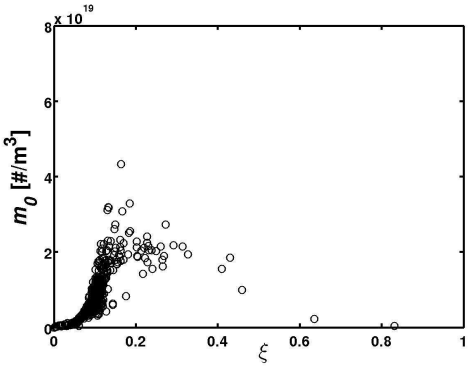

(a) Detailed flame, one-step nucleation

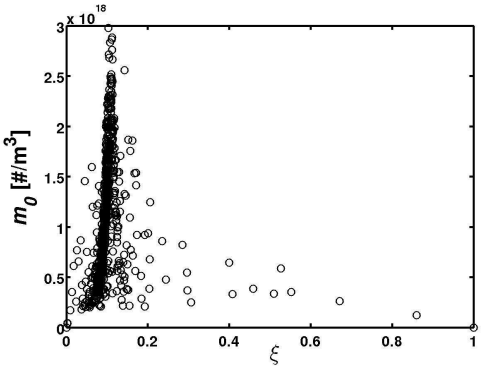

(b) Detailed flame, detailed nucleation

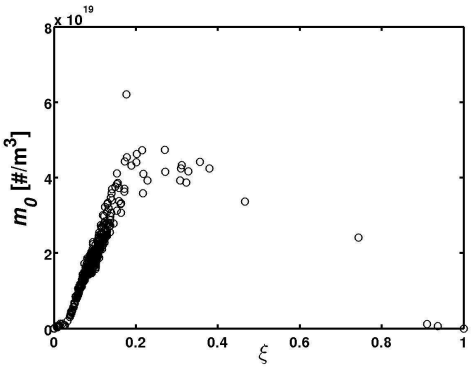

(c) Flamelet, one-step nucleation

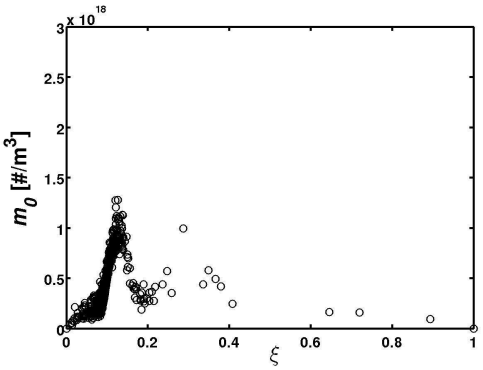

(d) Flamelet, detailed nucleation

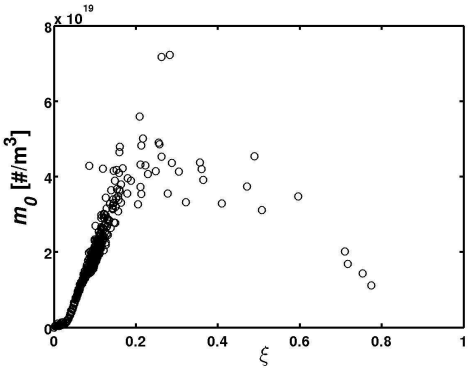

(e) All flamelet, one-step nucleation

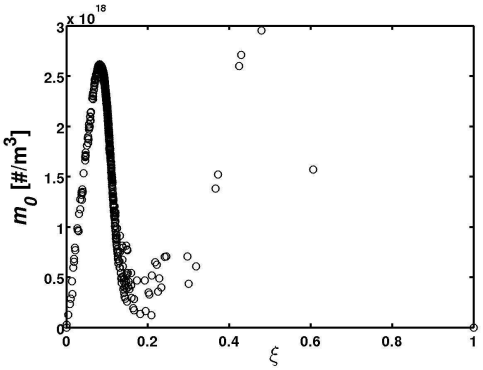

(f) All flamelet, detailed nucleation

Figure 3.6 Scatter plots of number density (m_0) versus mixture fraction (ξ) in PaSR.

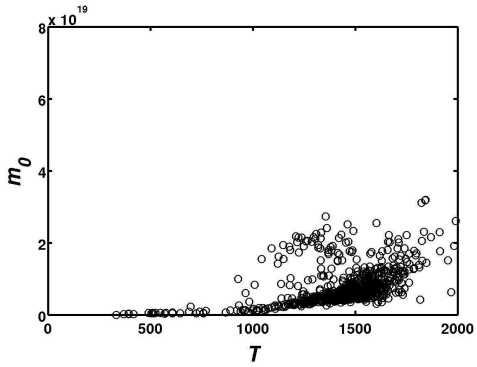

(a) Detailed flame, one-step nucleation

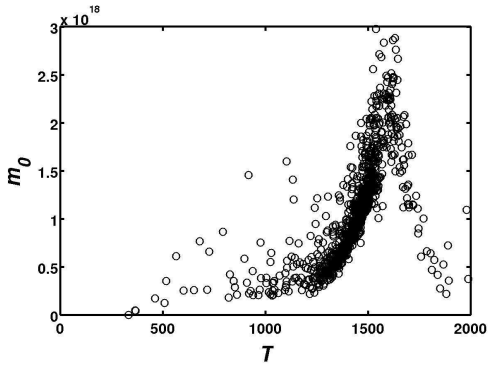

(b) Detailed flame, detailed nucleation

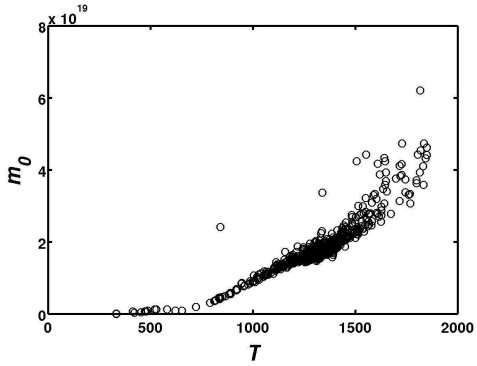

(c) Flamelet, one-step nucleation

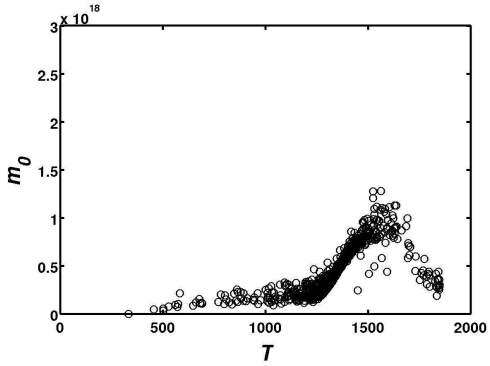

(d) Flamelet, detailed nucleation

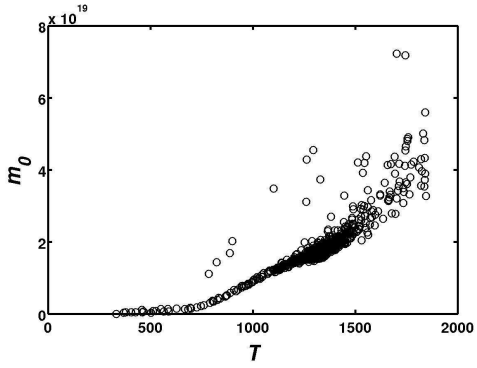

(e) All flamelet, one-step nucleation

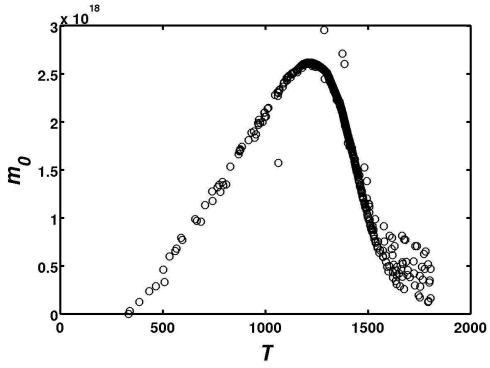

(f) All flamelet, detailed nucleation

Figure 3.7 Scatter plots of number density (m_0) versus temperature (T) in PaSR.

The effect of temperature on the chemical mechanisms is depicted by Figure 3.7. The one-step mechanism, as in the PFR, produces a large number of particles immediately at the nozzle. As in the PFR, it was observed that for the one-step nucleation higher temperatures lead to higher number densities (see Figures 3.7(a),3.7(c),3.7(e)). But for the detailed mechanism it is observed that the nucleation starts as the temperature approaches $T = 1500$ K, but at temperatures higher than $T = 1800$ K there is very little nucleation. This suggests, as we found in the PFR, that the particles undergo nucleation on both sides of the flame, as they cross from the rich side to the lean side due to mixing. The same trends are observed in the detailed flame, detailed nucleation and the flamelet, detailed nucleation cases (Figures 3.7(b) and 3.7(d)). Thus, both the highly idealized case of a PFR (with no back mixing) and the more realistic case of a PaSR (with back mixing) show us that the choice of the nucleation chemistry model will be very important in predicting product properties (e.g. the extent of sintering).

3.3 Effect of chemical mechanism on flow configuration

It has been found that using different flow configurations (fuel and oxidant flow rate and position) in flame reactors leads to very different product particle properties (refer Figure 3.8). It is seen from the Figure 3.8 that varying the flow configuration led to a wide range of particles. From loose aggregates shown in Figure 3.8a to almost spherical particles obtained in Figure 3.8d. In the previous Section 3.2, it was found that the different Ti-oxidation mechanisms (one-step vs. detailed) led to very different locations for the maximum nucleation rate. In this Section, the previous findings are expanded further with the help of a bivariate population balance model involving all particle evolution events. Hence, compared to last section, in which we only looked at nucleation, the PB model here is complete with all relevant particle evolution events including nucleation, surface growth, aggregation and sintering. The resulting bivariate PBE is solved using the conditional quadrature method of moments (CQMOM) (6).

This full population balance model is then applied to two different flame configurations, based on experimental work done by (70), studying both the one-step and detailed gas-phase kinetics for Ti oxidation. In order to focus on the role of the chemical mechanism, the flames

are modeled using a simple multi-environment plug flow reactor (PFR) (11), and product properties involving volume and surface area for each flame configuration using different chemical kinetics are compared. Using simple flow configurations enables the comparison of different chemical mechanisms and can help us develop and test different source terms that describe how gas-phase mechanisms effect the particle evolution. In particular, we intend to study the effects of precursor decomposition, nucleation and surface reactions on the particle evolution processes, providing a better understanding of the coupling between the chemistry and particle formation. By comparing with the experimental data (70), it is found for this study that the detailed mechanism is more accurate than the one-step mechanism in describing the particle evolution profiles. The simulation results demonstrate the importance of the location of nuclei formation in the flame, which depends strongly on the gas-phase kinetic model, and its effect on the final product properties. These results suggest that detailed gas-phase chemical kinetics are required to accurately model combustion-based synthesis of nanoparticles.

3.3.1 Model description

The primary objective of this study is to determine whether the detailed chemical mechanism is necessary to describe the properties of TiO_2 nanoparticles produced in flame reactors. For this purpose, we consider two flow configurations (flames A and D in Figure 3.9) that are known to produce very different particle properties (68), and compare results found with the one-step and detailed gas-phase mechanisms. The chemistry used here is complete, with methane combustion (Bowman et al.) as well as methane chlorination (79) present in the mechanisms. A bivariate PBE (Eqn. (2.5)) is solved to find the evolution of nanoparticles in the flame. Conditional quadrature method of moments technique (Section 2.6) is used to close the transport equations for moments. The PBE is resolved in terms of its moments following Section 2.5 (Eqn. 2.23). N_v and N_a sets of weights and abscissas are chosen in the volume and area direction, respectively ($N_v = N_a = 3$). The resolution of three nodes in both the directions requires the solution of a moment set involving 21 moments (as listed in Table 2.1). These moments evolve with nucleation, surface growth, aggregation and sintering and the corresponding models are taken from Section 2.7.

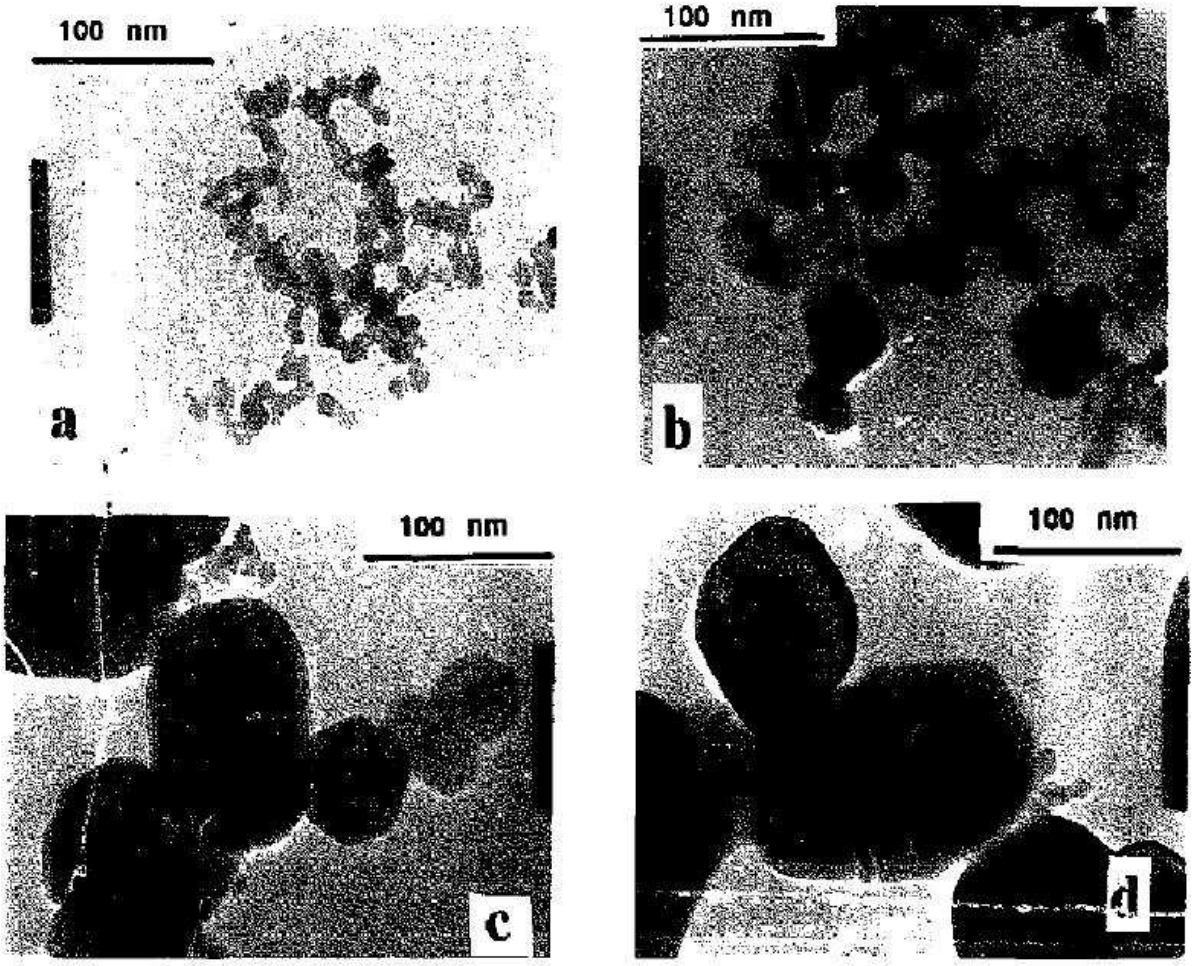

Figure 3.8 TEM micrographs of titania powders from (70).

We intend to model the two flame configurations with three different models for Ti nucleation and surface reactions. First, results are reported for flames A and D with the *simple* growth expressions (Eqs. 2.32 and 2.34) for both one-step and detailed gas-phase kinetics (referred in all the plots below as subfigures a and b respectively). Reported besides these are results reported using the *detailed* growth expressions (Eqs. 2.35 and 2.36) with detailed gas-phase kinetics (referred as subfigure c in the below plots).

3.3.2 Operator splitting

The nucleation event leads to the introduction of a large number of nuclei in the system in a short amount of time causing the moment equations for the bivariate PBE to be extremely stiff. Thus, the correct scaling of moments is very important for solution of the full PBE model. Similar to nucleation, the surface growth and sintering events make the moment set extremely stiff because of their dependence on gas-phase properties, such as temperature and concentrations. Other than stiffness of the moment equations, moment realizability must be verified (103). A set of moments is called realizable when there exists a solution for corresponding weights and abscissas. Hence, for the full PBE model operator splitting is used to alleviate stiffness and to guarantee that the moment set remains realizable.

The nanoparticle evolution events can be split based on their effect on the number density. It is noted that nucleation and aggregation are the only two processes that lead to a change in the number density. Thus, these two processes can be taken together to get the first approximation of the moments. After this, the number density of the system does not change, as number density only depends on weights w_i, $w_{i,j}$ (Eq. (2.25) with $k = l = 0$). But the volume and surface area can change due surface growth and sintering. Hence, the evolution of abscissas due to surface growth and sintering can be done in a separate step, keeping the weights constant. Using the updated values of weights and abscissas, the updated set is computed. Thus, given moments $m_{kl}(t)$ at time t, the algorithm for implementing operator splitting for time step Δt is as follows:

- Use CQMOM with $m_{kl}(t)$ to find the weights w_i, $w_{i,j}$ and abscissas v_i, $a_{i,j}$ at time t.

- Integrate the differential equations for the moments (Eq. 2.23) including only nucleation and aggregation to find m^*_{kl}.
- Use CQMOM with m^*_{kl} to compute new weights w_i, $w_{i,j}$ and abscissas v^*_i, $a^*_{i,j}$.
- Update the abscissas starting from v^*_i, $a^*_{i,j}$ by numerical integration of

$$\frac{da}{dt} = S_{\mathrm{a}} + G_{\mathrm{a}} \quad \text{and} \quad \frac{dv}{dt} = G_{\mathrm{v}}$$

  over the time step Δt.
- Compute the updated moments, $m_{kl}(t + \Delta t) = \sum_{i=1}^{N_{\mathrm{v}}} \sum_{j=1}^{N_{\mathrm{a}}} w_i w_{i,j} v_i^k a_{i,j}^l$.

In this work, the numerical integration is done using DLSODE (22).

3.3.3 Multi-environment PFR Model

The goal of this work is to study in detail the coupling between chemistry (one-step and detailed Ti oxidation) and particle evolution. Because the detailed mechanism cannot be coupled to a full turbulent flow solver without first simplifying the chemistry, the flames are modeled here using multi-environment micromixing models (11). The use of multi-environment PFR's enable the use of the complete chemistry for testing and deriving the PBE source terms and compared to the traditional PFR models, these models offer a more realistic representation of a diffusion flame as they involve turbulent mixing between streams issuing from the different nozzles. The mixing rate is dependent on the flow velocity of the stream. In related work (84), we have used a reduced model for the chemistry (flamelet approach) coupled to a detailed flow solver. The use of the simplified flow model allows us to determine whether it will be necessary to include the detailed mechanism in future work. It also gives an insight into which species and intermediates are necessary for the correct particle description and hence, will help us decide which specified features of the detailed mechanism should be included in the reduced chemistry mechanism for accurate modeling of this system.

In the multi-environment PFR model, we simulate particles following specified streamlines in the flame and also the interactions between these streamlines to provide realistic test conditions for the PBE models. The streamlines to be followed and the interactions between them is

decided based on the flame configuration. As stated earlier, it is found that flame reactors pass through different zones where only certain source terms of the population balance are dominant (9). Initially, mixing and kinetics dominate the system leading to nucleation and growth, which is followed by domination of aggregation and sintering terms. These zones are also observed in the CFD simulations of the flame reactor (84). The advantage of multi-environment PFR models lies in their ability to replicate these different zones. Although no substitute for CFD flow simulations because of their inability to capture all mixing and turbulence effects, these methods provide a fast and efficient way to develop and test models that can then be applied to full flame simulations.

Here, the full PBE model with both one-step and detailed mechanisms is simulated for two flame configurations given in (70). For flame A, air, precursor and a carrier gas (argon) come from the innermost nozzle, while fuel comes from the outermost nozzle (Figure 3.9(a)). In flame D, the fuel and precursor interchange positions (Figure 3.9(b)).

Applying this approach on flame A given in Pratsinis et al. (1996) (70), the system is modeled using a 3-environment model. Environment 1 consists of Air/$TiCl_4$/Ar, environment 2 contains CH_4 and environment 3 is ambient air. The mass balance on each environment leads to

$$\begin{aligned} \frac{d(\rho_1 p_1 V)}{dt} &= \gamma_1 \rho_2 p_2 V - \gamma_1 \rho_1 p_1 V, \\ \frac{d(\rho_2 p_2 V)}{dt} &= \gamma_1 \rho_1 p_1 V - \gamma_1 \rho_2 p_2 V + \gamma_2 \rho_3 p_3 (1 - p_3) V, \\ \frac{d(\rho_3 p_3 V)}{dt} &= -\gamma_2 \rho_3 p_3 (1 - p_3) V. \end{aligned} \tag{3.13}$$

where ρ_n is the density, p_n is the mass fraction of environment 'n' and V is the sum of the volume of all the environments.

The total mass remains constant

$$M = \rho_1 p_1 V + \rho_2 p_2 V + \rho_3 p_3 V \tag{3.14}$$

We define ρ as

$$\rho = \rho_1 p_1 + \rho_2 p_2 + \rho_3 p_3 \tag{3.15}$$

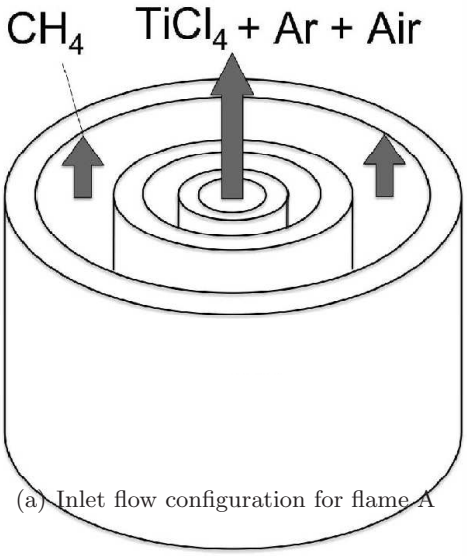

(a) Inlet flow configuration for flame A

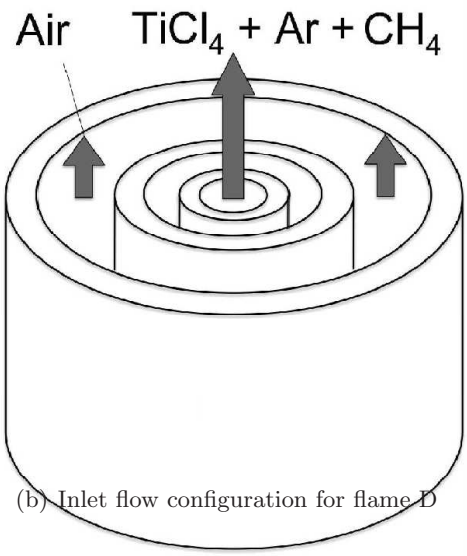

(b) Inlet flow configuration for flame D

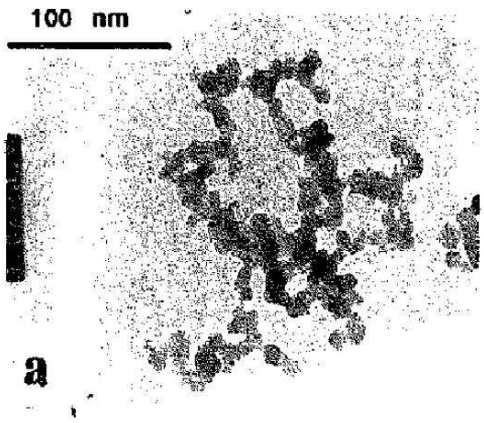

(c) Flame A: primary particle size is 11 nm.

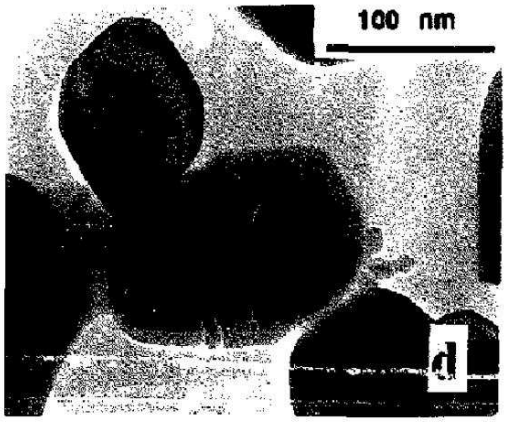

(d) Flame D: primary particle size is 105 nm.

Figure 3.9 Flow configuration and sample product from experiments by Pratsinis et al. (1996).

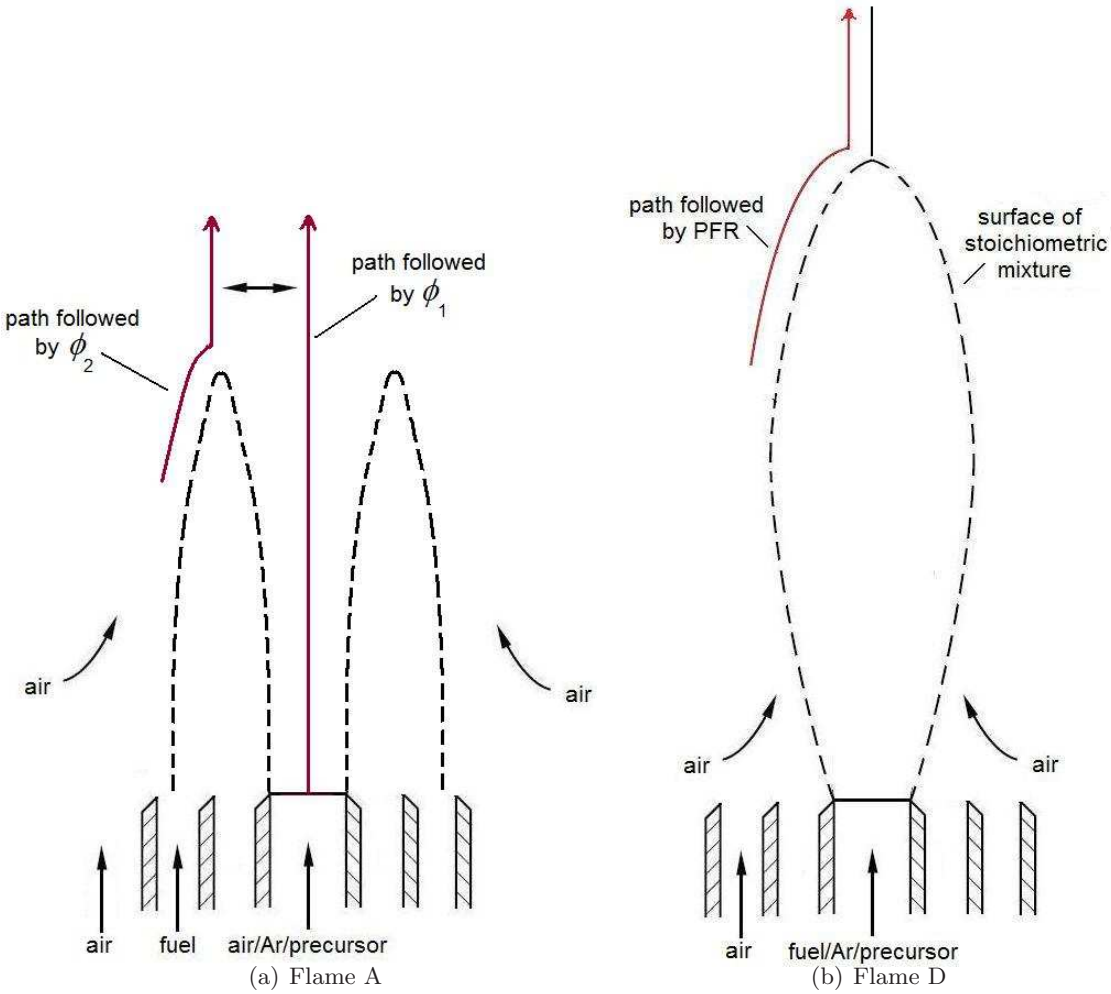

(a) Flame A (b) Flame D

Figure 3.10 Path followed by multi-environment PFR method

Then mass balance can be written as

$$M = V(t)\rho(t) \tag{3.16}$$

This implies that $V(t) = M/\rho(t)$. Instead of $(1 - p_3)$, we can get a simpler form using $(\rho - \rho_3 p_3)/\rho$. The equations below assume that the simpler form is used. Defining the normalized densities for each environment as $\theta_n = \rho_n/\rho$, we can eliminate V:

$$\begin{aligned} \frac{d(\theta_1 p_1)}{dt} &= \gamma_1\theta_2 p_2 - \gamma_1\theta_1 p_1, \\ \frac{d(\theta_2 p_2)}{dt} &= \gamma_1\theta_1 p_1 - \gamma_1\theta_2 p_2 + \gamma_2\theta_3 p_3(1 - \theta_3 p_3), \\ \frac{d(\theta_3 p_3)}{dt} &= -\gamma_2\theta_3 p_3(1 - \theta_3 p_3). \end{aligned} \tag{3.17}$$

where γ_n is the rate at which environment n mixes with its surrounding environment and is calculated by.

$$\gamma_n = \frac{sp \times v_{jet}}{d_{jet}} \tag{3.18}$$

here, $sp = 0.0094$ is the spreading rate of a turbulent round jet (67).

Since $\theta_n(t)$ can be computed from the temperature and composition of each environment, these equations can be solved for p_n. However, p_n is not needed since the equations can be written in terms of $p_n^* = \theta_n p_n$.

$$\begin{aligned} \frac{dp_1^*}{dt} &= \gamma_1 p_2^* - \gamma_1 p_1^*, \\ \frac{dp_2^*}{dt} &= \gamma_1 p_1^* - \gamma_1 p_2^* + \gamma_2 p_3^*(1 - p_3^*), \\ \frac{dp_3^*}{dt} &= -\gamma_2 p_3^*(1 - p_3^*) \end{aligned} \tag{3.19}$$

where $p_n^* = (\rho_n p_n)/\rho$, here ρ_n is the density and p_n is the volume fraction of environment n with $\rho = \sum_n \rho_n p_n$. An equation of state is used to find ρ_n and p_n is based on the volume flow rates. γ_n is the turbulent mixing rate is modeled as $\gamma_n = \kappa(vel_n/dia_n)$ where κ is the spreading rate of a turbulent jet (67), vel_n is the jet velocity and dia_n is the jet diameter for environment n. The jet diameters are based on experimental conditions and using both volume flow rate and jet diameter, the corresponding jet velocity vel_n is found. Based on Eq. (3.19), the evolution of composition variables in environments 1 and 2 ($\langle\phi\rangle_1$, $\langle\phi\rangle_2$) can be represented

by

$$\begin{aligned}\frac{d\langle\phi\rangle_1}{dt} &= \gamma_1\frac{p_2^*}{p_1^*}\left(\langle\phi\rangle_2 - \langle\phi\rangle_1\right) + S(\langle\phi\rangle_1),\\ \frac{d\langle\phi\rangle_2}{dt} &= \gamma_1\frac{p_1^*}{p_2^*}\left(\langle\phi\rangle_1 - \langle\phi\rangle_2\right) + \gamma_2\frac{p_3^*(1-p_3^*)}{p_2^*}(\langle\phi\rangle_3 - \langle\phi\rangle_2) + S(\langle\phi\rangle_2)\end{aligned} \tag{3.20}$$

where S represents the composition source term due to chemical reactions, particle evolution, etc. We assume no reactions takes place in ambient air, and thus $\langle\phi\rangle_3$ is constant. The streamlines tracked by the multi-environment method for this flame configuration are shown in Figure 3.10(a). The moment transport equation given in Eq. (2.29) is solved for environments containing nanoparticles by including the moments in the composition vectors in Eq. (3.20).

Flame D is essentially a diffusion flame with air diffusing into a jet of fuel and precursor. Optimal conditions for combustion in a diffusion flame are restricted to the vicinity of the surface of stoichiometric mixture (62). At the stoichiometric surface, fuel and air exist at a proportion that allows both to be entirely consumed. This will lead to high temperatures in the region and due to the temperature sensitivity of chemical reactions would result in fast reaction rates. The temperature along the stoichiometric surface is generally the highest in a diffusion flame. Hence, the particle evolution in the diffusion flame can be modeled by following the stoichiometric surface. Based on the flame height (taken from experiments) and fuel jet velocity, the time taken for all fuel to be consumed is computed (τ). Stoichiometric amounts of fuel and precursor are supplied to the flame up to time τ, after which air is engulfed into the flame. In essence, we follow the streamline along the stoichiometric surface for $t < \tau$, and then continue with air entrainment for $t > \tau$ (Figure 3.10(b)).

The inner jet (environment 1) containing $Ar/TiCl_4/CH_4$ is mixed with the outer jet of air (environment 3) into the stoichiometric surface (environment 2). Based on the diffusion flame the two sets of equations are derived based on τ. For the stoichiometric surface ($t < \tau$)

$$\begin{aligned}\frac{dp_1^*}{dt} &= -\gamma_{\text{fuel}},\\ \frac{dp_2^*}{dt} &= \gamma_{\text{fuel}} + \gamma_{\text{air}},\\ \frac{dp_3^*}{dt} &= -\gamma_{\text{air}}\\ \frac{d\langle\phi\rangle_2}{dt} &= \frac{\gamma_{\text{fuel}}}{p_2^*}\left(\langle\phi\rangle_1 - \langle\phi\rangle_2\right) + \frac{\gamma_{\text{air}}}{p_2^*}(\langle\phi\rangle_3 - \langle\phi\rangle_2) + S(\langle\phi\rangle_2)\end{aligned} \tag{3.21}$$

and then for air entrainment ($t > \tau$)

$$\begin{aligned} \frac{dp_1^*}{dt} &= 0, \\ \frac{dp_2^*}{dt} &= \gamma_{\text{engulf}}(1 - p_2^*)p_2^*, \\ \frac{dp_3^*}{dt} &= -\gamma_{\text{engulf}}(1 - p_2^*)p_2^* \\ \frac{d\langle\phi\rangle_2}{dt} &= \gamma_{\text{engulf}}(1 - p_2^*)(\langle\phi\rangle_3 - \langle\phi\rangle_2) + S(\langle\phi\rangle_2) \end{aligned} \tag{3.22}$$

where γ_{fuel} and γ_{air} are the stoichiometric rates of fuel and air supply. γ_{engulf} is the rate of air engulfment. As only the stoichiometric surface is followed, it is assumed no reactions take place in environments 1 and 3.

3.3.4 Results for flame A

Table 3.4 Initial conditions for flame A

Parameter	Environment 1	Environment 2	Environment 3
Temperature (K)	333	1450	298
Ar (mass fraction)	0.08	0	0
CH_4 (mass fraction)	0	0.185	0
N_2 (mass fraction)	0.686	0.605	0.767
O_2 (mass fraction)	0.209	0.21	0.233
$TiCl_4$ (mass fraction)	0.025	0	0
Volumetric flow rate (cm^3/s)	4050	1072	3800
Volume fraction	0.454	0.120	0.426

The inlet conditions for flame A are given in Table 3.4. It should be noted that the air flow rate (3800 cm^3/min) is considerably higher than the fuel flow rate (312 cm^3/min). Looking at the experimental results for flame A reported in (68), we find that it produces small open aggregates with primary particle size of around 11 nm (see Figure 3.9(c)). The high air flow rate leads to vigorous dilution of the $TiCl_4$ stream prior to its oxidation in the flame. Increasing the air flow rate reduces the flame height and residence time and, subsequently, reduces the oxidation rate of $TiCl_4$ and the yield of the process (70). The shorter residence time and increased dilution rate leads to fewer collisions between the newly formed titania particles, resulting in open aggregates with high surface area (see Figure 3.9(c)). From the

experimental results, it is expected that sintering does not play a prominent role in the final product properties.

Nucleation rate Using the PFR model for the three models, it is found that the temperature evolution for all cases is similar (dotted line in Figure 3.11). The maximum flame temperature occurs at a residence time of about 0.05 sec, but the nucleation rates are very different for each mechanism. The nucleation rates are normalized by dividing the rate (J in Eq. 2.30 and Eq. 2.31) by Avogadro's number. Looking at the plots, it is found that as the one-step rate primarily depends on temperature and increases with rise in temperature. This rapid increase in rate leads to consumption of most of the $TiCl_4$ and the nucleation for the one-step gas-phase mechanism is finished by a residence time of around 0.05 sec when the maximum temperature is reached (Figure 3.11(a)). In contrast, in the detailed gas-phase mechanism the rate of nucleation depends on intermediates leading to the formation of $Ti_5O_6Cl_8$. The rate initially increases as precursor is decomposed and intermediates are formed but the sharp rise in temperature leads to the decrease in the rate. It is further observed that after the high temperature region, the nucleation rate starts to increase again and reaches the maximum value around 0.12 sec. Concurrent with the results from our previous work (51), it is found that for the detailed gas-phase mechanism the region of maximum nucleation rate lies in the temperature range between 1500–1800 K (see Figure 3.11(b)). For flame A, this range occurs at residence times between 0.09–0.12 sec. Figure 3.11(c) plots the nucleation rate for the detailed gas-phase mechanism after the inclusion of the detailed surface growth rate. Consistent with the conclusions of (69), it is found that initially when enough surface area is not present, gas-phase reactions dominate the system and the nucleation rates are high. This can be observed up until around 0.05 sec in Figure 3.11(c). After this point the temperature of the system rises and similar to previous observations the rate decreases as temperatures go beyond the preferred range from 1500–1800 K. As mentioned before, this flame configuration consists of a $TiCl_4$/Ar/Air stream continuously diluting the system because of its high flow rate. As the temperature decreases the surface growth rate decreases but the temperature is still high enough for $TiCl_4$ to dissociate and for nucleation to occur and hence we find nucleation occur-

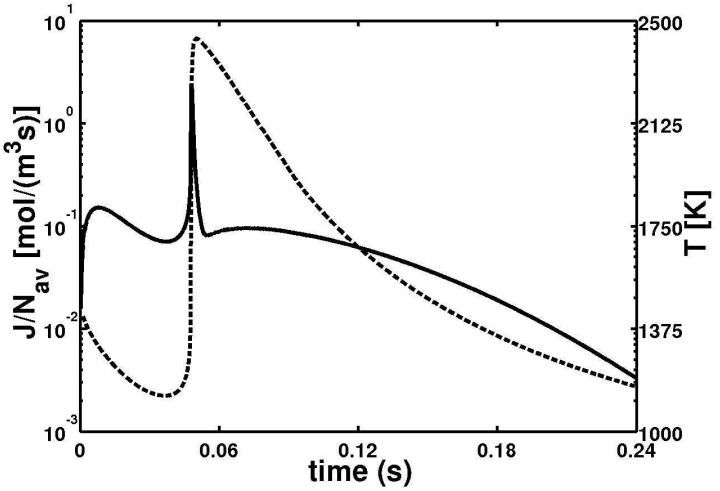

(a) One-step gas-phase mechanism

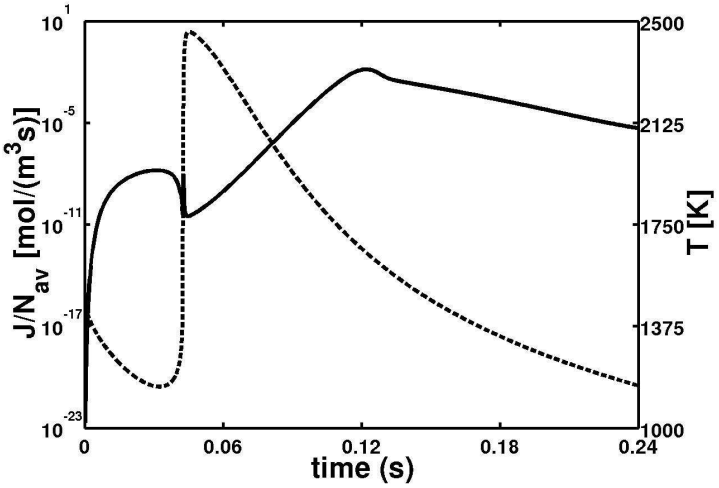

(b) Detailed gas-phase mechanism

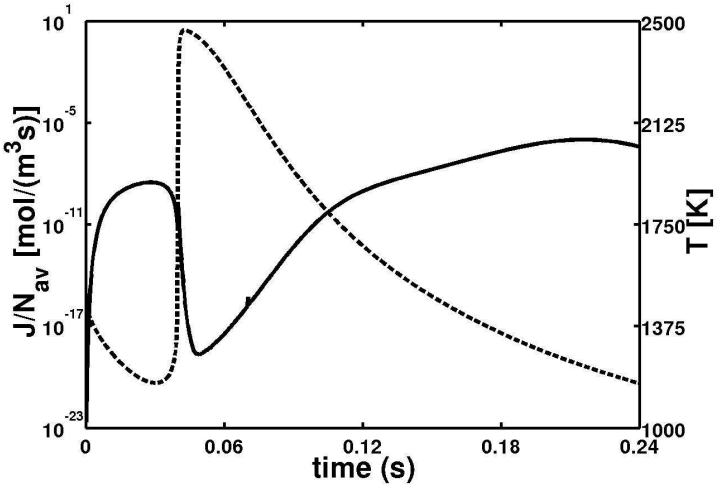

(c) Detailed surface growth

Figure 3.11 Nucleation rate (solid) and temperature (dashed) in flame A.

ring after 0.06 sec. Gas-phase reactions continue to dominate the system as sufficient surface area has not been created for surface reactions to take precedence.

Number density The evolution of number density (m_{00}) depends on both the nucleation and aggregation and again follows very different trends for each mechanism. For the one-step gas-phase mechanism, with increasing nucleation rates m_{00} first grows. Increasing number density and temperature leads to aggregation becoming active and this leads to a decrease in m_{00} after the flame front (Figure 3.12(a)). The falling nucleation rate results in aggregation becoming the dominant process, leading to a decrease in the number density in the later part of the flame, as observed after residence time of 0.05 sec. Compared to this, the detailed gas-phase mechanism produces a relatively small number of particles at the initial flame front and hence number density initially rises slowly. With most nucleation happening after the high-temperature flame, m_{00} starts to increase after the residence time of 0.05 sec. In the preferred temperature range (residence time between 0.09–0.12 sec), the number density rapidly rises (Figure 3.12(b)). After this period, the combined effect of lower nucleation rate, high aggregation and air entrainment leads to decrease in number density. Next observed is the evolution for number density for flame A with detailed surface growth expression. For this case, initially the evolution of number density is similar to detailed gas-phase mechanism with nucleation dominating the system (compare Figures 3.12(b) and 3.12(c)). But after this initial step the evolution for both cases is quite different. In the detailed gas-phase mechanism (Figure 3.12(b)), as intermediates were only involved in the nucleation event, m_{00} continues to increase and reaches the peak value between 1500–1800 K. With detailed surface growth (Figure 3.12(c)) the number density also increases in this region but as intermediates can now also take part in growth, we do not see a very sharp increase. After the initial nucleation, the increasing surface area and presence of intermediates lead to growth events also becoming important and hence the number of nuclei introduced into the system is much lower. The variation of number density as predicted by the three models follows similar trends to the nucleation rates. For one-step and detailed gas-phase mechanisms (with simple growth) the evolution of m_{00} affirms that nucleation remains the most important process. In contrast, the

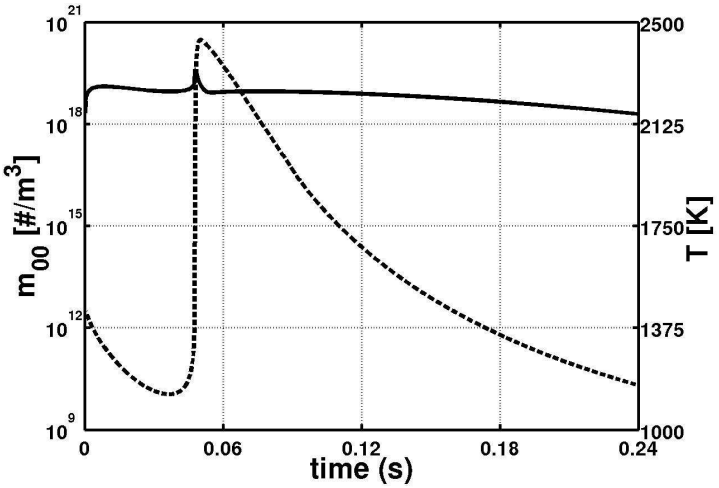

(a) One-step gas-phase mechanism

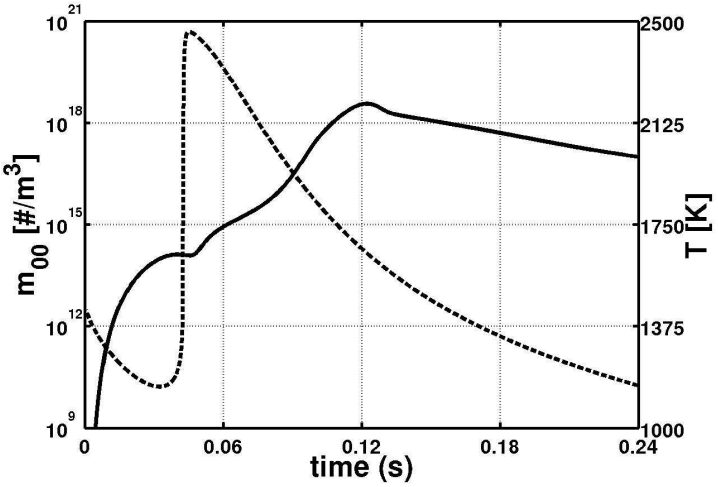

(b) Detailed gas-phase mechanism

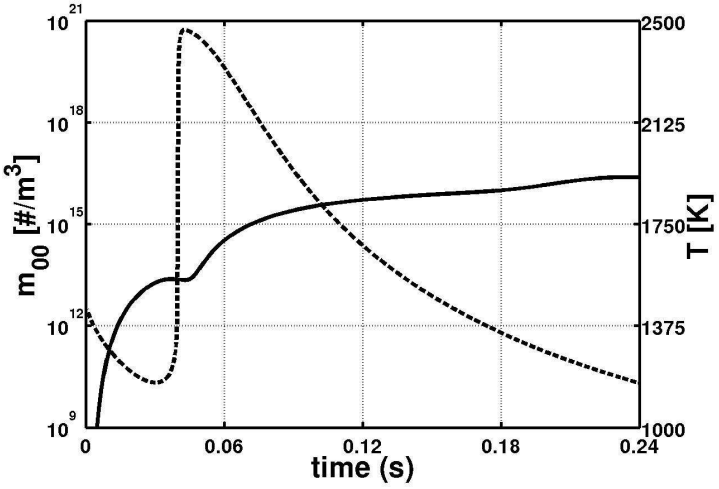

(c) Detailed surface growth

Figure 3.12 Predicted evolution of number density (solid) and temperature (dashed) for flame A.

number density with the surface growth model rises slowly as precursor is consumed both by nucleation and growth leading to much lower number of nuclei introduced.

Area concentration To understand the dynamics of particle evolution and the effect source terms have on final products it is useful to study the evolution of other moments of the distribution. The first candidate is the pure volume moment or volume concentration (m_{10}). m_{10} tracks the volume or the mass added to the system, hence it grows initially with nucleation. The surface growth events also lead to addition of volume in the system and the m_{10} grows with growth events as well. Both aggregation and sintering events have no consequence on the the total particle volume concentration. Similarly, the pure area moment or area concentration (m_{01}) grows with nucleation and growth. Sintering leads to a decrease in the surface area and hence a decrease in m_{01}. Aggregation has no direct effect on the pure area moment but it leads to the formation of agglomerates and it is this agglomerate size that determines sintering rates. First, the addition of a large number of nuclei in the system leads to the increase in area concentration of the system. These nuclei tend to agglomerate and when these large agglomerates pass through high temperature regions they undergo sintering. As m_{01} can only decrease by the sintering event, the period for which sintering is active can be found by studying m_{01}.

From Figure 3.13(a), it is found that the initial high nucleation of one-step gas-phase mechanism leads to first an increase in area concentration. But as these agglomerates pass through the flame, sintering becomes active. The importance of the sintering source term, in this case, can be observed by the decrease in the m_{01} curve (seen in Figure 3.13(a)) after the flame front. As most nucleation for the detailed gas-phase mechanism happens after the flame front, the area concentration for this case continues to increase up till nucleation is active (0.12 sec) as observed in Figure 3.13(b). At this point enough nuclei have been introduced to make large sized agglomerates and sintering begins to decrease the area concentration. But as these events occur after the flame surface, the role of sintering will be diminished for this flame. For the detailed growth expression, m_{01} increases initially with nucleation but unlike the one-step and detailed gas-phase mechanism, it continues to grow as for this

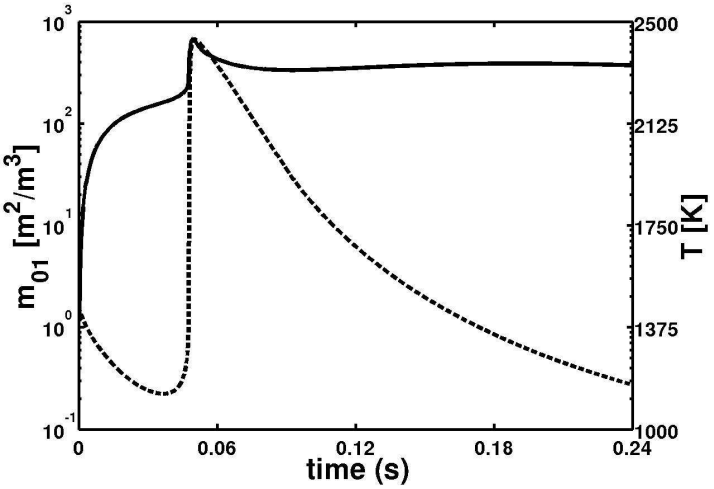

(a) One-step gas-phase mechanism

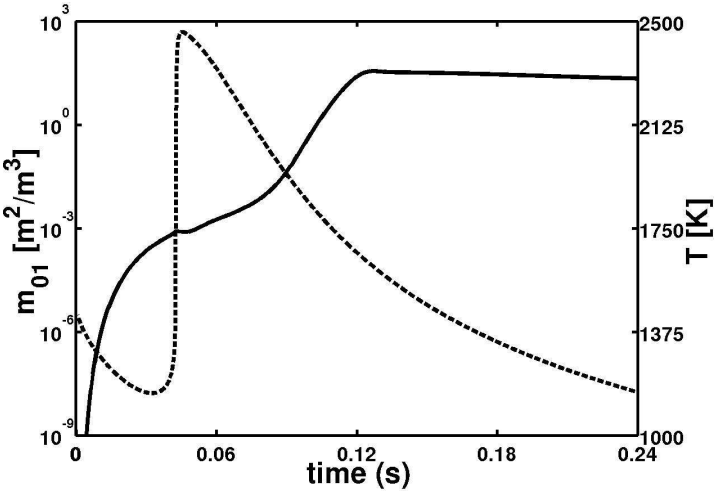

(b) Detailed gas-phase mechanism

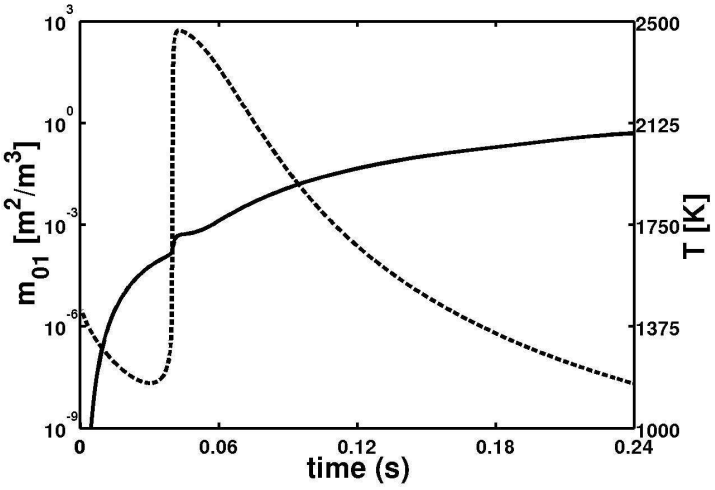

(c) Detailed surface growth

Figure 3.13 Evolution of area concentration (solid) and temperature (dashed) in flame A.

case as enough nuclei have not entered the system for aggregation and then sintering to take precedence (Figure 3.13(c)). Hence, the three models predict very different evolution of area concentration. For one-step m_{01} increases with nucleation and as these nuclei pass through the high temperature regions, sintering decreases the area concentration. In detailed gas-phase mechanism, m_{01} continues to rise with nucleation, but in contrast with one-step, this mechanism forms large aggregates after the high temperature region diminishing the effect of sintering. Finally, the detailed surface growth model predicts both slower increase and lower final surface area concentrations than other two models. Because the other models are nucleation dominant, hence, most of the precursor consumption leads to formation of nuclei. But in detailed surface growth model, growth leads to deposition of TiO_2 on the surface of existing particles and this leads to smaller increase in the area concentration as compared to the formation of nuclei.

Average area To obtain more detail, using the definitions of the moments, the average surface area of the aggregates can be defined as

$$A = \frac{m_{01}}{m_{00}} \quad (\mathrm{m}^2) \tag{3.23}$$

Observing the plots of the evolution of the average surface area evolution (Figure 3.14), it is found that for the one-step gas-phase mechanism first the average surface area of the aggregates decreases due to the introduction of nuclei. This can seen by the dip in the curve exactly at the high-temperature flame front in Figure 3.14(a) at a residence time of 0.05 sec. Thus, the initial flame region has high temperature and number density this results in intense aggregation just after the flame front. This rapid aggregation leads to an increase in the average aggregate area and as these aggregates pass through the high-temperature flame, they undergo sintering and decrease the average surface area. This is observed at a residence time of 0.06 sec in Figure 3.14(a). In contrast, in detailed gas-phase mechanism majority of the nucleation occurs after the high-temperature flame. With an increase in number density, the aggregation starts and the aggregate area starts to increase. But as these aggregates are formed after the high-temperature flame, they are less susceptible to sintering (Figure 3.14(b)). For detailed surface growth the initial evolution is similar to detailed gas-phase mechanism, with aggregate

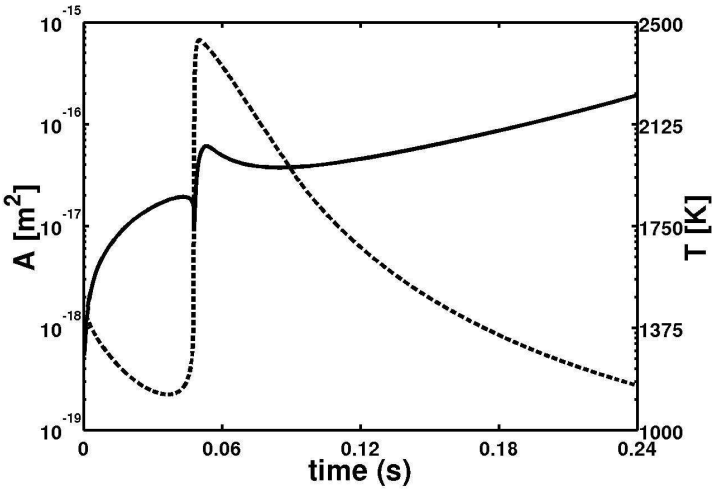

(a) One-step gas-phase mechanism

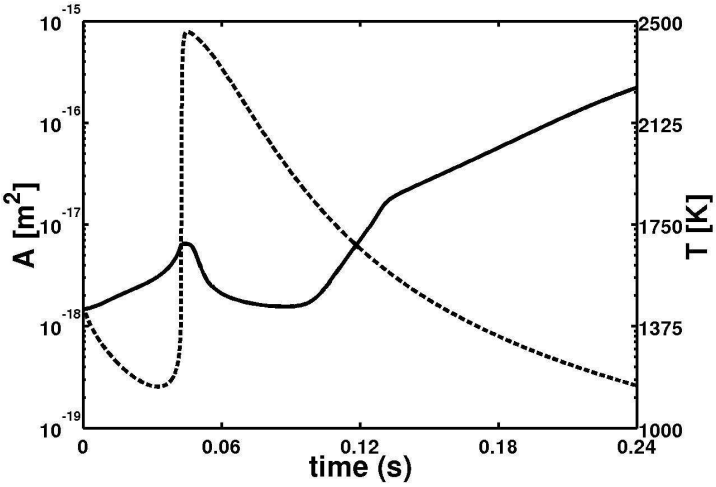

(b) Detailed gas-phase mechanism

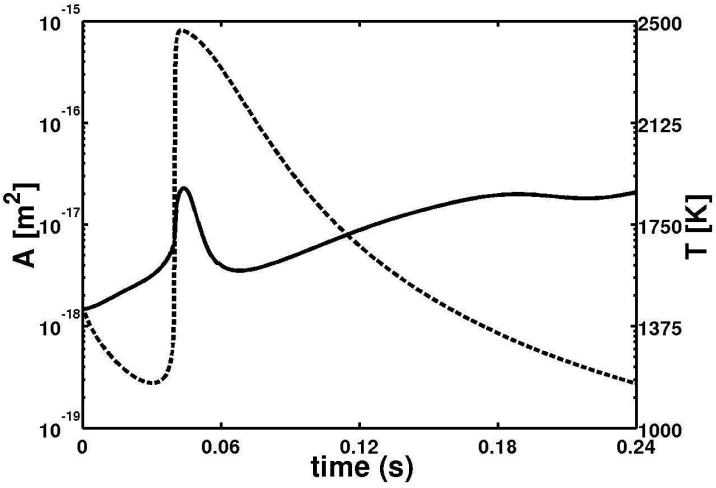

(c) Detailed surface growth

Figure 3.14 Evolution of average area of aggregates (solid) and temperature (dashed) in flame A.

area increasing with initial aggregation and then decreasing as a large number of nuclei enter the system (Figures 3.14(b) and 3.14(c)). In detailed gas-phase mechanism nuclei begin to aggregate and average area increases after 0.09 sec. But in detailed surface growth as the number density is not as high as the previous case, the average area does not rapidly increase by aggregation but still an increase is noticed due to surface growth (observed between 0.06 and 0.18 sec in Figure 3.14(c)).

These plots give an insight into the role of nucleation and surface growth on the three models. For one-step mechanism as nucleation followed by aggregation occurs with rising temperature in early part of the system, the model predicts that the average area reaches a high value initially. Using the detailed gas-phase mechanism leads to a change in nucleation region but still nucleation remains dominant and the aggregate area rises sharply after the zone of maximum nucleation. For detailed surface growth even with low number density, it is observed that aggregate area increases due to surface growth. Because the intermediates in this model are consumed by both nucleation and surface growth, the average area of aggregates is smaller when compared with the other two models.

Primary particle size To investigate further, the average primary particle size is calculated using the information stored in moments:

$$d_{\mathrm{p}} = \frac{6m_{10}}{m_{01}} \quad \text{(m)} \tag{3.24}$$

The average primary particle size for the one-step gas-phase mechanism starts to grow from the initial nuclei, but the large number of nuclei introduced lead to a small dip at a residence time of 0.05 sec (see Figure 3.15(a)). Intense aggregation leads to large agglomerates and as these agglomerates are present in the high-temperature region coalescence of primaries starts, leading to an increase in the primary particle size at residence times greater than 0.05 sec in Figure 3.15(a). But this rapid increase in d_{p} is checked as the temperature begins to decrease. The average primary particle size from the one-step gas-phase mechanism is 17 nm. Alternatively, with the detailed gas-phase mechanism, as most nucleation happens after the high-temperature flame, the average primary size remains almost constant until 0.09 sec (see Figure 3.15(b)). After 0.09 sec the increased number density results in enhanced aggregation

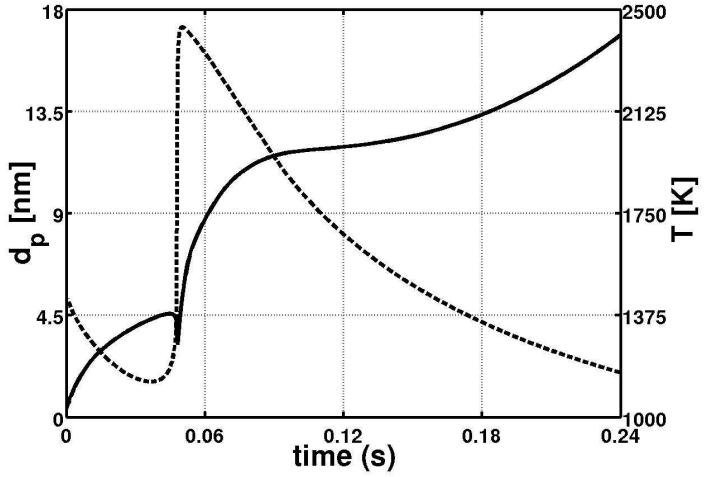

(a) One-step gas-phase mechanism

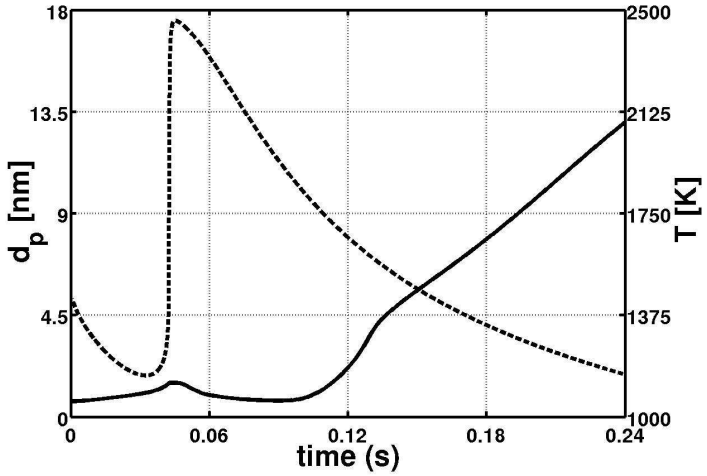

(b) Detailed gas-phase mechanism

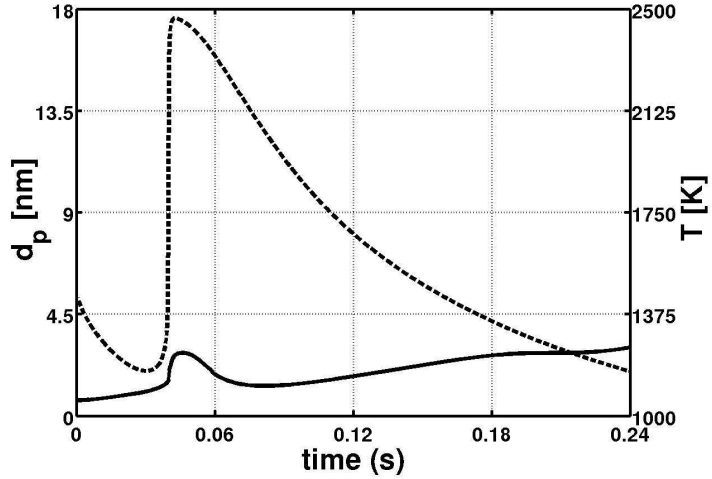

(c) Detailed surface growth

Figure 3.15 Evolution of average primary particle size (solid) and temperature (dashed) in flame A.

and both surface growth and sintering start to occur leading to an increase in the average primary size. But, unlike with one-step, these aggregates do not pass through the high-temperature region and hence, it is expected consistent with experiments, that sintering does not play an important role in the final properties for the detailed gas-phase mechanism. The average primary particle size obtained for the detailed gas-phase mechanism is 13 nm. With the new growth expression, intermediates are deposited on the surface of titania which effects the nucleation rate. Hence, instead of intense nucleation between 0.09–0.12 sec, we find surface growth and nucleation proceed throughout the length of the domain (Figure 3.15(c)). In the absence of a large number of nuclei, the aggregation process is not pronounced and this leads to small aggregates resulting in neither surface growth or sintering having a large effect on the primary size (Figure 3.15(c)). The resulting value of primary diameter is about 3 nm. The sintering behavior is still predicted accurately and consistent with experiments it is found for this flame sintering does not play an important role in the prediction of final products.

3.3.5 Results for flame D

Table 3.5 Initial conditions for flame D

Parameter	Environment 1	Environment 2	Environment 3
Temperature (K)	333	1100	298
Ar (mass fraction)	0.55	0	0
CH_4 (mass fraction)	0.278	0.026	0
N_2 (mass fraction)	0	0.512	0.767
O_2 (mass fraction)	0	0.155	0.233
$TiCl_4$ (mass fraction)	0.167	0.327	0
Volumetric flow rate (cm^3/s)	562	8	3800
Volume fraction	0.128	0.002	0.870

The inlet conditions for flame D are given in Table 3.5. In this configuration, CH_4 flows through the central nozzle and air diffuses inside making a narrow flame front. The flame is located at the first ring of the burner where the fuel meets the oxidizer. This results in a higher measured flame temperature than in flame A. The flame height is also longer resulting in increased residence times. These high temperatures and longer residence times lead to

almost spherical particles being obtained as products with primary particle size of 105 nm (see Figure 3.9(d)). From the experimental results for flame D, it is expected that sintering plays a major role in the final products for this flow configuration. Based on the experimental flame height (75 mm from Pratsinis et al. (1996) (70)) and fuel jet velocity based on flow rate of environment 1, the residence time for full consumption of fuel and precursor (τ) is found to be 0.1 sec. The simple growth expression is used for both the one-step and detailed gas-phase mechanism.

Nucleation rate Modeling this flame using the diffusion model, it is found that the temperature of the flame rises as stoichiometric amounts of fuel and air are supplied. From residence time 0 to 0.1 sec, when the stoichiometric surface is followed, the temperature rises and remains high. After 0.1 sec, air engulfment starts and the temperature starts to decrease (Figure 3.16). The nucleation rates again follow very different paths. As before, in Figure 3.16 the nucleation rates are normalized by Avogadro's number. The one-step nucleation rate depends on the temperature and consequently the rate is high on the stoichiometric surface. It remains high initially until $t < \tau$, as all the precursor present on the stoichiometric surface is consumed due to high temperature. After 0.1 sec, the one-step rate starts to fall sharply (Figure 3.16(a)). Similarly, in the detailed gas-phase mechanism the rate of nucleation first rises as temperature rises and remains high all through the stoichiometric surface. After 0.1 sec, as air engulfment begins the temperature falls. But in contrast with one-step, the rate for detailed gas-phase mechanism does not immediately decrease with falling temperature. It is observed that detailed gas-phase mechanism continues to produce nuclei till residence time of 0.15 sec when the temperature remains in the range of 1500–1800 K (Figure 3.16(b)). The rates fall after this, as temperature decreases and most of the precursor present has been consumed. Contrary to the above, as the detailed growth expression considers that all intermediates contribute to surface growth events we find that initially nucleation remains the dominant source term. But after sufficient surface area has been formed, the growth term begins to have a major impact on the particle properties. This is evident from Figure 3.16(c), the initial nucleation till 0.04 sec leads to the introduction of nuclei. The high temperatures present result in intense aggregation

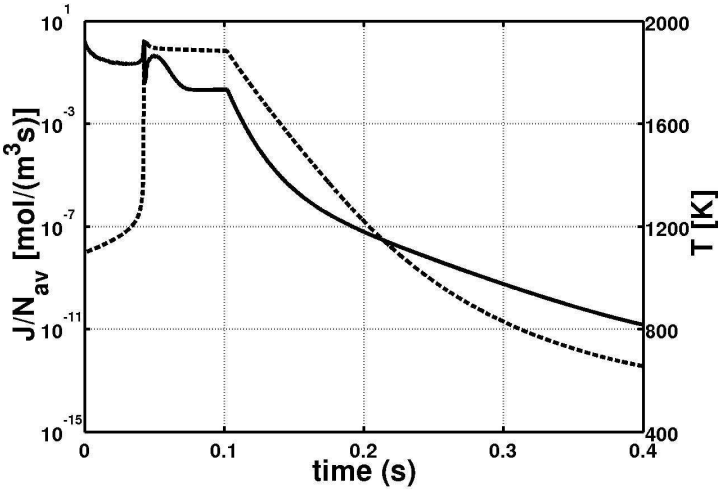

(a) One-step gas-phase mechanism

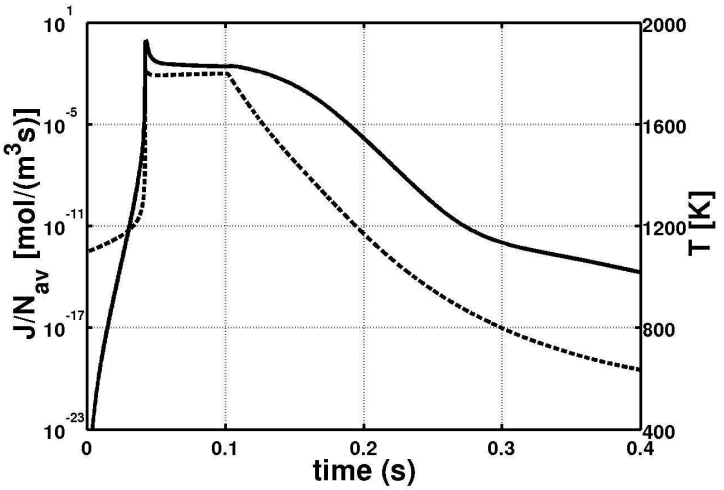

(b) Detailed gas-phase mechanism

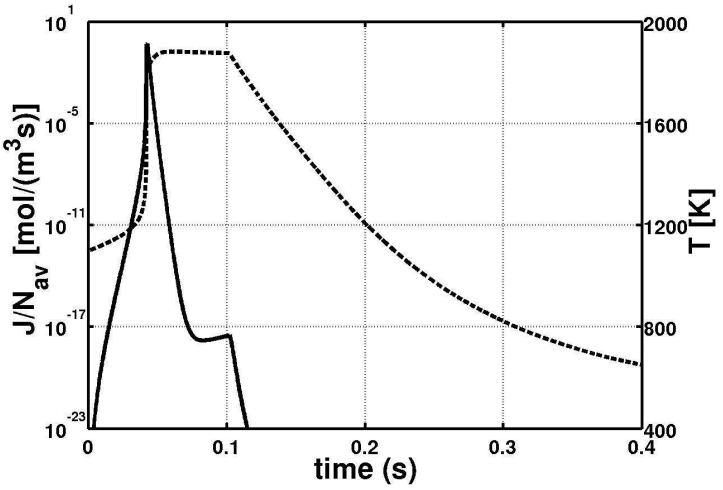

(c) Detailed surface growth

Figure 3.16 Nucleation rate (solid) and temperature (dashed) in flame D.

leading to high surfaces which results in growth becoming prominent. As observed from the plot the nucleation rate falls (after 0.04 sec in Figure 3.16(c)) and all the precursor added to the system from here on is consumed by surface reactions.

Number density Next compared is the number density (m_{00}) for the different mechanisms. For the one-step gas-phase mechanism, all along the stoichiometric surface the rapid nucleation leads to high number density. The high number density and temperature also help in large aggregation rates on the stoichiometric surface. After 0.1 sec, in the absence of nucleation, the aggregation event starts to decrease m_{00} with particle collisions (Figure 3.17(a)). Observing the plot for detailed gas-phase mechanism, it is found again that the increasing nucleation rate on the stoichiometric surface leads to rise in number density. But as nucleation continues even after stoichiometric surface, the decrease in number density is slower than one-step (Figure 3.17(b)). The evolution of number density for the detailed growth expression initially is similar, with initial high nucleation resulting in high number density (up till 0.04 sec in Figure 3.17(c)). But after this point as enough surface area is present growth takes over and nucleation stops. Thus, no more nuclei are introduced into the system and we observe the number density of the system starts to decrease due to aggregation (after 0.04 sec in Figure 3.17(c)). Hence, comparing the three models we conclude that for one-step and detailed gas-phase mechanism the number density remains high throughout the stoichiometric surface. In detailed surface growth model nuclei are introduced initially on the surface, but then surface growth takes over and number density starts to decrease.

Area concentration Figure 3.18 plots the area concentrations (m_{01}) for the the three cases. For one-step gas-phase mechanism, initially the area concentration rises with nucleation. The rapid rise in temperature at the residence time of 0.04 sec leads to large agglomerates and subsequently, sintering leads to decrease in the area concentration. The high temperature and continued aggregation results in sintering and decrease in area concentration all along the stoichiometric surface (Figure 3.18(a)). The area concentration for the detailed gas-phase mechanism increases expeditiously with nucleation. But this rapid increase in m_{01} is checked as these nuclei sinter on stoichiometric surface (Figure 3.18(b)). As both gas-phase mecha-

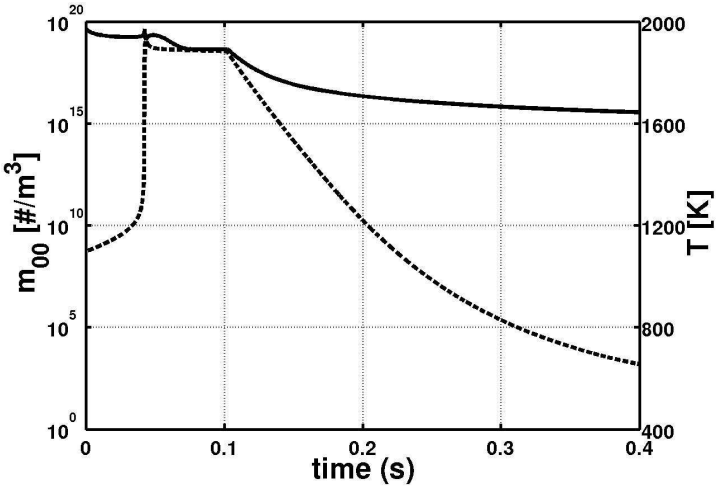

(a) One-step gas-phase mechanism

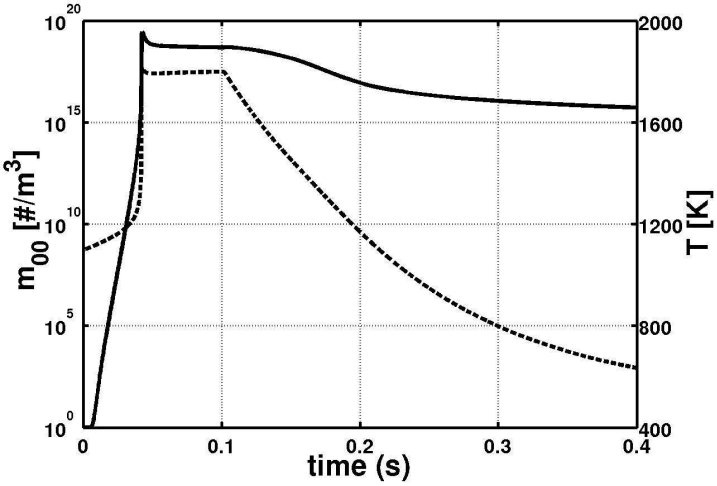

(b) Detailed gas-phase mechanism

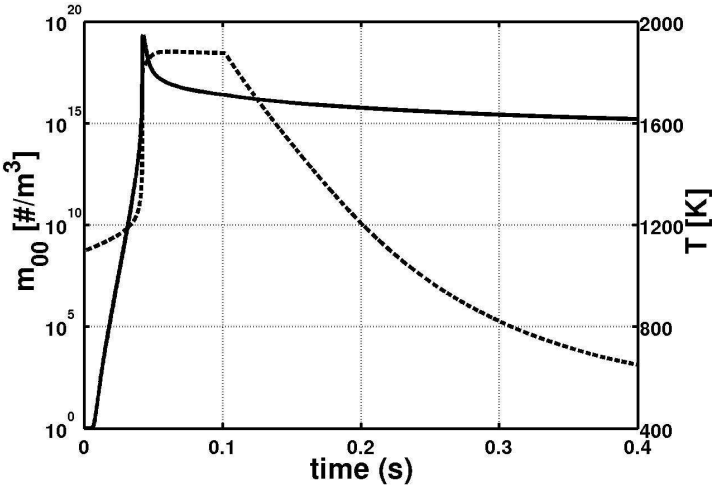

(c) Detailed surface growth

Figure 3.17 Evolution of number density (solid) and temperature (dashed) in flame D.

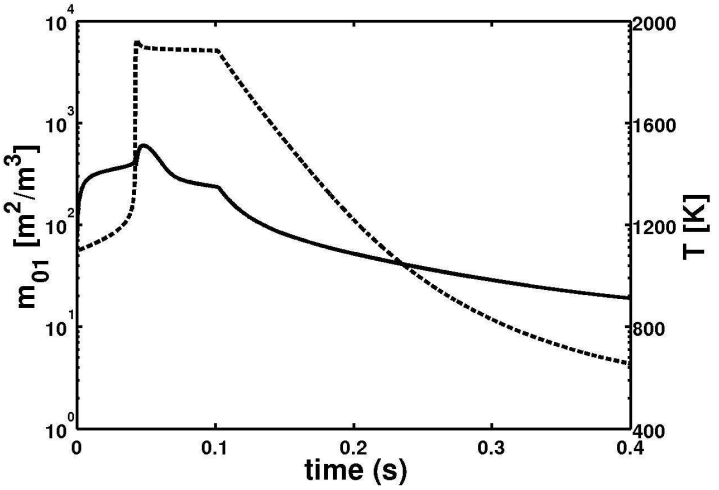

(a) One-step gas-phase mechanism

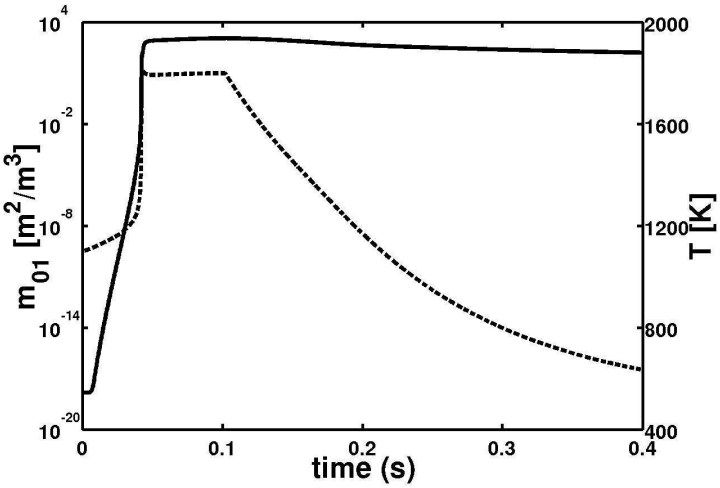

(b) Detailed gas-phase mechanism

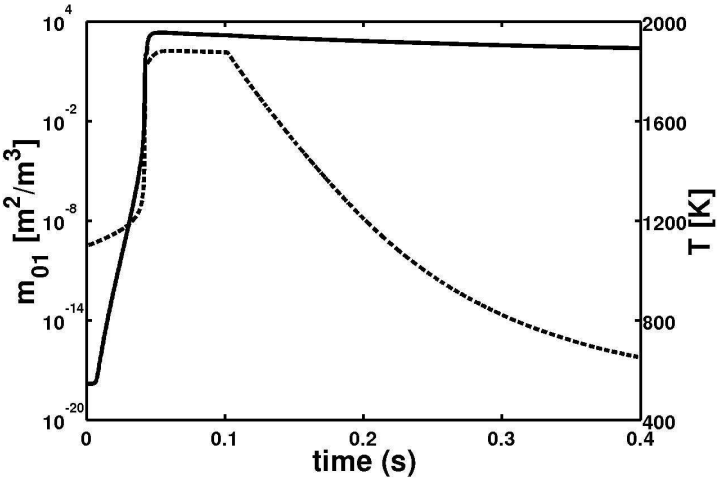

(c) Detailed surface growth

Figure 3.18 Evolution of area concentration (solid) and temperature (dashed) in flame D.

nisms predict nucleation and then sintering along the stoichiometric surface, it is found that sintering will play an important role in the final products for this flame configuration. The evolution of area concentration for detailed surface growth is almost identical to the detailed gas-phase mechanism (Figures 3.18(b) and 3.18(c)). The initial nucleation leads to increase in m_{01} but there is difference in the evolution after 0.04 sec, for detailed gas-phase reaction the area concentration continues to hold steady all along the stoichiometric surface as nucleation continues whereas for detailed surface growth we find that after the initial increase m_{01} starts to decrease. This is explained by the fact that for detailed gas-phase mechanism the precursor consumed leads to addition of nuclei which are extremely small and do not undergo sintering. But for the detailed surface growth mechanism the same precursor leads to deposition of TiO_2 on the surface of existing particles increasing there surface area and making them more susceptible to sintering. And it is this sintering event which leads to the decrease in m_{01} after 0.04 sec (Figure 3.18(c)). Consistent with the experimental observations, it is found from the detailed surface growth mechanism, that sintering will be very important in determining product properties.

Average area The average aggregate area (A), as defined in Eq. (3.23), is plotted in Figure 3.19. In the early part of the stoichiometric surface, the initial high nucleation and aggregation leads to large aggregates with high surface area. This can be observed from the initial jump in area shown in Figure 3.19 for one-step and detailed gas-phase mechanisms. But, as these aggregates go through the high-temperature region they tend to sinter and the sharp rise in average area due to aggregation is checked for both cases. This is observed until residence time of around 0.1 sec for one-step (Figure 3.19(a)) and 0.15 sec for detailed gas-phase mechanisms (Figure 3.19(b)). After this, particle evolution is mainly through aggregation and this leads to increase in the aggregate size. In comparison, for the new growth expression the initial rise in area due to nucleation is followed by surface growth and sintering along the stoichiometric surface (from 0.04–0.1 sec in Figure 3.19(c)). This results in the rapid increase in the average aggregate area observed in Figure 3.19(c) after 0.04 sec. As surface reactions lead to deposition of titania on the surface of already existing particle this results in a rapid

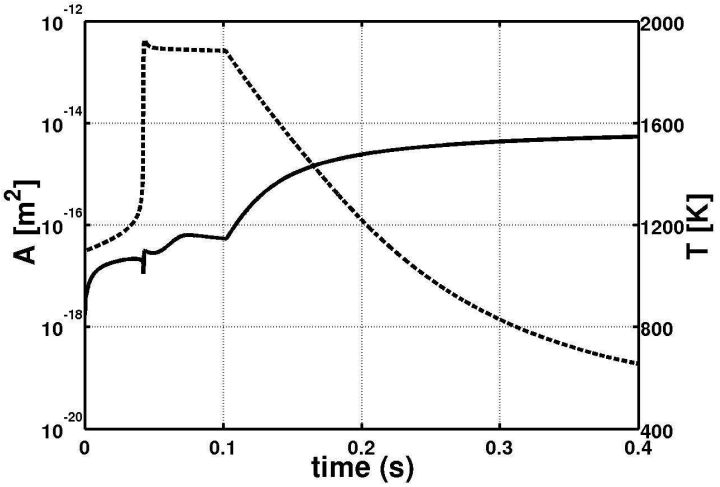

(a) One-step gas-phase mechanism

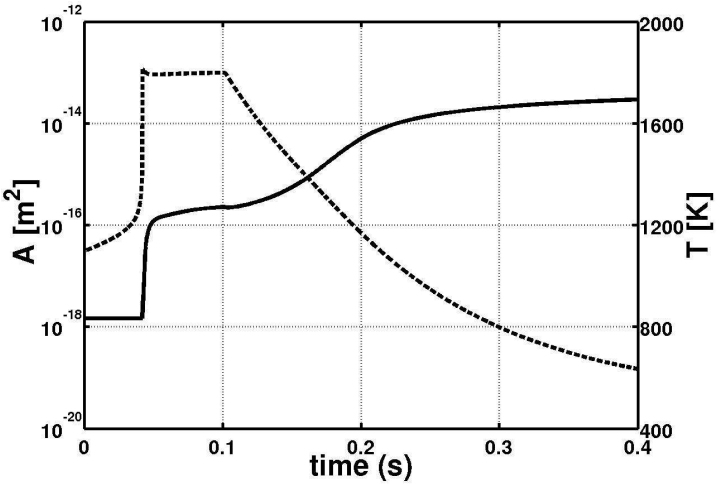

(b) Detailed gas-phase mechanism

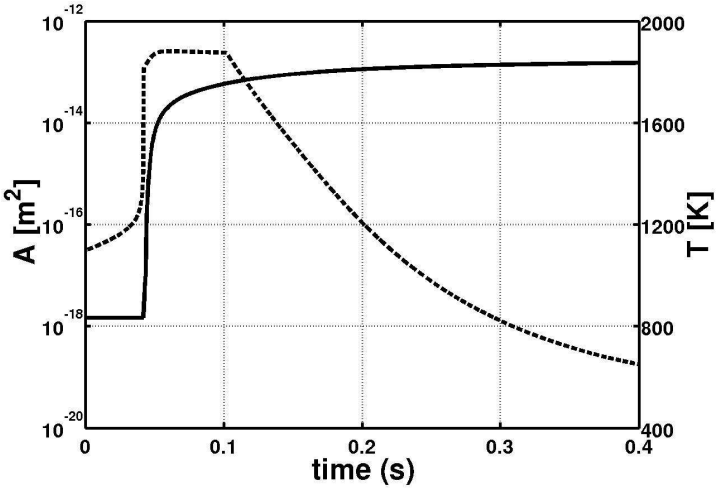

(c) Detailed surface growth

Figure 3.19 Evolution of average area of aggregates (solid) and temperature (dashed) in flame D.

increase in particle surface area. Hence, the three mechanisms predict different evolution of aggregate area. For one-step and detailed gas-phase mechanism the evolution is dominated by nucleation, hence, the aggregate area along the stoichiometric surface remains low. In comparison, the average aggregate area for detailed surface growth rises extremely rapidly after initial nucleation. As in this case titania deposits on the surface of already present aggregate surfaces, the models predicts aggregates with larger area as compared to the other two cases.

Primary particle size The average primary particle sizes (d_{p}) (as calculated in Eq. (3.24)), are plotted in Figure 3.20. The high temperatures and large aggregates along the stoichiometric surface result in sintering and as agglomerates coalesce they lead to an increase in size as primary centers fuse into each other. In the one-step gas-phase mechanism, as a large number of nuclei are introduced right at the jet entrance the nuclei size increases very rapidly. With no new nuclei entering the system after the residence time of 0.1 sec, the primary size continues to rise till sintering is active and reaches a steady value of 45 nm around 0.25 sec. In the case of the detailed gas-phase mechanism, the primary size remains constant until the residence time of 0.04 sec as not enough nuclei have been added to aggregate and then sinter into larger primaries. But after this the expeditious rise in nucleation, aggregation and sintering leads to increase in primary size. The continued nucleation after $t > \tau$ for the detailed gas-phase mechanism does lead to a slower increase in the average primary size when compared to one-step gas-phase mechanism. But the primary size for the detailed gas-phase mechanism also reaches a steady value of 42 nm at the residence time of 0.3 sec. For both one-step and detailed gas-phase mechanisms, nucleation and then the further agglomeration happens on the stoichiometric surface and it is observed for both the mechanisms sintering has a major effect on the final product properties. While using the detailed growth mechanism initially the primary size remains constant again till 0.04 sec. After this nucleation and subsequent aggregation leads to aggregates with high surface area which leads to both surface growth and sintering. The growth process becoming dominant results in a rapid increase in aggregate size and as these large aggregates undergo sintering this leads to a further increase in the primary diameter.

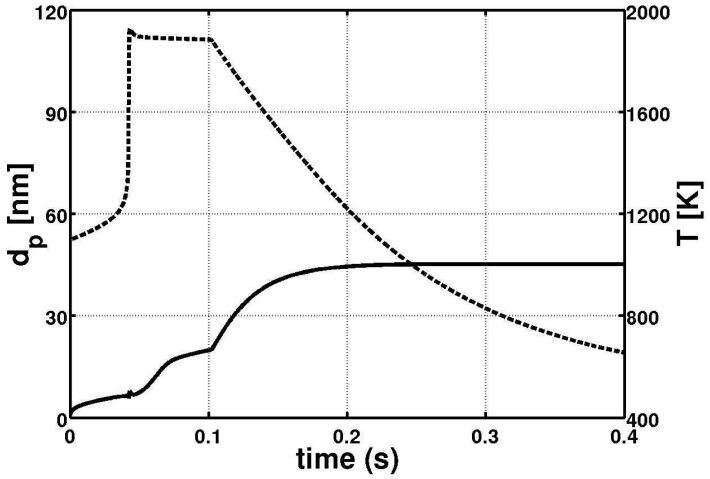

(a) One-step gas-phase mechanism

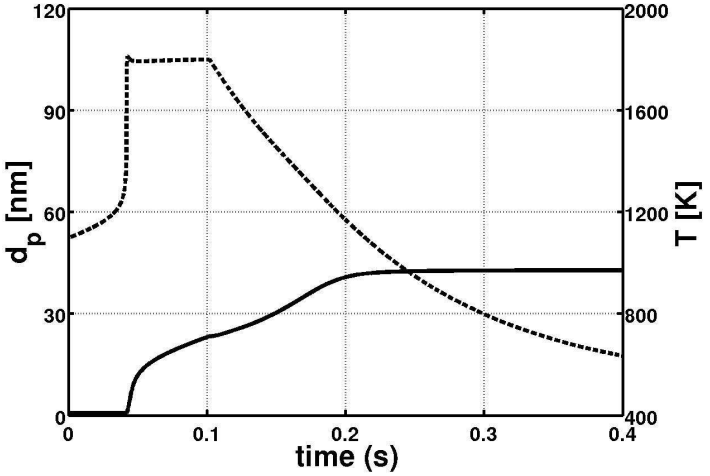

(b) Detailed gas-phase mechanism

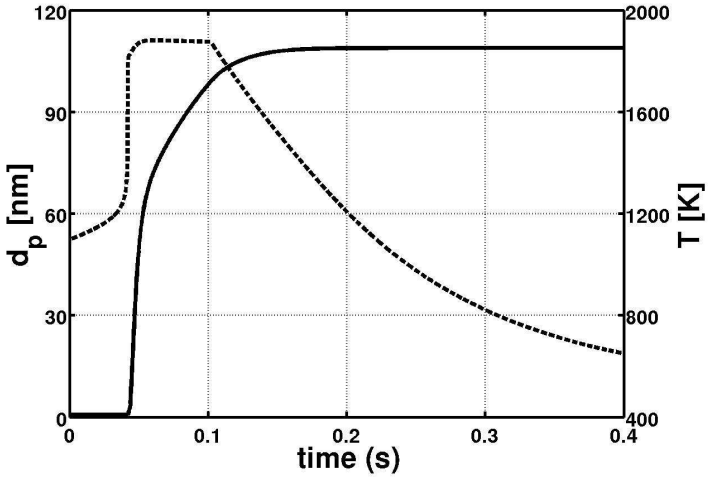

(c) Detailed surface growth

Figure 3.20 Evolution of average primary particle size (solid) and temperature (dashed) in flame D.

The final average primary diameter is 108 nm, which represents a good approximation when compared to the experimental value of 105 nm. More importantly, it is observed that sintering plays a vital role in the final product properties and hence, the detailed surface growth mechanism accurately describes the sintering trends observed for this flame configuration.

3.4 Chapter Summary

First, the effect of different gas-phase chemical mechanisms on nucleation of titania nanoparticles was studied. It was found that one-step nucleation rate increases with temperature and most nuclei are formed initially in the flame. The detailed nucleation rate is also a function of temperature and the maximum nucleation occurrs in a range from 1500–1800 K. The location of nuclei formation has an effect on the high-temperature sintering process and two flame configurations studied to highlight this effect. Three different models were used to study the two flames: one-step gas-phase mechanism with simple growth expression, detailed gas-phase mechanism with simple growth expression and detailed gas-phase mechanism with detailed surface growth expression.

It was found that the one-step gas-phase with simple growth model predicted that particles will be formed upstream of the high temperature region and hence sintering would be important for both cases. The detailed gas-phase with simple growth model predicted most nucleation after the flame surface for flame A and at the flame for flame D. Both one-step and detailed mechanisms with simple growth expressions were found to be nucleation dominated.

The results for the two flames with the detailed growth mechanism were very insightful. For flame A, both nucleation and growth occur throughout the domain. On account of nucleation not dominating the system, we do not get aggregates with large surface area and hence surface growth is also not very pronounced. Thus, particles with small primary sizes are observed and in agreement with experimental observations it is found that sintering does not play a big role in the products obtained. In contrast for flame D, the initial high nucleation leads to aggregates with large surface area, which leads to surface growth being more prominent and consistent with experiments it is found that sintering does play an important role in the final product properties. The above results show that the detailed growth expression does follow

the observation of Pratsinis and Spicer (1998) (69), that if enough surface area is present to consume $TiCl_4$ by surface reactions, this would effectively quench gas-phase reactions and surface reactions would take precedence.

At this point we have both the kinetics and the PBE model available to do a real flame simulation using computational fluid dynamics (CFD). However, the large size of detailed chemistry (107 species and 501 reactions) prevents the use of CFD methods because of the high computational cost. Hence, we have to reduce this chemistry size to couple it with flow simulations. The next chapter will addresses this problem and helps us find a reduced mechanism.

CHAPTER 4. Mechanism Reduction

The importance of applying detailed chemical kinetics in combustion simulations is now generally recognized. It is further recognized that, limited by current computer power, it is necessary to reduce these mechanisms to smaller sizes and with less stiffness such that the simulations are efficient and reasonably accurate. The need is particularly relevant in studies on turbulence and flow fields with complex geometries. Lu and Law, 2006.

4.1 Motivation

Using computational fluid dynamics (CFD) to model nanoparticle synthesis in chemical reactors has been proven to be an important tool for understanding and implementing coupling between transport processes and chemical reactions (11). Accurate modeling of titania synthesis in chemical reactors involves a highly detailed chemical kinetics for Ti oxidation as well as fuel combustion and chlorination. Also, required is the correct coupling of the complex interactions between chemical mechanism and transport processes. In developing a chemical mechanism we propose a list of species and take into account all feasible reactions. This leads to a large and highly detailed reaction mechanism involving species and reactions that might not have a significant effect on the reaction path of the species of our interest. As discussed above the detailed mechanism for TiO_2 nanoparticle formation involves 107 species and 501 reactions. CFD techniques are used to couple the reaction mechanism with the transport processes but due to the large number of species and reactions involved, coupling this chemistry with detailed flow solvers is computationally very expensive. Thus, for practical simulations reducing these highly detailed chemical kinetics to moderate size is very important.

Various methods for mechanism reduction have been proposed and reviews of most prevalent reduction methods can be found in literature (40). Several approaches have been used for

reduction, such as principal component analysis (93), sensitivity analysis (64), lumping (23), or Jacobian analysis (85). Recently, graph-based approaches (42) have gained increased interest due to their cost-effectiveness and reliability. One such graph-based method, called the directed relation graph with error propagation (DRGEP) (61), will be used here to carry out species and reaction elimination. DRGEP uses an error propagation algorithm to quantitatively estimate the role of each species and reaction in a mechanism based on the the production and consumption rates determined for a set of target species.

While mechanism reduction techniques have been effective in alleviating the problem of computational expense associated with large detailed mechanisms, the sampling approach used in these methods to identify the most important pathways may not be applicable for CFD applications. Common reduction approaches rely on dense sampling of a large number of simple flow configurations such as perfectly stirred or homogeneous reactors, covering relevant temperature, pressure, and initial composition ranges. Such sampling techniques provide access to a limited portion of the full composition space, which is unlikely to be representative of the actual composition space accessed during a two- or three-dimensional turbulent simulation, where mixing is expected to play a major role. Thus, to access a much larger region of the composition space than available through the more commonly used zero-dimensional plug flow or isochor reactors, we use partially stirred reactor (PaSR) model. Introduced in this chapter, is an extension on the directed relation graph with error propagation reduction (61) technique to access a much larger region of the composition space. The new model is based on partially stirred reactor model and extends the relevant sample size used by the reduction algorithm. By generating an expanded reduction sample space the detailed gas-phase mechanism for TiO_2 nanoparticle production is first reduced. The conditional errors show that the reduced mechanism proposed here is very accurate in predicting the kinetics of the system.

4.2 Reduction approach

The advent of computational quantum chemistry in chemical kinetics has to led to very large and detailed mechanisms being available to represent the chemical processes. CFD based methods can be used to track the evolution of all the species in the system but the solution of

this problem scales as N^3 where N is the number of species ($N \times N \times N$, the first N is the number of equations and the next N's are due to the Jacobian involved in solving the N equations). As the species equations have to solved in time at every grid cell, the solution of such large number of species is prohibitive with the use of CFD based methods. This proves to be a challenge as using detailed mechanism is imperative to represent the elaborate chemistry involved in the nanoparticle synthesis process. Hence, due to our limited computational resources such large mechanisms cannot be directly used in CFD methods. Thus, it is essential to reduce these mechanisms to smaller sizes and reduce stiffness such that the simulations are efficient and reasonably accurate, particularly in combustion studies on turbulence and flow fields.

Parametrization techniques, such as steady-flamelet assumption (66; 72; 33; 87; 63), have been used successfully to model different flame configurations. One such technique, the flamelet model parametrizes the thermochemical composition of the gas phase using the mixture fraction, which is a conserved (63). In this technique, one-dimensional flamelet equations are solved *a priori* and the results stored in a look-up table. For titania production, both Mehta et al. (2010) (51) and Sung et al. (2011) (84) have used the flamelet-based approach to model the turbulence-chemistry interactions. The use of a single mixture fraction restricts the applicability of the flamelet table to reactor with two inlet streams (11). But multiple inlet streams are used in flame reactors to get particles with different sizes and morphologies (70). Hence parametrization techniques, though useful in reducing the mechanism to be based on a small number of parameters, are not applicable for all the cases encountered in combustion based synthesis.

Thus, other methods are required to reduce these large mechanism to moderate sizes, which would lead to accurate representation of the chemistry with reasonable computational costs. A number of approaches are available to reduce the highly detailed mechanisms, reviews of the existing reduction methods can be found in (40). In general, they fall under two major categories: the reduction at a skeletal level through the elimination of negligible species and reactions, and the introduction of modeling assumptions, usually based on a time-scale analysis. For skeletal reduction graph-based reduction techniques which are derived on production rate analysis have become popular (42; 61) and is also the technique of our choice. For the reduction

process we use directed relation graph with error propagation (DRGEP), which postulates that the influence of an error introduced by the change of concentration of a species, or by discarding the species entirely, is damped as it propagates along the graph to reach the targets (61). Below is short description of DRGEP, more details can be found in (61).

4.2.1 DRGEP

For a detailed mechanism it is easy to identify and eliminate irrelevant reactions which contribute negligibly to production rate of species but it is harder to identify and eliminate unimportant species. For example, a species A can be strongly coupled to species B either directly if they appear together in a reaction or indirectly if both of them are strongly coupled to another species C. Thus, if we intend to keep one species in the reaction mechanism, it is also necessary to keep the group of species that are strongly coupled to it (85). It is important to note that this strong coupling can be defined by threshold value given by the user reducing the mechanism. Also, lower the threshold value, the larger the reduced mechanism would be.

In directed relation graph (DRG) based methods (42; 44; 61; 43), which are based on production rate analysis, unimportant species are identified by resolving species coupling efficiently and with minimum user input. The basic premise behind DRG method is to create a relation graph in which each point on the graph is uniquely mapped to a species in the detailed mechanism and there exists a directed edge between two species, A and B, if their coupling is above a threshold value (42). Based on this relation graph, decisions on the important species can be made to obtain a skeletal mechanism. Graph based techniques have been proven to resolve this complex couplings between species very reliably and fast to carry out skeletal reduction.

One such skeletal reduction method, proposed by Pepiot-Desjardins and Pitsch (61), is a reliable automatic reduction method called direct relation graph with error propagation (DRGEP) (60). DRGEP, which requires minimum user input, postulates that the influence of an error introduced by the change of the concentration of a species due the discarding of some related species, or by discarding the species entirely, is damped as the removed species appears further away from the target in the graph obtained from the network of chemical reactions. DRGEP is a promising method for reduction of large mechanism and has been successfully

used to reduce a very large mechanism for iso-octane oxidation (61).

The aim of this reduction procedure is to identify, for any number of species in the skeletal mechanism, N_{skel}, a group of species of size $N_{rm} = N_{det} - N_{skel}$ that can be removed with minimal impact on the targets. This is done by evaluating, based on the detailed mechanism, interaction coefficients for each species from their production and consumption rates. A skeletal mechanism of size N_{skel} can then be created by removing from the detailed mechanism the species with the lowest interaction coefficients and any reaction in which these species appears as reactant or product.

The direct interaction coefficient (r_{AB}) is defined to measure the coupling between two species that are related through reactions, that is, the two species appear concurrently in the same reaction. In the DRGEP method, this coupling coefficient between two related species A and B, where A is the target species and B is the species to be removed, is calculated as:

$$r_{AB} = \frac{|\sum_{i=1}^{n_R} \nu_{i,A}\omega_i\delta_B^i|}{max(P_A, C_A)} \tag{4.1}$$

where,

$$\omega_i = k_{f,i}\prod_{j=1}^{n_{E,i}}[S_j]^{\nu_{i,j}^{'}} - k_{b,i}\prod_{j=1}^{n_{P,i}}[S_j]^{\nu_{i,j}^{''}} \tag{4.2}$$

$$\nu_{i,j} = \nu_{i,j}^{''} - \nu_{i,j}^{'} \tag{4.3}$$

$$P_A = \sum_{i=1}^{n_R} max(0, \nu_{i,A}\omega_i) \tag{4.4}$$

$$C_A = \sum_{i=1}^{n_R} max(0, -\nu_{i,A}\omega_i) \tag{4.5}$$

$$\delta_B^i = \begin{cases} 1 & \text{if the reaction i involves species B,} \\ 0 & \text{otherwise.} \end{cases} \tag{4.6}$$

Here, n_R is the total reversible reactions, ω_i is the net reaction rate for the ith reaction. $\nu_{i,j}^{'}$ and $\nu_{i,j}^{''}$ are the stoichiometric coefficients of species j in reaction i for the reactants and products respectively, and $\nu_{i,j} = \nu_{i,j}^{''} - \nu_{i,j}^{'}$ is the net stoichiometric coefficient. $n_{E,i}$ and $n_{P,i}$

are the numbers of reactants and products in reaction i, respectively. $k_{f,i}$ and $k_{b,i}$ are the forward and backward rate coefficients of the ith reaction.

Eqn (4.1) provides an estimate of the error introduced by removing from the detailed mechanism any one species, B, on the target A. But the goal is to remove the largest possible set of species while keeping errors below the given tolerance. Considering one species independent of the group of removed species in which it will eventually belong might lead to a very inaccurate estimate of the importance of each species. The following example illustrates such a case.

A reactant A is consumed through four parallel reactions to form the four products $S_{i=1...4}$. All the reactions have the same rate coefficient k:

$$(\mathrm{R}_{i=1...4})\ A \longrightarrow S_i$$

If species S_1, for instance, is removed from this mechanism, that is, reaction R_1 is removed, the relative error introduced in the consumption rate of A will be

$$\epsilon_{C_A} = \frac{4k[A] - 3k[A]}{4k[A]} = \frac{1}{4}. \tag{4.7}$$

This is in perfect agreement with the direct interaction coefficient between A and species S_1 given by Eqn. (4.1):

$$r_{AS_1} = \frac{\omega_1}{\sum_{j=1}^{4} \omega_j} = \frac{1}{4}. \tag{4.8}$$

Suppose that an additional species S2 is removed. The error in the rate of consumption of A is now $\epsilon_{C_A} = 1/2$. This is not well represented by the direct interaction coefficient $r_{AS_2} = 1/4$, because the definition from Eqn. (4.1) does not take into account the contribution from the species S_1, previously removed.

Thus, Eqn (4.1) has to be extended for a given set of removed species,

$$r_{AB,S} = \frac{\mid \sum_{i=1}^{n_R} \nu_{i,A}\omega_i\delta^i_{B,S} \mid}{max(P_A, C_A)} \tag{4.9}$$

where S is the set of species already removed and

$$\delta^i_{B,S} = \begin{cases} 1 & \text{if the reaction i involves species B or any species from S,} \\ 0 & \text{otherwise.} \end{cases} \tag{4.10}$$

Using this extended definition, the contribution for S_2 is now

$$r_{AS_1} = \frac{\omega_1 + \omega_2}{\sum_{j=1}^{4} \omega_j} = \frac{1}{2}. \tag{4.11}$$

which is a better estimate of the effect of removing the both the species, S_1 and S_2, from the mechanism.

Thus, for each target species, A, a set of primary dependent species can be constructed. This set contains species which appear explicitly in elementary reactions involving A. The coupling between A and each of these species in the primary set can be defined by interaction coefficient defined in Eqn. (4.1). If a species, B, is not present in the primary set for A, then $r_{AB} = 0$.

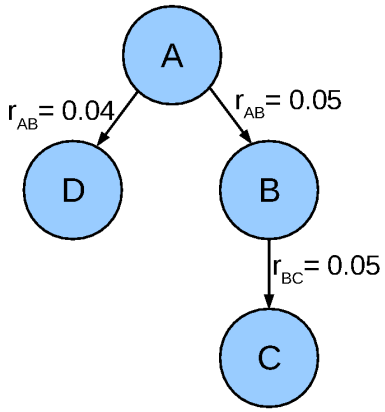

Figure 4.1 Error propagation in a mechanism with four species.

Now, removing of species from the primary dependent set leads to the introduction of some error in the target species. It should also be noted that removing of the species which are not in this primary set also would lead to some error in the specified target. Let species A be the target, and B and D are directly linked to A with another species C directly linked to B. The weakest link is r_{AD} with 4% error in the production rate of the target A. But it should be noted that, the farther away the removed species is from the target species, the smaller would

be the effect of its change or removal on the target. So removing species C would cause a 5% error is species B that has to propogate through to reach A. Thus, to take error propogation into account a geometric damping is introduced in the selection process

$$r_{AB,p} = \prod_{i=1}^{n-1} r_{S_i S_{i+1}} \tag{4.12}$$

$$R_{AB}^{DRGEP} = \max_{\text{all paths p}} (r_{AB,p}) \tag{4.13}$$

Thus, if an error is introduced in the prediction of a species B, the longer the way this error has to propagate to reach the target A, typically the smaller its effect would be. This technique will provide a better selection of chemical paths necessary for accurate prediction of the set of targets by keeping species associated with larger R coefficients and removing species with smaller R coefficients. Since the R coefficients are calculated based on target species, this technique is highly target driven.

The algorithm for mechanism reduction for the DRGEP method is as follows:

- A detailed mechanism for reduction is supplied.
- The direct interaction coefficient (r_{AB}) is calculated to measure the coupling between species.
- $r_{AB,S}$ is then computed to include the effect of removing a group of species.
- To take error propagation into account a geometric damping is taken into account and coefficient,R_{AB}^{DRGEP}, is finally calculated.
- Species with larger R_{AB}^{DRGEP} coefficients are kept in the mechanism while species with smaller R_{AB}^{DRGEP} coefficients are removed.

4.3 Reduction Domain

It is important to note that reduction is always carried out based on parameters derived from the detailed mechanism for a set of initial conditions. These conditions for example, initial temperature, pressure, species mass fractions, etc have a strong corelation with the kinetics and hence the value of reduction parameters calculated are strongly dependent on them. Even

though much progress has been made in developing efficient reduction techniques for gas phase combustion applications, most sampling approaches used by such techniques, to identify the most important pathways, may not be suitable for multi-phase configurations.

Most reduction approaches rely on sampling from flow configurations based on simple flow models such as plug flow reactors (PFR). Initial conditions are chosen for species mass fractions, timestep and total simulation time. The PFR is then run with the detailed chemistry and species values are stored at every timestep till the completion of simulation time. The species values stored at every timestep and considered as a sample point. These configurations usually cover only the temperature and composition space based on these initial conditions. Hence, samples taken from these configurations provide access to only a limited portion of the full composition space that is likely to be encountered during a two- or three-dimensional turbulent simulation. Also, PFR assumptions leads to a highly idealized condition of no back mixing and ignores the mixing effects on the samples. Again, under turbulent conditions, which are encountered in flame reactors, mixing is expected to play an important role. Also in these sampling methods cases involving both unreacted fuel and precursor are typically not included, which may result in important pathways being neglected in the reduced schemes. Another set of configurations, usually overlooked in PFR based sampling are pathways generated by mixing of intermediates before and during combustion.

The inadequacy of the sampling procedure for chemistry reduction would lead to mechanisms which are valid for only certain temperature and composition ranges. Hence, the sampling techniques of the traditional reduction methods have to be improved and expanded to result in reduced mechanisms which are valid for wider temperature and composition ranges. Partially stirred reactors (PaSR) provide access to a much larger region of the composition space than the more commonly used zero-dimensional plug flow or isochor reactors. PaSR models, which are essentially the application of a stochastic Monte-Carlo process, can be used to model well-macromixed turbulent reacting flows. The fluid composition in turbulent reacting flows changes by both reaction source terms and by mixing (11). The change in composition due to reaction is treated exactly, while molecular mixing has to be modeled. Modeling mixing in a PaSR involves prescribing the evolution of stochastic particles in such a way that they

mimic the change in composition of a fluid particle due to mixing in a turbulent reactive flow (73). A brief description of the PaSR model is given below.

The PaSR model is composed of n_p equally weighted notional particles, each particle carries information about species mass fractions (θ) and enthalpy. The system considered here is adiabatic and isobaric so the thermochemical state of the system can be completely described by θ and enthalpy. The PaSR is fed with inlet streams which determine the inflow/outflow conditions. The reactor is characterized by its residence time τ_{res} and mixing time τ_{mix}. The timestep for the PaSR is determined as $t_{step} = \frac{1}{10} min(\tau_{res}, \tau_{mix})$. The value of τ_{res} and τ_{mix} are chosen as 0.05 and 0.01 sec respectively. Each timestep includes an inflow/outflow step, in which the number of particles to be added and removed from the reactor are determined based on inlet conditions. At each timestep, $n_{replace} = t_{step}/\tau_{res}$ randomly selected notional particles have their composition replaced by new inflow composition. For flame reactors the inflow streams add fuel and oxidizer to the reactor. The amount of fuel or oxidizer added is based on the relative flow rates of the two streams.

This is followed by a mixing step, which models molecular mixing. In this work the modified curl approach (as described in (73)) is used. During the mixing step, $n_{mix} = n_p \times t_{step}/\tau_{mix}$ pair of particles are selected randomly, and their composition is modified according to the following equation:

$$\begin{aligned} \theta_1^{new} &= \theta_1 + \frac{1}{2} a(\theta_2 - \theta_1), \\ \theta_2^{new} &= \theta_2 + \frac{1}{2} a(\theta_1 - \theta_2) \end{aligned} \tag{4.14}$$

where a is a random variable uniformly distributed between 0 and 1. The same mixing rule is applied to the particle enthalpy, from which the temperature is recovered. Finally, the reactive part of the timestep is carried out. During this, the production rates of $S(\theta_i)$ are evaluated from the kinetics and species mass fractions are evolved using a stiff ODE solver (22):

$$\frac{d\theta_i}{dt} = S(\theta_i) \tag{4.15}$$

The other important parameter used to describe the PaSR calculations is the equivalence ratio ϕ, calculated based on definition described in (63):

$$\phi = \frac{Z}{(1-Z)} \frac{(1-Z_{st})}{Z_{st}} \tag{4.16}$$

where Z is the mixture fraction and Z_{st} is the stoichiometric mixture fraction. We assume that the value of mixture fraction in the fuel stream is unity and in the oxidizer field is zero. Equivalence ratio is very useful parameter as it can be used to determine which part of the flame our PaSR particles belong. When $\phi < 1$ the mixture is fuel deficient and the particle represents the fuel lean part of the flame. Correspondingly, $\phi > 1$ is oxygen deficient and the particle represents the fuel rich part of the flame. $\phi = 1$ represent the case where stoichiometric amounts of fuel and oxidizer are present and at this point $Z = Z_{st}$.

Using the PaSR based method, which involves mixing as well as effects of inflow/outflow conditions the composition space of samples collected for reduction can be expanded. Described now is the method for reduction based on PaSR sampling.

1. First step is the selection of initial conditions. We remember that reduced mechanisms will be valid in the range and applicability of the reduction space we create based on these initial conditions. To make certain that our reduced mechanism is valid for a full flame simulation we choose three conditions: when oxidizer and fuel are present below, at and above stoichiometric values. PaSR is then run for these three cases with the detailed reaction mechanism till steady state is reached for the input conditions chosen (shown in Table 4.1). The reduction sample space generated for these input conditions can be seen in Figure 4.2.

Table 4.1 Inlet conditions for generating reduction sample space

parameter	initial	stream 1	stream 2
flow rate (case 1)	fuel lean	0.96	0.04
flow rate (case 2)	fuel rich	0.9	0.1
flow rate (case 3)	stoichiometric	0.938	0.062
temperature (K)	1500	333	333
Ar (mass fraction)	0	0.08	0
CH_4 (mass fraction)	0.152	0	1
N_2 (mass fraction)	0.65	0.686	0
O_2 (mass fraction)	0.198	0.209	0
$TiCl_4$ (mass fraction)	0	0.025	0

2. For each case PaSR is run with n_p particles and after steady state is reached we begin recording particle composition data. To ensure steady state the PaSR is run till the duration

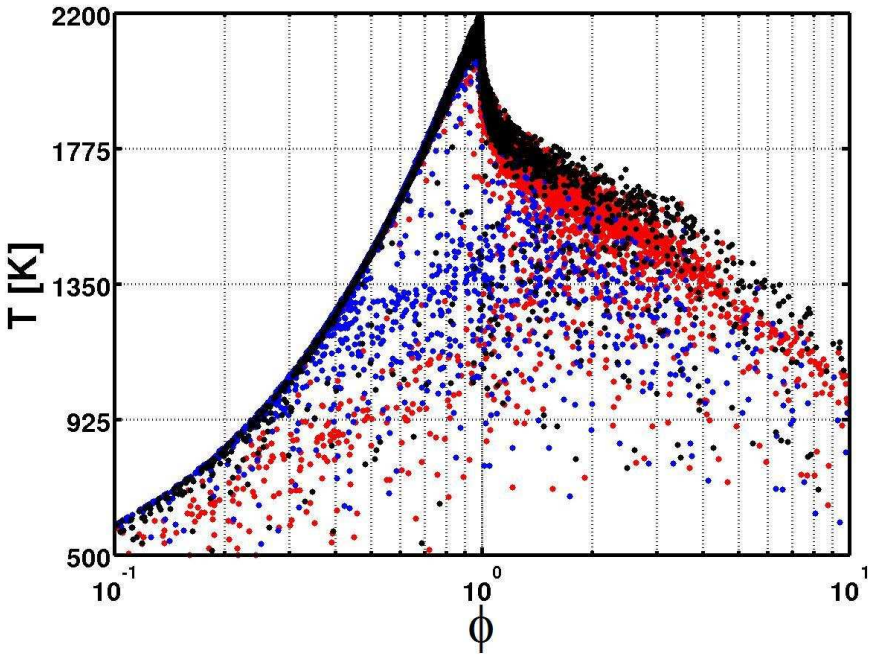

(a) Scatter plot

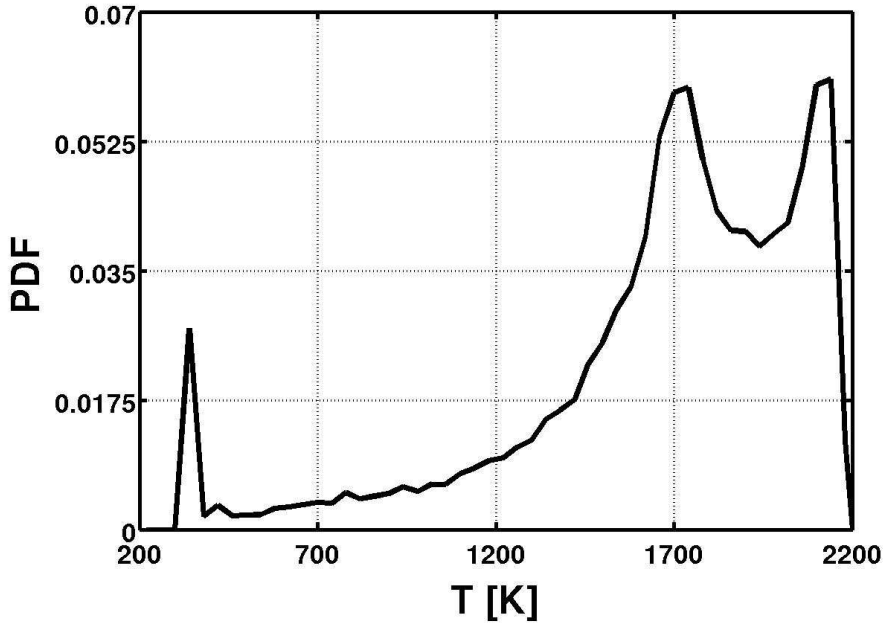

(b) PDF

Figure 4.2 Scatter plot and probability density function (PDF) of temperature at steady state for the three input conditions listed in 3.1. For the scatter plot case 1 (blue), case 2 (red) and case 3 (black).

of 4 residence times and after this particle data is stored at every τ_{res} till the simulation has run up till 10 τ_{res} (data collected six times between 5 and 10 τ_{res}). Data is collected multiple times at steady state to ensure that inlet/outlet conditions do not effect the sampling process. The value of n_p chosen for each PaSR is 1024. Hence, the total value of particles collected at steady state for this reduction is

$$n_{ss} = n_p \times 6 \tag{4.17}$$

3. It is important to remember that the reduced mechanism should replicate the complete reaction dynamics with accuracy, For CFD techniques, this means that the reduced mechanism should be accurate (as compared with the full mechanism) during the entire characterstic time step of the turbulent flow simulations. To ensure this dynamic performance by the reduced mechanism the following procedure is carried out. After steady state has been reached the chemistry of all n_{ss} particle is advanced for reduction timestep (t_{red}). During the advancement $nsub_{red}$ number of samples for each particle are recorded along t_{red} time. Therefore, the total number of samples collected for the complete reduction process are:

$$n_{sample} = n_{ss} \times nsub_{red} \tag{4.18}$$

Here the value of t_{red} is assumed to be the same as mixing time (τ_{mix}). For the input conditions chosen, the value of $nsub_red = 10$ was found to be accurate in describing the system.

4. After collection of n_{sample} number of samples, reduction procedure is carried out. For the given set of targets, the DRGEP coefficients for each species are calculated for every sample point. Now, the maximum DRGEP coefficient for each species is found out from all sample points. Taking the maximum DRGEP coefficient for each species ensures that even intermediates, which may not be coupled directly to the final products, are considered while generating the reduced mechanism. For example, let us assume that species A is very important for the early decomposition of the fuel. If species A is not include in the mechanism, fuel will not decompose, intermediate radicals will not be formed which would result in elimination of important pathways for the creation of products. For this species, the DRGEP coefficients will be very large for the sample points corresponding to the early stages of reactions, but negligible everywhere than that. Taking the maximum DRGEP coefficient would ensure that

the importance of species A in the early stages of mechanism would still be present in the reduced schemes. The maximum DRGEP coefficients for all the species are then tabulated in a sorted list of species.

5. Reduced mechanisms can now be generated based on this table by removing both the species with low DRGEP coefficients and the reactions associated with them. First, the normalized root mean square deviation (to be described in Section 4.4.1) are plotted for each reduced mechanism to help us determine the suitable reduced mechanism.

6. Finally, the PaSR is run with the chosen reduced mechanism and conditional mean and variance (described in Section4.4.2) for the targets are compared with the detailed mechanism to comment on the overall robustness of the reduced mechanism.

4.4 Error measurement

The reduction of detailed mechanism leads to introduction of errors in the resulting mechanisms. The representation of errors is very important as it serves as the parameter by which we decide the extent of reduction as well as the fidelity of the reduced mechanisms. Relevant error measurement is one of the most crucial, yet often ill-defined quantities for mechanism reduction. For instance, in the case of combustion, the relative error in ignition delay time is a preferred method for comparing reduced and detailed mechanisms. Though ignition delay is useful in predicting flame characteristics, errors in ignition delay may not be the correct measure for comparing errors in Ti chemistry. Hence, a small error in ignition timing does not mean that the reduced mechanism reproduces the complete dynamics of the detailed mechanism accurately. In addition, evaluating the error on intermediate species are nontrivial and the conventional techniques of error estimation may not accurately predict the errors for these species. With three basic families of reactions: Ti oxidation, CH_4 combustion and chlorination taking place in the flame interaction between species and intermediates is even more complex and care should be taken in estimating errors.

Accurate error measurement becomes even more important in the PaSR setting as the errors should also make statistical sense. This work aims to perform reduction on a wide composition space and hence, relatively poor performance of the reduced mechanism in certain regions

of the domain may not adversely effect the overall prediction. Hence, the calculated error should take this into account and perform averaging over the domain to provide an useful and balanced estimate for the overall system. But it should also be noted that failure to predict certain dynamics in the a small part of the system may lead to very inaccurate predictions. For example, in the case of auto-ignition the reduced mechanism required to predict a sustained flame can contain quite different species from the mechanism that is required initially to start the ignition process. If most of the particles in the PaSR for auto-ignition are at steady state than the reduced mechanism can predict low errors based on averaging. But the reduced mechanism is not accurate (and of no use), if it does not predict the initial radical and heat generation which leads to the thermal runaway. Therefore, the calculated errors should monitor that the reduced mechanism accurately predicts the dynamic behavior of the chemistry over the entire domain.

To accurately measure the performance of reduction, we define two types of error calculations on our system to compare detailed and reduced mechanisms: normalized root mean square deviation and conditional errors. Following is the description of the two errors.

4.4.1 Normalized root mean square deviation

As described above all reduction samples collected in the PaSR (n_{sample}) contain information about species mass fraction (θ) and enthalpy. If the detailed mechanism consists of N_{sp} number of species, then the length of vector θ for detailed mechanism is N_{sp}. Now as species reduction takes place the number of species (N_{sp}) used to describe the mechanism decreases. This leads to reduction in the length of the vector θ for the reduced mechanism. Hence, we need to define a method to efficiently compare two vectors (detailed vs reduced). This comparison is done by computing the reduced model error based on a normalized root mean square deviation. This ensures that the calculated error is averaged over the entire reduction domain and gives us a sense of how the reduced mechanism behaves globally. This error is calculated by progressing the detailed and reduced mechanism over the reduction time period (t_{red}).

Normalized root mean square deviation in this work will be denoted by ϵ and can be

calculated between the detailed solution (θ_d) and reduced solution (θ_r) for n_{sample} particles as:

$$\epsilon = \sqrt{\frac{\sum_{i=1}^{n_{sample}} (\theta_r - \theta_d)^2}{\sum_{i=1}^{n_{sample}} \theta_d^2}} \tag{4.19}$$

4.4.2 Conditional mean

The samples for the PaSR based reduction are collected after the PaSR becomes statistically steady. It is important to note that it is the PaSR which is in steady state but not the chemistry of the particles involved. Hence, while collecting samples for the PaSR based reduction we get a collection of particles at various stages of advancement, some of them close to equilibrium, some of them in the very reactive stages of the chemical reactions. Mixing and residence time of particles play an important role in the composition of these samples. Hence, these samples give a better estimation of the composition domain encountered in a turbulent flow simulation as compared to samples generated by a traditional PFR.

PaSR based method leads to samples over a large composition space and the errors can be calculated by computing the conditional means for the targets over this domain. For better representation of the flame, each particle is denoted by its equivalence ration (ϕ). Plotting this we find that PaSR simulations adequately cover a wide range of ϕ values (seen in Fig 4.2). By taking a large number samples over steady state we can cover every possible ϕ value for this configuration. We do this by collecting samples from the PaSR multiple times (n_{sample}) after the steady state has been reached. In this work, PaSR is again run till 4 τ_{red} and then samples are collected after each τ_{res} up till a period of the 10 τ_{res}.

After collection, n_{sample} samples are sorted in ascending order of ϕ and equally divided into N_{bin} bins. The number of samples in each bin (p) is then

$$p = \frac{n_{sample}}{N_{bin}} \tag{4.20}$$

The dimension of the bin is decided by the minimum and the maximum value of ϕ associated with the p particles inside it. The position of the bin is calculated as the mid point between the minimum and maximum ϕ. The mean and variance of the p particles for each bin are then reported. The results are then plotted to compare the mean for each bin for the compared mechanisms.

The conditional variables help us in calculating the errors introduced by reduction over the entire region of the flame. This gives us better insight about the regions where the reduced mechanism is not accurate and would help us in proposing better reduced schemes. As all conditional errors are calculated at steady state, with the system starting from initial conditions, the reduced mechanism has to accurately predict all the dynamic pathways accurately for the conditional errors to be small. Also, unlike the first technique these values are free of the numerical errors that can accumulate because of cumulative collection of samples.

4.5 Results and Discussion

Before discussing the results, it is important to note that DRGEP method is target specific. We define all the errors and carry out the reduction based on the target species. Hence, it is necessary to list our target species before starting the reduction process. Nanoparticle synthesis in flame reactors as described by the detailed gas-phase mechanism can be accurately described based on four variables (49), which are temperature, oxygen (O_2), the precursor ($TiCl_4$) and the nuclei (TiO_2). Hence, the goal of the reduced mechanism is to accurately predict these four variables in comparison with the detailed mechanism.

After generating the sample space reduction based on DRGEP is carried out find reduction coefficient based on the listed targets. This generates a sorted list which is shown in Table 4.2. Reduced mechanisms are generated by removing one species after the other starting from the highest species number (107).The reduction of mechanism leads to errors in prediction of the chemistry when compared to the detailed mechanism. By using error estimation techniques as described in Section 4.4 we can quantify these errors and comment on the accuracy of the reduced mechanisms.

4.5.1 Predicted errors

First reported are the normalized root mean square deviations, ϵ, for the targets with respect to number of species (N_{sp}) in the reduced mechanism (Figure 4.3). ϵ is calculated by progressively taking out one species after the other according to the sorted list (Table 4.2). With initial reduction, the errors remain quite small but as more species are taken out of the

Table 4.2 Species number and name according to sorted list. List in descending order with the most important species first.

No.	Name	No.	Name	No.	Name
1.	O_2	2.	N_2	3.	$TiCl_4$
4.	CH_4	5.	Ar	6.	Cl_2
7.	CO_2	8.	TiO_2(ru)	9.	$Ti_5O_6Cl_8$
10.	Cl	11.	TiO_2Cl_2	12.	$TiCl_2OCl$
13.	$Ti_2O_2Cl_4$	14.	$TiOCl_2$	15.	$Ti_3O_4Cl_4$
16.	$Ti_2O_2Cl_3$	17.	OH	18.	CO
19.	H	20.	CH_3	21.	CH_3Cl
22.	NO	23.	NO_2	24.	HO_2
25.	$TiCl_3$	26.	$Ti_2O_3Cl_2$	27.	O
28.	CH_2O	29.	HCO	30.	H_2O
31.	H_2O_2	32.	HCl	33.	H_2
34.	Cl	35.	$TiOCl_3$	36.	TiO_2Cl_3
37.	CH_2Cl	38.	CH_2Cl_2	39.	$Ti_2O_2Cl_6$
40.	C_2H_2	41.	C_2H_3	42.	CCl_4
43.	CCl_3	44.	$TiCl_2$	45.	CH_3O
46.	$Ti_2O_2Cl_3$	47.	C_2H_5	48.	C_2H_4
49.	$CHCl_2$	50.	$CHCl_3$	51.	HCCO
52.	C_2H_6	53.	O_3	54.	CH_2
55.	CH_2CH_2(s)	56.	CH_3OH	57.	$Ti_2O_2Cl_5$
58.	CH_2ClCH_2Cl	59.	CH_2CO	60.	HNO
61.	CCl_3CCl_3	62.	CH_2OH	63.	ClO_2
64.	NH_2	65.	NH_3	66.	CH
67.	NH	68.	$CHClCH_2$	69.	$CH_2ClCHCl$
70.	C_2H	71.	N_2O	72.	HCN
73.	CCl_3CHCl_2	74.	HNCO	75.	HCCOH
76.	$CHCl_2CHCl_2$	77.	CH_2ClCH_2	78.	C
79.	H_2CN	80.	CCl_3CHCl_2	81.	$CHCl_2CH_2$
82.	HCNO	83.	TiCl	84.	t-CHClCHCl
85.	$CHCl_2CHCl$	86.	t-CHClCCl	87.	CCHClCHCl
88.	CCHClCCl	89.	CCl_2CH_2	90.	CH_2ClCCl_2
91.	NCO	92.	CCl_2CHCl	93.	$CHCl_2CCl_2$
94.	$CHCl_2CH_2Cl$	95.	NNH	96.	HOCN
97.	CCl_3CHCl	98.	Cl_2O	99.	N
100.	CN	101.	Ti	102.	CCl_3CH_2
103.	HCNN	104.	CCl_3CCl_2	105.	CCl_2CCl_2
106.	CH_3CCl_2	107.	CCl_3CH_3		

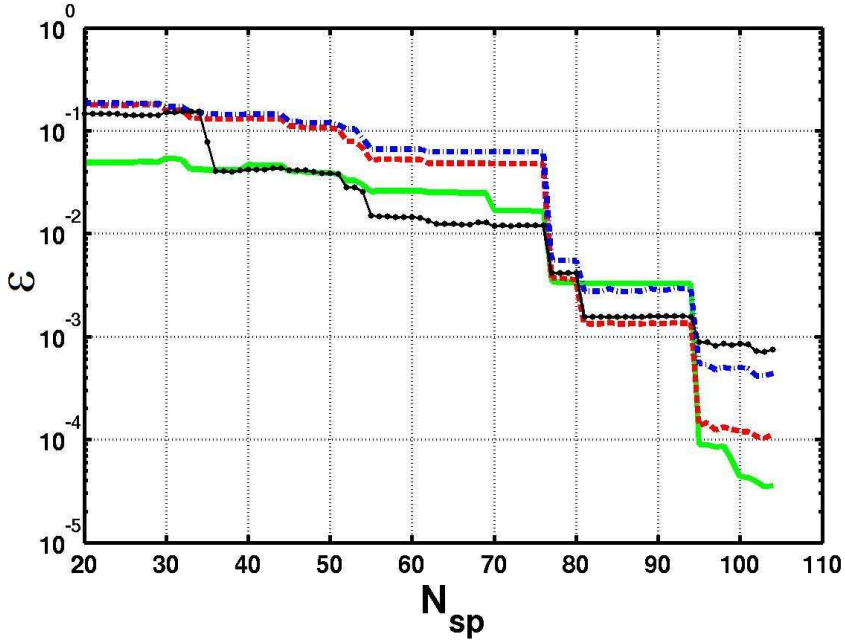

Figure 4.3 Computed ϵ error for targets with respect to the number of species in the reduced mechanism. Errors for temperature (green line), O_2 (red dashed), $TiCl_4$ (blue dash dot) and TiO_2 (black line with circles).

full mechanism the errors begin to rise. As seen in Figure 4.3, the errors for temperature remain quite low with reduction in species (below 10^{-1}). Thus, the reduced mechanism is accurate in predicting the combustion process. The predicted errors of the three species: O_2, $TiCl_4$ and TiO_2 are higher in comparison. Reduction leads to the removal of species and corresponding reactions from the system. By performing reduction we eliminate certain reaction pathways followed by the intermediates which contribute to errors in targets. Again it should be stressed that the reduction procedure is target specific and lower the species number in the sorted list the more important the species is for prediction of targets. The first major surge in error is seen after the removal of NNH (N_{sp} corresponding to 95). NNH radical is considered to be important to understand nitrogen oxide chemistry. The combustion chemistry used here (GRI Mech 2.11) considers the effect of nitrogen oxides on the flame and hence this radical has been included in the detailed mechanism. But as prediction of nitrogen oxides is not a priority (our targets remain temperature, O_2, $TiCl_4$ and TiO_2) NNH lies higher in the sorted list. Its removal does leads to a jump in the errors of targets but still the predicted errors are extremely low and the reduced mechanism estimates the targets with accuracy. The next jump in error comes after removal of another species important for nitrogen oxide chemistry (HCNO corresponding to $N_{sp} = 82$). After this the removal of C leads to further increase in error (N_{sp} corresponding to 78). Following this the value of ϵ remains almost constant and next significant increment in error occurs after the removal of CH_3OH ($N_{sp} = 56$). With further reduction the errors in the reduced mechanism rise and we find that removal of C_2H_6 would lead to errors in both O_2 and $TiCl_4$ rising above 0.01, which translates into an error greater than 10% in predicting these species in the simulation. After this the errors continue to rise for the three species ϵ reaches to a value of around 0.02.

In order to achieve reasonable accuracy in predicting the chemistry by the reduced mechanism we limit our reduction to the point where the errors in the four targets remain below 0.01. This results in a mechanism with 52 species and 161 reactions, which for the reminder of this article would be referred as the reduced mechanism.

After choosing the reduced mechanism based on desired accuracy from the ϵ error information, the chosen mechanism is used to simulate the PaSR to check if the reduced mechanism

can replicate the dynamic performance of the detailed scheme and also to find if the predictions from the reduced mechanism are accurate for the entire range of equivalence ratios. This is done by comparing the conditional mean and variance for both detailed and reduced mechanisms for all the n_{ss} sample point collected for the three PaSR runs as described in Table 4.1. The ϕ domain is decomposed into $N_{bin} = 30$ bins.

The results for conditional mean and variance for the four targets are shown in Figs. 4.4, 4.5, 4.6 and 4.7. As our simulations covered a wide range of particle composition, magnified plots around $\phi = 1$ are also included to give a closer look at the performance of the reduced mechanism. Also reported are the error bars describing the standard error for each bin. The length of the reported error bars represent probability of finding 99% of all particles in that interval. Observing Fig. 4.4(a) we find that the temperature of the system reaches its maximum value around $\phi = 1$ when stoichiometric amount of fuel and oxidizer are present and complete combustion occurs. Below and above stoichiometry the combustion is incomplete with either excess oxygen or fuel and thus, the corresponding temperatures are lower than the stoichiometric value. It is observed that the reduced mechanism represents the temperature quite accurately throughtout the ϕ domain (Fig. 4.4). Similar results are observed in the plots comparing variance and it is found that the predicted standard errors for the reduced mechanism are almost identical to that of the detailed mechanism. Hence, we can conclude that the prediction of combustion from the proposed reduced mechanism is reliable and accurate for the system.

Next compared are oxygen mass fractions for the detailed and reduced mechanisms. The mass fractions are high for both fuel lean and rich cases (corresponding to $\phi = 0.02$ and $\phi = 3$ respectively in Figure 4.5(a)) with the value being highest for the fuel lean cases. But as the fuel and oxidizer streams mix and equivalence ratios move towards the stoichiometric value the mass fractions of available oxygen decreases as most oxygen is now involved in the combustion process. From Figure 4.5(b), it is observed that the reduced mechanism is again very accurate in predicting the mean oxygen mass fraction over the whole ϕ domain. The maximum error occurs when the oxygen mass fractions are almost negligible at stoichiometric conditions ($\phi = 1$), where according to the detailed mechanism the mass fraction is 10^{-4} whereas the predicted

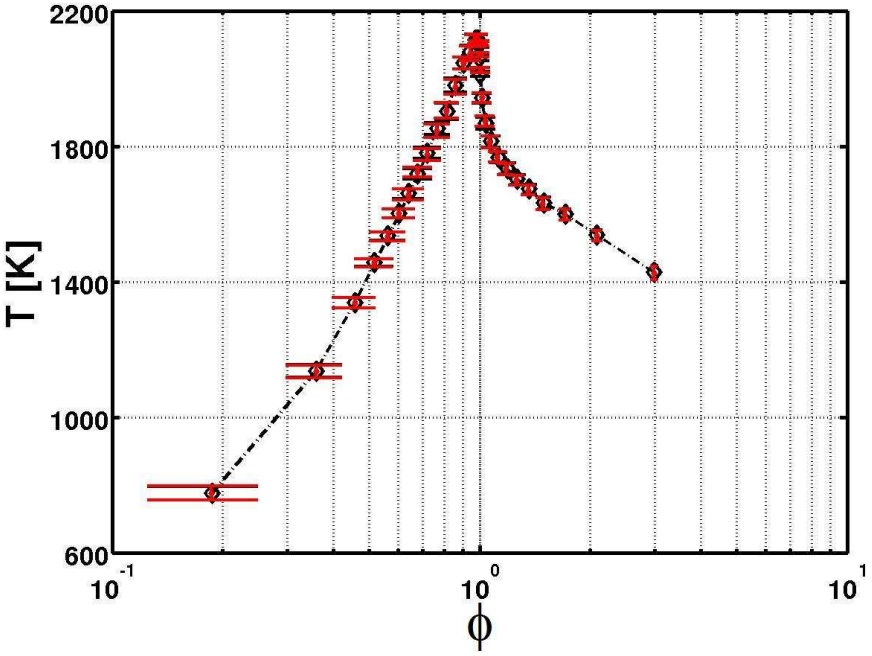

(a) Temperature

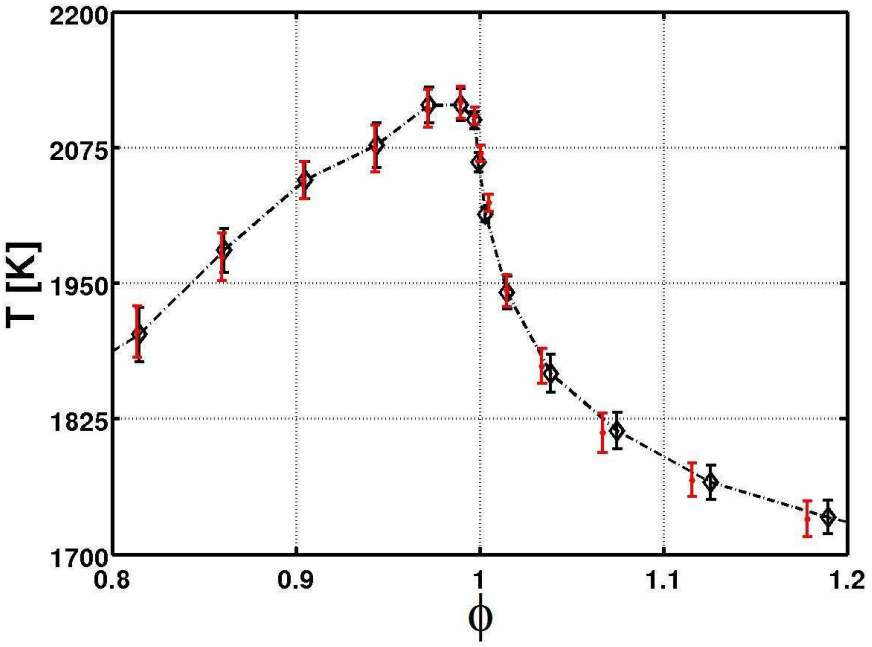

(b) Magnified view of Temperature

Figure 4.4 Conditional mean and variance for temperature.

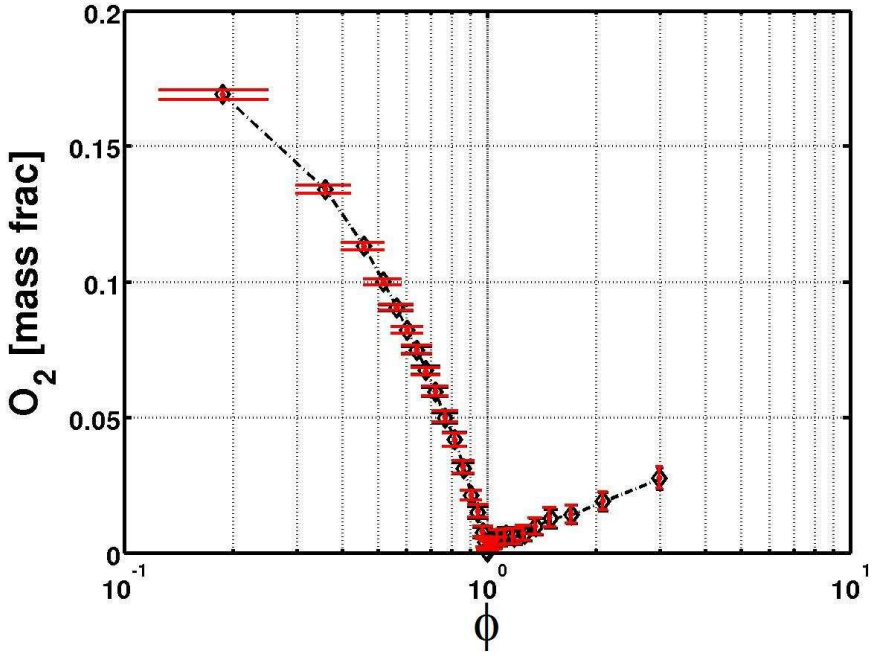

(a) O_2

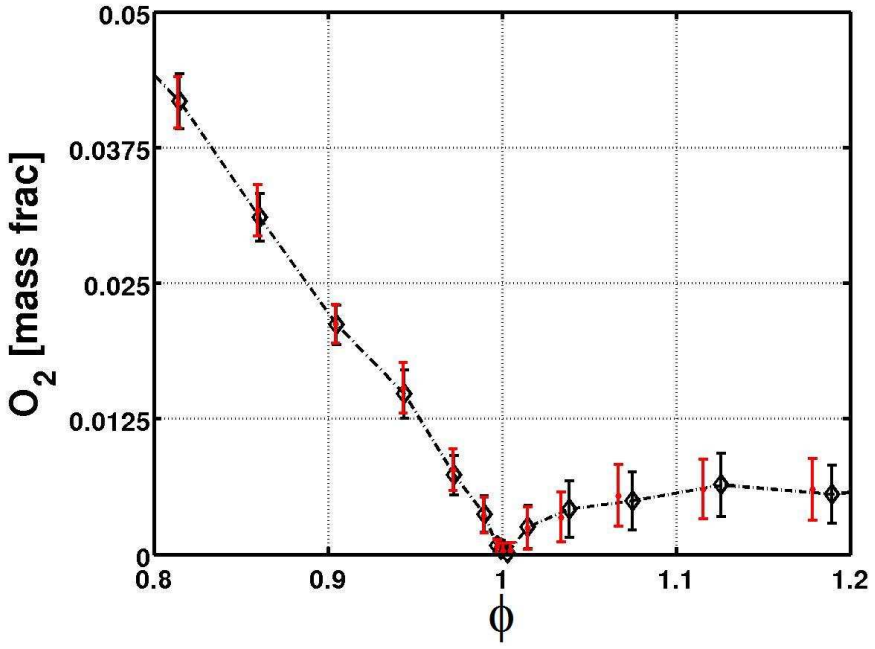

(b) Magnified view of O_2

Figure 4.5 Conditional mean and variance for O_2.

value by the reduced scheme is 3×10^{-4}. Analyzing the standard error between detailed and reduced mechanisms, we see that the reduced schemes are accurate in predicting not only the mean values of particles in each bin but also the variations in them.

Following this, we study the predicted mass fractions of the precursor, $TiCl_4$ (Figure 4.6). As the precursor decomposition increase with temperature, it is found that mass fractions of $TiCl_4$ are high for the fuel lean region. With the rise in temperature due mixing of the fuel and oxidizer the precursor decomposition increases and hence the mass fractions of $TiCl_4$ are very low in these regions (Figure 4.6(b)). For fuel rich regions ($\phi > 1$) the mass fractions again increase as lower temperatures lead to slower decomposition of the precursor (Figure 4.6(a)). The reduced mechanism is very accurate in predicting this behavior for the entire ϕ domain encountered. These predictions remain true even when extremely low amounts of $TiCl_4$ are present when the equivalence ratio is near unity. By observing standard error we conclude that the reduced mechanism very accurately predicts the mean and the variance of the precursor over the whole ϕ domain.

Finally, compared are the mass fractions of TiO_2 for both detailed and reduced chemistry. The mass fraction of TiO_2 increases with temperature in the oxygen rich portion of the flame ($\phi < 1$). Consistent with our previous work (51; 49) it is found that the mass fractions of TiO_2 are highest when the temperature is in the range from 1500-1800 K (Figure 4.8). After passing through this preferential temperature range the the mass fractions of TiO_2 begin to decrease. This behavior is not observed in the oxygen deficient region of the flame ($\phi > 1$). As stated earlier, in the flame both hydrocarbons and titanium containing species compete for the available oxygen and as hydrocarbon oxidation is the preferred reaction, the mass fractions of TiO_2 in the fuel rich side remain low. Observing Figure 4.7 we find that the reduced mechanism very accurately describes the evolution of TiO_2 for all equivalence ratios. Both the mean and variance of predicted TiO_2 mass fractions is very accurate, suggesting that the reduced mechanism can successfully describe the evolution of titania nanoparticles over all regions in the flame.

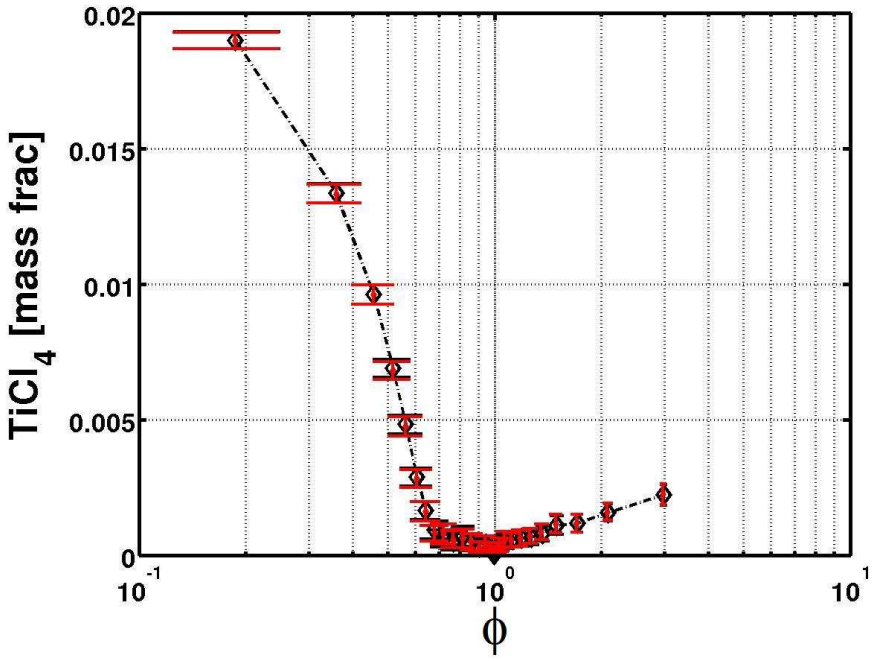

(a) $TiCl_4$

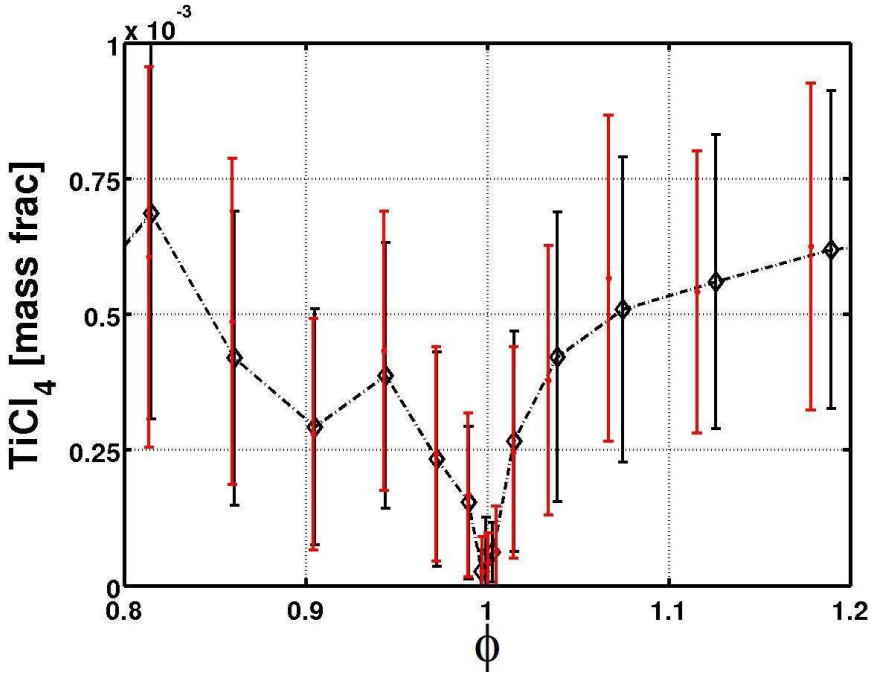

(b) Magnified view of $TiCl_4$

Figure 4.6 Conditional mean and variance for $TiCl_4$.

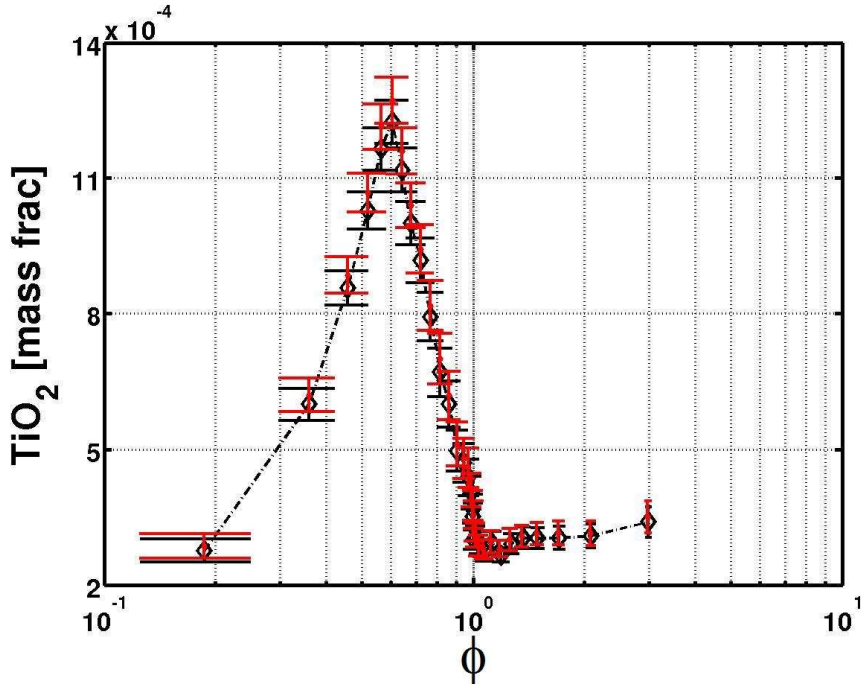

(a) TiO_2

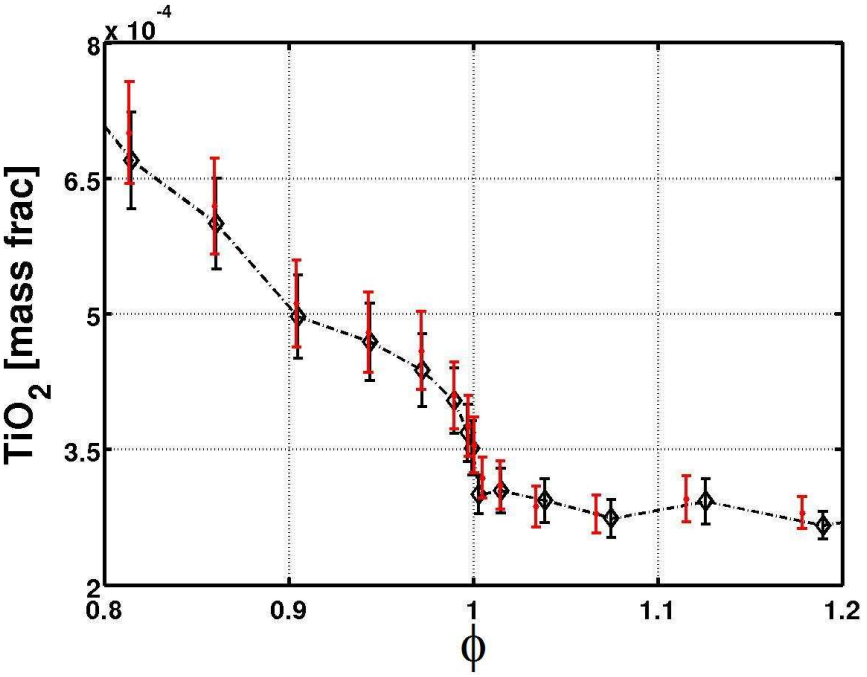

(b) Magnified view of TiO_2

Figure 4.7 Conditional mean and variance for TiO_2.

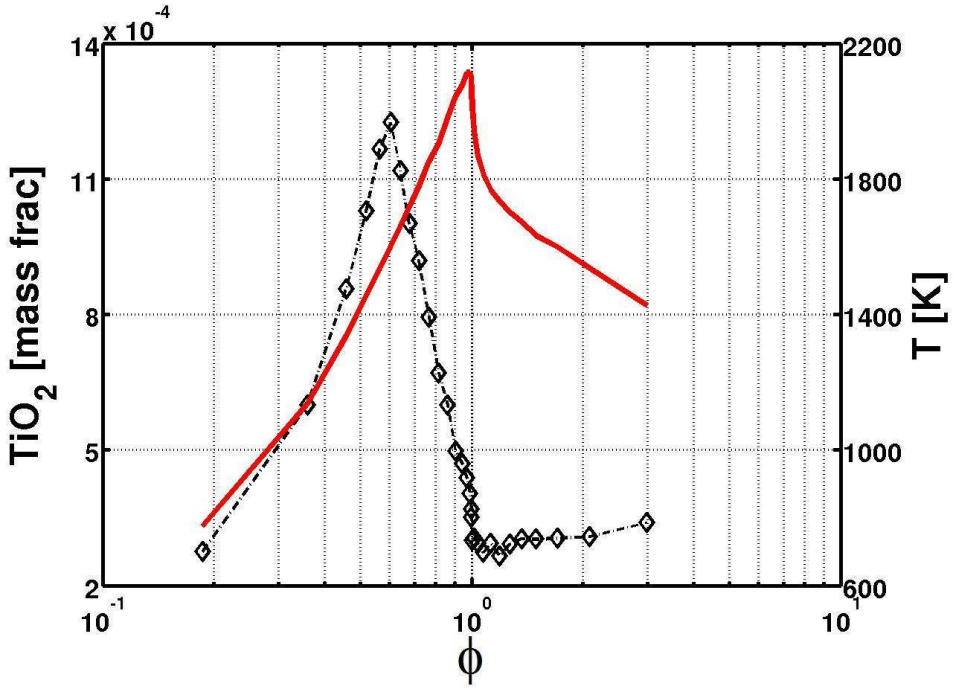

Figure 4.8 TiO_2 mass fractions (black symbols) with temperature (red line).

4.6 Chapter Summary

Detailed chemistry is essential for the correct modeling of TiO_2 nanoparticles in flame reactors. But due to their extensive size the use of detailed mechanisms is prohibitive in computational fluid dynamics solvers. Turbulent nature of the flame renders the traditional sampling methods based on simple flow configurations unsuitable for reduction strategies. In this work, the initial sample space used for reduction was expanded by using partially stirred reactor model. This new sampling technique was coupled with directed relation graph with error propagation to propose an improved model for mechanism reduction.

Multiple PaSR's with distinct flow conditions were used with the extended sampling technique to reduce the detailed chemistry for titania nanoparticle production in flames. The flow conditions were chosen to cover fuel lean, stoichiometric and fuel rich regions of the flame. Four variables (temperature, O_2, $TiCl_4$ and TiO_2) essential to describe the particle properties are chosen as targets for reduction. Using DRGEP on the extended sample space the mechanism

was reduced and normalized root mean squared deviation was computed. Based on this error reduced mechanism which lowered the detailed mechanism from 107 species and 501 reactions to 52 species and 161 reactions was chosen to compute conditional errors and compare both mechanisms over the entire range of equivalence ratios. The results for both conditional means and variances show that the reduced mechanism was successful in predicting the four target variables very accurately. The predictions were accurate over all regions of the flame, leading us to conclude that extended sampling does provide robust reduced mechanism which can be used for turbulent flow simulations.

Proposed in this chapter was an extension to directed relation graph with error propagation by more realistic sampling. The reduced mechanism calculated was extremely robust and accurate. Hence, we now have a reduced mechanism mechanism which can be coupled to CFD based approaches to accurately model chemistry in full flame simulations.

CHAPTER 5. Industrial Application

In which the results from authors research internship at DuPont Titanium Technologies are discussed.

5.1 Introduction

From July till December of 2011, the author interned at DuPont's Experimental Station for DuPont Titanium Technologies (DTT) Process Modeling Group. This was a great opportunity to apply all the methods and models developed, during the course of author's dissertation work, in an industrial environment. DuPont Titanium Technologies is the market leader in titania pigment industry and was the inventor of the *chloride* process for titanium dioxide production. It remains the chief innovator of the *chloride* process and the sponsor of a large amount of academic work done by both Pratsinis' group at University of Cincinnati (106; 104) as well as Morrison's group at Case Western Reserve University (71).

The objective of this work was to develop and implement the population balance approach for the oxidation reactor to get better insight in the production method, in order to understand the role kinetics, particle evolution, mixing and turbulence play in the final product particles. This required coupling of the PBE model with popular commercial applications: ASPEN Plus and Fluent configurations to give a complete and detailed model for chemistry, particle description and transport.

The PBE model was applied within two approximations of the oxidation reactor flow field: first, with the simpler plug flow reactor (PFR) model and finishing with the more complex CFD based reactor simulation. Included below are results based on the PFR model and their discussion. First, reported are the primary particle sizes. Secondly, the robustness and flexibility of the model is checked by changing particle evolution with addition of ionic additives.

The results show that we have been successful in developing and implementing a detailed and robust model for the titania oxidation process.

5.2 Model Description

The first aspect to be considered in particle description is the transformation of gas-phase species to solid phase particles by nucleation. After nucleation, the particles can undergo other particle evolution processes such as growth, aggregation and sintering. The evolution of the size distribution of particles in a reactor can be represented again by using a population balance equation (PBE), which describes the evolution of the particle size distribution (PSD). When describing the PSD evolution due to nucleation, volume growth and aggregation, the PBE can be represented by a single variable (e.g. particle volume). However, the presence of surface growth and sintering requires the introduction of an additional variable, surface area.

Before we define the process of aggregation and sintering, let us establish some definitions which we will continue to use throughout this section. The event defined as aggregation in this section is the collisional growth process which occurs due to particle-particle collisions. This aggregation process leads to the formation of agglomerates which is an ensemble of particles attached by only point contact. When these collisional products pass through high temperature regions this ensemble tries to minimize its surface area by sintering or coalescence, leading to the formation of aggregates. In contrast with agglomerate, in the aggregate the particles have started to fuse into each other. It is important to note that coalescence (or sintering) cannot happen without collision (or aggregation). Hence, only after the formation of agglomerate, coalescence leads to the formation of aggregates. Full coalescence leads to a new primary particle while partial coalescence leads to the formation of aggregates.

Aggregation, as noted above, occurs by a sequence of binary collision events in which two particles combine to form new agglomerate. As these large agglomerates pass through the high temperature regions they try to minimize their surface area by undergoing temperature-dependent surface-relaxation process wherein the agglomerate with a given volume tends towards a spherical shape, which is know as sintering. The collision products start as agglomerates and with solid-state sintering may become aggregates and given sufficient time and

temperature, ultimately become new, larger primary particles. This complete transformation occurs in the high temperature region of the reactor. If the transition region is relatively narrow, the transformation is arrested short of full coalescence into new primaries and as a result aggregates are formed. At lower temperatures, these aggregates agglomerate into particles that can be easily be brought back to the aggregate state.

The PBE thus derived has a bivariate form, which depends on two internal coordinates, volume (v) and surface area (a). The PBE has the same form as listed in Eqn.(2.5) but instead of time *'t'* the PBE will be written in terms of a dimensionless distance Z. The equation by which this distribution function ($f(v,a)$) evolves in terms of a dimensionless distance Z can be written as

$$\frac{\partial(u_Z f(v,a))}{\partial Z} + \frac{\partial(G_v(v,a)f(v,a))}{\partial v} + \frac{\partial(G_a(v,a)f(v,a))}{\partial a} - \frac{\partial(S_a(v,a)f(v,a))}{\partial a} = J(T,\phi)\delta(v-v_0)\delta(a-a_0) + B(v,a) - D(v,a) \quad (5.1)$$

where u_Z is the velocity in the Z direction. All the other terms have the same definitions as described in Section 2.

The derived moment equations remain the same as described in Eqn.(2.23) only the first term changes to

$$\int_0^\infty \int_0^\infty a^l v^k \frac{\partial(u_Z f(v,a))}{\partial t} dvda = \frac{d}{dZ}\int_0^\infty \int_0^\infty (u_Z a^l v^k f(v,a))dvda = \frac{d(u_Z m_{k,l})}{dZ}. \quad (5.2)$$

Hence, the final equation is

$$\begin{aligned}\frac{d(u_Z m_{k,l})}{dZ} = J(T,\phi)v_0^k a_0^l &- \int_0^\infty \int_0^\infty k v^{k-1} a^l G_v(v,a) f(v,a) dvda \\ &- \int_0^\infty \int_0^\infty l v^k a^{l-1} \left[G_a(v,a) - S_a(v,a)\right] f(v,a) dvda \\ &+ \frac{1}{2}\int_0^\infty \int_0^\infty \int_0^\infty \int_0^\infty \left[(v+v^*)^k (a+a^*)^l - v^k a^l - v^{*k} a^{*l}\right] \\ &\beta(v,v^*,a,a^*) f(v,a) f(v^*,a^*) dv^* da^* dvda. \quad (5.3)\end{aligned}$$

Both nucleation and surface growth events depend on chemical kinetics of titania oxidation. Surface growth is neglected in the results shown in this section and it is assumed that the entire precursor is consumed in the nucleation event. This assumption can be justified by arguing

that in absence of surface growth the given model would produce more nuclei (higher number density) which would undergo faster aggregation (aggregation event increase quadratically with number density). Thus, it is assumed that the inaccuracies in tracking volume while neglecting surface growth would be compensated by larger agglomerates (more nuclei hence larger number density). Larger agglomerates would also result in increased sintering rates as rate increase with number of particles in the agglomerate and their surface area (more nuclei). This increased sintering rate would act to balance the increased surface area due to large number of nuclei. Figure (5.1) explains the stated assumption.

Figure 5.1 Figure showing the difference in particle description with (left) and without (right) surface growth. The volume is conserved and as both the number of particles and surface area is greater on the right, it would lead increased sintering.

Brownian aggregation kernel with a constant fractal dimension (d_f) of 2.5 corresponding to diffusion limited aggregation is used to model the collisional growth. The frequency of aggregation is assumed to be Brownian. In aerosol manufacture of particulate particles, electrolytes are sprayed into the process stream to control the phase and size characteristics of the products. These electrolytes dissociate into their constitutive ions, some of which preferentially adsorb onto the particle surface and give rise to electrostatic repulsion forces between particles that affect particle-particle interactions, and hence, particle growth by aggregation (107). Following (107) we can calculate the effect this repulsion will have on the aggregation event.

In presence of charged particles, the collision kernel must be corrected by (following Eqn. (6) from (107))

$$\beta(v, v^*, a, a^*) = \frac{\beta(v, v^*, a, a^*)}{Q_{ij}} \tag{5.4}$$

where

$$Q_{ij} = \frac{\exp^{\kappa} - 1}{\kappa} \tag{5.5}$$

and

$$\kappa = \frac{\xi_i \xi_j e^2}{\varepsilon(r_i + r_j)kT} \tag{5.6}$$

here, ε is dielectric constant of the medium, r_i is the particle radius, z_i is the number of charges on a particle, e is unit charge in cgs units 4.8x10-10 statC, k is the Boltzmann constant and T is the temperature. Using Bjerrums criterion the upper limit for particle charging is set and the number of charges (z) on the particle are found as

$$\xi = \frac{2kT}{e^2} r \tag{5.7}$$

The rate of sintering of a particle, consisting initially of two separate, spherical particles contacting each other, can be approximately described by (36)

$$S_a(v, a) = \frac{1}{\tau_{\mathrm{f}}}(a - a_{\mathrm{s}}) \tag{5.8}$$

where a is the surface area, v the volume of the particle and a_{s} is the surface area of a solid sphere with the same volume as the sintering particle.

Several attempts have been done to extend Eqn. (2.39) for more complicated shapes (37; 12; 92; 41). The points-of-contact (POC) model introduced by Johannessen (28) is used in this work:

$$S_a(v, a) = \begin{cases} \frac{(a - a_{\mathrm{s}})}{\tau_{\mathrm{f}}(d_{\mathrm{p}}^*)} & \text{if } n_{\mathrm{p}} \leq 2 \\ (n_{\mathrm{p}} - 1)\left(\frac{0.41 a_{\mathrm{p}}}{\tau_{\mathrm{f}}(d_{\mathrm{p}})}\right) & \text{if } n_{\mathrm{p}} > 2 \end{cases} \tag{5.9}$$

where $a_{\mathrm{s}} = (36\pi v^2)^{1/3}$, $d_{\mathrm{p}}^* = (3v/\pi)^{1/3}$, $d_{\mathrm{p}} = 6v/a$, $a_{\mathrm{p}} = 36\pi v^2/a^2$ and $n_{\mathrm{p}} = a^3/(36\pi v^2)$. The sintering time τ_{f} is taken from (35).

ASPEN Plus is used by the Process Modeling Team at DTT to model the oxidation process. ASPEN Plus calculations can deal with chemical kinetics and unit operation part of oxidation but give no information about particle evolution. Our goal was to couple population balance modeling with ASPEN Plus to provide a detailed view of particle evolution. This would give the modeler an insight on how particle evolution takes place in the reactor and also the effect of change in initial conditions on product particles can be tracked. The population balance

model was run as a post processing step after finishing the ASPEN Plus calculations. For this work a test case was considered and the process flowsheet used is given in Figure (5.2), it consists of a PFR being fed premixed stream of reactants and is cooled using coolant flow.

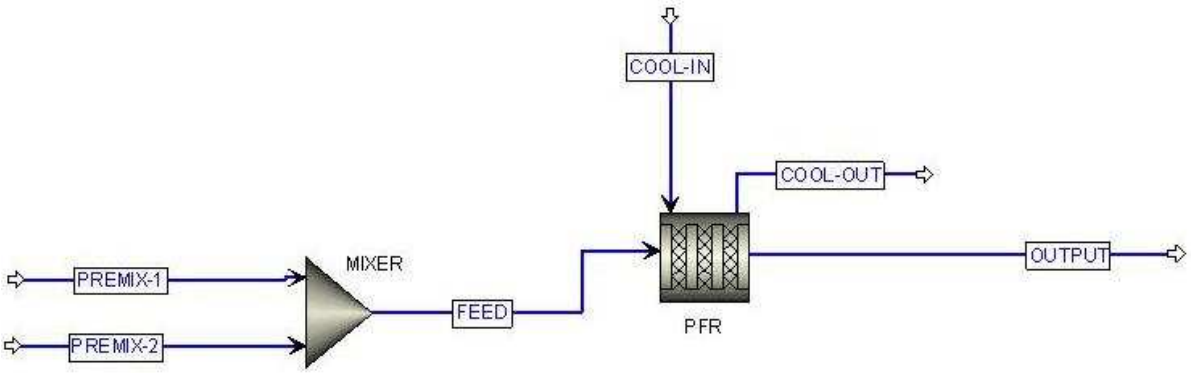

Figure 5.2 ASPEN Plus process flowsheet used for this work.

5.3 Results

For confidentiality purposes all resulted reported in this section have been normalized and made dimensionless. Hence, we only comment on the evolution profile of the variables.

5.3.1 Estimation of primary size

First observed is the particle number density (m_{00}) which evolves due to only nucleation and aggregation events. We observe in plot Figure (5.3), that as the temperature rises and the precursor is consumed a large number of particles are introduced into the system. Hence, the nucleation event leads to a sharp rise in m_{00} with rapid consumption of the precursor. But the large number of particles introduced in the system and rising temperature results in the aggregation event becoming active and subsequently leads to the decrease in number density. Around $0.04Z$ distance in the reactor most of nucleation is complete and now the aggregation event becomes dominant and a decrease in m_{00} is observed. With both high temperature and number density occurring initially, the aggregation term continues to remain dominating until around $0.2Z$. After this aggregation slows down and the number density decrease more gradually as shown in the right hand part of Figure (5.3).

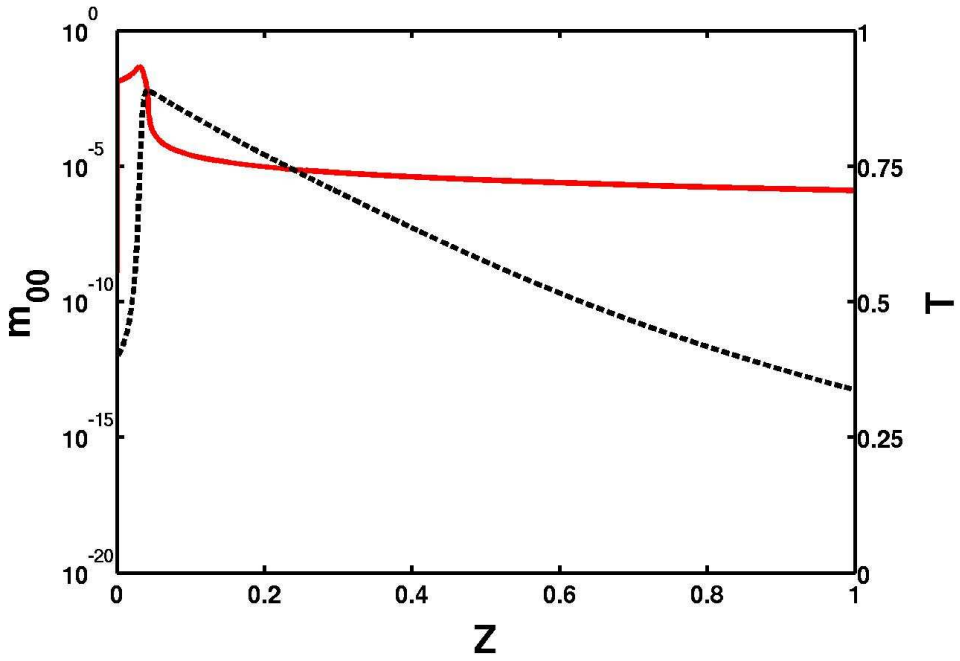

Figure 5.3 Evolution of number density with reactor length.

Observing the pure volume moment (m_{10}) evolution in Figure (5.4), it is noted that m_{10} increases initially as nucleation occurs and then reaches a constant value at around $0.04Z$ when nucleation stops. This is expected as both aggregation and sintering events have no consequence on the total particle volume concentration. In contrast the pure area moment (m_{01}) grows initially as nucleation occurs. Again aggregation has no effect on the pure area moment but sintering leads to decrease in the particle area and hence a decrease in m_{01}. First, the addition of large number of nuclei in the system leads to the increase in area concentration of the system. With the addition of large number of nuclei, these nuclei tend to agglomerate and when these large agglomerates pass through high temperature regions they undergo sintering. This is observed around $0.05Z$ in the plot Figure (5.5) and leads to the decrease in the area concentration of the system. As m_{01} can only decrease by the sintering event, the period for which sintering is active can be found by studying m_{01}. In this case we find that sintering is active till distance $0.65Z$ as until this point m_{01} continues to decrease.

Now we can use particle volume and area concentrations to estimate the primary particle

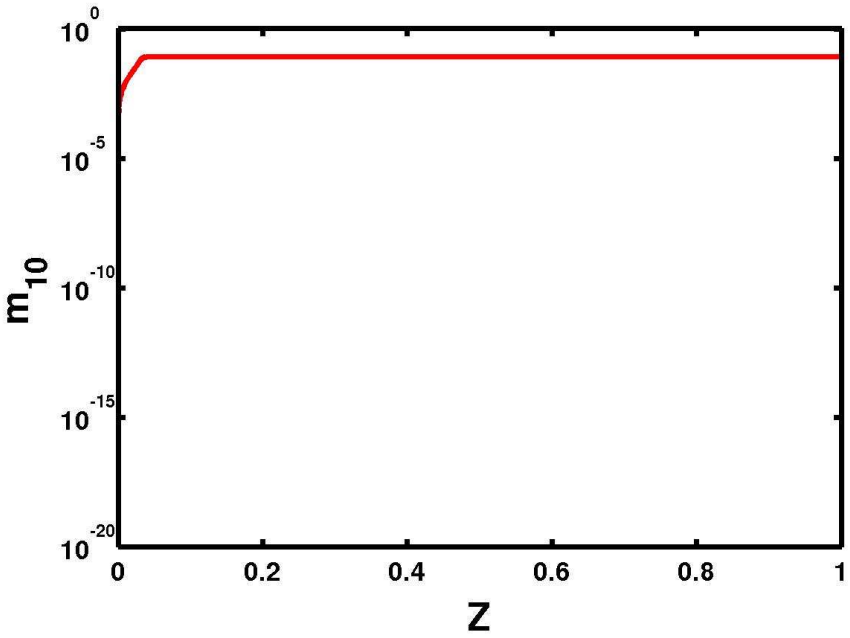

Figure 5.4 Evolution of volume concentration or the pure volume moment m_{10}.

size. Hence, we use the below definition (taken from (48; 50)) to estimate this size

$$d_p = \frac{6m_{10}}{m_{01}} \tag{5.10}$$

In aerosol production of pigments it is found that the reactors pass through different zones where only certain source terms of the population balance equation are dominant. Initially, mixing and kinetics are very important which leads to the consumption of the precursor. Precursor consumption leads to introduction of particles in the system and both the nucleation and growth term account for this increase in particle mass. After the initial stages in the evolution of product particles, the system is generally governed by aggregation and sintering (9).

Nucleation leads the introduction of nuclei in the system and aggregation results in formation of agglomerates from the nuclei population. Now, we assume that growth leads to addition of both volume and area to all the constituents of the agglomerate. Then the effect of growth is to increase the primary particle size in the agglomerate while also changing the size of agglomerate. Hence, nucleation and growth events can be assumed to control the primary

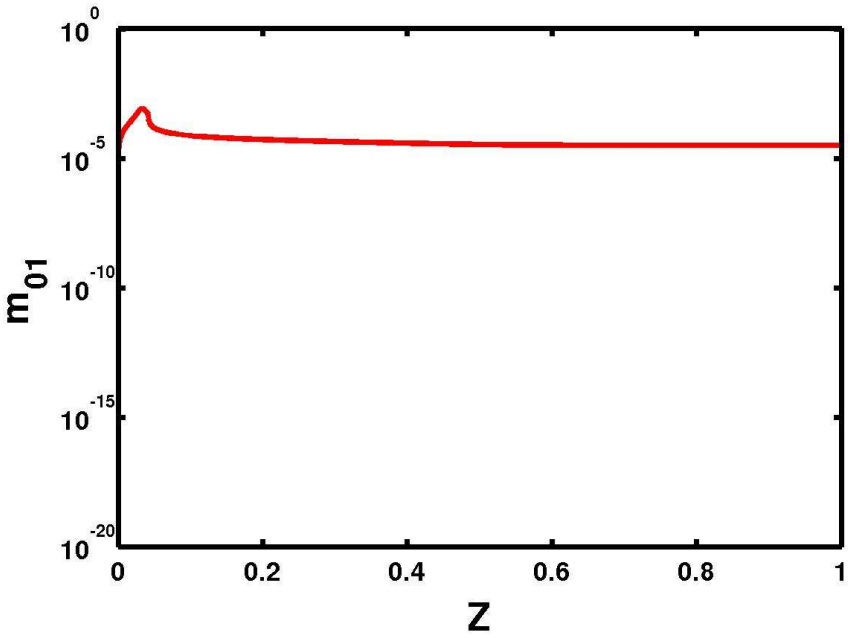

Figure 5.5 Evolution of area concentration or the pure area moment m_{01}.

particle size whereas aggregation process only affects the agglomerate size. We assume that in these agglomerates primary particles sit close to each with point contacts but can be separated easily as no coalescence has taken place. Sintering however, is interesting, because when it occurs agglomerates lose area. Also, the primary particle centers in the agglomerate coalesce so that centers are eliminated which leads to an effect on both primary particle size as well as the agglomerate area. This partially coalesced ensemble is called an aggregate. Thus, sintering leads to increase in primary size but decrease in the area concentration of the system. After sintering stops the aggregates continue to collide but this does not affect the primary size as no coalescence takes place. Hence, we can assume that when the sintering event stops so would the evolution of primary size.

Now as discussed above, different population balance source terms are active in different parts of the flow regime. Also, nucleation, growth and sintering all affect the primary particle size but aggregation only leads to change in the size of the agglomerates. Keeping this in mind, we find that the pure area moment (m_{01}) is the correct indicator to tell us when primary particle evolution has stopped. Looking at the plots for m_{01} we find that its evolution stops at around

$0.65Z$ (by observing plot Figure (5.5).

After $0.65Z$, the aggregation event continues but as discussed above this has no affect on the primary size. Hence, the primary size would be frozen at the value found when m_{01} stops evolving. The value of primary size (d_p) at the point when m_{01} stops evolving is $0.95\mathrm{d}_p$ as shown in Figure (5.6). The primary size thus obtained is consistent with primary values expected for these conditions.

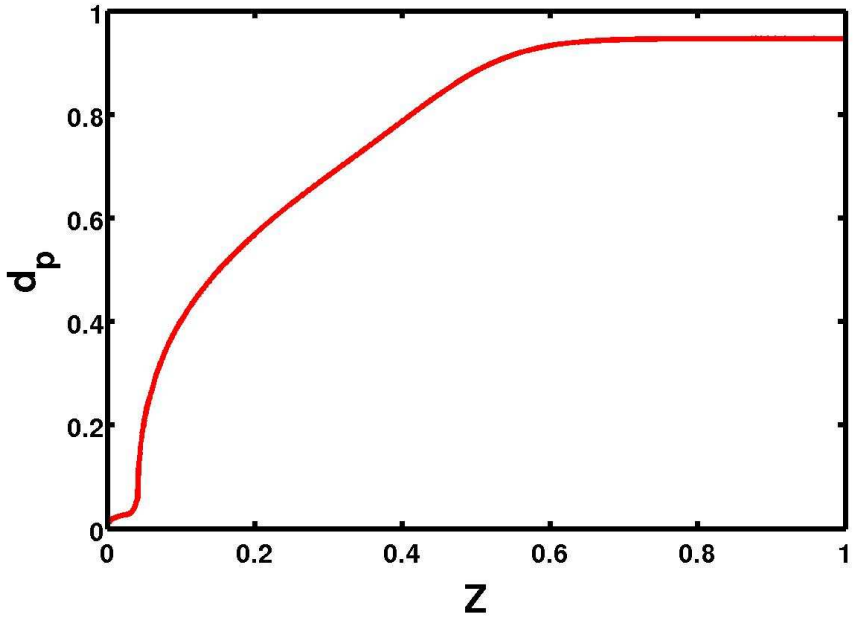

Figure 5.6 Primary size evolution with Z.

5.3.2 Effect of Ionic Additives

As described before in Section 5.2, ionic additives (such as KCl, NaCl, RbCl) are added to the process stream in aerosol manufacture to control phase and size of products. Now investigated is the affect these additives will have on the above configuration. We assume that the particles are at their charging limit given by Bjerrums criterion (Eqn. (5.7)).

(34) indicated that the traces of water adsorbed at the surface of polar particles, such as TiO_2 in nonpolar media, render them basic. If any metal cation is adsorbed on the surface of polar particles in nonpolar media, the result is a positive surface potential. Hence, the addition

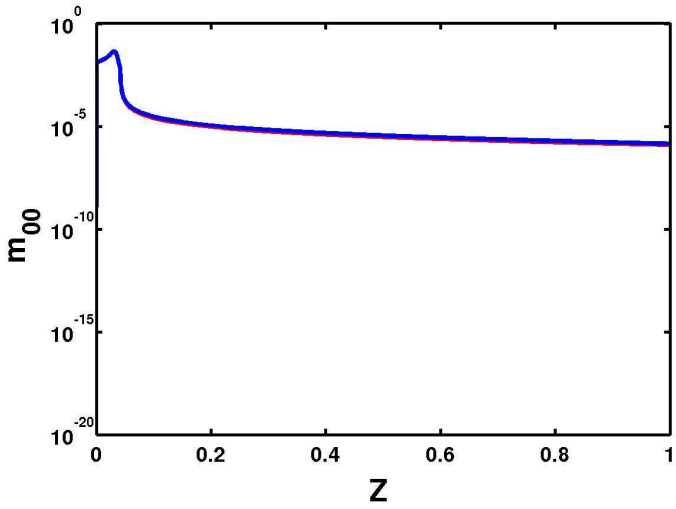

(a) Evolution of number density along the reactor length

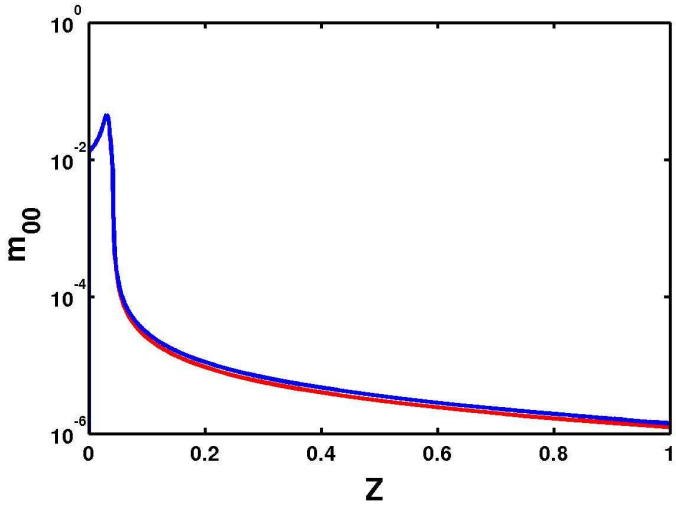

(b) Enhanced view of the evolution of m_{00}

Figure 5.7 Evolution of number density along the reactor length for the uncharged case (red) and charged case (blue) showing that addition of charge leads to higher number density.

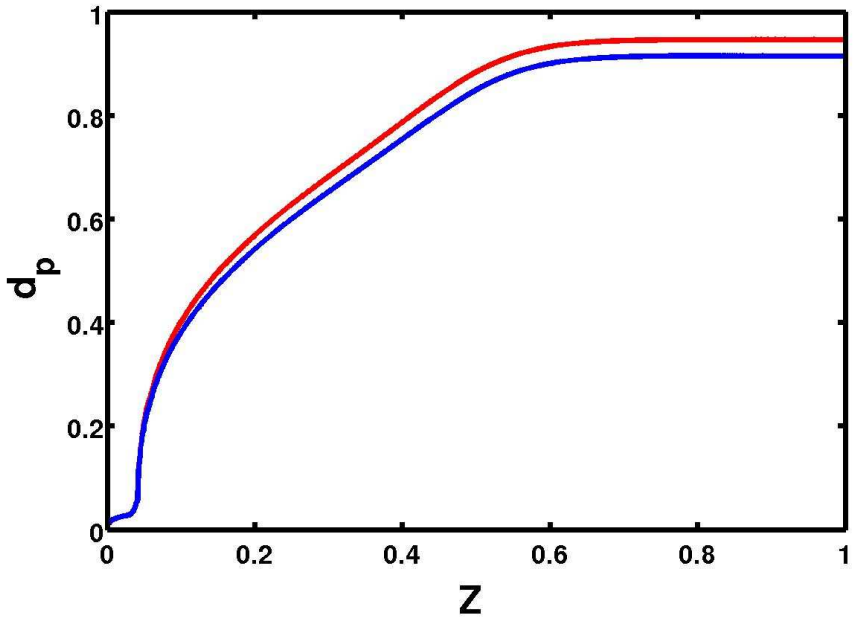

Figure 5.8 Evolution of d_p along the reactor length without ionic additives (red) and with ionic additives (blue).

of aquatic electrolyte solutions (e.g. KCl) into a titania system leads to a polar TiO_2 surface. The smaller ionic radius of the alkali metal compared to Cl^- leads to a preferential adsorption of cations on the titania surface and hence titania surfaces are unipolarly charged with positive metal ions. It should be noted that charges present on the particle would depend on its surface area so larger particles would carry more charge than smaller ones.

The affect of these additives is best observed on number density as it evolves by nucleation and aggregation. Looking at the plot for m_{00} (Figure (5.7(a))), we are tempted to conclued that there is no discernable change in the evolution after the addition of electrolyte solutions. But looking closely in Figure (5.7(b)), it is found that the number density for the charged case is greater than that of the uncharged distribution. This implies that the addition of charge does effect aggregation as the positively charged titania surfaces are repelled from each other leading to lesser collisions and higher number density.

The physical picture of suppression of aggregation by addition of ions can be described as follows. Initially with the formation on nuclei, the majority of particles that exist are very small

in size and hence retain very small amount of charge. Due to the presence of negligible energy barrier between small particles they tend to aggregate rapidly. As aggregation proceeds, large aggregates retain formidable charges that begin to introduce substantial electrostatic repulsion between larger particles. Meanwhile, smaller particles continue to aggregate among themselves and with larger aggregates. Eventually, the system would reach a stage of relatively uniform particle size and particles are held stable due to electrostatic repulsion forces.

After accounting the effects of ions our primary particle size drops from $0.95\mathrm{d}_p$ to $0.91\mathrm{d}_p$ (Figure (5.8)). Similar to (107) findings, it is observed that the ionic effect leads to suppression in aggregation and consequently, as smaller agglomerates undergo coalescence, the primary size decreases.

5.4 Chapter Summary

This work has successfully derived and solved the population balance model for an industrial titania oxidation system. The population balance model is bivariate in volume and area and has all the necessary information required to calculate results which are of practical importance. This model was used for a test PFR reactor with realistic initial conditions to predict the primary particle size. Also, considered are the ionic effects of additives on the primary sizes. It was found that the model was successful in predicting both the primary size as well as in accounting for the electrostatic repulsion due to ionic additives.

The model was written as a post processing step after Aspen Plus and was very quick with the whole calculation taking under two minutes. The model is robust and can easily handle change in chemistry or particle source terms. The fast calculation speed and flexibility, together with prediction of important parameters such as primary size, makes this model a powerful tool for titania oxidation process modeling and optimization.

CHAPTER 6. Summary and Future Work

In which the findings from this work are summarized and conclusions are drawn. Also, future avenues for further investigation are discussed.

6.1 Summary

This dissertation details the development of a comprehensive computational model for titania nanoparticle synthesis in flame reactors. Proposed here is a detailed chemical mechanism consisting of detailed Ti oxidation chemistry together with methane combustion and chlorination to represent the kinetics of this system. This detailed scheme has been compared to the one-step mechanism, used previously in literature, to study the effects different mechanisms have on particle inception as well as on predicted product properties for different flow configurations. Simple models, like plug flow and partially stirred reactors, have been used to model flow fields and thus, compare the two gas-phase mechanisms (one-step and detailed) with experiments done in the literature. A bivariate population balance model with expressions for nucleation, surface growth, aggregation and sintering has been proposed and solved using the conditional quadrature method of moments. A new model for surface growth has been developed which takes Ti intermediates into account to give a more accurate representation of the growth term. As the detailed mechanism is extensive, with 107 species and 501 reactions, mechanism reduction has been carried out to give a reduced mechanism which can accurately represent the chemistry while being computationally viable for full flame simulations. Finally, the models and techniques developed in the previous sections have been successfully applied to an industrial system proving that the approach detailed in this dissertation is of both academic and commercial interest.

6.2 Conclusions

The effect of the chemical mechanism on the nucleation of TiO_2 was studied for two flow models to take into account the turbulent flames in which these nanoparticles are produced. Three different gas-phase mechanisms – one-step, detailed and flamelet – were used to simulate the nanoparticle nucleation process in a flame configuration for an experimental setup (70). First, a combination of one-step/detailed and flamelet table was used to predict nanoparticle nucleation (for flame D in (70)). The experimental conditions result in most of the nucleation taking place immediately downstream of the nozzle. The results from the plug flow model show that for one-step nucleation, the bulk of the nuclei are formed upstream of the flame surface and subsequently pass through the high-temperature region of the flame. In contrast, with the detailed nucleation model the bulk of the nuclei are formed downstream of the flame surface. These results suggest that the one-step nucleation model should predict very different high-temperature sintering behavior as compared to the detailed nucleation model.

The results from partially stirred reactor simulations show that vigorous back mixing within the turbulent flow results in more uniform particle properties, but the differences between the one-step and detailed nucleation models are still evident. The nucleation rate increases with temperature in the one-step nucleation and most of the nucleation happens on the lean side of the flame. By observing the evolution of species for detailed mechanism it is found that the most stable intermediates for this scheme are $TiOCl_2$ at high temperatures (above 1800 K) but at lower temperatures its dimer $Ti_2O_2Cl_4$ is the more abundant intermediate. It is also observed that detailed mechanism has a preference of producing nuclei in a temperature range. Thus, in contrast with one-step, for the detailed mechanism nucleation happens in the range of 1500–1800 K, and occurs both on the lean and the rich side of the flame. The location of nucleation is important as it would effect other particle evolution terms (e.g. sintering).

The population balance model is then extended to include other particle evolution events and also to study the effects of flow configuration on particle properties (flame A and flame D in (70)). This work uses a bivariate population balance approach to model titania nanoparticle synthesis in flames. The PBE is complete with source terms for nucleation, growth, aggregation

and sintering. To counter the stiffness and moment realizability, an operator splitting scheme is introduced that first accounts for changes in number density due to nucleation and aggregation and then takes into consideration the effect of growth and sintering. A multi-environment PFR approach was used to simulate two different flames for the one-step and detailed gas-phase chemistry with both simple and detailed surface growth models.

The different gas-phase chemical mechanisms for nucleation of titania nanoparticles yielded significantly distinct results for the two experimental flame. As before, in the one-step mechanism nucleation increases with temperature and nuclei always formed upstream of the flame surface. For the detailed mechanism with the simple growth expression, the nucleation is again a function of temperature and maximum nucleation occurs in a range from 1500–1800 K. The location of nuclei formation has an effect on the temperature-dependent sintering process and hence, the particle evolution as predicted by the two gas-phase mechanisms were quite different. The one-step mechanism predicted that for both flame configurations, particles will be formed upstream and hence the final products will be highly sintered in both the cases. Whereas, the detailed mechanism predicted particle formation after the flame surface for flame A and upstream for flame D. Based on experiments, the particle evolution profiles as described by the detailed gas-phase mechanism were more accurate. Hence, the full PBE model with the detailed gas-phase mechanism was able to capture the sintering trends in both the flames studied.

It is observed that the detailed surface growth rate leads to a change in the dynamics of particle nucleation. The rate of nucleation for one-step gas-phase mechanism depends on the precursor, overall oxidation and surface oxidation rates. As the rate expressions are dependent on temperature, the one-step mechanism will predict higher nucleation rates with rising temperatures. Even though the one-step mechanism has a growth dependence (Eq. 2.30) the consumption of $TiCl_4$ in flames is almost instantaneous and most of the precursor gets converted to the nuclei. Compared to that in the detailed mechanism nucleation is relatively slower as the precursor first has to decompose and form other intermediates, which eventually lead to the nuclei. In flames the decomposition of $TiCl_4$ is very fast but the formation of nuclei, according to the detailed Ti oxidation mechanism, depends on a preferred temperature

range. As most of the precursor entering the flame reactor decomposes, the effect of the simple growth expression (which depends on $TiCl_4$ concentrations) is not very pronounced. Thus, both the one-step and detailed gas-phase mechanisms with simple growth expressions become nucleation dominated. Because the detailed surface growth model considers that intermediates can undergo surface growth, initially gas-phase reactions leading to nucleation are dominant but later when enough surface area is formed surface reactions begin to contribute significantly to the particle properties.

With majority of the introduced precursor dissociating in the flame reactor, the simple growth expression tends to discount the effect of surface growth. For the one-step gas-phase mechanism as the conversion of precursor to titania is instantaneous, this leads to restrained effect of growth while for the detailed gas-phase mechanism because most of the titanium is present in the intermediates after precursor decomposition, growth expression remains negligible. As the detailed surface growth model allows intermediates to account for surface growth, it represents a more realistic approximation of the detailed chemistry. Also important to note is the effect the growth expression has on the nucleation events because in the presence of appropriate conditions titanium intermediates can react directly on the nuclei surface instead of forming new nuclei. We acknowledge that involving all intermediates in the growth process could be an overestimate of the growth rate but these results point to understanding and distinguishing the intermediates involved in growth and nucleation processes.

The presence of intermediates in the detailed gas-phase mechanism demands that interactions between fuel and precursor are considered and this proves important in predicting the location of nucleation. As the properties of the final product are determined by the amount of time spent inside the flame, the location is critical in understanding the differences between products formed by various flame configurations. The difference in results for the detailed mechanism based on the two growth expressions leads us to conclude that the surface growth event does have a very important role in predicting the final products. In a flame, as high temperatures lead to dissociation of precursor and formation of various intermediates, there is a need to understand the role intermediates have in the both nucleation and surface-growth processes. This would entail acquiring more accurate information on the surface chemistry of

the intermediates to properly describe the growth process. These results also point to the merits of exploring the detailed mechanism more thoroughly with the help of CFD-based methods, which would capture the effects of mixing and turbulence more accurately than the PFR model to better predict the titania product properties.

The application of the detailed chemistry model in full flow solvers is computationally expensive and thus, reduced mechanisms have to be proposed to represent chemistry. Used here is a graph-based method, called the directed relation graph with error propagation (DRGEP), to carry out species and reaction elimination. Turbulent nature of the flame renders the traditional sampling methods based on simple flow configurations unsuitable for reduction strategies. In this work, the initial sample space used for reduction was expanded by using partially stirred reactor model. This new sampling technique was coupled with directed relation graph with error propagation to propose an improved model for mechanism reduction. Using this technique a reduced mechanism with 52 species and 161 reactions is derived for titania synthesis. The reduced mechanism was able to predict the properties of the important variables (T, O_2, $TiCl_4$ and $Ti_5O_6Cl_8$) with reasonable accuracy.

Finally, the author applied the methods and models developed during the course of this dissertation work in an industrial environment during a six month internship at DuPont Titanitum Technologies. Population balance approach for the oxidation reactor was successfully coupled to ASPEN Plus commercial solver to get better insight of the production method. This model for a test PFR reactor with realistic initial conditions accurately predicted the primary particle size in an industrial setting. Also, the model was robust and flexible enough to describe the effect of ionic additives on the primary sizes.

In conclusion, a comprehensive model for titania production in flame reactors has been proposed. The model includes all possible particle evolution events and detailed chemistry. As turbulence is expected to play a major role in the product particle properties, a reduced mechanism has been proposed which facilitates the use of this extensive model with computational fluid dynamics applications. These models were also successfully applied to an industrial reactor to accurately predict titania oxidation process.

6.3 Future Work

Even though a lot of progress has been made in modeling of titania nanoparticles in flame reactors, there are still avenues for further research and improvement. Titania production remains commercially lucrative and academically challenging problem and hence the author would like to point some areas for further exploration.

The particle evolution events in the population balance model are based on the chemical mechanisms. The detailed chemical mechanism for Ti oxidation used in this work is given by West et al. (2009) (100) and is a first approximation. Thus, majority of the reaction rates supplied in the mechanism are approximated by the collision limit (99; 5). Hence, the first area in need of improvement, is of course the gas-phase and surface phase kinetics. It has been seen in this work that the global one-step description is not very accurate in flame reactors. The detailed mechanism promises to both expand our understanding and better predict particle properties. But still the question remains, as it has remained since the start of the *chloride* process, what exactly constitutes the nucleation step. The importance of this question has been magnified by the results from the detailed growth model and based on the knowledge that both gas-phase and surface phase reactions are active during titania formation. Hence, more detail into the nucleation step would help not only in prediction of correct nucleation but will also help in modeling the transition from gas-phase to surface phase chemistry in the system. Also, required is a study of the intermediates to determine which species do take part in the surface reactions and the rates at which these reactions occur.

In this work we simulated the flame using relatively simple approximations of plug flow and partially stirred reactor. But in the flame reactor, turbulence would play a major role in both the chemical reactions as well as particle evolution events. Hence, the detailed kinetics and model developed in this work have to be coupled with computational fluid dynamics based methods, to study model predictions before further improvement can be made. Progress in coupling the models presented in this work with detailed turbulent solvers has been made, with (84) using large-eddy simulation (LES) methodology in conjunction with detailed gas-phase chemical kinetics to model the system using a monovariate population balance model for

particle evolution. Recently, these findings were expanded to include a bivariate population balance model (83).

The challenge in using detailed flow solvers still remains the extensive computational time required to model this system accurately. Due to the large size of the chemical mechanism both of the above publications (84; 83) have used the flamelet approach to used to model turbulence-chemistry interactions. But the flamelet approach is applicable only for a single mixture fraction (11). Hence, in order to model the more complex flow configurations we would require a different method to represent chemistry. The reduced mechanisms proposed in this work are the first step towards coupling chemistry with flow solvers. But still, the 52 species and 161 reactions based reaction set remains a computational challenge for certain fluid dynamics methods. Hence, work on getting mechanisms or methods which could compute and supply the chemistry faster to the flow solver would be very beneficial. The usual methods are the parametrization of the detailed chemistry based on the some parameters to be tracked by the flow solver.

6.4 Time line

- Year 1 (Aug 07 - July 08):
  - Literature Survey.
  - Development of source term models for one-step Ti oxidation chemistry.
  - Development of a univarite PBE model with closure based on QMOM.
- Year 2 (Aug 08 - July 09):
  - Comparison of moment methods to full PBE solvers.
  - Mechanism reduction using QSSA.
  - Development of source term models for detailed Ti oxidation chemistry.
  - Development of PFR and PaSR configurations to model flow field.
- Year 3 (Aug 09 - July 10):

  - Mehta, M., Raman, V., Fox, R. O., " Reducing reaction mechanism for synthesis of TiO2 nanoparticles ", Gas Phase Synthesis of Nanoparticles, Particle Technology Forum, 2009 AIChE annual meeting, Nashville.
  - Fox, R. O., " Multiscale models for nanoparticle synthesis in turbulent flames ", Multi-scale Modelling for Industrial Flow System, Melbourne, 2009.
  - Mehta, M. Sung, Y., Raman, V., Fox, R. O., " Multiscale simulation of titania nanoparticle evolution in a turbulent flame ", Submitted to International Journal for Multiscale Computational Engineering, 2010.
  - Development of complete detailed mechanism with 107 species and 500 reactions.
  - Study of one-step, detailed and flamelet mechanisms and their effect on nucleation.
  - Mehta, M., Sung, Y., Raman, V., Fox, R. O., " Multiscale Modeling of TiO2 Nanoparticle Production in Flame Reactors: Effect of Chemical Mechanism ", Ind. Eng. Chem. Res., 2010, 49 (21), pp 10663 - 10673.
  - Mehta, M., Sung, Y., Raman, V., Fox, R. O., " Multiscale Modeling of TiO2 Nanoparticle Production in Flame Reactors: Effect of Chemical Mechanism ", ISCRE 21, Philadelphia.

- Year 4 (Aug 10 - July 11):
  - Development of a full bivariate PBE model with closure based on CQMOM.
  - Reduction of the detailed mechanism based on DRGEP and QSSA.
  - Mehta, M., Raman, V., Fox, R. O., " Effect of Reaction Mechanism on the Multiscale Modeling of Titanium Dioxide Nanoparticles ", Gas Phase Synthesis of Nanoparticles, Particle Technology Forum, 2010 AIChE annual meeting, Salt Lake City.
  - Mehta, M., Fox, R.O., " Application of Detailed Chemical Mechanism for Titania Nanoparticle Production in Turbulent Flames ", 7th International Workshop on Mathematics in Chemical Kinetics and Engineering, Heidelberg, Germany May 2011.

  - Mehta, M., Pepiot, P., Fox, R.O.,“ Reduction of Detailed Kinetics for Modeling TiO2 Nanoparticles synthesis in Flame Reactors ”, 7th International Conference on Chemical Kinetics @ MIT, Cambridge, MA. Jul. 2011.

- Year 5 (Aug 11 - May 12):

  - July 11 - Jan 12 Associate Investigator at DuPont Titanium Technologies, Wilmington, DE.

  - Sung, Y., Mehta, M., Raman, V., Fox, R. O., “ Large-eddy-simulation based computational modeling of flame synthesis of titania nanoparticles in a turbulent reactor using bivariate particle number distribution ”, AiChE Journal, Submitted.

  - Mehta, M., Raman, V., Fox, R. O., “ On the role of gas-phase chemistry in the production of titania nanoparticles in turbulent flames ”, Chemical Engineering Science, Submitted.

  - Mehta, M., Fox, R.O., Pepiot, P.,“ Reduction and Analysis of Detailed Kinetics for Modeling TiO_2 Nanoparticle Synthesis in Flame Reactors ”, Combustion and Flame, to be submitted.

APPENDIX A. Mechanism Files

Listed below are the chemkin output files for the five mechanism used in this work.

One-step Mechanism

CHEMKIN INTERPRETER OUTPUT: CHEMKIN–II Version 3.9 Aug. 1994
DOUBLE PRECISION

ELEMENTS CONSIDERED	ATOMIC WEIGHT
1. O	15.9994
2. CL	35.4530
3. Ti	47.9000
4. AR	39.9480
5. H	1.00797
6. C	12.0112
7. N	14.0067

SPECIES CONSIDERED	PHASE	CHARGE	MOLECULAR WEIGHT	TEMPERATURE LOW	TEMPERATURE HIGH	ELEMENT COUNT O	CL	Ti	AR	H	C	N
1. H2	G	0	2.01594	200	3500	0	0	0	0	2	0	0
2. H	G	0	1.00797	200	3500	0	0	0	0	1	0	0
3. O	G	0	15.99940	200	3500	1	0	0	0	0	0	0
4. O2	G	0	31.99880	200	3500	2	0	0	0	0	0	0
5. OH	G	0	17.00737	200	3500	1	0	0	0	1	0	0
6. H2O	G	0	18.01534	200	3500	1	0	0	0	2	0	0
7. HO2	G	0	33.00677	200	3500	2	0	0	0	1	0	0
8. H2O2	G	0	34.01474	200	3500	2	0	0	0	2	0	0
9. C	G	0	12.01115	200	3500	0	0	0	0	0	1	0
10. CH	G	0	13.01912	200	3500	0	0	0	0	1	1	0
11. CH2	G	0	14.02709	200	3500	0	0	0	0	2	1	0
12. CH2(S)	G	0	14.02709	200	3500	0	0	0	0	2	1	0
13. CH3	G	0	15.03506	200	3500	0	0	0	0	3	1	0
14. CH4	G	0	16.04303	200	3500	0	0	0	0	4	1	0

```
15. CO                G  0   28.01055   200   3500   1  0  0  0  0  1  0
16. CO2               G  0   44.00995   200   3500   2  0  0  0  0  1  0
17. HCO               G  0   29.01852   200   3500   1  0  0  0  1  1  0
18. CH2O              G  0   30.02649   200   3500   1  0  0  0  2  1  0
19. CH2OH             G  0   31.03446   200   3500   1  0  0  0  3  1  0
20. CH3O              G  0   31.03446   300   3000   1  0  0  0  3  1  0
21. CH3OH             G  0   32.04243   200   3500   1  0  0  0  4  1  0
22. C2H               G  0   25.03027   200   3500   0  0  0  0  1  2  0
23. C2H2              G  0   26.03824   200   3500   0  0  0  0  2  2  0
24. C2H3              G  0   27.04621   200   3500   0  0  0  0  3  2  0
25. C2H4              G  0   28.05418   200   3500   0  0  0  0  4  2  0
26. C2H5              G  0   29.06215   200   3500   0  0  0  0  5  2  0
27. C2H6              G  0   30.07012   200   3500   0  0  0  0  6  2  0
28. HCCO              G  0   41.02967   300   4000   1  0  0  0  1  2  0
29. CH2CO             G  0   42.03764   200   3500   1  0  0  0  2  2  0
30. HCCOH             G  0   42.03764   300   5000   1  0  0  0  2  2  0
31. N                 G  0   14.00670   200   6000   0  0  0  0  0  0  1
32. NH                G  0   15.01467   200   6000   0  0  0  0  1  0  1
33. NH2               G  0   16.02264   200   6000   0  0  0  0  2  0  1
34. NH3               G  0   17.03061   200   6000   0  0  0  0  3  0  1
35. NNH               G  0   29.02137   200   6000   0  0  0  0  1  0  2
36. NO                G  0   30.00610   200   6000   1  0  0  0  0  0  1
37. NO2               G  0   46.00550   200   6000   2  0  0  0  0  0  1
38. N2O               G  0   44.01280   200   6000   1  0  0  0  0  0  2
39. HNO               G  0   31.01407   200   6000   1  0  0  0  1  0  1
40. CN                G  0   26.01785   200   6000   0  0  0  0  0  1  1
41. HCN               G  0   27.02582   200   6000   0  0  0  0  1  1  1
42. H2CN              G  0   28.03379   300   4000   0  0  0  0  2  1  1
43. HCNN              G  0   41.03252   300   5000   0  0  0  0  1  1  2
44. HCNO              G  0   43.02522   300   5000   1  0  0  0  1  1  1
45. HOCN              G  0   43.02522   300   5000   1  0  0  0  1  1  1
46. HNCO              G  0   43.02522   300   5000   1  0  0  0  1  1  1
47. NCO               G  0   42.01725   200   6000   1  0  0  0  0  1  1
48. N2                G  0   28.01340   300   5000   0  0  0  0  0  0  2
49. AR                G  0   39.94800   300   5000   0  0  0  1  0  0  0
50. CL                G  0   35.45300   298   5000   0  1  0  0  0  0  0
51. CL2               G  0   70.90600   298   5000   0  2  0  0  0  0  0
52. TiCL4             G  0  189.71200   300   5000   0  4  1  0  0  0  0
53. TiO2(ru)          G  0   79.89880   300   2130   2  0  1  0  0  0  0
54. HCL               G  0   36.46097   200   6000   0  1  0  0  1  0  0
55. CH3CL             G  0   50.48806   298   5000   0  1  0  0  3  1  0
56. CH2CL2            G  0   84.93309   298   5000   0  2  0  0  2  1  0
57. CHCL3             G  0  119.37812   298   5000   0  3  0  0  1  1  0
58. CCL4              G  0  153.82315   298   5000   0  4  0  0  0  1  0
59. CHCL2–CH2CL       G  0  133.40521   298   5000   0  3  0  0  3  2  0
60. CH2CL–CH2CL       G  0   98.96018   298   5000   0  2  0  0  4  2  0
61. CHCL2–CHCL2       G  0  167.85024   298   5000   0  4  0  0  2  2  0
62. CCL3–CCL3         G  0  236.74030   298   5000   0  6  0  0  0  2  0
63. CCL3–CH2CL        G  0  167.85024   298   5000   0  4  0  0  2  2  0
64. CCL3–CHCL2        G  0  202.29527   298   5000   0  5  0  0  1  2  0
65. CCL2–CH2          G  0   96.94424   298   5000   0  2  0  0  2  2  0
66. tCHCL–CHCL        G  0   96.94424   298   5000   0  2  0  0  2  2  0
67. cCHCL–CHCL        G  0   96.94424   298   5000   0  2  0  0  2  2  0
68. CHCL–CH2          G  0   62.49921   298   5000   0  1  0  0  3  2  0
69. CCL2–CHCL         G  0  131.38927   298   5000   0  3  0  0  1  2  0
70. CCL2–CCL2         G  0  165.83430   298   5000   0  4  0  0  0  2  0
```

71. CCL3–CH3	G	0	133.40521	298	5000	0	3	0	0	3	2	0
72. CH2CL	G	0	49.48009	298	5000	0	1	0	0	2	1	0
73. CHCL2	G	0	83.92512	298	5000	0	2	0	0	1	1	0
74. CCL3	G	0	118.37015	298	5000	0	3	0	0	0	1	0
75. CH2CL–CH2	G	0	63.50718	298	5000	0	1	0	0	4	2	0
76. CH2CL–CCL2	G	0	132.39724	298	5000	0	3	0	0	2	2	0
77. CHCL2–CHCL	G	0	132.39724	298	5000	0	3	0	0	2	2	0
78. CH2CL–CHCL	G	0	97.95221	298	5000	0	2	0	0	3	2	0
79. CHCL2–CH2	G	0	97.95221	298	5000	0	2	0	0	3	2	0
80. CHCL2–CCL2	G	0	166.84227	298	5000	0	4	0	0	1	2	0
81. CCL3–CCL2	G	0	201.28730	298	5000	0	5	0	0	0	2	0
82. CCL3–CH2	G	0	132.39724	298	5000	0	3	0	0	2	2	0
83. CCL3–CHCL	G	0	166.84227	298	5000	0	4	0	0	1	2	0
84. cCHCL–CCL	G	0	95.93627	298	5000	0	2	0	0	1	2	0
85. tCHCL–CCL	G	0	95.93627	298	5000	0	2	0	0	1	2	0
86. CH3–CCL2	G	0	97.95221	298	5000	0	2	0	0	3	2	0

REACTIONS CONSIDERED			(k = A T**b exp(−E/RT)) A	b	E
1. 2O+M<=>O2+M			1.20E+17	−1.0	0.0
H2	Enhanced by	2.400E+00			
H2O	Enhanced by	1.540E+01			
CH4	Enhanced by	2.000E+00			
CO	Enhanced by	1.750E+00			
CO2	Enhanced by	3.600E+00			
C2H6	Enhanced by	3.000E+00			
AR	Enhanced by	8.300E−01			
2. O+H+M<=>OH+M			5.00E+17	−1.0	0.0
H2	Enhanced by	2.000E+00			
H2O	Enhanced by	6.000E+00			
CH4	Enhanced by	2.000E+00			
CO	Enhanced by	1.500E+00			
CO2	Enhanced by	2.000E+00			
C2H6	Enhanced by	3.000E+00			
AR	Enhanced by	7.000E−01			
3. O+H2<=>H+OH			5.00E+04	2.7	6290.0
4. O+HO2<=>OH+O2			2.00E+13	0.0	0.0
5. O+H2O2<=>OH+HO2			9.63E+06	2.0	4000.0
6. O+CH<=>H+CO			5.70E+13	0.0	0.0
7. O+CH2<=>H+HCO			8.00E+13	0.0	0.0
8. O+CH2(S)<=>H2+CO			1.50E+13	0.0	0.0
9. O+CH2(S)<=>H+HCO			1.50E+13	0.0	0.0
10. O+CH3<=>H+CH2O			8.43E+13	0.0	0.0
11. O+CH4<=>OH+CH3			1.02E+09	1.5	8600.0
12. O+CO+M<=>CO2+M			6.02E+14	0.0	3000.0
H2	Enhanced by	2.000E+00			
O2	Enhanced by	6.000E+00			
H2O	Enhanced by	6.000E+00			
CH4	Enhanced by	2.000E+00			
CO	Enhanced by	1.500E+00			
CO2	Enhanced by	3.500E+00			
C2H6	Enhanced by	3.000E+00			

AR	Enhanced by	5.000E−01			
13. O+HCO<=>OH+CO			3.00E+13	0.0	0.0
14. O+HCO<=>H+CO2			3.00E+13	0.0	0.0
15. O+CH2O<=>OH+HCO			3.90E+13	0.0	3540.0
16. O+CH2OH<=>OH+CH2O			1.00E+13	0.0	0.0
17. O+CH3O<=>OH+CH2O			1.00E+13	0.0	0.0
18. O+CH3OH<=>OH+CH2OH			3.88E+05	2.5	3100.0
19. O+CH3OH<=>OH+CH3O			1.30E+05	2.5	5000.0
20. O+C2H<=>CH+CO			5.00E+13	0.0	0.0
21. O+C2H2<=>H+HCCO			1.02E+07	2.0	1900.0
22. O+C2H2<=>OH+C2H			4.60E+19	−1.4	28950.0
23. O+C2H2<=>CO+CH2			1.02E+07	2.0	1900.0
24. O+C2H3<=>H+CH2CO			3.00E+13	0.0	0.0
25. O+C2H4<=>CH3+HCO			1.92E+07	1.8	220.0
26. O+C2H5<=>CH3+CH2O			1.32E+14	0.0	0.0
27. O+C2H6<=>OH+C2H5			8.98E+07	1.9	5690.0
28. O+HCCO<=>H+2CO			1.00E+14	0.0	0.0
29. O+CH2CO<=>OH+HCCO			1.00E+13	0.0	8000.0
30. O+CH2CO<=>CH2+CO2			1.75E+12	0.0	1350.0
31. O2+CO<=>O+CO2			2.50E+12	0.0	47800.0
32. O2+CH2O<=>HO2+HCO			1.00E+14	0.0	40000.0
33. H+O2+M<=>HO2+M			2.80E+18	−0.9	0.0
O2	Enhanced by	0.000E+00			
H2O	Enhanced by	0.000E+00			
CO	Enhanced by	7.500E−01			
CO2	Enhanced by	1.500E+00			
C2H6	Enhanced by	1.500E+00			
N2	Enhanced by	0.000E+00			
AR	Enhanced by	0.000E+00			
34. H+2O2<=>HO2+O2			3.00E+20	−1.7	0.0
35. H+O2+H2O<=>HO2+H2O			9.38E+18	−0.8	0.0
36. H+O2+N2<=>HO2+N2			3.75E+20	−1.7	0.0
37. H+O2+AR<=>HO2+AR			7.00E+17	−0.8	0.0
38. H+O2<=>O+OH			8.30E+13	0.0	14413.0
39. 2H+M<=>H2+M			1.00E+18	−1.0	0.0
H2	Enhanced by	0.000E+00			
H2O	Enhanced by	0.000E+00			
CH4	Enhanced by	2.000E+00			
CO2	Enhanced by	0.000E+00			
C2H6	Enhanced by	3.000E+00			
AR	Enhanced by	6.300E−01			
40. 2H+H2<=>2H2			9.00E+16	−0.6	0.0
41. 2H+H2O<=>H2+H2O			6.00E+19	−1.2	0.0
42. 2H+CO2<=>H2+CO2			5.50E+20	−2.0	0.0
43. H+OH+M<=>H2O+M			2.20E+22	−2.0	0.0
H2	Enhanced by	7.300E−01			
H2O	Enhanced by	3.650E+00			
CH4	Enhanced by	2.000E+00			
C2H6	Enhanced by	3.000E+00			
AR	Enhanced by	3.800E−01			
44. H+HO2<=>O+H2O			3.97E+12	0.0	671.0
45. H+HO2<=>O2+H2			2.80E+13	0.0	1068.0
46. H+HO2<=>2OH			1.34E+14	0.0	635.0
47. H+H2O2<=>HO2+H2			1.21E+07	2.0	5200.0
48. H+H2O2<=>OH+H2O			1.00E+13	0.0	3600.0
49. H+CH<=>C+H2			1.10E+14	0.0	0.0

```
50. H+CH2(+M)<=>CH3(+M)                                 2.50E+16   -0.8        0.0
    Low pressure limit:  0.32000E+28 -0.31400E+01  0.12300E+04
    TROE centering:      0.68000E+00  0.78000E+02  0.19950E+04  0.55900E+04
       H2                Enhanced by    2.000E+00
       H2O               Enhanced by    6.000E+00
       CH4               Enhanced by    2.000E+00
       CO                Enhanced by    1.500E+00
       CO2               Enhanced by    2.000E+00
       C2H6              Enhanced by    3.000E+00
       AR                Enhanced by    7.000E-01
51. H+CH2(S)<=>CH+H2                                    3.00E+13    0.0        0.0
52. H+CH3(+M)<=>CH4(+M)                                 1.27E+16   -0.6      383.0
    Low pressure limit:  0.24770E+34 -0.47600E+01  0.24400E+04
    TROE centering:      0.78300E+00  0.74000E+02  0.29410E+04  0.69640E+04
       H2                Enhanced by    2.000E+00
       H2O               Enhanced by    6.000E+00
       CH4               Enhanced by    2.000E+00
       CO                Enhanced by    1.500E+00
       CO2               Enhanced by    2.000E+00
       C2H6              Enhanced by    3.000E+00
       AR                Enhanced by    7.000E-01
53. H+CH4<=>CH3+H2                                      6.60E+08    1.6    10840.0
54. H+HCO(+M)<=>CH2O(+M)                                1.09E+12    0.5     -260.0
    Low pressure limit:  0.13500E+25 -0.25700E+01  0.14250E+04
    TROE centering:      0.78240E+00  0.27100E+03  0.27550E+04  0.65700E+04
       H2                Enhanced by    2.000E+00
       H2O               Enhanced by    6.000E+00
       CH4               Enhanced by    2.000E+00
       CO                Enhanced by    1.500E+00
       CO2               Enhanced by    2.000E+00
       C2H6              Enhanced by    3.000E+00
       AR                Enhanced by    7.000E-01
55. H+HCO<=>H2+CO                                       7.34E+13    0.0        0.0
56. H+CH2O(+M)<=>CH2OH(+M)                              5.40E+11    0.5     3600.0
    Low pressure limit:  0.12700E+33 -0.48200E+01  0.65300E+04
    TROE centering:      0.71870E+00  0.10300E+03  0.12910E+04  0.41600E+04
       H2                Enhanced by    2.000E+00
       H2O               Enhanced by    6.000E+00
       CH4               Enhanced by    2.000E+00
       CO                Enhanced by    1.500E+00
       CO2               Enhanced by    2.000E+00
       C2H6              Enhanced by    3.000E+00
57. H+CH2O(+M)<=>CH3O(+M)                               5.40E+11    0.5     2600.0
    Low pressure limit:  0.22000E+31 -0.48000E+01  0.55600E+04
    TROE centering:      0.75800E+00  0.94000E+02  0.15550E+04  0.42000E+04
       H2                Enhanced by    2.000E+00
       H2O               Enhanced by    6.000E+00
       CH4               Enhanced by    2.000E+00
       CO                Enhanced by    1.500E+00
       CO2               Enhanced by    2.000E+00
       C2H6              Enhanced by    3.000E+00
58. H+CH2O<=>HCO+H2                                     2.30E+10    1.1     3275.0
59. H+CH2OH(+M)<=>CH3OH(+M)                             1.80E+13    0.0        0.0
    Low pressure limit:  0.30000E+32 -0.48000E+01  0.33000E+04
    TROE centering:      0.76790E+00  0.33800E+03  0.18120E+04  0.50810E+04
       H2                Enhanced by    2.000E+00
```

```
        H2O                 Enhanced by     6.000E+00
        CH4                 Enhanced by     2.000E+00
        CO                  Enhanced by     1.500E+00
        CO2                 Enhanced by     2.000E+00
        C2H6                Enhanced by     3.000E+00
60. H+CH2OH<=>H2+CH2O                                   2.00E+13    0.0         0.0
61. H+CH2OH<=>OH+CH3                                    1.20E+13    0.0         0.0
62. H+CH2OH<=>CH2(S)+H2O                                6.00E+12    0.0         0.0
63. H+CH3O(+M)<=>CH3OH(+M)                              5.00E+13    0.0         0.0
    Low pressure limit:  0.86000E+29 -0.40000E+01  0.30250E+04
    TROE centering:      0.89020E+00  0.14400E+03  0.28380E+04  0.45569E+05
        H2                  Enhanced by     2.000E+00
        H2O                 Enhanced by     6.000E+00
        CH4                 Enhanced by     2.000E+00
        CO                  Enhanced by     1.500E+00
        CO2                 Enhanced by     2.000E+00
        C2H6                Enhanced by     3.000E+00
64. H+CH3O<=>H+CH2OH                                    3.40E+06    1.6         0.0
65. H+CH3O<=>H2+CH2O                                    2.00E+13    0.0         0.0
66. H+CH3O<=>OH+CH3                                     3.20E+13    0.0         0.0
67. H+CH3O<=>CH2(S)+H2O                                 1.60E+13    0.0         0.0
68. H+CH3OH<=>CH2OH+H2                                  1.70E+07    2.1      4870.0
69. H+CH3OH<=>CH3O+H2                                   4.20E+06    2.1      4870.0
70. H+C2H(+M)<=>C2H2(+M)                                1.00E+17   -1.0         0.0
    Low pressure limit:  0.37500E+34 -0.48000E+01  0.19000E+04
    TROE centering:      0.64640E+00  0.13200E+03  0.13150E+04  0.55660E+04
        H2                  Enhanced by     2.000E+00
        H2O                 Enhanced by     6.000E+00
        CH4                 Enhanced by     2.000E+00
        CO                  Enhanced by     1.500E+00
        CO2                 Enhanced by     2.000E+00
        C2H6                Enhanced by     3.000E+00
        AR                  Enhanced by     7.000E-01
71. H+C2H2(+M)<=>C2H3(+M)                               5.60E+12    0.0      2400.0
    Low pressure limit:  0.38000E+41 -0.72700E+01  0.72200E+04
    TROE centering:      0.75070E+00  0.98500E+02  0.13020E+04  0.41670E+04
        H2                  Enhanced by     2.000E+00
        H2O                 Enhanced by     6.000E+00
        CH4                 Enhanced by     2.000E+00
        CO                  Enhanced by     1.500E+00
        CO2                 Enhanced by     2.000E+00
        C2H6                Enhanced by     3.000E+00
        AR                  Enhanced by     7.000E-01
72. H+C2H3(+M)<=>C2H4(+M)                               6.08E+12    0.3       280.0
    Low pressure limit:  0.14000E+31 -0.38600E+01  0.33200E+04
    TROE centering:      0.78200E+00  0.20750E+03  0.26630E+04  0.60950E+04
        H2                  Enhanced by     2.000E+00
        H2O                 Enhanced by     6.000E+00
        CH4                 Enhanced by     2.000E+00
        CO                  Enhanced by     1.500E+00
        CO2                 Enhanced by     2.000E+00
        C2H6                Enhanced by     3.000E+00
        AR                  Enhanced by     7.000E-01
73. H+C2H3<=>H2+C2H2                                    3.00E+13    0.0         0.0
74. H+C2H4(+M)<=>C2H5(+M)                               1.08E+12    0.5      1820.0
    Low pressure limit:  0.12000E+43 -0.76200E+01  0.69700E+04
```

```
    TROE centering:       0.97530E+00  0.21000E+03  0.98400E+03  0.43740E+04
       H2                 Enhanced by    2.000E+00
       H2O                Enhanced by    6.000E+00
       CH4                Enhanced by    2.000E+00
       CO                 Enhanced by    1.500E+00
       CO2                Enhanced by    2.000E+00
       C2H6               Enhanced by    3.000E+00
       AR                 Enhanced by    7.000E-01
75. H+C2H4<=>C2H3+H2                                 1.32E+06    2.5     12240.0
76. H+C2H5(+M)<=>C2H6(+M)                            5.21E+17   -1.0      1580.0
    Low pressure limit:  0.19900E+42 -0.70800E+01  0.66850E+04
    TROE centering:       0.84220E+00  0.12500E+03  0.22190E+04  0.68820E+04
       H2                 Enhanced by    2.000E+00
       H2O                Enhanced by    6.000E+00
       CH4                Enhanced by    2.000E+00
       CO                 Enhanced by    1.500E+00
       CO2                Enhanced by    2.000E+00
       C2H6               Enhanced by    3.000E+00
       AR                 Enhanced by    7.000E-01
77. H+C2H5<=>H2+C2H4                                 2.00E+12    0.0        0.0
78. H+C2H6<=>C2H5+H2                                 1.15E+08    1.9     7530.0
79. H+HCCO<=>CH2(S)+CO                               1.00E+14    0.0        0.0
80. H+CH2CO<=>HCCO+H2                                5.00E+13    0.0     8000.0
81. H+CH2CO<=>CH3+CO                                 1.13E+13    0.0     3428.0
82. H+HCCOH<=>H+CH2CO                                1.00E+13    0.0        0.0
83. H2+CO(+M)<=>CH2O(+M)                             4.30E+07    1.5    79600.0
    Low pressure limit:  0.50700E+28 -0.34200E+01  0.84350E+05
    TROE centering:       0.93200E+00  0.19700E+03  0.15400E+04  0.10300E+05
       H2                 Enhanced by    2.000E+00
       H2O                Enhanced by    6.000E+00
       CH4                Enhanced by    2.000E+00
       CO                 Enhanced by    1.500E+00
       CO2                Enhanced by    2.000E+00
       C2H6               Enhanced by    3.000E+00
       AR                 Enhanced by    7.000E-01
84. OH+H2<=>H+H2O                                    2.16E+08    1.5     3430.0
85. 2OH(+M)<=>H2O2(+M)                               7.40E+13   -0.4        0.0
    Low pressure limit:  0.23000E+19 -0.90000E+00 -0.17000E+04
    TROE centering:       0.73460E+00  0.94000E+02  0.17560E+04  0.51820E+04
       H2                 Enhanced by    2.000E+00
       H2O                Enhanced by    6.000E+00
       CH4                Enhanced by    2.000E+00
       CO                 Enhanced by    1.500E+00
       CO2                Enhanced by    2.000E+00
       C2H6               Enhanced by    3.000E+00
       AR                 Enhanced by    7.000E-01
86. 2OH<=>O+H2O                                      3.57E+04    2.4    -2110.0
87. OH+HO2<=>O2+H2O                                  2.90E+13    0.0     -500.0
88. OH+H2O2<=>HO2+H2O                                1.75E+12    0.0      320.0
    Declared duplicate reaction...
89. OH+H2O2<=>HO2+H2O                                5.80E+14    0.0     9560.0
    Declared duplicate reaction...
90. OH+C<=>H+CO                                      5.00E+13    0.0        0.0
91. OH+CH<=>H+HCO                                    3.00E+13    0.0        0.0
92. OH+CH2<=>H+CH2O                                  2.00E+13    0.0        0.0
93. OH+CH2<=>CH+H2O                                  1.13E+07    2.0     3000.0
```

```
 94. OH+CH2(S)<=>H+CH2O                                3.00E+13    0.0         0.0
 95. OH+CH3(+M)<=>CH3OH(+M)                            6.30E+13    0.0         0.0
     Low pressure limit:  0.27000E+39 -0.63000E+01  0.31000E+04
     TROE centering:      0.21050E+00  0.83500E+02  0.53980E+04  0.83700E+04
        H2                Enhanced by    2.000E+00
        H2O               Enhanced by    6.000E+00
        CH4               Enhanced by    2.000E+00
        CO                Enhanced by    1.500E+00
        CO2               Enhanced by    2.000E+00
        C2H6              Enhanced by    3.000E+00
 96. OH+CH3<=>CH2+H2O                                  5.60E+07    1.6      5420.0
 97. OH+CH3<=>CH2(S)+H2O                               2.50E+13    0.0         0.0
 98. OH+CH4<=>CH3+H2O                                  1.00E+08    1.6      3120.0
 99. OH+CO<=>H+CO2                                     4.76E+07    1.2        70.0
100. OH+HCO<=>H2O+CO                                   5.00E+13    0.0         0.0
101. OH+CH2O<=>HCO+H2O                                 3.43E+09    1.2      -447.0
102. OH+CH2OH<=>H2O+CH2O                               5.00E+12    0.0         0.0
103. OH+CH3O<=>H2O+CH2O                                5.00E+12    0.0         0.0
104. OH+CH3OH<=>CH2OH+H2O                              1.44E+06    2.0      -840.0
105. OH+CH3OH<=>CH3O+H2O                               6.30E+06    2.0      1500.0
106. OH+C2H<=>H+HCCO                                   2.00E+13    0.0         0.0
107. OH+C2H2<=>H+CH2CO                                 2.18E-04    4.5     -1000.0
108. OH+C2H2<=>H+HCCOH                                 5.04E+05    2.3     13500.0
109. OH+C2H2<=>C2H+H2O                                 3.37E+07    2.0     14000.0
110. OH+C2H2<=>CH3+CO                                  4.83E-04    4.0     -2000.0
111. OH+C2H3<=>H2O+C2H2                                5.00E+12    0.0         0.0
112. OH+C2H4<=>C2H3+H2O                                3.60E+06    2.0      2500.0
113. OH+C2H6<=>C2H5+H2O                                3.54E+06    2.1       870.0
114. OH+CH2CO<=>HCCO+H2O                               7.50E+12    0.0      2000.0
115. 2HO2<=>O2+H2O2                                    1.30E+11    0.0     -1630.0
     Declared duplicate reaction...
116. 2HO2<=>O2+H2O2                                    4.20E+14    0.0     12000.0
     Declared duplicate reaction...
117. HO2+CH2<=>OH+CH2O                                 2.00E+13    0.0         0.0
118. HO2+CH3<=>O2+CH4                                  1.00E+12    0.0         0.0
119. HO2+CH3<=>OH+CH3O                                 2.00E+13    0.0         0.0
120. HO2+CO<=>OH+CO2                                   1.50E+14    0.0     23600.0
121. HO2+CH2O<=>HCO+H2O2                               1.00E+12    0.0      8000.0
122. C+O2<=>O+CO                                       5.80E+13    0.0       576.0
123. C+CH2<=>H+C2H                                     5.00E+13    0.0         0.0
124. C+CH3<=>H+C2H2                                    5.00E+13    0.0         0.0
125. CH+O2<=>O+HCO                                     3.30E+13    0.0         0.0
126. CH+H2<=>H+CH2                                     1.11E+08    1.8      1670.0
127. CH+H2O<=>H+CH2O                                   1.71E+13    0.0      -755.0
128. CH+CH2<=>H+C2H2                                   4.00E+13    0.0         0.0
129. CH+CH3<=>H+C2H3                                   3.00E+13    0.0         0.0
130. CH+CH4<=>H+C2H4                                   6.00E+13    0.0         0.0
131. CH+CO(+M)<=>HCCO(+M)                              5.00E+13    0.0         0.0
     Low pressure limit:  0.26900E+29 -0.37400E+01  0.19360E+04
     TROE centering:      0.57570E+00  0.23700E+03  0.16520E+04  0.50690E+04
        H2                Enhanced by    2.000E+00
        H2O               Enhanced by    6.000E+00
        CH4               Enhanced by    2.000E+00
        CO                Enhanced by    1.500E+00
        CO2               Enhanced by    2.000E+00
        C2H6              Enhanced by    3.000E+00
```

```
        AR                  Enhanced by     7.000E-01
132. CH+CO2<=>HCO+CO                                    3.40E+12    0.0       690.0
133. CH+CH2O<=>H+CH2CO                                  9.46E+13    0.0      -515.0
134. CH+HCCO<=>CO+C2H2                                  5.00E+13    0.0         0.0
135. CH2+O2<=>OH+HCO                                    1.32E+13    0.0      1500.0
136. CH2+H2<=>H+CH3                                     5.00E+05    2.0      7230.0
137. 2CH2<=>H2+C2H2                                     3.20E+13    0.0         0.0
138. CH2+CH3<=>H+C2H4                                   4.00E+13    0.0         0.0
139. CH2+CH4<=>2CH3                                     2.46E+06    2.0      8270.0
140. CH2+CO(+M)<=>CH2CO(+M)                             8.10E+11    0.5      4510.0
     Low pressure limit:  0.26900E+34 -0.51100E+01  0.70950E+04
     TROE centering:      0.59070E+00  0.27500E+03  0.12260E+04  0.51850E+04
        H2                  Enhanced by     2.000E+00
        H2O                 Enhanced by     6.000E+00
        CH4                 Enhanced by     2.000E+00
        CO                  Enhanced by     1.500E+00
        CO2                 Enhanced by     2.000E+00
        C2H6                Enhanced by     3.000E+00
        AR                  Enhanced by     7.000E-01
141. CH2+HCCO<=>C2H3+CO                                 3.00E+13    0.0         0.0
142. CH2(S)+N2<=>CH2+N2                                 1.50E+13    0.0       600.0
143. CH2(S)+AR<=>CH2+AR                                 9.00E+12    0.0       600.0
144. CH2(S)+O2<=>H+OH+CO                                2.80E+13    0.0         0.0
145. CH2(S)+O2<=>CO+H2O                                 1.20E+13    0.0         0.0
146. CH2(S)+H2<=>CH3+H                                  7.00E+13    0.0         0.0
147. CH2(S)+H2O(+M)<=>CH3OH(+M)                         2.00E+13    0.0         0.0
     Low pressure limit:  0.27000E+39 -0.63000E+01  0.31000E+04
     TROE centering:      0.15070E+00  0.13400E+03  0.23830E+04  0.72650E+04
        H2                  Enhanced by     2.000E+00
        H2O                 Enhanced by     6.000E+00
        CH4                 Enhanced by     2.000E+00
        CO                  Enhanced by     1.500E+00
        CO2                 Enhanced by     2.000E+00
        C2H6                Enhanced by     3.000E+00
148. CH2(S)+H2O<=>CH2+H2O                               3.00E+13    0.0         0.0
149. CH2(S)+CH3<=>H+C2H4                                1.20E+13    0.0      -570.0
150. CH2(S)+CH4<=>2CH3                                  1.60E+13    0.0      -570.0
151. CH2(S)+CO<=>CH2+CO                                 9.00E+12    0.0         0.0
152. CH2(S)+CO2<=>CH2+CO2                               7.00E+12    0.0         0.0
153. CH2(S)+CO2<=>CO+CH2O                               1.40E+13    0.0         0.0
154. CH2(S)+C2H6<=>CH3+C2H5                             4.00E+13    0.0      -550.0
155. CH3+O2<=>O+CH3O                                    2.68E+13    0.0     28800.0
156. CH3+O2<=>OH+CH2O                                   3.60E+10    0.0      8940.0
157. CH3+H2O2<=>HO2+CH4                                 2.45E+04    2.5      5180.0
158. 2CH3(+M)<=>C2H6(+M)                                2.12E+16   -1.0       620.0
     Low pressure limit:  0.17700E+51 -0.96700E+01  0.62200E+04
     TROE centering:      0.53250E+00  0.15100E+03  0.10380E+04  0.49700E+04
        H2                  Enhanced by     2.000E+00
        H2O                 Enhanced by     6.000E+00
        CH4                 Enhanced by     2.000E+00
        CO                  Enhanced by     1.500E+00
        CO2                 Enhanced by     2.000E+00
        C2H6                Enhanced by     3.000E+00
        AR                  Enhanced by     7.000E-01
159. 2CH3<=>H+C2H5                                      4.99E+12    0.1     10600.0
160. CH3+HCO<=>CH4+CO                                   2.65E+13    0.0         0.0
```

```
161. CH3+CH2O<=>HCO+CH4                                3.32E+03    2.8      5860.0
162. CH3+CH3OH<=>CH2OH+CH4                             3.00E+07    1.5      9940.0
163. CH3+CH3OH<=>CH3O+CH4                              1.00E+07    1.5      9940.0
164. CH3+C2H4<=>C2H3+CH4                               2.27E+05    2.0      9200.0
165. CH3+C2H6<=>C2H5+CH4                               6.14E+06    1.7     10450.0
166. HCO+H2O<=>H+CO+H2O                                2.24E+18   -1.0     17000.0
167. HCO+M<=>H+CO+M                                    1.87E+17   -1.0     17000.0
         H2                  Enhanced by    2.000E+00
         H2O                 Enhanced by    0.000E+00
         CH4                 Enhanced by    2.000E+00
         CO                  Enhanced by    1.500E+00
         CO2                 Enhanced by    2.000E+00
         C2H6                Enhanced by    3.000E+00
168. HCO+O2<=>HO2+CO                                   7.60E+12    0.0       400.0
169. CH2OH+O2<=>HO2+CH2O                               1.80E+13    0.0       900.0
170. CH3O+O2<=>HO2+CH2O                                4.28E-13    7.6     -3530.0
171. C2H+O2<=>HCO+CO                                   5.00E+13    0.0      1500.0
172. C2H+H2<=>H+C2H2                                   4.07E+05    2.4       200.0
173. C2H3+O2<=>HCO+CH2O                                3.98E+12    0.0      -240.0
174. C2H4(+M)<=>H2+C2H2(+M)                            8.00E+12    0.4     88770.0
     Low pressure limit:  0.70000E+51 -0.93100E+01  0.99860E+05
     TROE centering:      0.73450E+00  0.18000E+03  0.10350E+04  0.54170E+04
         H2                  Enhanced by    2.000E+00
         H2O                 Enhanced by    6.000E+00
         CH4                 Enhanced by    2.000E+00
         CO                  Enhanced by    1.500E+00
         CO2                 Enhanced by    2.000E+00
         C2H6                Enhanced by    3.000E+00
         AR                  Enhanced by    7.000E-01
175. C2H5+O2<=>HO2+C2H4                                8.40E+11    0.0      3875.0
176. HCCO+O2<=>OH+2CO                                  1.60E+12    0.0       854.0
177. 2HCCO<=>2CO+C2H2                                  1.00E+13    0.0         0.0
178. N+NO<=>N2+O                                       3.50E+13    0.0       330.0
179. N+O2<=>NO+O                                       2.65E+12    0.0      6400.0
180. N+OH<=>NO+H                                       7.33E+13    0.0      1120.0
181. N2O+O<=>N2+O2                                     1.40E+12    0.0     10810.0
182. N2O+O<=>2NO                                       2.90E+13    0.0     23150.0
183. N2O+H<=>N2+OH                                     4.40E+14    0.0     18880.0
184. N2O+OH<=>N2+HO2                                   2.00E+12    0.0     21060.0
185. N2O(+M)<=>N2+O(+M)                                1.30E+11    0.0     59620.0
     Low pressure limit:  0.62000E+15  0.00000E+00  0.56100E+05
         H2                  Enhanced by    2.000E+00
         H2O                 Enhanced by    6.000E+00
         CH4                 Enhanced by    2.000E+00
         CO                  Enhanced by    1.500E+00
         CO2                 Enhanced by    2.000E+00
         C2H6                Enhanced by    3.000E+00
         AR                  Enhanced by    7.000E-01
186. HO2+NO<=>NO2+OH                                   2.11E+12    0.0      -480.0
187. NO+O+M<=>NO2+M                                    1.06E+20   -1.4         0.0
         H2                  Enhanced by    2.000E+00
         H2O                 Enhanced by    6.000E+00
         CH4                 Enhanced by    2.000E+00
         CO                  Enhanced by    1.500E+00
         CO2                 Enhanced by    2.000E+00
         C2H6                Enhanced by    3.000E+00
```

	AR	Enhanced by	7.000E−01			
188.	NO2+O<=>NO+O2			3.90E+12	0.0	−240.0
189.	NO2+H<=>NO+OH			1.32E+14	0.0	360.0
190.	NH+O<=>NO+H			5.00E+13	0.0	0.0
191.	NH+H<=>N+H2			3.20E+13	0.0	330.0
192.	NH+OH<=>HNO+H			2.00E+13	0.0	0.0
193.	NH+OH<=>N+H2O			2.00E+09	1.2	0.0
194.	NH+O2<=>HNO+O			4.61E+05	2.0	6500.0
195.	NH+O2<=>NO+OH			1.28E+06	1.5	100.0
196.	NH+N<=>N2+H			1.50E+13	0.0	0.0
197.	NH+H2O<=>HNO+H2			2.00E+13	0.0	13850.0
198.	NH+NO<=>N2+OH			2.16E+13	−0.2	0.0
199.	NH+NO<=>N2O+H			4.16E+14	−0.5	0.0
200.	NH2+O<=>OH+NH			7.00E+12	0.0	0.0
201.	NH2+O<=>H+HNO			4.60E+13	0.0	0.0
202.	NH2+H<=>NH+H2			4.00E+13	0.0	3650.0
203.	NH2+OH<=>NH+H2O			9.00E+07	1.5	−460.0
204.	NNH<=>N2+H			3.30E+08	0.0	0.0
205.	NNH+M<=>N2+H+M			1.30E+14	−0.1	4980.0
	H2	Enhanced by	2.000E+00			
	H2O	Enhanced by	6.000E+00			
	CH4	Enhanced by	2.000E+00			
	CO	Enhanced by	1.500E+00			
	CO2	Enhanced by	2.000E+00			
	C2H6	Enhanced by	3.000E+00			
	AR	Enhanced by	7.000E−01			
206.	NNH+O2<=>HO2+N2			5.00E+12	0.0	0.0
207.	NNH+O<=>OH+N2			2.50E+13	0.0	0.0
208.	NNH+O<=>NH+NO			7.00E+13	0.0	0.0
209.	NNH+H<=>H2+N2			5.00E+13	0.0	0.0
210.	NNH+OH<=>H2O+N2			2.00E+13	0.0	0.0
211.	NNH+CH3<=>CH4+N2			2.50E+13	0.0	0.0
212.	H+NO+M<=>HNO+M			8.95E+19	−1.3	740.0
	H2	Enhanced by	2.000E+00			
	H2O	Enhanced by	6.000E+00			
	CH4	Enhanced by	2.000E+00			
	CO	Enhanced by	1.500E+00			
	CO2	Enhanced by	2.000E+00			
	C2H6	Enhanced by	3.000E+00			
	AR	Enhanced by	7.000E−01			
213.	HNO+O<=>NO+OH			2.50E+13	0.0	0.0
214.	HNO+H<=>H2+NO			4.50E+11	0.7	660.0
215.	HNO+OH<=>NO+H2O			1.30E+07	1.9	−950.0
216.	HNO+O2<=>HO2+NO			1.00E+13	0.0	13000.0
217.	CN+O<=>CO+N			7.70E+13	0.0	0.0
218.	CN+OH<=>NCO+H			4.00E+13	0.0	0.0
219.	CN+H2O<=>HCN+OH			8.00E+12	0.0	7460.0
220.	CN+O2<=>NCO+O			6.14E+12	0.0	−440.0
221.	CN+H2<=>HCN+H			2.10E+13	0.0	4710.0
222.	NCO+O<=>NO+CO			2.35E+13	0.0	0.0
223.	NCO+H<=>NH+CO			5.40E+13	0.0	0.0
224.	NCO+OH<=>NO+H+CO			2.50E+12	0.0	0.0
225.	NCO+N<=>N2+CO			2.00E+13	0.0	0.0
226.	NCO+O2<=>NO+CO2			2.00E+12	0.0	20000.0
227.	NCO+M<=>N+CO+M			8.80E+16	−0.5	48000.0
	H2	Enhanced by	2.000E+00			

	H2O	Enhanced by	6.000E+00			
	CH4	Enhanced by	2.000E+00			
	CO	Enhanced by	1.500E+00			
	CO2	Enhanced by	2.000E+00			
	C2H6	Enhanced by	3.000E+00			
	AR	Enhanced by	7.000E-01			
228.	NCO+NO<=>N2O+CO			2.85E+17	-1.5	740.0
229.	NCO+NO<=>N2+CO2			5.70E+18	-2.0	800.0
230.	HCN+M<=>H+CN+M			1.04E+29	-3.3	126600.0
	H2	Enhanced by	2.000E+00			
	H2O	Enhanced by	6.000E+00			
	CH4	Enhanced by	2.000E+00			
	CO	Enhanced by	1.500E+00			
	CO2	Enhanced by	2.000E+00			
	C2H6	Enhanced by	3.000E+00			
	AR	Enhanced by	7.000E-01			
231.	HCN+O<=>NCO+H			1.11E+04	2.6	4980.0
232.	HCN+O<=>NH+CO			2.77E+03	2.6	4980.0
233.	HCN+O<=>CN+OH			2.13E+09	1.6	26600.0
234.	HCN+OH<=>HOCN+H			1.10E+06	2.0	13370.0
235.	HCN+OH<=>HNCO+H			4.40E+03	2.3	6400.0
236.	HCN+OH<=>NH2+CO			1.60E+02	2.6	9000.0
237.	H+HCN+M<=>H2CN+M			1.40E+26	-3.4	1900.0
	H2	Enhanced by	2.000E+00			
	H2O	Enhanced by	6.000E+00			
	CH4	Enhanced by	2.000E+00			
	CO	Enhanced by	1.500E+00			
	CO2	Enhanced by	2.000E+00			
	C2H6	Enhanced by	3.000E+00			
	AR	Enhanced by	7.000E-01			
238.	H2CN+N<=>N2+CH2			6.00E+13	0.0	400.0
239.	C+N2<=>CN+N			6.30E+13	0.0	46020.0
240.	CH+N2<=>HCN+N			2.86E+08	1.1	20400.0
241.	CH+N2(+M)<=>HCNN(+M)			3.10E+12	0.1	0.0
	Low pressure limit:	0.13000E+26	-0.31600E+01	0.74000E+03		
	TROE centering:	0.66700E+00	0.23500E+03	0.21170E+04	0.45360E+04	
	H2	Enhanced by	2.000E+00			
	H2O	Enhanced by	6.000E+00			
	CH4	Enhanced by	2.000E+00			
	CO	Enhanced by	1.500E+00			
	CO2	Enhanced by	2.000E+00			
	C2H6	Enhanced by	3.000E+00			
	AR	Enhanced by	7.000E-01			
242.	CH2+N2<=>HCN+NH			1.00E+13	0.0	74000.0
243.	CH2(S)+N2<=>NH+HCN			1.00E+11	0.0	65000.0
244.	C+NO<=>CN+O			1.90E+13	0.0	0.0
245.	C+NO<=>CO+N			2.90E+13	0.0	0.0
246.	CH+NO<=>HCN+O			5.00E+13	0.0	0.0
247.	CH+NO<=>H+NCO			2.00E+13	0.0	0.0
248.	CH+NO<=>N+HCO			3.00E+13	0.0	0.0
249.	CH2+NO<=>H+HNCO			3.10E+17	-1.4	1270.0
250.	CH2+NO<=>OH+HCN			2.90E+14	-0.7	760.0
251.	CH2+NO<=>H+HCNO			3.80E+13	-0.4	580.0
252.	CH2(S)+NO<=>H+HNCO			3.10E+17	-1.4	1270.0
253.	CH2(S)+NO<=>OH+HCN			2.90E+14	-0.7	760.0
254.	CH2(S)+NO<=>H+HCNO			3.80E+13	-0.4	580.0

255. CH3+NO<=>HCN+H2O		9.60E+13	0.0	28800.0
256. CH3+NO<=>H2CN+OH		1.00E+12	0.0	21750.0
257. HCNN+O<=>CO+H+N2		2.20E+13	0.0	0.0
258. HCNN+O<=>HCN+NO		2.00E+12	0.0	0.0
259. HCNN+O2<=>O+HCO+N2		1.20E+13	0.0	0.0
260. HCNN+OH<=>H+HCO+N2		1.20E+13	0.0	0.0
261. HCNN+H<=>CH2+N2		1.00E+14	0.0	0.0
262. HNCO+O<=>NH+CO2		9.80E+07	1.4	8500.0
263. HNCO+O<=>HNO+CO		1.50E+08	1.6	44000.0
264. HNCO+O<=>NCO+OH		2.20E+06	2.1	11400.0
265. HNCO+H<=>NH2+CO		2.25E+07	1.7	3800.0
266. HNCO+H<=>H2+NCO		1.05E+05	2.5	13300.0
267. HNCO+OH<=>NCO+H2O		4.65E+12	0.0	6850.0
268. HNCO+OH<=>NH2+CO2		1.55E+12	0.0	6850.0
269. HNCO+M<=>NH+CO+M		1.18E+16	0.0	84720.0
H2	Enhanced by 2.000E+00			
H2O	Enhanced by 6.000E+00			
CH4	Enhanced by 2.000E+00			
CO	Enhanced by 1.500E+00			
CO2	Enhanced by 2.000E+00			
C2H6	Enhanced by 3.000E+00			
AR	Enhanced by 7.000E-01			
270. HCNO+H<=>H+HNCO		2.10E+15	-0.7	2850.0
271. HCNO+H<=>OH+HCN		2.70E+11	0.2	2120.0
272. HCNO+H<=>NH2+CO		1.70E+14	-0.8	2890.0
273. HOCN+H<=>H+HNCO		2.00E+07	2.0	2000.0
274. HCCO+NO<=>HCNO+CO		2.35E+13	0.0	0.0
275. CH3+N<=>H2CN+H		6.10E+14	-0.3	290.0
276. CH3+N<=>HCN+H2		3.70E+12	0.1	-90.0
277. NH3+H<=>NH2+H2		5.40E+05	2.4	9915.0
278. NH3+OH<=>NH2+H2O		5.00E+07	1.6	955.0
279. NH3+O<=>NH2+OH		9.40E+06	1.9	6460.0
280. TiCL4+O2=>TiO2(ru)+CL2+CL2		8.26E+04	0.0	21202.0
Warning...changing order for reactant...O2				
O2	Forward order 0.000E+00			
281. CH3CL<=>CH3+CL		1.00E+16	0.0	84370.0
282. CH2CL2<=>CH2CL+CL		1.00E+16	0.0	81140.0
283. CHCL2-CH2CL<=>CHCL2+CH2CL		1.00E+15	0.0	88350.0
284. CH2CL-CH2CL<=>2CH2CL		1.00E+17	0.0	90060.0
285. CHCL3<=>CHCL2+CL		1.00E+16	0.0	77630.0
286. CHCL2-CHCL2<=>2CHCL2		1.00E+15	0.0	82430.0
287. CCL3-CCL3<=>2CCL3		1.00E+15	0.0	71400.0
288. CCL3-CH2CL<=>CCL3+CH2CL		1.00E+15	0.0	82670.0
289. CCL3-CHCL2<=>CCL3+CHCL2		1.00E+15	0.0	75860.0
290. CCL4<=>CCL3+CL		1.00E+16	0.0	70930.0
291. CH2CL-CH2<=>C2H4+CL		1.00E+14	0.0	20330.0
292. CH2CL-CCL2<=>CCL2-CH2+CL		1.00E+14	0.0	25850.0
293. CHCL2-CHCL<=>tCHCL-CHCL+CL		1.00E+14	0.0	21630.0
294. CHCL2-CHCL<=>cCHCL-CHCL+CL		1.00E+14	0.0	21080.0
295. CH2CL-CHCL<=>CHCL-CH2+CL		1.00E+14	0.0	22890.0
296. CHCL2-CH2<=>CHCL-CH2+CL		1.00E+14	0.0	19190.0
297. CHCL2-CCL2<=>CCL2-CHCL+CL		1.00E+14	0.0	21220.0
298. CCL3-CCL2<=>CCL2-CCL2+CL		1.00E+14	0.0	19350.0
299. CCL3-CH2<=>CCL2-CH2+CL		1.00E+14	0.0	17470.0
300. CCL3-CHCL<=>CCL2-CHCL+CL		1.00E+14	0.0	18450.0
301. cCHCL-CHCL+CL<=>cCHCL-CCL+HCL		1.00E+13	0.0	1960.0

302.	tCHCL–CHCL+CL<=>tCHCL–CCL+HCL	1.00E+13	0.0	1510.0
303.	CH3CL+CL<=>CH2CL+HCL	1.00E+13	0.0	460.0
304.	CH3CL+CL<=>CH3+CL2	1.00E+14	0.0	25620.0
305.	CH4+CL<=>CH3+HCL	4.59E+11	2.5	1171.1
306.	CH4+CH2CL<=>CH3+CH3CL	3.00E+11	0.0	15800.0
307.	CH2CL2+CL<=>CHCL2+HCL	1.00E+13	0.0	460.0
308.	CH2CL2+CH3<=>CHCL2+CH4	3.00E+11	0.0	11000.0
309.	CH2CL2+CH2CL<=>CHCL2+CH3CL	3.00E+11	0.0	11000.0
310.	CH2CL2+CL<=>CH2CL+CL2	1.00E+14	0.0	22390.0
311.	CH2CL2+CH3<=>CH2CL+CH3CL	3.00E+11	0.0	11000.0
312.	CHCL2–CH2CL+CL<=>CHCL2–CHCL+HCL	1.00E+13	0.0	460.0
313.	CHCL2–CH2CL+CL<=>CH2CL–CCL2+HCL	1.00E+13	0.0	460.0
314.	CH2CL–CH2CL+CL<=>CH2CL–CHCL+HCL	1.00E+13	0.0	460.0
315.	CHCL3+CL<=>CCL3+HCL	1.00E+13	0.0	460.0
316.	CHCL3+CH3<=>CCL3+CH4	3.00E+11	0.0	11000.0
317.	CHCL3+CH2CL<=>CCL3+CH3CL	3.00E+11	0.0	11000.0
318.	CHCL3+CHCL2<=>CCL3+CH2CL2	3.00E+11	0.0	11000.0
319.	CHCL3+CL<=>CHCL2+CL2	1.00E+14	0.0	18880.0
320.	CHCL3+CH3<=>CHCL2+CH3CL	3.00E+11	0.0	11000.0
321.	CHCL3+CH2CL<=>CHCL2+CH2CL2	3.00E+11	0.0	11000.0
322.	CHCL2–CHCL2+CL<=>CHCL2–CCL2+HCL	1.00E+13	0.0	460.0
323.	CCL4+CL<=>CCL3+CL2	1.00E+14	0.0	12180.0
324.	CCL4+CH3<=>CCL3+CH3CL	3.00E+11	0.0	11000.0
325.	CCL4+CH2CL<=>CCL3+CH2CL2	3.00E+11	0.0	11000.0
326.	CCL4+CHCL2<=>CCL3+CHCL3	3.00E+11	0.0	11000.0
327.	CCL2–CCL2+CL2<=>CCL3–CCL2+CL	1.00E+13	0.0	39860.0
328.	CCL2–CHCL+CL2<=>CHCL2–CCL2+CL	1.00E+13	0.0	37990.0
329.	CCL2–CHCL+CL2<=>CCL3–CHCL+CL	1.00E+13	0.0	40760.0
330.	cCHCL–CHCL+CL2<=>CHCL2–CHCL+CL	1.00E+13	0.0	37480.0
331.	tCHCL–CHCL+CL2<=>CHCL2–CHCL+CL	1.00E+13	0.0	37380.0
332.	CCL2–CH2+CL2<=>CH2CL–CCL2+CL	1.00E+13	0.0	34560.0
333.	CCL2–CH2+CL2<=>CCL3–CH2+CL	1.00E+13	0.0	42940.0
334.	CHCL–CH2+CL2<=>CH2CL–CHCL+CL	1.00E+13	0.0	37320.0
335.	CHCL–CH2+CL2<=>CHCL2–CH2+CL	1.00E+13	0.0	41020.0
336.	CHCL–CH2+CH2CL–CH2CL<=>CHCL2–CH2+CH2CL–CH2	3.00E+14	0.0	66400.0
337.	CHCL–CH2+CHCL2–CH2CL<=>CHCL2–CH2+CHCL2–CH2	3.00E+14	0.0	64740.0
338.	CHCL–CH2+CCL3–CH3<=>CHCL2–CH2+CH3–CCL2	3.00E+14	0.0	56660.0
339.	CHCL–CH2+CCL3–CH2CL<=>CHCL2–CH2+CCL3–CH2	3.00E+14	0.0	61440.0
340.	CHCL–CH2+CCL3–CH2CL<=>CHCL2–CH2+CH2CL–CCL2	3.00E+14	0.0	53060.0
341.	CHCL–CH2+CCL3–CHCL2<=>CHCL2–CH2+CCL3–CHCL	3.00E+14	0.0	55340.0
342.	CHCL–CH2+CCL3–CHCL2<=>CHCL2–CH2+CHCL2–CCL2	3.00E+14	0.0	52570.0
343.	CHCL–CH2+CCL3–CCL3<=>CHCL2–CH2+CCL3–CCL2	3.00E+14	0.0	54180.0
344.	CHCL–CH2+CCL4<=>CHCL2–CH2+CCL3	3.00E+14	0.0	52740.0
345.	CHCL–CH2+CHCL2–CHCL2<=>CHCL2–CH2+CHCL2–CHCL	3.00E+14	0.0	56830.0
346.	CHCL–CH2+CH2CL–CH2CL<=>CH2CL–CHCL+CH2CL–CH2	3.00E+14	0.0	62700.0
347.	CHCL–CH2+CHCL2–CH2CL<=>CH2CL–CHCL+CHCL2–CH2	3.00E+14	0.0	61040.0
348.	CHCL–CH2+CHCL2–CH2CL<=>CH2CL–CHCL+CH2CL–CHCL	3.00E+14	0.0	57340.0
349.	CHCL–CH2+CCL3–CH3<=>CH2CL–CHCL+CH3–CCL2	3.00E+14	0.0	52960.0
350.	CHCL–CH2+CCL3–CH2CL<=>CH2CL–CHCL+CCL3–CH2	3.00E+14	0.0	57740.0
351.	CHCL–CH2+CCL3–CH2CL<=>CH2CL–CHCL+CH2CL–CCL2	3.00E+14	0.0	49360.0
352.	CHCL–CH2+CCL3–CHCL2<=>CH2CL–CHCL+CCL3–CHCL	3.00E+14	0.0	51640.0
353.	CHCL–CH2+CCL3–CHCL2<=>CH2CL–CHCL+CHCL2–CCL2	3.00E+14	0.0	48870.0
354.	CHCL–CH2+CCL3–CCL3<=>CH2CL–CHCL+CCL3–CCL2	3.00E+14	0.0	50480.0
355.	CHCL–CH2+CCL4<=>CH2CL–CHCL+CCL3	3.00E+14	0.0	49040.0
356.	CHCL–CH2+CHCL2–CHCL2<=>CH2CL–CHCL+CHCL2–CHCL	3.00E+14	0.0	53130.0
357.	CCL2–CH2+CH2CL–CH2CL<=>CCL3–CH2+CH2CL–CH2	3.00E+14	0.0	68320.0

358. CCL2–CH2+CHCL2–CH2CL<=>CCL3–CH2+CHCL2–CH2 3.00E+14 0.0 66660.0
359. CCL2–CH2+CHCL2–CH2CL<=>CCL3–CH2+CH2CL–CHCL 3.00E+14 0.0 62960.0
360. CCL2–CH2+CCL3–CH3<=>CCL3–CH2+CH3–CCL2 3.00E+14 0.0 58580.0
361. CCL2–CH2+CCL3–CH2CL<=>CCL3–CH2+CCL3–CH2 3.00E+14 0.0 63360.0
362. CCL2–CH2+CCL3–CHCL2<=>CCL3–CH2+CCL3–CHCL 3.00E+14 0.0 57260.0
363. CCL2–CH2+CCL3–CHCL2<=>CCL3–CH2+CHCL2–CCL2 3.00E+14 0.0 54490.0
364. CCL2–CH2+CCL3–CCL3<=>CCL3–CH2+CCL3–CCL2 3.00E+14 0.0 56100.0
365. CCL2–CH2+CCL4<=>CCL3–CH2+CCL3 3.00E+14 0.0 54660.0
366. CCL2–CH2+CHCL2–CHCL2<=>CCL3–CH2+CHCL2–CHCL 3.00E+14 0.0 58750.0
367. CCL2–CH2+CH2CL–CH2CL<=>CH2CL–CCL2+CH2CL–CH2 3.00E+14 0.0 59940.0
368. CCL2–CH2+CHCL2–CH2CL<=>CH2CL–CCL2+CHCL2–CH2 3.00E+14 0.0 58280.0
369. CCL2–CH2+CHCL2–CH2CL<=>CH2CL–CCL2+CH2CL–CHCL 3.00E+14 0.0 54580.0
370. CCL2–CH2+CCL3–CH3<=>CH2CL–CCL2+CH3–CCL2 3.00E+14 0.0 50200.0
371. CCL2–CH2+CCL3–CH2CL<=>CH2CL–CCL2+CCL3–CH2 3.00E+14 0.0 54980.0
372. CCL2–CH2+CCL3–CH2CL<=>CH2CL–CCL2+CH2CL–CCL2 3.00E+14 0.0 46600.0
373. CCL2–CH2+CCL3–CHCL2<=>CH2CL–CCL2+CCL3–CHCL 3.00E+14 0.0 48880.0
374. CCL2–CH2+CCL3–CHCL2<=>CH2CL–CCL2+CHCL2–CCL2 3.00E+14 0.0 46110.0
375. CCL2–CH2+CCL3–CCL3<=>CH2CL–CCL2+CCL3–CCL2 3.00E+14 0.0 47720.0
376. CCL2–CH2+CCL4<=>CH2CL–CCL2+CCL3 3.00E+14 0.0 46280.0
377. CCL2–CH2+CHCL2–CHCL2<=>CH2CL–CCL2+CHCL2–CHCL 3.00E+14 0.0 50370.0
378. tCHCL–CHCL+CH2CL–CH2CL 3.00E+14 0.0 62760.0
<=>CHCL2–CHCL+CH2CL–CH2
379. tCHCL–CHCL+CHCL2–CH2CL 3.00E+14 0.0 61100.0
<=>CHCL2–CHCL+CHCL2–CH2
380. tCHCL–CHCL+CHCL2–CH2CL 3.00E+14 0.0 57400.0
<=>CHCL2–CHCL+CH2CL–CHCL
381. tCHCL–CHCL+CCL3–CH3<=>CHCL2–CHCL+CH3–CCL2 3.00E+14 0.0 53020.0
382. tCHCL–CHCL+CCL3–CH2CL<=>CHCL2–CHCL+CCL3–CH2 3.00E+14 0.0 57800.0
383. tCHCL–CHCL+CCL3–CH2CL 3.00E+14 0.0 49420.0
<=>CHCL2–CHCL+CH2CL–CCL2
384. tCHCL–CHCL+CCL3–CHCL2<=>CHCL2–CHCL+CCL3–CHCL 3.00E+14 0.0 51700.0
385. tCHCL–CHCL+CCL3–CHCL2 3.00E+14 0.0 48930.0
<=>CHCL2–CHCL+CHCL2–CCL2
386. tCHCL–CHCL+CCL3–CCL3<=>CHCL2–CHCL+CCL3–CCL2 3.00E+14 0.0 50540.0
387. tCHCL–CHCL+CCL4<=>CHCL2–CHCL+CCL3 3.00E+14 0.0 49100.0
388. tCHCL–CHCL+CHCL2–CHCL2 3.00E+14 0.0 53190.0
<=>CHCL2–CHCL+CHCL2–CHCL
389. cCHCL–CHCL+CH2CL–CH2CL 3.00E+14 0.0 62860.0
<=>CHCL2–CHCL+CH2CL–CH2
390. cCHCL–CHCL+CHCL2–CH2CL 3.00E+14 0.0 61200.0
<=>CHCL2–CHCL+CHCL2–CH2
391. cCHCL–CHCL+CHCL2–CH2CL 3.00E+14 0.0 57500.0
<=>CHCL2–CHCL+CH2CL–CHCL
392. cCHCL–CHCL+CCL3–CH3<=>CHCL2–CHCL+CH3–CCL2 3.00E+14 0.0 53120.0
393. cCHCL–CHCL+CCL3–CH2CL<=>CHCL2–CHCL+CCL3–CH2 3.00E+14 0.0 57900.0
394. cCHCL–CHCL+CCL3–CH2CL 3.00E+14 0.0 49520.0
<=>CHCL2–CHCL+CH2CL–CCL2
395. cCHCL–CHCL+CCL3–CHCL2<=>CHCL2–CHCL+CCL3–CHCL 3.00E+14 0.0 51800.0
396. cCHCL–CHCL+CCL3–CHCL2 3.00E+14 0.0 49030.0
<=>CHCL2–CHCL+CHCL2–CCL2
397. cCHCL–CHCL+CCL3–CCL3<=>CHCL2–CHCL+CCL3–CCL2 3.00E+14 0.0 50640.0
398. cCHCL–CHCL+CCL4<=>CHCL2–CHCL+CCL3 3.00E+14 0.0 49200.0
399. cCHCL–CHCL+CHCL2–CHCL2 3.00E+14 0.0 53290.0
<=>CHCL2–CHCL+CHCL2–CHCL
400. CCL2–CHCL+CH2CL–CH2CL<=>CCL3–CHCL+CH2CL–CH2 3.00E+14 0.0 66140.0
401. CCL2–CHCL+CHCL2–CH2CL<=>CCL3–CHCL+CHCL2–CH2 3.00E+14 0.0 64480.0

```
402. CCL2–CHCL+CHCL2–CH2CL<=>CCL3–CHCL+CH2CL–CHCL   3.00E+14   0.0   60780.0
403. CCL2–CHCL+CCL3–CH3<=>CCL3–CHCL+CH3–CCL2        3.00E+14   0.0   56400.0
404. CCL2–CHCL+CCL3–CH2CL<=>CCL3–CHCL+CCL3–CH2      3.00E+14   0.0   61180.0
405. CCL2–CHCL+CCL3–CH2CL<=>CCL3–CHCL+CH2CL–CCL2    3.00E+14   0.0   52800.0
406. CCL2–CHCL+CCL3–CHCL2<=>CCL3–CHCL+CCL3–CHCL     3.00E+14   0.0   55080.0
407. CCL2–CHCL+CCL3–CCL3<=>CCL3–CHCL+CCL3–CCL2      3.00E+14   0.0   53920.0
408. CCL2–CHCL+CCL4<=>CCL3–CHCL+CCL3                3.00E+14   0.0   52480.0
409. CCL2–CHCL+CHCL2–CHCL2<=>CCL3–CHCL+CHCL2–CHCL  3.00E+14   0.0   56570.0
410. CCL2–CHCL+CH2CL–CH2CL<=>CHCL2–CCL2+CH2CL–CH2  3.00E+14   0.0   63370.0
411. CCL2–CHCL+CHCL2–CH2CL<=>CHCL2–CCL2+CHCL2–CH2  3.00E+14   0.0   61710.0
412. CCL2–CHCL+CHCL2–CH2CL                         3.00E+14   0.0   58010.0
     <=>CHCL2–CCL2+CH2CL–CHCL
413. CCL2–CHCL+CCL3–CH3<=>CHCL2–CCL2+CH3–CCL2      3.00E+14   0.0   53630.0
414. CCL2–CHCL+CCL3–CH2CL<=>CHCL2–CCL2+CCL3–CH2    3.00E+14   0.0   58410.0
415. CCL2–CHCL+CCL3–CH2CL<=>CHCL2–CCL2+CH2CL–CCL2  3.00E+14   0.0   50030.0
416. CCL2–CHCL+CCL3–CHCL2<=>CHCL2–CCL2+CCL3–CHCL   3.00E+14   0.0   52310.0
417. CCL2–CHCL+CCL3–CHCL2<=>CHCL2–CCL2+CHCL2–CCL2  3.00E+14   0.0   49540.0
418. CCL2–CHCL+CCL3–CCL3<=>CHCL2–CCL2+CCL3–CCL2    3.00E+14   0.0   51150.0
419. CCL2–CHCL+CCL4<=>CHCL2–CCL2+CCL3              3.00E+14   0.0   49710.0
420. CCL2–CHCL+CHCL2–CHCL2                         3.00E+14   0.0   53800.0
     <=>CHCL2–CCL2+CHCL2–CHCL
421. CCL2–CCL2+CH2CL–CH2CL<=>CCL3–CCL2+CH2CL–CH2  3.00E+14   0.0   65240.0
422. CCL2–CCL2+CHCL2–CH2CL<=>CCL3–CCL2+CHCL2–CH2  3.00E+14   0.0   63580.0
423. CCL2–CCL2+CHCL2–CH2CL<=>CCL3–CCL2+CH2CL–CHCL  3.00E+14   0.0   59880.0
424. CCL2–CCL2+CCL3–CH3<=>CCL3–CCL2+CH3–CCL2      3.00E+14   0.0   55500.0
425. CCL2–CCL2+CCL3–CH2CL<=>CCL3–CCL2+CCL3–CH2    3.00E+14   0.0   60280.0
426. CCL2–CCL2+CCL3–CH2CL<=>CCL3–CCL2+CH2CL–CCL2  3.00E+14   0.0   51900.0
427. CCL2–CCL2+CCL3–CHCL2<=>CCL3–CCL2+CCL3–CHCL   3.00E+14   0.0   54180.0
428. CCL2–CCL2+CCL3–CHCL2<=>CCL3–CCL2+CHCL2–CCL2  3.00E+14   0.0   51410.0
429. CCL2–CCL2+CCL3–CCL3<=>CCL3–CCL2+CCL3–CCL2    3.00E+14   0.0   53020.0
430. CCL2–CCL2+CCL4<=>CCL3–CCL2+CCL3              3.00E+14   0.0   51580.0
431. CCL2–CCL2+CHCL2–CHCL2<=>CCL3–CCL2+CHCL2–CHCL  3.00E+14   0.0   55670.0

 NOTE:  A units mole–cm–sec–K, E units cal/mole


NO ERRORS FOUND ON INPUT...CHEMKIN LINKING FILE WRITTEN.

WORKING SPACE REQUIREMENTS ARE
    INTEGER:      7544
    REAL:         6898
    CHARACTER:      93
```

Detailed Mechanism

```
CHEMKIN INTERPRETER OUTPUT: CHEMKIN–II Version 3.9  Aug. 1994
                        DOUBLE PRECISION

                  ____________________
                  ELEMENTS     ATOMIC
                  CONSIDERED   WEIGHT
                  ____________________
```

1. O	15.9994
2. CL	35.4530
3. Ti	47.9000
4. AR	39.9480
5. H	1.00797
6. C	12.0112
7. N	14.0067

SPECIES CONSIDERED	PHASE	CHARGE	MOLECULAR WEIGHT	TEMPERATURE LOW	TEMPERATURE HIGH	ELEMENT COUNT O	CL	Ti	AR	H	C	N
1. H2	G	0	2.01594	200	3500	0	0	0	0	2	0	0
2. H	G	0	1.00797	200	3500	0	0	0	0	1	0	0
3. O	G	0	15.99940	200	3500	1	0	0	0	0	0	0
4. O2	G	0	31.99880	200	3500	2	0	0	0	0	0	0
5. OH	G	0	17.00737	200	3500	1	0	0	0	1	0	0
6. H2O	G	0	18.01534	200	3500	1	0	0	0	2	0	0
7. HO2	G	0	33.00677	200	3500	2	0	0	0	1	0	0
8. H2O2	G	0	34.01474	200	3500	2	0	0	0	2	0	0
9. C	G	0	12.01115	200	3500	0	0	0	0	0	1	0
10. CH	G	0	13.01912	200	3500	0	0	0	0	1	1	0
11. CH2	G	0	14.02709	200	3500	0	0	0	0	2	1	0
12. CH2(S)	G	0	14.02709	200	3500	0	0	0	0	2	1	0
13. CH3	G	0	15.03506	200	3500	0	0	0	0	3	1	0
14. CH4	G	0	16.04303	200	3500	0	0	0	0	4	1	0
15. CO	G	0	28.01055	200	3500	1	0	0	0	0	1	0
16. CO2	G	0	44.00995	200	3500	2	0	0	0	0	1	0
17. HCO	G	0	29.01852	200	3500	1	0	0	0	1	1	0
18. CH2O	G	0	30.02649	200	3500	1	0	0	0	2	1	0
19. CH2OH	G	0	31.03446	200	3500	1	0	0	0	3	1	0
20. CH3O	G	0	31.03446	300	3000	1	0	0	0	3	1	0
21. CH3OH	G	0	32.04243	200	3500	1	0	0	0	4	1	0
22. C2H	G	0	25.03027	200	3500	0	0	0	0	1	2	0
23. C2H2	G	0	26.03824	200	3500	0	0	0	0	2	2	0
24. C2H3	G	0	27.04621	200	3500	0	0	0	0	3	2	0
25. C2H4	G	0	28.05418	200	3500	0	0	0	0	4	2	0
26. C2H5	G	0	29.06215	200	3500	0	0	0	0	5	2	0
27. C2H6	G	0	30.07012	200	3500	0	0	0	0	6	2	0
28. HCCO	G	0	41.02967	300	4000	1	0	0	0	1	2	0
29. CH2CO	G	0	42.03764	200	3500	1	0	0	0	2	2	0
30. HCCOH	G	0	42.03764	300	5000	1	0	0	0	2	2	0
31. N	G	0	14.00670	200	6000	0	0	0	0	0	0	1
32. NH	G	0	15.01467	200	6000	0	0	0	0	1	0	1
33. NH2	G	0	16.02264	200	6000	0	0	0	0	2	0	1
34. NH3	G	0	17.03061	200	6000	0	0	0	0	3	0	1
35. NNH	G	0	29.02137	200	6000	0	0	0	0	1	0	2
36. NO	G	0	30.00610	200	6000	1	0	0	0	0	0	1
37. NO2	G	0	46.00550	200	6000	2	0	0	0	0	0	1
38. N2O	G	0	44.01280	200	6000	1	0	0	0	0	0	2
39. HNO	G	0	31.01407	200	6000	1	0	0	0	1	0	1
40. CN	G	0	26.01785	200	6000	0	0	0	0	0	1	1

41. HCN	G	0	27.02582	200	6000	0	0	0	0	1	1	1
42. H2CN	G	0	28.03379	300	4000	0	0	0	0	2	1	1
43. HCNN	G	0	41.03252	300	5000	0	0	0	0	1	1	2
44. HCNO	G	0	43.02522	300	5000	1	0	0	0	1	1	1
45. HOCN	G	0	43.02522	300	5000	1	0	0	0	1	1	1
46. HNCO	G	0	43.02522	300	5000	1	0	0	0	1	1	1
47. NCO	G	0	42.01725	200	6000	1	0	0	0	0	1	1
48. N2	G	0	28.01340	300	5000	0	0	0	0	0	0	2
49. AR	G	0	39.94800	300	5000	0	0	0	1	0	0	0
50. CL	G	0	35.45300	298	5000	0	1	0	0	0	0	0
51. CL2	G	0	70.90600	298	5000	0	2	0	0	0	0	0
52. TiCL4	G	0	189.71200	300	5000	0	4	1	0	0	0	0
53. TiCL3	G	0	154.25900	300	2000	0	3	1	0	0	0	0
54. TiO2CL3	G	0	186.25780	100	3000	2	3	1	0	0	0	0
55. TiOCL3	G	0	170.25840	100	3000	1	3	1	0	0	0	0
56. TiOCL2	G	0	134.80540	100	3000	1	2	1	0	0	0	0
57. Ti2O3CL2	G	0	214.70420	100	3000	3	2	2	0	0	0	0
58. Ti2O2CL4	G	0	269.61080	100	3000	2	4	2	0	0	0	0
59. Ti3O4CL4	G	0	349.50960	100	3000	4	4	3	0	0	0	0
60. Ti5O6CL8	G	0	619.12040	100	3000	6	8	5	0	0	0	0
61. Ti2O2CL6	G	0	340.51680	100	3000	2	6	2	0	0	0	0
62. Ti2O3CL3	G	0	250.15720	100	3000	3	3	2	0	0	0	0
63. TiCL2	G	0	118.80600	300	2000	0	2	1	0	0	0	0
64. TiCL	G	0	83.35300	300	2000	0	1	1	0	0	0	0
65. TiO2CL2	G	0	150.80480	100	3000	2	2	1	0	0	0	0
66. Ti2O2CL3	G	0	234.15780	100	3000	2	3	2	0	0	0	0
67. Ti2O2CL5	G	0	305.06380	100	3000	2	5	2	0	0	0	0
68. TiCL2OCL	G	0	170.25840	100	3000	1	3	1	0	0	0	0
69. Ti	G	0	47.90000	200	6000	0	0	1	0	0	0	0
70. CLO	G	0	51.45240	300	4000	1	1	0	0	0	0	0
71. CL2O	G	0	86.90540	300	5000	1	2	0	0	0	0	0
72. CLOO	G	0	67.45180	300	4000	2	1	0	0	0	0	0
73. O3	G	0	47.99820	300	5000	3	0	0	0	0	0	0
74. TiO2(ru)	G	0	79.89880	300	2130	2	0	1	0	0	0	0
75. HCL	G	0	36.46097	200	6000	0	1	0	0	1	0	0
76. CH3CL	G	0	50.48806	298	5000	0	1	0	0	3	1	0
77. CH2CL2	G	0	84.93309	298	5000	0	2	0	0	2	1	0
78. CHCL3	G	0	119.37812	298	5000	0	3	0	0	1	1	0
79. CCL4	G	0	153.82315	298	5000	0	4	0	0	0	1	0
80. CHCL2–CH2CL	G	0	133.40521	298	5000	0	3	0	0	3	2	0
81. CH2CL–CH2CL	G	0	98.96018	298	5000	0	2	0	0	4	2	0
82. CHCL2–CHCL2	G	0	167.85024	298	5000	0	4	0	0	2	2	0
83. CCL3–CCL3	G	0	236.74030	298	5000	0	6	0	0	0	2	0
84. CCL3–CH2CL	G	0	167.85024	298	5000	0	4	0	0	2	2	0
85. CCL3–CHCL2	G	0	202.29527	298	5000	0	5	0	0	1	2	0
86. CCL2–CH2	G	0	96.94424	298	5000	0	2	0	0	2	2	0
87. tCHCL–CHCL	G	0	96.94424	298	5000	0	2	0	0	2	2	0
88. cCHCL–CHCL	G	0	96.94424	298	5000	0	2	0	0	2	2	0
89. CHCL–CH2	G	0	62.49921	298	5000	0	1	0	0	3	2	0
90. CCL2–CHCL	G	0	131.38927	298	5000	0	3	0	0	1	2	0
91. CCL2–CCL2	G	0	165.83430	298	5000	0	4	0	0	0	2	0
92. CCL3–CH3	G	0	133.40521	298	5000	0	3	0	0	3	2	0
93. CH2CL	G	0	49.48009	298	5000	0	1	0	0	2	1	0
94. CHCL2	G	0	83.92512	298	5000	0	2	0	0	1	1	0
95. CCL3	G	0	118.37015	298	5000	0	3	0	0	0	1	0
96. CH2CL–CH2	G	0	63.50718	298	5000	0	1	0	0	4	2	0

97.	CH2CL–CCL2	G	0	132.39724	298	5000	0	3	0	0	2	2	0
98.	CHCL2–CHCL	G	0	132.39724	298	5000	0	3	0	0	2	2	0
99.	CH2CL–CHCL	G	0	97.95221	298	5000	0	2	0	0	3	2	0
100.	CHCL2–CH2	G	0	97.95221	298	5000	0	2	0	0	3	2	0
101.	CHCL2–CCL2	G	0	166.84227	298	5000	0	4	0	0	1	2	0
102.	CCL3–CCL2	G	0	201.28730	298	5000	0	5	0	0	0	2	0
103.	CCL3–CH2	G	0	132.39724	298	5000	0	3	0	0	2	2	0
104.	CCL3–CHCL	G	0	166.84227	298	5000	0	4	0	0	1	2	0
105.	cCHCL–CCL	G	0	95.93627	298	5000	0	2	0	0	1	2	0
106.	tCHCL–CCL	G	0	95.93627	298	5000	0	2	0	0	1	2	0
107.	CH3–CCL2	G	0	97.95221	298	5000	0	2	0	0	3	2	0

	REACTIONS CONSIDERED			(k = A T**b exp(−E/RT)) A	b	E
1.	2O+M<=>O2+M			1.20E+17	−1.0	0.0
	H2	Enhanced by	2.400E+00			
	H2O	Enhanced by	1.540E+01			
	CH4	Enhanced by	2.000E+00			
	CO	Enhanced by	1.750E+00			
	CO2	Enhanced by	3.600E+00			
	C2H6	Enhanced by	3.000E+00			
	AR	Enhanced by	8.300E−01			
2.	O+H+M<=>OH+M			5.00E+17	−1.0	0.0
	H2	Enhanced by	2.000E+00			
	H2O	Enhanced by	6.000E+00			
	CH4	Enhanced by	2.000E+00			
	CO	Enhanced by	1.500E+00			
	CO2	Enhanced by	2.000E+00			
	C2H6	Enhanced by	3.000E+00			
	AR	Enhanced by	7.000E−01			
3.	O+H2<=>H+OH			5.00E+04	2.7	6290.0
4.	O+HO2<=>OH+O2			2.00E+13	0.0	0.0
5.	O+H2O2<=>OH+HO2			9.63E+06	2.0	4000.0
6.	O+CH<=>H+CO			5.70E+13	0.0	0.0
7.	O+CH2<=>H+HCO			8.00E+13	0.0	0.0
8.	O+CH2(S)<=>H2+CO			1.50E+13	0.0	0.0
9.	O+CH2(S)<=>H+HCO			1.50E+13	0.0	0.0
10.	O+CH3<=>H+CH2O			8.43E+13	0.0	0.0
11.	O+CH4<=>OH+CH3			1.02E+09	1.5	8600.0
12.	O+CO+M<=>CO2+M			6.02E+14	0.0	3000.0
	H2	Enhanced by	2.000E+00			
	O2	Enhanced by	6.000E+00			
	H2O	Enhanced by	6.000E+00			
	CH4	Enhanced by	2.000E+00			
	CO	Enhanced by	1.500E+00			
	CO2	Enhanced by	3.500E+00			
	C2H6	Enhanced by	3.000E+00			
	AR	Enhanced by	5.000E−01			
13.	O+HCO<=>OH+CO			3.00E+13	0.0	0.0
14.	O+HCO<=>H+CO2			3.00E+13	0.0	0.0
15.	O+CH2O<=>OH+HCO			3.90E+13	0.0	3540.0
16.	O+CH2OH<=>OH+CH2O			1.00E+13	0.0	0.0

17.	O+CH3O<=>OH+CH2O		1.00E+13	0.0	0.0
18.	O+CH3OH<=>OH+CH2OH		3.88E+05	2.5	3100.0
19.	O+CH3OH<=>OH+CH3O		1.30E+05	2.5	5000.0
20.	O+C2H<=>CH+CO		5.00E+13	0.0	0.0
21.	O+C2H2<=>H+HCCO		1.02E+07	2.0	1900.0
22.	O+C2H2<=>OH+C2H		4.60E+19	−1.4	28950.0
23.	O+C2H2<=>CO+CH2		1.02E+07	2.0	1900.0
24.	O+C2H3<=>H+CH2CO		3.00E+13	0.0	0.0
25.	O+C2H4<=>CH3+HCO		1.92E+07	1.8	220.0
26.	O+C2H5<=>CH3+CH2O		1.32E+14	0.0	0.0
27.	O+C2H6<=>OH+C2H5		8.98E+07	1.9	5690.0
28.	O+HCCO<=>H+2CO		1.00E+14	0.0	0.0
29.	O+CH2CO<=>OH+HCCO		1.00E+13	0.0	8000.0
30.	O+CH2CO<=>CH2+CO2		1.75E+12	0.0	1350.0
31.	O2+CO<=>O+CO2		2.50E+12	0.0	47800.0
32.	O2+CH2O<=>HO2+HCO		1.00E+14	0.0	40000.0
33.	H+O2+M<=>HO2+M		2.80E+18	−0.9	0.0
	O2	Enhanced by 0.000E+00			
	H2O	Enhanced by 0.000E+00			
	CO	Enhanced by 7.500E−01			
	CO2	Enhanced by 1.500E+00			
	C2H6	Enhanced by 1.500E+00			
	N2	Enhanced by 0.000E+00			
	AR	Enhanced by 0.000E+00			
34.	H+2O2<=>HO2+O2		3.00E+20	−1.7	0.0
35.	H+O2+H2O<=>HO2+H2O		9.38E+18	−0.8	0.0
36.	H+O2+N2<=>HO2+N2		3.75E+20	−1.7	0.0
37.	H+O2+AR<=>HO2+AR		7.00E+17	−0.8	0.0
38.	H+O2<=>O+OH		8.30E+13	0.0	14413.0
39.	2H+M<=>H2+M		1.00E+18	−1.0	0.0
	H2	Enhanced by 0.000E+00			
	H2O	Enhanced by 0.000E+00			
	CH4	Enhanced by 2.000E+00			
	CO2	Enhanced by 0.000E+00			
	C2H6	Enhanced by 3.000E+00			
	AR	Enhanced by 6.300E−01			
40.	2H+H2<=>2H2		9.00E+16	−0.6	0.0
41.	2H+H2O<=>H2+H2O		6.00E+19	−1.2	0.0
42.	2H+CO2<=>H2+CO2		5.50E+20	−2.0	0.0
43.	H+OH+M<=>H2O+M		2.20E+22	−2.0	0.0
	H2	Enhanced by 7.300E−01			
	H2O	Enhanced by 3.650E+00			
	CH4	Enhanced by 2.000E+00			
	C2H6	Enhanced by 3.000E+00			
	AR	Enhanced by 3.800E−01			
44.	H+HO2<=>O+H2O		3.97E+12	0.0	671.0
45.	H+HO2<=>O2+H2		2.80E+13	0.0	1068.0
46.	H+HO2<=>2OH		1.34E+14	0.0	635.0
47.	H+H2O2<=>HO2+H2		1.21E+07	2.0	5200.0
48.	H+H2O2<=>OH+H2O		1.00E+13	0.0	3600.0
49.	H+CH<=>C+H2		1.10E+14	0.0	0.0
50.	H+CH2(+M)<=>CH3(+M)		2.50E+16	−0.8	0.0
	Low pressure limit:	0.32000E+28 −0.31400E+01 0.12300E+04			
	TROE centering:	0.68000E+00 0.78000E+02 0.19950E+04 0.55900E+04			
	H2	Enhanced by 2.000E+00			
	H2O	Enhanced by 6.000E+00			

```
      CH4                 Enhanced by     2.000E+00
      CO                  Enhanced by     1.500E+00
      CO2                 Enhanced by     2.000E+00
      C2H6                Enhanced by     3.000E+00
      AR                  Enhanced by     7.000E-01
51. H+CH2(S)<=>CH+H2                                  3.00E+13    0.0         0.0
52. H+CH3(+M)<=>CH4(+M)                               1.27E+16   -0.6       383.0
    Low pressure limit:  0.24770E+34 -0.47600E+01  0.24400E+04
    TROE centering:      0.78300E+00  0.74000E+02  0.29410E+04  0.69640E+04
      H2                  Enhanced by     2.000E+00
      H2O                 Enhanced by     6.000E+00
      CH4                 Enhanced by     2.000E+00
      CO                  Enhanced by     1.500E+00
      CO2                 Enhanced by     2.000E+00
      C2H6                Enhanced by     3.000E+00
      AR                  Enhanced by     7.000E-01
53. H+CH4<=>CH3+H2                                    6.60E+08    1.6     10840.0
54. H+HCO(+M)<=>CH2O(+M)                              1.09E+12    0.5      -260.0
    Low pressure limit:  0.13500E+25 -0.25700E+01  0.14250E+04
    TROE centering:      0.78240E+00  0.27100E+03  0.27550E+04  0.65700E+04
      H2                  Enhanced by     2.000E+00
      H2O                 Enhanced by     6.000E+00
      CH4                 Enhanced by     2.000E+00
      CO                  Enhanced by     1.500E+00
      CO2                 Enhanced by     2.000E+00
      C2H6                Enhanced by     3.000E+00
      AR                  Enhanced by     7.000E-01
55. H+HCO<=>H2+CO                                     7.34E+13    0.0         0.0
56. H+CH2O(+M)<=>CH2OH(+M)                            5.40E+11    0.5      3600.0
    Low pressure limit:  0.12700E+33 -0.48200E+01  0.65300E+04
    TROE centering:      0.71870E+00  0.10300E+03  0.12910E+04  0.41600E+04
      H2                  Enhanced by     2.000E+00
      H2O                 Enhanced by     6.000E+00
      CH4                 Enhanced by     2.000E+00
      CO                  Enhanced by     1.500E+00
      CO2                 Enhanced by     2.000E+00
      C2H6                Enhanced by     3.000E+00
57. H+CH2O(+M)<=>CH3O(+M)                             5.40E+11    0.5      2600.0
    Low pressure limit:  0.22000E+31 -0.48000E+01  0.55600E+04
    TROE centering:      0.75800E+00  0.94000E+02  0.15550E+04  0.42000E+04
      H2                  Enhanced by     2.000E+00
      H2O                 Enhanced by     6.000E+00
      CH4                 Enhanced by     2.000E+00
      CO                  Enhanced by     1.500E+00
      CO2                 Enhanced by     2.000E+00
      C2H6                Enhanced by     3.000E+00
58. H+CH2O<=>HCO+H2                                   2.30E+10    1.1      3275.0
59. H+CH2OH(+M)<=>CH3OH(+M)                           1.80E+13    0.0         0.0
    Low pressure limit:  0.30000E+32 -0.48000E+01  0.33000E+04
    TROE centering:      0.76790E+00  0.33800E+03  0.18120E+04  0.50810E+04
      H2                  Enhanced by     2.000E+00
      H2O                 Enhanced by     6.000E+00
      CH4                 Enhanced by     2.000E+00
      CO                  Enhanced by     1.500E+00
      CO2                 Enhanced by     2.000E+00
      C2H6                Enhanced by     3.000E+00
```

```
60. H+CH2OH<=>H2+CH2O                                 2.00E+13    0.0          0.0
61. H+CH2OH<=>OH+CH3                                  1.20E+13    0.0          0.0
62. H+CH2OH<=>CH2(S)+H2O                              6.00E+12    0.0          0.0
63. H+CH3O(+M)<=>CH3OH(+M)                            5.00E+13    0.0          0.0
    Low pressure limit:  0.86000E+29 -0.40000E+01  0.30250E+04
    TROE centering:      0.89020E+00  0.14400E+03  0.28380E+04  0.45569E+05
       H2                Enhanced by    2.000E+00
       H2O               Enhanced by    6.000E+00
       CH4               Enhanced by    2.000E+00
       CO                Enhanced by    1.500E+00
       CO2               Enhanced by    2.000E+00
       C2H6              Enhanced by    3.000E+00
64. H+CH3O<=>H+CH2OH                                  3.40E+06    1.6          0.0
65. H+CH3O<=>H2+CH2O                                  2.00E+13    0.0          0.0
66. H+CH3O<=>OH+CH3                                   3.20E+13    0.0          0.0
67. H+CH3O<=>CH2(S)+H2O                               1.60E+13    0.0          0.0
68. H+CH3OH<=>CH2OH+H2                                1.70E+07    2.1       4870.0
69. H+CH3OH<=>CH3O+H2                                 4.20E+06    2.1       4870.0
70. H+C2H(+M)<=>C2H2(+M)                              1.00E+17   -1.0          0.0
    Low pressure limit:  0.37500E+34 -0.48000E+01  0.19000E+04
    TROE centering:      0.64640E+00  0.13200E+03  0.13150E+04  0.55660E+04
       H2                Enhanced by    2.000E+00
       H2O               Enhanced by    6.000E+00
       CH4               Enhanced by    2.000E+00
       CO                Enhanced by    1.500E+00
       CO2               Enhanced by    2.000E+00
       C2H6              Enhanced by    3.000E+00
       AR                Enhanced by    7.000E-01
71. H+C2H2(+M)<=>C2H3(+M)                             5.60E+12    0.0       2400.0
    Low pressure limit:  0.38000E+41 -0.72700E+01  0.72200E+04
    TROE centering:      0.75070E+00  0.98500E+02  0.13020E+04  0.41670E+04
       H2                Enhanced by    2.000E+00
       H2O               Enhanced by    6.000E+00
       CH4               Enhanced by    2.000E+00
       CO                Enhanced by    1.500E+00
       CO2               Enhanced by    2.000E+00
       C2H6              Enhanced by    3.000E+00
       AR                Enhanced by    7.000E-01
72. H+C2H3(+M)<=>C2H4(+M)                             6.08E+12    0.3        280.0
    Low pressure limit:  0.14000E+31 -0.38600E+01  0.33200E+04
    TROE centering:      0.78200E+00  0.20750E+03  0.26630E+04  0.60950E+04
       H2                Enhanced by    2.000E+00
       H2O               Enhanced by    6.000E+00
       CH4               Enhanced by    2.000E+00
       CO                Enhanced by    1.500E+00
       CO2               Enhanced by    2.000E+00
       C2H6              Enhanced by    3.000E+00
       AR                Enhanced by    7.000E-01
73. H+C2H3<=>H2+C2H2                                  3.00E+13    0.0          0.0
74. H+C2H4(+M)<=>C2H5(+M)                             1.08E+12    0.5       1820.0
    Low pressure limit:  0.12000E+43 -0.76200E+01  0.69700E+04
    TROE centering:      0.97530E+00  0.21000E+03  0.98400E+03  0.43740E+04
       H2                Enhanced by    2.000E+00
       H2O               Enhanced by    6.000E+00
       CH4               Enhanced by    2.000E+00
       CO                Enhanced by    1.500E+00
```

```
      CO2                 Enhanced by     2.000E+00
      C2H6                Enhanced by     3.000E+00
      AR                  Enhanced by     7.000E-01
75. H+C2H4<=>C2H3+H2                                  1.32E+06    2.5     12240.0
76. H+C2H5(+M)<=>C2H6(+M)                             5.21E+17   -1.0      1580.0
    Low pressure limit:  0.19900E+42 -0.70800E+01  0.66850E+04
    TROE centering:      0.84220E+00  0.12500E+03  0.22190E+04  0.68820E+04
      H2                  Enhanced by     2.000E+00
      H2O                 Enhanced by     6.000E+00
      CH4                 Enhanced by     2.000E+00
      CO                  Enhanced by     1.500E+00
      CO2                 Enhanced by     2.000E+00
      C2H6                Enhanced by     3.000E+00
      AR                  Enhanced by     7.000E-01
77. H+C2H5<=>H2+C2H4                                  2.00E+12    0.0         0.0
78. H+C2H6<=>C2H5+H2                                  1.15E+08    1.9      7530.0
79. H+HCCO<=>CH2(S)+CO                                1.00E+14    0.0         0.0
80. H+CH2CO<=>HCCO+H2                                 5.00E+13    0.0      8000.0
81. H+CH2CO<=>CH3+CO                                  1.13E+13    0.0      3428.0
82. H+HCCOH<=>H+CH2CO                                 1.00E+13    0.0         0.0
83. H2+CO(+M)<=>CH2O(+M)                              4.30E+07    1.5     79600.0
    Low pressure limit:  0.50700E+28 -0.34200E+01  0.84350E+05
    TROE centering:      0.93200E+00  0.19700E+03  0.15400E+04  0.10300E+05
      H2                  Enhanced by     2.000E+00
      H2O                 Enhanced by     6.000E+00
      CH4                 Enhanced by     2.000E+00
      CO                  Enhanced by     1.500E+00
      CO2                 Enhanced by     2.000E+00
      C2H6                Enhanced by     3.000E+00
      AR                  Enhanced by     7.000E-01
84. OH+H2<=>H+H2O                                     2.16E+08    1.5      3430.0
85. 2OH(+M)<=>H2O2(+M)                                7.40E+13   -0.4         0.0
    Low pressure limit:  0.23000E+19 -0.90000E+00 -0.17000E+04
    TROE centering:      0.73460E+00  0.94000E+02  0.17560E+04  0.51820E+04
      H2                  Enhanced by     2.000E+00
      H2O                 Enhanced by     6.000E+00
      CH4                 Enhanced by     2.000E+00
      CO                  Enhanced by     1.500E+00
      CO2                 Enhanced by     2.000E+00
      C2H6                Enhanced by     3.000E+00
      AR                  Enhanced by     7.000E-01
86. 2OH<=>O+H2O                                       3.57E+04    2.4     -2110.0
87. OH+HO2<=>O2+H2O                                   2.90E+13    0.0      -500.0
88. OH+H2O2<=>HO2+H2O                                 1.75E+12    0.0       320.0
    Declared duplicate reaction...
89. OH+H2O2<=>HO2+H2O                                 5.80E+14    0.0      9560.0
    Declared duplicate reaction...
90. OH+C<=>H+CO                                       5.00E+13    0.0         0.0
91. OH+CH<=>H+HCO                                     3.00E+13    0.0         0.0
92. OH+CH2<=>H+CH2O                                   2.00E+13    0.0         0.0
93. OH+CH2<=>CH+H2O                                   1.13E+07    2.0      3000.0
94. OH+CH2(S)<=>H+CH2O                                3.00E+13    0.0         0.0
95. OH+CH3(+M)<=>CH3OH(+M)                            6.30E+13    0.0         0.0
    Low pressure limit:  0.27000E+39 -0.63000E+01  0.31000E+04
    TROE centering:      0.21050E+00  0.83500E+02  0.53980E+04  0.83700E+04
      H2                  Enhanced by     2.000E+00
```

```
        H2O                 Enhanced by    6.000E+00
        CH4                 Enhanced by    2.000E+00
        CO                  Enhanced by    1.500E+00
        CO2                 Enhanced by    2.000E+00
        C2H6                Enhanced by    3.000E+00
 96. OH+CH3<=>CH2+H2O                                  5.60E+07    1.6      5420.0
 97. OH+CH3<=>CH2(S)+H2O                               2.50E+13    0.0         0.0
 98. OH+CH4<=>CH3+H2O                                  1.00E+08    1.6      3120.0
 99. OH+CO<=>H+CO2                                     4.76E+07    1.2        70.0
100. OH+HCO<=>H2O+CO                                   5.00E+13    0.0         0.0
101. OH+CH2O<=>HCO+H2O                                 3.43E+09    1.2      -447.0
102. OH+CH2OH<=>H2O+CH2O                               5.00E+12    0.0         0.0
103. OH+CH3O<=>H2O+CH2O                                5.00E+12    0.0         0.0
104. OH+CH3OH<=>CH2OH+H2O                              1.44E+06    2.0      -840.0
105. OH+CH3OH<=>CH3O+H2O                               6.30E+06    2.0      1500.0
106. OH+C2H<=>H+HCCO                                   2.00E+13    0.0         0.0
107. OH+C2H2<=>H+CH2CO                                 2.18E-04    4.5     -1000.0
108. OH+C2H2<=>H+HCCOH                                 5.04E+05    2.3     13500.0
109. OH+C2H2<=>C2H+H2O                                 3.37E+07    2.0     14000.0
110. OH+C2H2<=>CH3+CO                                  4.83E-04    4.0     -2000.0
111. OH+C2H3<=>H2O+C2H2                                5.00E+12    0.0         0.0
112. OH+C2H4<=>C2H3+H2O                                3.60E+06    2.0      2500.0
113. OH+C2H6<=>C2H5+H2O                                3.54E+06    2.1       870.0
114. OH+CH2CO<=>HCCO+H2O                               7.50E+12    0.0      2000.0
115. 2HO2<=>O2+H2O2                                    1.30E+11    0.0     -1630.0
     Declared duplicate reaction...
116. 2HO2<=>O2+H2O2                                    4.20E+14    0.0     12000.0
     Declared duplicate reaction...
117. HO2+CH2<=>OH+CH2O                                 2.00E+13    0.0         0.0
118. HO2+CH3<=>O2+CH4                                  1.00E+12    0.0         0.0
119. HO2+CH3<=>OH+CH3O                                 2.00E+13    0.0         0.0
120. HO2+CO<=>OH+CO2                                   1.50E+14    0.0     23600.0
121. HO2+CH2O<=>HCO+H2O2                               1.00E+12    0.0      8000.0
122. C+O2<=>O+CO                                       5.80E+13    0.0       576.0
123. C+CH2<=>H+C2H                                     5.00E+13    0.0         0.0
124. C+CH3<=>H+C2H2                                    5.00E+13    0.0         0.0
125. CH+O2<=>O+HCO                                     3.30E+13    0.0         0.0
126. CH+H2<=>H+CH2                                     1.11E+08    1.8      1670.0
127. CH+H2O<=>H+CH2O                                   1.71E+13    0.0      -755.0
128. CH+CH2<=>H+C2H2                                   4.00E+13    0.0         0.0
129. CH+CH3<=>H+C2H3                                   3.00E+13    0.0         0.0
130. CH+CH4<=>H+C2H4                                   6.00E+13    0.0         0.0
131. CH+CO(+M)<=>HCCO(+M)                              5.00E+13    0.0         0.0
     Low pressure limit:  0.26900E+29 -0.37400E+01  0.19360E+04
     TROE centering:      0.57570E+00  0.23700E+03  0.16520E+04  0.50690E+04
        H2                  Enhanced by    2.000E+00
        H2O                 Enhanced by    6.000E+00
        CH4                 Enhanced by    2.000E+00
        CO                  Enhanced by    1.500E+00
        CO2                 Enhanced by    2.000E+00
        C2H6                Enhanced by    3.000E+00
        AR                  Enhanced by    7.000E-01
132. CH+CO2<=>HCO+CO                                   3.40E+12    0.0       690.0
133. CH+CH2O<=>H+CH2CO                                 9.46E+13    0.0      -515.0
134. CH+HCCO<=>CO+C2H2                                 5.00E+13    0.0         0.0
135. CH2+O2<=>OH+HCO                                   1.32E+13    0.0      1500.0
```

```
136. CH2+H2<=>H+CH3                                    5.00E+05    2.0      7230.0
137. 2CH2<=>H2+C2H2                                    3.20E+13    0.0         0.0
138. CH2+CH3<=>H+C2H4                                  4.00E+13    0.0         0.0
139. CH2+CH4<=>2CH3                                    2.46E+06    2.0      8270.0
140. CH2+CO(+M)<=>CH2CO(+M)                            8.10E+11    0.5      4510.0
     Low pressure limit:  0.26900E+34 -0.51100E+01  0.70950E+04
     TROE centering:      0.59070E+00  0.27500E+03  0.12260E+04  0.51850E+04
        H2                Enhanced by    2.000E+00
        H2O               Enhanced by    6.000E+00
        CH4               Enhanced by    2.000E+00
        CO                Enhanced by    1.500E+00
        CO2               Enhanced by    2.000E+00
        C2H6              Enhanced by    3.000E+00
        AR                Enhanced by    7.000E-01
141. CH2+HCCO<=>C2H3+CO                                3.00E+13    0.0         0.0
142. CH2(S)+N2<=>CH2+N2                                1.50E+13    0.0       600.0
143. CH2(S)+AR<=>CH2+AR                                9.00E+12    0.0       600.0
144. CH2(S)+O2<=>H+OH+CO                               2.80E+13    0.0         0.0
145. CH2(S)+O2<=>CO+H2O                                1.20E+13    0.0         0.0
146. CH2(S)+H2<=>CH3+H                                 7.00E+13    0.0         0.0
147. CH2(S)+H2O(+M)<=>CH3OH(+M)                        2.00E+13    0.0         0.0
     Low pressure limit:  0.27000E+39 -0.63000E+01  0.31000E+04
     TROE centering:      0.15070E+00  0.13400E+03  0.23830E+04  0.72650E+04
        H2                Enhanced by    2.000E+00
        H2O               Enhanced by    6.000E+00
        CH4               Enhanced by    2.000E+00
        CO                Enhanced by    1.500E+00
        CO2               Enhanced by    2.000E+00
        C2H6              Enhanced by    3.000E+00
148. CH2(S)+H2O<=>CH2+H2O                              3.00E+13    0.0         0.0
149. CH2(S)+CH3<=>H+C2H4                               1.20E+13    0.0      -570.0
150. CH2(S)+CH4<=>2CH3                                 1.60E+13    0.0      -570.0
151. CH2(S)+CO<=>CH2+CO                                9.00E+12    0.0         0.0
152. CH2(S)+CO2<=>CH2+CO2                              7.00E+12    0.0         0.0
153. CH2(S)+CO2<=>CO+CH2O                              1.40E+13    0.0         0.0
154. CH2(S)+C2H6<=>CH3+C2H5                            4.00E+13    0.0      -550.0
155. CH3+O2<=>O+CH3O                                   2.68E+13    0.0     28800.0
156. CH3+O2<=>OH+CH2O                                  3.60E+10    0.0      8940.0
157. CH3+H2O2<=>HO2+CH4                                2.45E+04    2.5      5180.0
158. 2CH3(+M)<=>C2H6(+M)                               2.12E+16   -1.0       620.0
     Low pressure limit:  0.17700E+51 -0.96700E+01  0.62200E+04
     TROE centering:      0.53250E+00  0.15100E+03  0.10380E+04  0.49700E+04
        H2                Enhanced by    2.000E+00
        H2O               Enhanced by    6.000E+00
        CH4               Enhanced by    2.000E+00
        CO                Enhanced by    1.500E+00
        CO2               Enhanced by    2.000E+00
        C2H6              Enhanced by    3.000E+00
        AR                Enhanced by    7.000E-01
159. 2CH3<=>H+C2H5                                     4.99E+12    0.1     10600.0
160. CH3+HCO<=>CH4+CO                                  2.65E+13    0.0         0.0
161. CH3+CH2O<=>HCO+CH4                                3.32E+03    2.8      5860.0
162. CH3+CH3OH<=>CH2OH+CH4                             3.00E+07    1.5      9940.0
163. CH3+CH3OH<=>CH3O+CH4                              1.00E+07    1.5      9940.0
164. CH3+C2H4<=>C2H3+CH4                               2.27E+05    2.0      9200.0
165. CH3+C2H6<=>C2H5+CH4                               6.14E+06    1.7     10450.0
```

```
166. HCO+H2O<=>H+CO+H2O                                 2.24E+18   -1.0     17000.0
167. HCO+M<=>H+CO+M                                     1.87E+17   -1.0     17000.0
        H2                  Enhanced by     2.000E+00
        H2O                 Enhanced by     0.000E+00
        CH4                 Enhanced by     2.000E+00
        CO                  Enhanced by     1.500E+00
        CO2                 Enhanced by     2.000E+00
        C2H6                Enhanced by     3.000E+00
168. HCO+O2<=>HO2+CO                                    7.60E+12    0.0       400.0
169. CH2OH+O2<=>HO2+CH2O                                1.80E+13    0.0       900.0
170. CH3O+O2<=>HO2+CH2O                                 4.28E-13    7.6     -3530.0
171. C2H+O2<=>HCO+CO                                    5.00E+13    0.0      1500.0
172. C2H+H2<=>H+C2H2                                    4.07E+05    2.4       200.0
173. C2H3+O2<=>HCO+CH2O                                 3.98E+12    0.0      -240.0
174. C2H4(+M)<=>H2+C2H2(+M)                             8.00E+12    0.4     88770.0
     Low pressure limit:  0.70000E+51 -0.93100E+01  0.99860E+05
     TROE centering:      0.73450E+00  0.18000E+03  0.10350E+04  0.54170E+04
        H2                  Enhanced by     2.000E+00
        H2O                 Enhanced by     6.000E+00
        CH4                 Enhanced by     2.000E+00
        CO                  Enhanced by     1.500E+00
        CO2                 Enhanced by     2.000E+00
        C2H6                Enhanced by     3.000E+00
        AR                  Enhanced by     7.000E-01
175. C2H5+O2<=>HO2+C2H4                                 8.40E+11    0.0      3875.0
176. HCCO+O2<=>OH+2CO                                   1.60E+12    0.0       854.0
177. 2HCCO<=>2CO+C2H2                                   1.00E+13    0.0         0.0
178. N+NO<=>N2+O                                        3.50E+13    0.0       330.0
179. N+O2<=>NO+O                                        2.65E+12    0.0      6400.0
180. N+OH<=>NO+H                                        7.33E+13    0.0      1120.0
181. N2O+O<=>N2+O2                                      1.40E+12    0.0     10810.0
182. N2O+O<=>2NO                                        2.90E+13    0.0     23150.0
183. N2O+H<=>N2+OH                                      4.40E+14    0.0     18880.0
184. N2O+OH<=>N2+HO2                                    2.00E+12    0.0     21060.0
185. N2O(+M)<=>N2+O(+M)                                 1.30E+11    0.0     59620.0
     Low pressure limit:  0.62000E+15  0.00000E+00  0.56100E+05
        H2                  Enhanced by     2.000E+00
        H2O                 Enhanced by     6.000E+00
        CH4                 Enhanced by     2.000E+00
        CO                  Enhanced by     1.500E+00
        CO2                 Enhanced by     2.000E+00
        C2H6                Enhanced by     3.000E+00
        AR                  Enhanced by     7.000E-01
186. HO2+NO<=>NO2+OH                                    2.11E+12    0.0      -480.0
187. NO+O+M<=>NO2+M                                     1.06E+20   -1.4         0.0
        H2                  Enhanced by     2.000E+00
        H2O                 Enhanced by     6.000E+00
        CH4                 Enhanced by     2.000E+00
        CO                  Enhanced by     1.500E+00
        CO2                 Enhanced by     2.000E+00
        C2H6                Enhanced by     3.000E+00
        AR                  Enhanced by     7.000E-01
188. NO2+O<=>NO+O2                                      3.90E+12    0.0      -240.0
189. NO2+H<=>NO+OH                                      1.32E+14    0.0       360.0
190. NH+O<=>NO+H                                        5.00E+13    0.0         0.0
191. NH+H<=>N+H2                                        3.20E+13    0.0       330.0
```

192.	NH+OH<=>HNO+H			2.00E+13	0.0	0.0
193.	NH+OH<=>N+H2O			2.00E+09	1.2	0.0
194.	NH+O2<=>HNO+O			4.61E+05	2.0	6500.0
195.	NH+O2<=>NO+OH			1.28E+06	1.5	100.0
196.	NH+N<=>N2+H			1.50E+13	0.0	0.0
197.	NH+H2O<=>HNO+H2			2.00E+13	0.0	13850.0
198.	NH+NO<=>N2+OH			2.16E+13	−0.2	0.0
199.	NH+NO<=>N2O+H			4.16E+14	−0.5	0.0
200.	NH2+O<=>OH+NH			7.00E+12	0.0	0.0
201.	NH2+O<=>H+HNO			4.60E+13	0.0	0.0
202.	NH2+H<=>NH+H2			4.00E+13	0.0	3650.0
203.	NH2+OH<=>NH+H2O			9.00E+07	1.5	−460.0
204.	NNH<=>N2+H			3.30E+08	0.0	0.0
205.	NNH+M<=>N2+H+M			1.30E+14	−0.1	4980.0
	H2	Enhanced by	2.000E+00			
	H2O	Enhanced by	6.000E+00			
	CH4	Enhanced by	2.000E+00			
	CO	Enhanced by	1.500E+00			
	CO2	Enhanced by	2.000E+00			
	C2H6	Enhanced by	3.000E+00			
	AR	Enhanced by	7.000E−01			
206.	NNH+O2<=>HO2+N2			5.00E+12	0.0	0.0
207.	NNH+O<=>OH+N2			2.50E+13	0.0	0.0
208.	NNH+O<=>NH+NO			7.00E+13	0.0	0.0
209.	NNH+H<=>H2+N2			5.00E+13	0.0	0.0
210.	NNH+OH<=>H2O+N2			2.00E+13	0.0	0.0
211.	NNH+CH3<=>CH4+N2			2.50E+13	0.0	0.0
212.	H+NO+M<=>HNO+M			8.95E+19	−1.3	740.0
	H2	Enhanced by	2.000E+00			
	H2O	Enhanced by	6.000E+00			
	CH4	Enhanced by	2.000E+00			
	CO	Enhanced by	1.500E+00			
	CO2	Enhanced by	2.000E+00			
	C2H6	Enhanced by	3.000E+00			
	AR	Enhanced by	7.000E−01			
213.	HNO+O<=>NO+OH			2.50E+13	0.0	0.0
214.	HNO+H<=>H2+NO			4.50E+11	0.7	660.0
215.	HNO+OH<=>NO+H2O			1.30E+07	1.9	−950.0
216.	HNO+O2<=>HO2+NO			1.00E+13	0.0	13000.0
217.	CN+O<=>CO+N			7.70E+13	0.0	0.0
218.	CN+OH<=>NCO+H			4.00E+13	0.0	0.0
219.	CN+H2O<=>HCN+OH			8.00E+12	0.0	7460.0
220.	CN+O2<=>NCO+O			6.14E+12	0.0	−440.0
221.	CN+H2<=>HCN+H			2.10E+13	0.0	4710.0
222.	NCO+O<=>NO+CO			2.35E+13	0.0	0.0
223.	NCO+H<=>NH+CO			5.40E+13	0.0	0.0
224.	NCO+OH<=>NO+H+CO			2.50E+12	0.0	0.0
225.	NCO+N<=>N2+CO			2.00E+13	0.0	0.0
226.	NCO+O2<=>NO+CO2			2.00E+12	0.0	20000.0
227.	NCO+M<=>N+CO+M			8.80E+16	−0.5	48000.0
	H2	Enhanced by	2.000E+00			
	H2O	Enhanced by	6.000E+00			
	CH4	Enhanced by	2.000E+00			
	CO	Enhanced by	1.500E+00			
	CO2	Enhanced by	2.000E+00			
	C2H6	Enhanced by	3.000E+00			

	AR	Enhanced by	7.000E−01			
228.	NCO+NO<=>N2O+CO			2.85E+17	−1.5	740.0
229.	NCO+NO<=>N2+CO2			5.70E+18	−2.0	800.0
230.	HCN+M<=>H+CN+M			1.04E+29	−3.3	126600.0
	H2	Enhanced by	2.000E+00			
	H2O	Enhanced by	6.000E+00			
	CH4	Enhanced by	2.000E+00			
	CO	Enhanced by	1.500E+00			
	CO2	Enhanced by	2.000E+00			
	C2H6	Enhanced by	3.000E+00			
	AR	Enhanced by	7.000E−01			
231.	HCN+O<=>NCO+H			1.11E+04	2.6	4980.0
232.	HCN+O<=>NH+CO			2.77E+03	2.6	4980.0
233.	HCN+O<=>CN+OH			2.13E+09	1.6	26600.0
234.	HCN+OH<=>HOCN+H			1.10E+06	2.0	13370.0
235.	HCN+OH<=>HNCO+H			4.40E+03	2.3	6400.0
236.	HCN+OH<=>NH2+CO			1.60E+02	2.6	9000.0
237.	H+HCN+M<=>H2CN+M			1.40E+26	−3.4	1900.0
	H2	Enhanced by	2.000E+00			
	H2O	Enhanced by	6.000E+00			
	CH4	Enhanced by	2.000E+00			
	CO	Enhanced by	1.500E+00			
	CO2	Enhanced by	2.000E+00			
	C2H6	Enhanced by	3.000E+00			
	AR	Enhanced by	7.000E−01			
238.	H2CN+N<=>N2+CH2			6.00E+13	0.0	400.0
239.	C+N2<=>CN+N			6.30E+13	0.0	46020.0
240.	CH+N2<=>HCN+N			2.86E+08	1.1	20400.0
241.	CH+N2(+M)<=>HCNN(+M)			3.10E+12	0.1	0.0
	Low pressure limit:	0.13000E+26	−0.31600E+01	0.74000E+03		
	TROE centering:	0.66700E+00	0.23500E+03	0.21170E+04	0.45360E+04	
	H2	Enhanced by	2.000E+00			
	H2O	Enhanced by	6.000E+00			
	CH4	Enhanced by	2.000E+00			
	CO	Enhanced by	1.500E+00			
	CO2	Enhanced by	2.000E+00			
	C2H6	Enhanced by	3.000E+00			
	AR	Enhanced by	7.000E−01			
242.	CH2+N2<=>HCN+NH			1.00E+13	0.0	74000.0
243.	CH2(S)+N2<=>NH+HCN			1.00E+11	0.0	65000.0
244.	C+NO<=>CN+O			1.90E+13	0.0	0.0
245.	C+NO<=>CO+N			2.90E+13	0.0	0.0
246.	CH+NO<=>HCN+O			5.00E+13	0.0	0.0
247.	CH+NO<=>H+NCO			2.00E+13	0.0	0.0
248.	CH+NO<=>N+HCO			3.00E+13	0.0	0.0
249.	CH2+NO<=>H+HNCO			3.10E+17	−1.4	1270.0
250.	CH2+NO<=>OH+HCN			2.90E+14	−0.7	760.0
251.	CH2+NO<=>H+HCNO			3.80E+13	−0.4	580.0
252.	CH2(S)+NO<=>H+HNCO			3.10E+17	−1.4	1270.0
253.	CH2(S)+NO<=>OH+HCN			2.90E+14	−0.7	760.0
254.	CH2(S)+NO<=>H+HCNO			3.80E+13	−0.4	580.0
255.	CH3+NO<=>HCN+H2O			9.60E+13	0.0	28800.0
256.	CH3+NO<=>H2CN+OH			1.00E+12	0.0	21750.0
257.	HCNN+O<=>CO+H+N2			2.20E+13	0.0	0.0
258.	HCNN+O<=>HCN+NO			2.00E+12	0.0	0.0
259.	HCNN+O2<=>O+HCO+N2			1.20E+13	0.0	0.0

260.	HCNN+OH<=>H+HCO+N2		1.20E+13	0.0	0.0
261.	HCNN+H<=>CH2+N2		1.00E+14	0.0	0.0
262.	HNCO+O<=>NH+CO2		9.80E+07	1.4	8500.0
263.	HNCO+O<=>HNO+CO		1.50E+08	1.6	44000.0
264.	HNCO+O<=>NCO+OH		2.20E+06	2.1	11400.0
265.	HNCO+H<=>NH2+CO		2.25E+07	1.7	3800.0
266.	HNCO+H<=>H2+NCO		1.05E+05	2.5	13300.0
267.	HNCO+OH<=>NCO+H2O		4.65E+12	0.0	6850.0
268.	HNCO+OH<=>NH2+CO2		1.55E+12	0.0	6850.0
269.	HNCO+M<=>NH+CO+M		1.18E+16	0.0	84720.0
	H2	Enhanced by 2.000E+00			
	H2O	Enhanced by 6.000E+00			
	CH4	Enhanced by 2.000E+00			
	CO	Enhanced by 1.500E+00			
	CO2	Enhanced by 2.000E+00			
	C2H6	Enhanced by 3.000E+00			
	AR	Enhanced by 7.000E-01			
270.	HCNO+H<=>H+HNCO		2.10E+15	-0.7	2850.0
271.	HCNO+H<=>OH+HCN		2.70E+11	0.2	2120.0
272.	HCNO+H<=>NH2+CO		1.70E+14	-0.8	2890.0
273.	HOCN+H<=>H+HNCO		2.00E+07	2.0	2000.0
274.	HCCO+NO<=>HCNO+CO		2.35E+13	0.0	0.0
275.	CH3+N<=>H2CN+H		6.10E+14	-0.3	290.0
276.	CH3+N<=>HCN+H2		3.70E+12	0.1	-90.0
277.	NH3+H<=>NH2+H2		5.40E+05	2.4	9915.0
278.	NH3+OH<=>NH2+H2O		5.00E+07	1.6	955.0
279.	NH3+O<=>NH2+OH		9.40E+06	1.9	6460.0
280.	TiCL4+M=TiCL3+CL+M		5.40E+18	0.0	80236.8
281.	TiCL3+M=TiCL2+CL+M		7.70E+18	0.0	92415.6
282.	TiCL2+M=TiCL+CL+M		3.20E+17	0.0	122026.8
283.	Ti+CL=TiCL		1.00E+13	0.0	0.0
284.	TiCL2+CL2=TiCL4		1.00E+13	0.0	0.0
285.	TiCL+CL2=TiCL3		1.00E+13	0.0	0.0
286.	TiCL3+CL2=TiCL4+CL		1.00E+13	0.0	0.0
287.	TiCL2+CL2=TiCL3+CL		1.00E+13	0.0	0.0
288.	TiCL+CL2=TiCL2+CL		1.00E+13	0.0	0.0
289.	Ti+CL2=TiCL+CL		1.00E+13	0.0	0.0
290.	TiCL4+TiCL=TiCL3+TiCL2		1.00E+13	0.0	0.0
291.	TiCL4+Ti=TiCL3+TiCL		1.00E+13	0.0	0.0
292.	TiCL2+TiCL=TiCL3+Ti		1.00E+13	0.0	0.0
293.	TiCL+TiCL=TiCL2+Ti		1.00E+13	0.0	0.0
294.	CL2+TiO2CL2=CL+TiO2CL3		1.00E+13	0.0	0.0
295.	CL2+Ti2O2CL3=CL+Ti2O2CL4		1.00E+13	0.0	0.0
296.	2TiCL3=TiCL2+TiCL4		9.60E+12	0.0	8358.0
297.	TiCL3+TiCL=2TiCL2		1.00E+13	0.0	0.0
298.	TiCL3+O2(+M)<=>TiO2CL3(+M)		1.92E+35	-6.6	9890.9
	Low pressure limit:	0.10596E+37 -0.63189E+01 0.00000E+00			
	TROE centering:	0.11832E+00 0.26931E+02 0.10000E+06 0.52193E+04			
299.	TiOCL3+CLO=TiO2CL3+CL		1.00E+13	0.0	0.0
300.	TiOCL2+CL=TiOCL3		1.00E+13	0.0	0.0
301.	TiOCL3+O=TiO2CL3		1.00E+13	0.0	0.0
302.	TiO2CL2+CL=TiO2CL3		1.00E+13	0.0	0.0
303.	TiO2CL2+CL=TiCL3+O2		1.00E+13	0.0	0.0
304.	TiOCL3+O=TiCL3+O2		1.00E+13	0.0	0.0
305.	TiCL2+O2=TiOCL2+O		1.00E+13	0.0	0.0
306.	TiO2CL2+O=TiOCL2+O2		1.00E+13	0.0	0.0

307.	TiCL3+CLO=TiCL4+O	1.00E+13	0.0	0.0
308.	TiCL2+CLO=TiCL3+O	1.00E+13	0.0	0.0
309.	TiCL+CLO=TiCL2+O	1.00E+13	0.0	0.0
310.	Ti+CLO=TiCL+O	1.00E+13	0.0	0.0
311.	TiCL3+O=TiOCL2+CL	1.00E+13	0.0	0.0
312.	TiCL3+CL2O=TiCL4+CLO	1.00E+13	0.0	0.0
313.	TiCL3+CLO=TiOCL3+CL	1.00E+13	0.0	0.0
314.	TiO2CL2+CL=TiOCL2+CLO	1.00E+13	0.0	0.0
315.	O+O2+M=O3+M	1.84E+21	−2.8	0.0
316.	CLOO+M=>CL+O2+M	1.69E+14	0.0	3613.0
317.	CL+O2+M=>CLOO+M	8.68E+21	−2.9	0.0
318.	CL+O3=CLO+O2	1.75E+13	0.0	520.6
319.	CL2O+CL=CL2+CLO	3.73E+13	0.0	−260.3
320.	CL+O2=CLO+O	8.79E+14	0.0	55043.4
321.	O+CL2=CLO+CL	4.46E+12	0.0	3278.7
322.	2CL+M=CL2+M	2.23E+14	0.0	−1798.2
323.	2TiOCL2=Ti2O2CL4	1.00E+13	0.0	0.0
324.	TiO2CL2+TiCL3=Ti2O2CL4+CL	1.00E+13	0.0	0.0
325.	TiO2CL2+TiOCL2=Ti2O3CL3+CL	1.00E+13	0.0	0.0
326.	TiOCL2+TiOCL3=Ti2O2CL4+CL	1.00E+13	0.0	0.0
327.	Ti2O3CL3+TiOCL2=Ti3O4CL4+CL	1.00E+13	0.0	0.0
328.	Ti2O3CL2+CL=Ti2O3CL3	1.00E+13	0.0	0.0
329.	Ti2O2CL3+TiCL4=Ti2O2CL4+TiCL3	1.00E+13	0.0	0.0
330.	TiO2CL3+TiCL3=Ti2O2CL6	1.00E+13	0.0	0.0
331.	2TiOCL3=Ti2O2CL6	1.00E+13	0.0	0.0
332.	CL2+Ti2O2CL5=CL+Ti2O2CL6	1.00E+13	0.0	0.0
333.	CL+Ti2O2CL5=CL2+Ti2O2CL4	1.00E+13	0.0	0.0
334.	TiCL3+Ti2O2CL5=TiCL4+Ti2O2CL4	1.00E+13	0.0	0.0
335.	TiCL3+Ti2O2CL6=TiCL4+Ti2O2CL5	1.00E+13	0.0	0.0
336.	TiCL2OCL=TiOCL2+CL	1.00E+13	0.0	0.0
337.	TiCL2OCL+CL=TiCL3+CLO	1.00E+13	0.0	0.0
338.	TiCL2OCL+CL=TiOCL3+CL	1.00E+13	0.0	0.0
339.	TiCL2OCL+CL=CL2+TiOCL2	1.00E+13	0.0	0.0
340.	CLOO+CL=CL2+O2	1.39E+14	0.0	0.0
341.	TiCL3+CLOO=TiCL4+O2	1.00E+13	0.0	0.0
342.	TiCL4+O3=TiCL3+CLO+O2	1.00E+13	0.0	53992.1
343.	O3+O=2O2	5.47E+12	0.0	4156.9
344.	TiOCL3+O3=TiO2CL3+O2	1.00E+13	0.0	0.0
345.	TiO2CL2+CLOO=TiO2CL3+O2	1.00E+13	0.0	0.0
346.	Ti2O2CL4+Ti3O4CL4=>Ti5O6CL8	1.00E+13	0.0	0.0
347.	Ti2O2CL6+Ti3O4CL4=>Ti5O6CL8+CL2	1.00E+13	0.0	0.0
348.	Ti2O2CL5+Ti3O4CL4=>Ti5O6CL8+CL	1.00E+13	0.0	0.0
349.	Ti5O6CL8+2O2=>5TiO2(ru)+4CL2	1.00E+25	0.0	0.0
350.	CL2<=>2CL	1.85E+12	0.0	57980.0
351.	CH3CL<=>CH3+CL	1.00E+16	0.0	84370.0
352.	CH2CL2<=>CH2CL+CL	1.00E+16	0.0	81140.0
353.	CHCL2–CH2CL<=>CHCL2+CH2CL	1.00E+15	0.0	88350.0
354.	CH2CL–CH2CL<=>2CH2CL	1.00E+17	0.0	90060.0
355.	CHCL3<=>CHCL2+CL	1.00E+16	0.0	77630.0
356.	CHCL2–CHCL2<=>2CHCL2	1.00E+15	0.0	82430.0
357.	CCL3–CCL3<=>2CCL3	1.00E+15	0.0	71400.0
358.	CCL3–CH2CL<=>CCL3+CH2CL	1.00E+15	0.0	82670.0
359.	CCL3–CHCL2<=>CCL3+CHCL2	1.00E+15	0.0	75860.0
360.	CCL4<=>CCL3+CL	1.00E+16	0.0	70930.0
361.	CH2CL–CH2<=>C2H4+CL	1.00E+14	0.0	20330.0
362.	CH2CL–CCL2<=>CCL2–CH2+CL	1.00E+14	0.0	25850.0

363.	CHCL2–CHCL<=>tCHCL–CHCL+CL	1.00E+14	0.0	21630.0
364.	CHCL2–CHCL<=>cCHCL–CHCL+CL	1.00E+14	0.0	21080.0
365.	CH2CL–CHCL<=>CHCL–CH2+CL	1.00E+14	0.0	22890.0
366.	CHCL2–CH2<=>CHCL–CH2+CL	1.00E+14	0.0	19190.0
367.	CHCL2–CCL2<=>CCL2–CHCL+CL	1.00E+14	0.0	21220.0
368.	CCL3–CCL2<=>CCL2–CCL2+CL	1.00E+14	0.0	19350.0
369.	CCL3–CH2<=>CCL2–CH2+CL	1.00E+14	0.0	17470.0
370.	CCL3–CHCL<=>CCL2–CHCL+CL	1.00E+14	0.0	18450.0
371.	cCHCL–CHCL+CL<=>cCHCL–CCL+HCL	1.00E+13	0.0	1960.0
372.	tCHCL–CHCL+CL<=>tCHCL–CCL+HCL	1.00E+13	0.0	1510.0
373.	CH3CL+CL<=>CH2CL+HCL	1.00E+13	0.0	460.0
374.	CH3CL+CL<=>CH3+CL2	1.00E+14	0.0	25620.0
375.	CH4+CL<=>CH3+HCL	1.00E+13	0.0	2110.0
376.	CH4+CH2CL<=>CH3+CH3CL	3.00E+11	0.0	15800.0
377.	CH2CL2+CL<=>CHCL2+HCL	1.00E+13	0.0	460.0
378.	CH2CL2+CH3<=>CHCL2+CH4	3.00E+11	0.0	11000.0
379.	CH2CL2+CH2CL<=>CHCL2+CH3CL	3.00E+11	0.0	11000.0
380.	CH2CL2+CL<=>CH2CL+CL2	1.00E+14	0.0	22390.0
381.	CH2CL2+CH3<=>CH2CL+CH3CL	3.00E+11	0.0	11000.0
382.	CHCL2–CH2CL+CL<=>CHCL2–CHCL+HCL	1.00E+13	0.0	460.0
383.	CHCL2–CH2CL+CL<=>CH2CL–CCL2+HCL	1.00E+13	0.0	460.0
384.	CH2CL–CH2CL+CL<=>CH2CL–CHCL+HCL	1.00E+13	0.0	460.0
385.	CHCL3+CL<=>CCL3+HCL	1.00E+13	0.0	460.0
386.	CHCL3+CH3<=>CCL3+CH4	3.00E+11	0.0	11000.0
387.	CHCL3+CH2CL<=>CCL3+CH3CL	3.00E+11	0.0	11000.0
388.	CHCL3+CHCL2<=>CCL3+CH2CL2	3.00E+11	0.0	11000.0
389.	CHCL3+CL<=>CHCL2+CL2	1.00E+14	0.0	18880.0
390.	CHCL3+CH3<=>CHCL2+CH3CL	3.00E+11	0.0	11000.0
391.	CHCL3+CH2CL<=>CHCL2+CH2CL2	3.00E+11	0.0	11000.0
392.	CHCL2–CHCL2+CL<=>CHCL2–CCL2+HCL	1.00E+13	0.0	460.0
393.	CCL4+CL<=>CCL3+CL2	1.00E+14	0.0	12180.0
394.	CCL4+CH3<=>CCL3+CH3CL	3.00E+11	0.0	11000.0
395.	CCL4+CH2CL<=>CCL3+CH2CL2	3.00E+11	0.0	11000.0
396.	CCL4+CHCL2<=>CCL3+CHCL3	3.00E+11	0.0	11000.0
397.	CCL2–CCL2+CL2<=>CCL3–CCL2+CL	1.00E+13	0.0	39860.0
398.	CCL2–CHCL+CL2<=>CHCL2–CCL2+CL	1.00E+13	0.0	37990.0
399.	CCL2–CHCL+CL2<=>CCL3–CHCL+CL	1.00E+13	0.0	40760.0
400.	cCHCL–CHCL+CL2<=>CHCL2–CHCL+CL	1.00E+13	0.0	37480.0
401.	tCHCL–CHCL+CL2<=>CHCL2–CHCL+CL	1.00E+13	0.0	37380.0
402.	CCL2–CH2+CL2<=>CH2CL–CCL2+CL	1.00E+13	0.0	34560.0
403.	CCL2–CH2+CL2<=>CCL3–CH2+CL	1.00E+13	0.0	42940.0
404.	CHCL–CH2+CL2<=>CH2CL–CHCL+CL	1.00E+13	0.0	37320.0
405.	CHCL–CH2+CL2<=>CHCL2–CH2+CL	1.00E+13	0.0	41020.0
406.	CHCL–CH2+CH2CL–CH2CL<=>CHCL2–CH2+CH2CL–CH2	3.00E+14	0.0	66400.0
407.	CHCL–CH2+CHCL2–CH2CL<=>CHCL2–CH2+CHCL2–CH2	3.00E+14	0.0	64740.0
408.	CHCL–CH2+CCL3–CH3<=>CHCL2–CH2+CH3–CCL2	3.00E+14	0.0	56660.0
409.	CHCL–CH2+CCL3–CH2CL<=>CHCL2–CH2+CCL3–CH2	3.00E+14	0.0	61440.0
410.	CHCL–CH2+CCL3–CH2CL<=>CHCL2–CH2+CH2CL–CCL2	3.00E+14	0.0	53060.0
411.	CHCL–CH2+CCL3–CHCL2<=>CHCL2–CH2+CCL3–CHCL	3.00E+14	0.0	55340.0
412.	CHCL–CH2+CCL3–CHCL2<=>CHCL2–CH2+CHCL2–CCL2	3.00E+14	0.0	52570.0
413.	CHCL–CH2+CCL3–CCL3<=>CHCL2–CH2+CCL3–CCL2	3.00E+14	0.0	54180.0
414.	CHCL–CH2+CCL4<=>CHCL2–CH2+CCL3	3.00E+14	0.0	52740.0
415.	CHCL–CH2+CHCL2–CHCL2<=>CHCL2–CH2+CHCL2–CHCL	3.00E+14	0.0	56830.0
416.	CHCL–CH2+CH2CL–CH2CL<=>CH2CL–CHCL+CH2CL–CH2	3.00E+14	0.0	62700.0
417.	CHCL–CH2+CHCL2–CH2CL<=>CH2CL–CHCL+CHCL2–CH2	3.00E+14	0.0	61040.0
418.	CHCL–CH2+CHCL2–CH2CL<=>CH2CL–CHCL+CH2CL–CHCL	3.00E+14	0.0	57340.0

419. CHCL–CH2+CCL3–CH3<=>CH2CL–CHCL+CH3–CCL2 3.00E+14 0.0 52960.0
420. CHCL–CH2+CCL3–CH2CL<=>CH2CL–CHCL+CCL3–CH2 3.00E+14 0.0 57740.0
421. CHCL–CH2+CCL3–CH2CL<=>CH2CL–CHCL+CH2CL–CCL2 3.00E+14 0.0 49360.0
422. CHCL–CH2+CCL3–CHCL2<=>CH2CL–CHCL+CCL3–CHCL 3.00E+14 0.0 51640.0
423. CHCL–CH2+CCL3–CHCL2<=>CH2CL–CHCL+CHCL2–CCL2 3.00E+14 0.0 48870.0
424. CHCL–CH2+CCL3–CCL3<=>CH2CL–CHCL+CCL3–CCL2 3.00E+14 0.0 50480.0
425. CHCL–CH2+CCL4<=>CH2CL–CHCL+CCL3 3.00E+14 0.0 49040.0
426. CHCL–CH2+CHCL2–CHCL2<=>CH2CL–CHCL+CHCL2–CHCL 3.00E+14 0.0 53130.0
427. CCL2–CH2+CH2CL–CH2CL<=>CCL3–CH2+CH2CL–CH2 3.00E+14 0.0 68320.0
428. CCL2–CH2+CHCL2–CH2CL<=>CCL3–CH2+CHCL2–CH2 3.00E+14 0.0 66660.0
429. CCL2–CH2+CHCL2–CH2CL<=>CCL3–CH2+CH2CL–CHCL 3.00E+14 0.0 62960.0
430. CCL2–CH2+CCL3–CH3<=>CCL3–CH2+CH3–CCL2 3.00E+14 0.0 58580.0
431. CCL2–CH2+CCL3–CH2CL<=>CCL3–CH2+CCL3–CH2 3.00E+14 0.0 63360.0
432. CCL2–CH2+CCL3–CHCL2<=>CCL3–CH2+CCL3–CHCL 3.00E+14 0.0 57260.0
433. CCL2–CH2+CCL3–CHCL2<=>CCL3–CH2+CHCL2–CCL2 3.00E+14 0.0 54490.0
434. CCL2–CH2+CCL3–CCL3<=>CCL3–CH2+CCL3–CCL2 3.00E+14 0.0 56100.0
435. CCL2–CH2+CCL4<=>CCL3–CH2+CCL3 3.00E+14 0.0 54660.0
436. CCL2–CH2+CHCL2–CHCL2<=>CCL3–CH2+CHCL2–CHCL 3.00E+14 0.0 58750.0
437. CCL2–CH2+CH2CL–CH2CL<=>CH2CL–CCL2+CH2CL–CH2 3.00E+14 0.0 59940.0
438. CCL2–CH2+CHCL2–CH2CL<=>CH2CL–CCL2+CHCL2–CH2 3.00E+14 0.0 58280.0
439. CCL2–CH2+CHCL2–CH2CL<=>CH2CL–CCL2+CH2CL–CHCL 3.00E+14 0.0 54580.0
440. CCL2–CH2+CCL3–CH3<=>CH2CL–CCL2+CH3–CCL2 3.00E+14 0.0 50200.0
441. CCL2–CH2+CCL3–CH2CL<=>CH2CL–CCL2+CCL3–CH2 3.00E+14 0.0 54980.0
442. CCL2–CH2+CCL3–CH2CL<=>CH2CL–CCL2+CH2CL–CCL2 3.00E+14 0.0 46600.0
443. CCL2–CH2+CCL3–CHCL2<=>CH2CL–CCL2+CCL3–CHCL 3.00E+14 0.0 48880.0
444. CCL2–CH2+CCL3–CHCL2<=>CH2CL–CCL2+CHCL2–CCL2 3.00E+14 0.0 46110.0
445. CCL2–CH2+CCL3–CCL3<=>CH2CL–CCL2+CCL3–CCL2 3.00E+14 0.0 47720.0
446. CCL2–CH2+CCL4<=>CH2CL–CCL2+CCL3 3.00E+14 0.0 46280.0
447. CCL2–CH2+CHCL2–CHCL2<=>CH2CL–CCL2+CHCL2–CHCL 3.00E+14 0.0 50370.0
448. tCHCL–CHCL+CH2CL–CH2CL 3.00E+14 0.0 62760.0
<=>CHCL2–CHCL+CH2CL–CH2
449. tCHCL–CHCL+CHCL2–CH2CL 3.00E+14 0.0 61100.0
<=>CHCL2–CHCL+CHCL2–CH2
450. tCHCL–CHCL+CHCL2–CH2CL 3.00E+14 0.0 57400.0
<=>CHCL2–CHCL+CH2CL–CHCL
451. tCHCL–CHCL+CCL3–CH3<=>CHCL2–CHCL+CH3–CCL2 3.00E+14 0.0 53020.0
452. tCHCL–CHCL+CCL3–CH2CL<=>CHCL2–CHCL+CCL3–CH2 3.00E+14 0.0 57800.0
453. tCHCL–CHCL+CCL3–CH2CL 3.00E+14 0.0 49420.0
<=>CHCL2–CHCL+CH2CL–CCL2
454. tCHCL–CHCL+CCL3–CHCL2<=>CHCL2–CHCL+CCL3–CHCL 3.00E+14 0.0 51700.0
455. tCHCL–CHCL+CCL3–CHCL2 3.00E+14 0.0 48930.0
<=>CHCL2–CHCL+CHCL2–CCL2
456. tCHCL–CHCL+CCL3–CCL3<=>CHCL2–CHCL+CCL3–CCL2 3.00E+14 0.0 50540.0
457. tCHCL–CHCL+CCL4<=>CHCL2–CHCL+CCL3 3.00E+14 0.0 49100.0
458. tCHCL–CHCL+CHCL2–CHCL2 3.00E+14 0.0 53190.0
<=>CHCL2–CHCL+CHCL2–CHCL
459. cCHCL–CHCL+CH2CL–CH2CL 3.00E+14 0.0 62860.0
<=>CHCL2–CHCL+CH2CL–CH2
460. cCHCL–CHCL+CHCL2–CH2CL 3.00E+14 0.0 61200.0
<=>CHCL2–CHCL+CHCL2–CH2
461. cCHCL–CHCL+CHCL2–CH2CL 3.00E+14 0.0 57500.0
<=>CHCL2–CHCL+CH2CL–CHCL
462. cCHCL–CHCL+CCL3–CH3<=>CHCL2–CHCL+CH3–CCL2 3.00E+14 0.0 53120.0
463. cCHCL–CHCL+CCL3–CH2CL<=>CHCL2–CHCL+CCL3–CH2 3.00E+14 0.0 57900.0
464. cCHCL–CHCL+CCL3–CH2CL 3.00E+14 0.0 49520.0
<=>CHCL2–CHCL+CH2CL–CCL2

465.	cCHCL–CHCL+CCL3–CHCL2<=>CHCL2–CHCL+CCL3–CHCL	3.00E+14	0.0	51800.0
466.	cCHCL–CHCL+CCL3–CHCL2 <=>CHCL2–CHCL+CHCL2–CCL2	3.00E+14	0.0	49030.0
467.	cCHCL–CHCL+CCL3–CCL3<=>CHCL2–CHCL+CCL3–CCL2	3.00E+14	0.0	50640.0
468.	cCHCL–CHCL+CCL4<=>CHCL2–CHCL+CCL3	3.00E+14	0.0	49200.0
469.	cCHCL–CHCL+CHCL2–CHCL2 <=>CHCL2–CHCL+CHCL2–CHCL	3.00E+14	0.0	53290.0
470.	CCL2–CHCL+CH2CL–CH2CL<=>CCL3–CHCL+CH2CL–CH2	3.00E+14	0.0	66140.0
471.	CCL2–CHCL+CHCL2–CH2CL<=>CCL3–CHCL+CHCL2–CH2	3.00E+14	0.0	64480.0
472.	CCL2–CHCL+CHCL2–CH2CL<=>CCL3–CHCL+CH2CL–CHCL	3.00E+14	0.0	60780.0
473.	CCL2–CHCL+CCL3–CH3<=>CCL3–CHCL+CH3–CCL2	3.00E+14	0.0	56400.0
474.	CCL2–CHCL+CCL3–CH2CL<=>CCL3–CHCL+CCL3–CH2	3.00E+14	0.0	61180.0
475.	CCL2–CHCL+CCL3–CH2CL<=>CCL3–CHCL+CH2CL–CCL2	3.00E+14	0.0	52800.0
476.	CCL2–CHCL+CCL3–CHCL2<=>CCL3–CHCL+CCL3–CHCL	3.00E+14	0.0	55080.0
477.	CCL2–CHCL+CCL3–CCL3<=>CCL3–CHCL+CCL3–CCL2	3.00E+14	0.0	53920.0
478.	CCL2–CHCL+CCL4<=>CCL3–CHCL+CCL3	3.00E+14	0.0	52480.0
479.	CCL2–CHCL+CHCL2–CHCL2<=>CCL3–CHCL+CHCL2–CHCL	3.00E+14	0.0	56570.0
480.	CCL2–CHCL+CH2CL–CH2CL<=>CHCL2–CCL2+CH2CL–CH2	3.00E+14	0.0	63370.0
481.	CCL2–CHCL+CHCL2–CH2CL<=>CHCL2–CCL2+CHCL2–CH2	3.00E+14	0.0	61710.0
482.	CCL2–CHCL+CHCL2–CH2CL <=>CHCL2–CCL2+CH2CL–CHCL	3.00E+14	0.0	58010.0
483.	CCL2–CHCL+CCL3–CH3<=>CHCL2–CCL2+CH3–CCL2	3.00E+14	0.0	53630.0
484.	CCL2–CHCL+CCL3–CH2CL<=>CHCL2–CCL2+CCL3–CH2	3.00E+14	0.0	58410.0
485.	CCL2–CHCL+CCL3–CH2CL<=>CHCL2–CCL2+CH2CL–CCL2	3.00E+14	0.0	50030.0
486.	CCL2–CHCL+CCL3–CHCL2<=>CHCL2–CCL2+CCL3–CHCL	3.00E+14	0.0	52310.0
487.	CCL2–CHCL+CCL3–CHCL2<=>CHCL2–CCL2+CHCL2–CCL2	3.00E+14	0.0	49540.0
488.	CCL2–CHCL+CCL3–CCL3<=>CHCL2–CCL2+CCL3–CCL2	3.00E+14	0.0	51150.0
489.	CCL2–CHCL+CCL4<=>CHCL2–CCL2+CCL3	3.00E+14	0.0	49710.0
490.	CCL2–CHCL+CHCL2–CHCL2 <=>CHCL2–CCL2+CHCL2–CHCL	3.00E+14	0.0	53800.0
491.	CCL2–CCL2+CH2CL–CH2CL<=>CCL3–CCL2+CH2CL–CH2	3.00E+14	0.0	65240.0
492.	CCL2–CCL2+CHCL2–CH2CL<=>CCL3–CCL2+CHCL2–CH2	3.00E+14	0.0	63580.0
493.	CCL2–CCL2+CHCL2–CH2CL<=>CCL3–CCL2+CH2CL–CHCL	3.00E+14	0.0	59880.0
494.	CCL2–CCL2+CCL3–CH3<=>CCL3–CCL2+CH3–CCL2	3.00E+14	0.0	55500.0
495.	CCL2–CCL2+CCL3–CH2CL<=>CCL3–CCL2+CCL3–CH2	3.00E+14	0.0	60280.0
496.	CCL2–CCL2+CCL3–CH2CL<=>CCL3–CCL2+CH2CL–CCL2	3.00E+14	0.0	51900.0
497.	CCL2–CCL2+CCL3–CHCL2<=>CCL3–CCL2+CCL3–CHCL	3.00E+14	0.0	54180.0
498.	CCL2–CCL2+CCL3–CHCL2<=>CCL3–CCL2+CHCL2–CCL2	3.00E+14	0.0	51410.0
499.	CCL2–CCL2+CCL3–CCL3<=>CCL3–CCL2+CCL3–CCL2	3.00E+14	0.0	53020.0
500.	CCL2–CCL2+CCL4<=>CCL3–CCL2+CCL3	3.00E+14	0.0	51580.0
501.	CCL2–CCL2+CHCL2–CHCL2<=>CCL3–CCL2+CHCL2–CHCL	3.00E+14	0.0	55670.0

NOTE: A units mole–cm–sec–K, E units cal/mole

NO ERRORS FOUND ON INPUT . . . CHEMKIN LINKING **FILE** WRITTEN.

WORKING SPACE REQUIREMENTS ARE

INTEGER: 8833

REAL: 8148

CHARACTER: 114

52 species Reduced Mechanism

CHEMKIN INTERPRETER OUTPUT: CHEMKIN–II Version 3.9 Aug. 1994

DOUBLE PRECISION

ELEMENTS CONSIDERED	ATOMIC WEIGHT
1. N	14.0067
2. AR	39.9480
3. O	15.9994
4. H	1.00797
5. C	12.0112
6. Ti	47.9000
7. CL	35.4530

SPECIES CONSIDERED	PHASE	CHARGE	MOLECULAR WEIGHT	TEMPERATURE LOW	TEMPERATURE HIGH	ELEMENT COUNT N	AR	O	H	C	Ti	CL
1. N2	G	0	28.01340	300	5000	2	0	0	0	0	0	0
2. AR	G	0	39.94800	300	5000	0	1	0	0	0	0	0
3. O	G	0	15.99940	200	3500	0	0	1	0	0	0	0
4. O2	G	0	31.99880	200	3500	0	0	2	0	0	0	0
5. H	G	0	1.00797	200	3500	0	0	0	1	0	0	0
6. OH	G	0	17.00737	200	3500	0	0	1	1	0	0	0
7. H2	G	0	2.01594	200	3500	0	0	0	2	0	0	0
8. HO2	G	0	33.00677	200	3500	0	0	2	1	0	0	0
9. H2O2	G	0	34.01474	200	3500	0	0	2	2	0	0	0
10. CH3	G	0	15.03506	200	3500	0	0	0	3	1	0	0
11. CH2O	G	0	30.02649	200	3500	0	0	1	2	1	0	0
12. CH4	G	0	16.04303	200	3500	0	0	0	4	1	0	0
13. CO	G	0	28.01055	200	3500	0	0	1	0	1	0	0
14. CO2	G	0	44.00995	200	3500	0	0	2	0	1	0	0
15. HCO	G	0	29.01852	200	3500	0	0	1	1	1	0	0
16. CH3O	G	0	31.03446	300	3000	0	0	1	3	1	0	0
17. C2H2	G	0	26.03824	200	3500	0	0	0	2	2	0	0
18. HCCO	G	0	41.02967	300	4000	0	0	1	1	2	0	0
19. C2H4	G	0	28.05418	200	3500	0	0	0	4	2	0	0
20. C2H5	G	0	29.06215	200	3500	0	0	0	5	2	0	0
21. C2H6	G	0	30.07012	200	3500	0	0	0	6	2	0	0
22. H2O	G	0	18.01534	200	3500	0	0	1	2	0	0	0
23. C2H3	G	0	27.04621	200	3500	0	0	0	3	2	0	0
24. NO	G	0	30.00610	200	6000	1	0	1	0	0	0	0
25. NO2	G	0	46.00550	200	6000	1	0	2	0	0	0	0
26. TiCL4	G	0	189.71200	300	5000	0	0	0	0	0	1	4
27. TiCL3	G	0	154.25900	300	2000	0	0	0	0	0	1	3
28. CL	G	0	35.45300	298	5000	0	0	0	0	0	0	1
29. TiCL2	G	0	118.80600	300	2000	0	0	0	0	0	1	2
30. CL2	G	0	70.90600	298	5000	0	0	0	0	0	0	2
31. TiO2CL2	G	0	150.80480	100	3000	0	0	2	0	0	1	2

32. TiO2CL3	G	0	186.25780	100	3000	0	0	2	0	0	1	3
33. Ti2O2CL3	G	0	234.15780	100	3000	0	0	2	0	0	2	3
34. Ti2O2CL4	G	0	269.61080	100	3000	0	0	2	0	0	2	4
35. TiOCL3	G	0	170.25840	100	3000	0	0	1	0	0	1	3
36. CLO	G	0	51.45240	300	4000	0	0	1	0	0	0	1
37. TiOCL2	G	0	134.80540	100	3000	0	0	1	0	0	1	2
38. Ti2O3CL3	G	0	250.15720	100	3000	0	0	3	0	0	2	3
39. Ti3O4CL4	G	0	349.50960	100	3000	0	0	4	0	0	3	4
40. Ti2O3CL2	G	0	214.70420	100	3000	0	0	3	0	0	2	2
41. Ti2O2CL6	G	0	340.51680	100	3000	0	0	2	0	0	2	6
42. TiCL2OCL	G	0	170.25840	100	3000	0	0	1	0	0	1	3
43. Ti5O6CL8	G	0	619.12040	100	3000	0	0	6	0	0	5	8
44. TiO2(ru)	G	0	79.89880	300	2130	0	0	2	0	0	1	0
45. CH3CL	G	0	50.48806	298	5000	0	0	0	3	1	0	1
46. CH2CL2	G	0	84.93309	298	5000	0	0	0	2	1	0	2
47. CH2CL	G	0	49.48009	298	5000	0	0	0	2	1	0	1
48. CHCL3	G	0	119.37812	298	5000	0	0	0	1	1	0	3
49. CHCL2	G	0	83.92512	298	5000	0	0	0	1	1	0	2
50. CCL4	G	0	153.82315	298	5000	0	0	0	0	1	0	4
51. CCL3	G	0	118.37015	298	5000	0	0	0	0	1	0	3
52. HCL	G	0	36.46097	200	6000	0	0	0	1	0	0	1

REACTIONS CONSIDERED			(k = A T**b exp(−E/RT)) A	b	E
1. 2O+M<=>O2+M			1.20E+17	−1.0	0.0
AR	Enhanced by	8.300E−01			
H2	Enhanced by	2.400E+00			
CH4	Enhanced by	2.000E+00			
CO	Enhanced by	1.750E+00			
CO2	Enhanced by	3.600E+00			
C2H6	Enhanced by	3.000E+00			
H2O	Enhanced by	1.540E+01			
2. O+H+M<=>OH+M			5.00E+17	−1.0	0.0
AR	Enhanced by	7.000E−01			
H2	Enhanced by	2.000E+00			
CH4	Enhanced by	2.000E+00			
CO	Enhanced by	1.500E+00			
CO2	Enhanced by	2.000E+00			
C2H6	Enhanced by	3.000E+00			
H2O	Enhanced by	6.000E+00			
3. O+H2<=>H+OH			5.00E+04	2.7	6289.9
4. O+HO2<=>OH+O2			2.00E+13	0.0	0.0
5. O+H2O2<=>OH+HO2			9.63E+06	2.0	4000.0
6. O+CH3<=>H+CH2O			8.43E+13	0.0	0.0
7. O+CH4<=>OH+CH3			1.02E+09	1.5	8599.9
8. O+CO+M<=>CO2+M			6.02E+14	0.0	3000.0
AR	Enhanced by	5.000E−01			
O2	Enhanced by	6.000E+00			
H2	Enhanced by	2.000E+00			
CH4	Enhanced by	2.000E+00			
CO	Enhanced by	1.500E+00			
CO2	Enhanced by	3.500E+00			

C2H6	Enhanced by	3.000E+00			
H2O	Enhanced by	6.000E+00			
9. O+HCO<=>OH+CO			3.00E+13	0.0	0.0
10. O+HCO<=>H+CO2			3.00E+13	0.0	0.0
11. O+CH2O<=>OH+HCO			3.90E+13	0.0	3539.9
12. O+CH3O<=>OH+CH2O			1.00E+13	0.0	0.0
13. O+C2H2<=>H+HCCO			1.02E+07	2.0	1900.1
14. O+C2H4<=>CH3+HCO			1.92E+07	1.8	219.9
15. O+C2H5<=>CH3+CH2O			1.32E+14	0.0	0.0
16. O+C2H6<=>OH+C2H5			8.98E+07	1.9	5690.0
17. O+HCCO<=>H+2CO			1.00E+14	0.0	0.0
18. O2+CO<=>O+CO2			2.50E+12	0.0	47799.9
19. O2+CH2O<=>HO2+HCO			1.00E+14	0.0	40000.0
20. H+O2+M<=>HO2+M			2.80E+18	−0.9	0.0
N2	Enhanced by	0.000E+00			
AR	Enhanced by	0.000E+00			
O2	Enhanced by	0.000E+00			
CO	Enhanced by	7.500E−01			
CO2	Enhanced by	1.500E+00			
C2H6	Enhanced by	1.500E+00			
H2O	Enhanced by	0.000E+00			
21. H+2O2<=>HO2+O2			3.00E+20	−1.7	0.0
22. H+O2+H2O<=>HO2+H2O			9.38E+18	−0.8	0.0
23. H+O2+N2<=>HO2+N2			3.75E+20	−1.7	0.0
24. H+O2+AR<=>HO2+AR			7.00E+17	−0.8	0.0
25. H+O2<=>O+OH			8.30E+13	0.0	14413.0
26. 2H+M<=>H2+M			1.00E+18	−1.0	0.0
AR	Enhanced by	6.300E−01			
H2	Enhanced by	0.000E+00			
CH4	Enhanced by	2.000E+00			
CO2	Enhanced by	0.000E+00			
C2H6	Enhanced by	3.000E+00			
H2O	Enhanced by	0.000E+00			
27. 2H+H2<=>2H2			9.00E+16	−0.6	0.0
28. 2H+H2O<=>H2+H2O			6.00E+19	−1.2	0.0
29. 2H+CO2<=>H2+CO2			5.50E+20	−2.0	0.0
30. H+OH+M<=>H2O+M			2.20E+22	−2.0	0.0
AR	Enhanced by	3.800E−01			
H2	Enhanced by	7.300E−01			
CH4	Enhanced by	2.000E+00			
C2H6	Enhanced by	3.000E+00			
H2O	Enhanced by	3.650E+00			
31. H+HO2<=>O+H2O			3.97E+12	0.0	670.9
32. H+HO2<=>O2+H2			2.80E+13	0.0	1068.1
33. H+HO2<=>2OH			1.34E+14	0.0	635.0
34. H+H2O2<=>HO2+H2			1.21E+07	2.0	5200.1
35. H+H2O2<=>OH+H2O			1.00E+13	0.0	3599.9
36. H+CH3(+M)<=>CH4(+M)			1.27E+16	−0.6	382.9
AR	Enhanced by	7.000E−01			
H2	Enhanced by	2.000E+00			
CH4	Enhanced by	2.000E+00			
CO	Enhanced by	1.500E+00			
CO2	Enhanced by	2.000E+00			
C2H6	Enhanced by	3.000E+00			
H2O	Enhanced by	6.000E+00			
Low pressure limit:	0.24770E+34	−0.47600E+01	0.24400E+04		

```
    TROE centering:       0.78300E+00  0.74000E+02  0.29410E+04  0.69640E+04
37. H+CH4<=>CH3+H2                                   6.60E+08     1.6      10840.1
38. H+HCO(+M)<=>CH2O(+M)                             1.09E+12     0.5       -260.0
        AR                  Enhanced by     7.000E-01
        H2                  Enhanced by     2.000E+00
        CH4                 Enhanced by     2.000E+00
        CO                  Enhanced by     1.500E+00
        CO2                 Enhanced by     2.000E+00
        C2H6                Enhanced by     3.000E+00
        H2O                 Enhanced by     6.000E+00
    Low pressure limit:   0.13500E+25 -0.25700E+01  0.14250E+04
    TROE centering:       0.78240E+00  0.27100E+03  0.27550E+04  0.65700E+04
39. H+HCO<=>H2+CO                                    7.34E+13     0.0          0.0
40. H+CH2O(+M)<=>CH3O(+M)                            5.40E+11     0.5       2599.9
        H2                  Enhanced by     2.000E+00
        CH4                 Enhanced by     2.000E+00
        CO                  Enhanced by     1.500E+00
        CO2                 Enhanced by     2.000E+00
        C2H6                Enhanced by     3.000E+00
        H2O                 Enhanced by     6.000E+00
    Low pressure limit:   0.22000E+31 -0.48000E+01  0.55600E+04
    TROE centering:       0.75800E+00  0.94000E+02  0.15550E+04  0.42000E+04
41. H+CH2O<=>HCO+H2                                  2.30E+10     1.1       3275.1
42. H+CH3O<=>H2+CH2O                                 2.00E+13     0.0          0.0
43. H+CH3O<=>OH+CH3                                  3.20E+13     0.0          0.0
44. H+C2H2(+M)<=>C2H3(+M)                            5.60E+12     0.0       2400.1
        AR                  Enhanced by     7.000E-01
        H2                  Enhanced by     2.000E+00
        CH4                 Enhanced by     2.000E+00
        CO                  Enhanced by     1.500E+00
        CO2                 Enhanced by     2.000E+00
        C2H6                Enhanced by     3.000E+00
        H2O                 Enhanced by     6.000E+00
    Low pressure limit:   0.38000E+41 -0.72700E+01  0.72199E+04
    TROE centering:       0.75070E+00  0.98500E+02  0.13020E+04  0.41670E+04
45. H+C2H3(+M)<=>C2H4(+M)                            6.08E+12     0.3        280.1
        AR                  Enhanced by     7.000E-01
        H2                  Enhanced by     2.000E+00
        CH4                 Enhanced by     2.000E+00
        CO                  Enhanced by     1.500E+00
        CO2                 Enhanced by     2.000E+00
        C2H6                Enhanced by     3.000E+00
        H2O                 Enhanced by     6.000E+00
    Low pressure limit:   0.14000E+31 -0.38600E+01  0.33200E+04
    TROE centering:       0.78200E+00  0.20750E+03  0.26630E+04  0.60950E+04
46. H+C2H3<=>H2+C2H2                                 3.00E+13     0.0          0.0
47. H+C2H4(+M)<=>C2H5(+M)                            1.08E+12     0.5       1820.0
        AR                  Enhanced by     7.000E-01
        H2                  Enhanced by     2.000E+00
        CH4                 Enhanced by     2.000E+00
        CO                  Enhanced by     1.500E+00
        CO2                 Enhanced by     2.000E+00
        C2H6                Enhanced by     3.000E+00
        H2O                 Enhanced by     6.000E+00
    Low pressure limit:   0.12000E+43 -0.76200E+01  0.69699E+04
    TROE centering:       0.97530E+00  0.21000E+03  0.98400E+03  0.43740E+04
```

```
48. H+C2H4<=>C2H3+H2                                  1.32E+06    2.5     12240.0
49. H+C2H5(+M)<=>C2H6(+M)                             5.21E+17   -1.0      1580.1
      AR                  Enhanced by    7.000E-01
      H2                  Enhanced by    2.000E+00
      CH4                 Enhanced by    2.000E+00
      CO                  Enhanced by    1.500E+00
      CO2                 Enhanced by    2.000E+00
      C2H6                Enhanced by    3.000E+00
      H2O                 Enhanced by    6.000E+00
    Low pressure limit:  0.19900E+42 -0.70800E+01  0.66850E+04
    TROE centering:      0.84220E+00  0.12500E+03  0.22190E+04  0.68820E+04
50. H+C2H5<=>H2+C2H4                                  2.00E+12    0.0        0.0
51. H+C2H6<=>C2H5+H2                                  1.15E+08    1.9     7530.1
52. H2+CO(+M)<=>CH2O(+M)                              4.30E+07    1.5    79599.9
      AR                  Enhanced by    7.000E-01
      H2                  Enhanced by    2.000E+00
      CH4                 Enhanced by    2.000E+00
      CO                  Enhanced by    1.500E+00
      CO2                 Enhanced by    2.000E+00
      C2H6                Enhanced by    3.000E+00
      H2O                 Enhanced by    6.000E+00
    Low pressure limit:  0.50700E+28 -0.34200E+01  0.84350E+05
    TROE centering:      0.93200E+00  0.19700E+03  0.15400E+04  0.10300E+05
53. OH+H2<=>H+H2O                                     2.16E+08    1.5     3430.0
54. 2OH(+M)<=>H2O2(+M)                                7.40E+13   -0.4        0.0
      AR                  Enhanced by    7.000E-01
      H2                  Enhanced by    2.000E+00
      CH4                 Enhanced by    2.000E+00
      CO                  Enhanced by    1.500E+00
      CO2                 Enhanced by    2.000E+00
      C2H6                Enhanced by    3.000E+00
      H2O                 Enhanced by    6.000E+00
    Low pressure limit:  0.23000E+19 -0.90000E+00 -0.17000E+04
    TROE centering:      0.73460E+00  0.94000E+02  0.17560E+04  0.51820E+04
55. 2OH<=>O+H2O                                       3.57E+04    2.4    -2109.9
56. OH+HO2<=>O2+H2O                                   2.90E+13    0.0     -500.0
57. OH+H2O2<=>HO2+H2O                                 1.75E+12    0.0      320.0
    Declared duplicate reaction...
58. OH+H2O2<=>HO2+H2O                                 5.80E+14    0.0     9560.0
    Declared duplicate reaction...
59. OH+CH4<=>CH3+H2O                                  1.00E+08    1.6     3120.0
60. OH+CO<=>H+CO2                                     4.76E+07    1.2       70.0
61. OH+HCO<=>H2O+CO                                   5.00E+13    0.0        0.0
62. OH+CH2O<=>HCO+H2O                                 3.43E+09    1.2     -446.9
63. OH+CH3O<=>H2O+CH2O                                5.00E+12    0.0        0.0
64. OH+C2H2<=>CH3+CO                                  4.83E-04    4.0    -2000.0
65. OH+C2H3<=>H2O+C2H2                                5.00E+12    0.0        0.0
66. OH+C2H4<=>C2H3+H2O                                3.60E+06    2.0     2500.0
67. OH+C2H6<=>C2H5+H2O                                3.54E+06    2.1      870.0
68. 2HO2<=>O2+H2O2                                    1.30E+11    0.0    -1630.0
    Declared duplicate reaction...
69. 2HO2<=>O2+H2O2                                    4.20E+14    0.0    12000.0
    Declared duplicate reaction...
70. HO2+CH3<=>O2+CH4                                  1.00E+12    0.0        0.0
71. HO2+CH3<=>OH+CH3O                                 2.00E+13    0.0        0.0
72. HO2+CO<=>OH+CO2                                   1.50E+14    0.0    23599.9
```

73.	HO2+CH2O<=>HCO+H2O2		1.00E+12	0.0	8000.0
74.	CH3+O2<=>O+CH3O		2.68E+13	0.0	28800.0
75.	CH3+O2<=>OH+CH2O		3.60E+10	0.0	8940.0
76.	CH3+H2O2<=>HO2+CH4		2.45E+04	2.5	5180.0
77.	2CH3(+M)<=>C2H6(+M)		2.12E+16	−1.0	620.0
	AR	Enhanced by 7.000E−01			
	H2	Enhanced by 2.000E+00			
	CH4	Enhanced by 2.000E+00			
	CO	Enhanced by 1.500E+00			
	CO2	Enhanced by 2.000E+00			
	C2H6	Enhanced by 3.000E+00			
	H2O	Enhanced by 6.000E+00			
	Low pressure limit:	0.17700E+51 −0.96700E+01 0.62199E+04			
	TROE centering:	0.53250E+00 0.15100E+03 0.10380E+04 0.49700E+04			
78.	2CH3<=>H+C2H5		4.99E+12	0.1	10599.9
79.	CH3+HCO<=>CH4+CO		2.65E+13	0.0	0.0
80.	CH3+CH2O<=>HCO+CH4		3.32E+03	2.8	5859.9
81.	CH3+C2H4<=>C2H3+CH4		2.27E+05	2.0	9200.0
82.	CH3+C2H6<=>C2H5+CH4		6.14E+06	1.7	10450.0
83.	HCO+H2O<=>H+CO+H2O		2.24E+18	−1.0	17000.0
84.	HCO+M<=>H+CO+M		1.87E+17	−1.0	17000.0
	H2	Enhanced by 2.000E+00			
	CH4	Enhanced by 2.000E+00			
	CO	Enhanced by 1.500E+00			
	CO2	Enhanced by 2.000E+00			
	C2H6	Enhanced by 3.000E+00			
	H2O	Enhanced by 0.000E+00			
85.	HCO+O2<=>HO2+CO		7.60E+12	0.0	400.1
86.	CH3O+O2<=>HO2+CH2O		4.28E−13	7.6	−3530.1
87.	C2H3+O2<=>HCO+CH2O		3.98E+12	0.0	−240.0
88.	C2H4(+M)<=>H2+C2H2(+M)		8.00E+12	0.4	88770.1
	AR	Enhanced by 7.000E−01			
	H2	Enhanced by 2.000E+00			
	CH4	Enhanced by 2.000E+00			
	CO	Enhanced by 1.500E+00			
	CO2	Enhanced by 2.000E+00			
	C2H6	Enhanced by 3.000E+00			
	H2O	Enhanced by 6.000E+00			
	Low pressure limit:	0.70000E+51 −0.93100E+01 0.99860E+05			
	TROE centering:	0.73450E+00 0.18000E+03 0.10350E+04 0.54170E+04			
89.	C2H5+O2<=>HO2+C2H4		8.40E+11	0.0	3875.0
90.	HCCO+O2<=>OH+2CO		1.60E+12	0.0	854.0
91.	2HCCO<=>2CO+C2H2		1.00E+13	0.0	0.0
92.	HO2+NO<=>NO2+OH		2.11E+12	0.0	−479.9
93.	NO+O+M<=>NO2+M		1.06E+20	−1.4	0.0
	AR	Enhanced by 7.000E−01			
	H2	Enhanced by 2.000E+00			
	CH4	Enhanced by 2.000E+00			
	CO	Enhanced by 1.500E+00			
	CO2	Enhanced by 2.000E+00			
	C2H6	Enhanced by 3.000E+00			
	H2O	Enhanced by 6.000E+00			
94.	NO2+O<=>NO+O2		3.90E+12	0.0	−240.0
95.	NO2+H<=>NO+OH		1.32E+14	0.0	359.9
96.	TiCL4+M<=>TiCL3+CL+M		5.40E+18	0.0	80236.9
97.	TiCL3+M<=>TiCL2+CL+M		7.70E+18	0.0	92415.6

98.	TiCL2+CL2<=>TiCL4	1.00E+13	0.0	0.0
99.	TiCL3+CL2<=>TiCL4+CL	1.00E+13	0.0	0.0
100.	TiCL2+CL2<=>TiCL3+CL	1.00E+13	0.0	0.0
101.	CL2+TiO2CL2<=>CL+TiO2CL3	1.00E+13	0.0	0.0
102.	CL2+Ti2O2CL3<=>CL+Ti2O2CL4	1.00E+13	0.0	0.0
103.	2TiCL3<=>TiCL2+TiCL4	9.60E+12	0.0	8358.0
104.	TiCL3+O2(+M)<=>TiO2CL3(+M)	1.92E+35	−6.6	9891.0
	Low pressure limit: 0.10600E+37 −0.63190E+01 0.00000E+00			
	TROE centering: 0.11830E+00 0.26930E+02 0.10000E+06 0.52190E+04			
105.	TiOCL3+CLO<=>TiO2CL3+CL	1.00E+13	0.0	0.0
106.	TiOCL2+CL<=>TiOCL3	1.00E+13	0.0	0.0
107.	TiOCL3+O<=>TiO2CL3	1.00E+13	0.0	0.0
108.	TiO2CL2+CL<=>TiO2CL3	1.00E+13	0.0	0.0
109.	TiO2CL2+CL<=>TiCL3+O2	1.00E+13	0.0	0.0
110.	TiOCL3+O<=>TiCL3+O2	1.00E+13	0.0	0.0
111.	TiCL2+O2<=>TiOCL2+O	1.00E+13	0.0	0.0
112.	TiO2CL2+O<=>TiOCL2+O2	1.00E+13	0.0	0.0
113.	TiCL3+CLO<=>TiCL4+O	1.00E+13	0.0	0.0
114.	TiCL2+CLO<=>TiCL3+O	1.00E+13	0.0	0.0
115.	TiCL3+O<=>TiOCL2+CL	1.00E+13	0.0	0.0
116.	TiCL3+CLO<=>TiOCL3+CL	1.00E+13	0.0	0.0
117.	TiO2CL2+CL<=>TiOCL2+CLO	1.00E+13	0.0	0.0
118.	CL+O2<=>CLO+O	8.79E+14	0.0	55043.5
119.	O+CL2<=>CLO+CL	4.46E+12	0.0	3278.7
120.	2CL+M<=>CL2+M	2.23E+14	0.0	−1798.3
121.	2TiOCL2<=>Ti2O2CL4	1.00E+13	0.0	0.0
122.	TiO2CL2+TiCL3<=>Ti2O2CL4+CL	1.00E+13	0.0	0.0
123.	TiO2CL2+TiOCL2<=>Ti2O3CL3+CL	1.00E+13	0.0	0.0
124.	TiOCL2+TiOCL3<=>Ti2O2CL4+CL	1.00E+13	0.0	0.0
125.	Ti2O3CL3+TiOCL2<=>Ti3O4CL4+CL	1.00E+13	0.0	0.0
126.	Ti2O3CL2+CL<=>Ti2O3CL3	1.00E+13	0.0	0.0
127.	Ti2O2CL3+TiCL4<=>Ti2O2CL4+TiCL3	1.00E+13	0.0	0.0
128.	TiO2CL3+TiCL3<=>Ti2O2CL6	1.00E+13	0.0	0.0
129.	2TiOCL3<=>Ti2O2CL6	1.00E+13	0.0	0.0
130.	TiCL2OCL<=>TiOCL2+CL	1.00E+13	0.0	0.0
131.	TiCL2OCL+CL<=>TiCL3+CLO	1.00E+13	0.0	0.0
132.	TiCL2OCL+CL<=>TiOCL3+CL	1.00E+13	0.0	0.0
133.	TiCL2OCL+CL<=>CL2+TiOCL2	1.00E+13	0.0	0.0
134.	Ti2O2CL4+Ti3O4CL4=>Ti5O6CL8	1.00E+13	0.0	0.0
135.	Ti2O2CL6+Ti3O4CL4=>Ti5O6CL8+CL2	1.00E+13	0.0	0.0
136.	Ti5O6CL8+2O2=>5TiO2(ru)+4CL2	1.00E+25	0.0	0.0
137.	CL2<=>2CL	1.85E+12	0.0	57979.9
138.	CH3CL<=>CH3+CL	1.00E+16	0.0	84370.0
139.	CH2CL2<=>CH2CL+CL	1.00E+16	0.0	81140.1
140.	CHCL3<=>CHCL2+CL	1.00E+16	0.0	77630.0
141.	CCL4<=>CCL3+CL	1.00E+16	0.0	70930.0
142.	CH3CL+CL<=>CH2CL+HCL	1.00E+13	0.0	460.1
143.	CH3CL+CL<=>CH3+CL2	1.00E+14	0.0	25620.0
144.	CH4+CL<=>CH3+HCL	1.00E+13	0.0	2109.9
145.	CH4+CH2CL<=>CH3+CH3CL	3.00E+11	0.0	15800.0
146.	CH2CL2+CL<=>CHCL2+HCL	1.00E+13	0.0	460.1
147.	CH2CL2+CH3<=>CHCL2+CH4	3.00E+11	0.0	11000.0
148.	CH2CL2+CH2CL<=>CHCL2+CH3CL	3.00E+11	0.0	11000.0
149.	CH2CL2+CL<=>CH2CL+CL2	1.00E+14	0.0	22390.1
150.	CH2CL2+CH3<=>CH2CL+CH3CL	3.00E+11	0.0	11000.0
151.	CHCL3+CL<=>CCL3+HCL	1.00E+13	0.0	460.1

152. CHCL3+CH3<=>CCL3+CH4	3.00E+11	0.0	11000.0
153. CHCL3+CH2CL<=>CCL3+CH3CL	3.00E+11	0.0	11000.0
154. CHCL3+CHCL2<=>CCL3+CH2CL2	3.00E+11	0.0	11000.0
155. CHCL3+CL<=>CHCL2+CL2	1.00E+14	0.0	18880.0
156. CHCL3+CH3<=>CHCL2+CH3CL	3.00E+11	0.0	11000.0
157. CHCL3+CH2CL<=>CHCL2+CH2CL2	3.00E+11	0.0	11000.0
158. CCL4+CL<=>CCL3+CL2	1.00E+14	0.0	12180.0
159. CCL4+CH3<=>CCL3+CH3CL	3.00E+11	0.0	11000.0
160. CCL4+CH2CL<=>CCL3+CH2CL2	3.00E+11	0.0	11000.0
161. CCL4+CHCL2<=>CCL3+CHCL3	3.00E+11	0.0	11000.0

NOTE: A units mole-cm-sec-K, E units cal/mole

NO ERRORS FOUND ON INPUT ... CHEMKIN LINKING **FILE** WRITTEN.

WORKING SPACE REQUIREMENTS ARE

INTEGER: 3087
REAL: 3090
CHARACTER: 59

APPENDIX B. Code for PaSR

Listed below is the code used to perform the partially stirred reactor approximation.

```
subroutine pasr_step(nstep,nreact)

  implicit none
  ! Total no. of timesteps
  integer :: nstep
  ! If the reaction part is stiff solve it in multiple division of the timestep
  integer :: nreact
  integer :: i, k, ierror1, ierror2
  character(len=40), parameter :: filename='Mean.dat', filename3='Var.dat'

  open(unit=25,file=filename,status='replace',action='write',iostat=ierror1)
  open(unit=35,file=filename3,status='replace',action='write',iostat=ierror2)

  do i = 1,nstep

    ! Takes out and introduces particles in the PaSR
    call inflow_outflow

 !   do k = 1, nreact
       ! Compute Mean of the PaSR particles
       call mean_compute
       ! Model Mixing in the PaSR
       call pasr_mix
       ! The reaction step
       call pasr_react
 !   end do

    ! Print Output
    call pasr_op(i)
    ! Write values
    call pasr_dump(i)


  enddo

 close(unit=25)
 close(unit=35)

end subroutine pasr_step
```

```
subroutine inflow_outflow

  implicit none

  integer :: i,nout,nin,n1,nfin,nold
  integer :: nstr1,nstr2,istrm,getstream
  real(WP) :: g
  real(WP) :: m1, m2, wt, wtout

  ! Particle 'i' has composition f(i)%conc
  ! n = no. of particles in PaSR
  ! tres = residence time
  ! nout = no. of particles to be taken out
  ! wt = weight of particles
  ! f(i)%stop whether particle 'i' is (0=in 1=out) inside the PaSR

  nout = floor(dt/tres*n)
  wtout = real(nout,WP)
  nfin = 0
  wt = 0.0_WP
  do while (nfin.lt.nout)
     call random_number(g)
     n1 = max(1,floor(g*n))
     if (f(n1)%stop.eq.0) then
        f(n1)%stop = 1
        wt = wt + f(n1)%wt
        nfin = nfin + 1
     endif
!      print *,' N1,nfin', n1,wt,nfin,f(n1)%stop
  enddo

!  print *,' After outflow'

  ! After taking particle out
  call compactor

!  print *,' After compactor'

  nin = nout

  nold = n
  ! After puting particles in
  call expander(nin)

  !print*, 'nin', nin
!  print *,' After expander'

  ! (n - nold) is the number of particles coming in
  do i = nold+1,n

     ! Decides from which stream the particles come
     ! nstr = no. of streams
     ! flstrm = flow rate of streams
     istrm = getstream(nstr,flstrm)

     !print*, 'stream', istrm
```

```
      f(i)%wt = 1.0
      f(i)%conc = cin(istrm,:)
      f(i)%stop = 0

  enddo


end subroutine inflow_outflow


integer function getstream(nstr,flstrm)

  use precision
  implicit none


  integer, parameter :: nstrd = 100
  integer :: ifst,i,infl,nstr

  real(WP), dimension(nstr) :: flstrm
  real(WP), dimension(nstrd) :: xstrm
  real(WP) :: flsum,xmax


  save xstrm
  data ifst /0/

  if (ifst.eq.0) then
       ifst = 1
       xstrm = 0.0_WP
  endif

  flsum = 0.0_WP
  xmax = 0.0_WP

  do i = 1,nstr

     xstrm(i) = xstrm(i) + flstrm(i)
     flsum = flsum + flstrm(i)

     if (xstrm(i).gt.xmax) then
          infl = i
          xmax = xstrm(i)
     endif

  enddo

  if (flsum.le.0) then
     write(*,*) 'inflow flsum < 0', flsum
     stop
  endif

  xstrm(infl) = xstrm(infl) - flsum
  getstream = infl

end function
```

```
subroutine compactor

  implicit none

  type(particle), dimension(:), allocatable :: dummy
  integer :: i,n1

  n1 = 0
  do i = 1,n
     if (f(i)%stop.eq.0) n1 = n1+ 1
  enddo
  allocate(dummy(n1))

  n1 = 0
  do i = 1,n
     if (f(i)%stop.eq.0) then
        n1 = n1 + 1
        allocate(dummy(n1)%conc(ns))
        dummy(n1) = f(i)
     endif
  enddo

 ! print*, 'In compactor'!, f(i)%conc(ns-6)

  deallocate(f)
  allocate(f(n1))

  do i = 1,n1
     allocate(f(i)%conc(ns))
     f(i) = dummy(i)
  enddo

  n = n1
  deallocate(dummy)

end subroutine compactor

subroutine expander(nadd)

  implicit none

  integer :: nadd, i

  type(particle), dimension(:), allocatable :: dummy

  allocate(dummy(n))
  do i = 1,n
     allocate(dummy(i)%conc(ns))
     dummy(i) = f(i)
  enddo

  deallocate(f)
  allocate(f(n+nadd))
```

```
  do i = 1,n
     allocate(f(i)%conc(ns))
     f(i) = dummy(i)
  enddo
  deallocate(dummy)
  do i = n+1,n+nadd
     allocate(f(i)%conc(ns))
     f(i)%wt = 1.0_WP
     f(i)%conc = 0.0_WP
     f(i)%stop = 0
  enddo


  n = n + nadd

end subroutine expander



subroutine mean_compute

  implicit none

  integer :: i
  real(WP) :: wt,c(4),d(4),dens1,T

  ! Mean
  cmean = 0.0_WP
  ! Variance
  cvar = 0.0_WP
  ! Total number
  wt = 0.0_WP


  do i = 1,n
     cmean = cmean + f(i)%wt*f(i)%conc
     cvar  = cvar  + f(i)%wt*f(i)%conc**2.0_WP
     wt = wt + f(i)%wt
  enddo

  cmean = cmean/wt
  cvar = cvar/wt - cmean*cmean

end subroutine mean_compute

subroutine pasr_mix

  use pasr_mod
  implicit none

  integer :: i, j
  integer :: nmix

  real(WP) :: g1, g2, a1, chk, finalt
  real(WP), dimension(ns) :: sendin
```

```
  ! Based on Modified Curl
  ! dt = timestep, tmix = mixing time
  nmix = floor(dt/tmix*n)
  nmix = 3.0_WP*nmix

  do i = 1, nmix
     call random_number(g1)
     g1 = max(1,floor(g1*n))
     call random_number(g2)
     g2 = max(1,floor(g2*n))
     call random_number(a1)


     diff(2:ns) = (f(g2)%conc(2:ns)-f(g1)%conc(2:ns))


     f(g1)%conc(2:ns) = f(g1)%conc(2:ns) + 0.5_WP*a1*diff(2:ns)
     f(g2)%conc(2:ns) = f(g2)%conc(2:ns) - 0.5_WP*a1*diff(2:ns)


     chk = f(g1)%conc(ns)
     sendin(1:ns) = f(g1)%conc(1:ns)
     ! Find Temp based on enthalpy and species conc.(or mass fractions)
     call findt(sendin,ns,finalt)
     f(g1)%conc(1) = finalt

     chk = f(g2)%conc(ns)
     sendin(1:ns) = f(g2)%conc(1:ns)
     call findt(sendin,ns,finalt)
     f(g2)%conc(1) = finalt

  end do

!!$!   Based on IEM
!!$
!!$ do i = 1,n
!!$     f(i)%conc = f(i)%conc + (dt*(cmean - f(i)%conc))/(cphi*tmix)!dt/(cphi*tmix)*(cmean - f(i)%conc)
!!$  end do

end subroutine pasr_mix



subroutine pasr_react

  implicit none

  integer :: i
  integer :: sendode

  sendode = no_ode
  if (trim(simname).eq.'Chemkin') then
  ! Calculating the reaction part through Chemkin using ODE solver
  ! Moments calculated inside this as well
     do i = 1,n
```

```
        call chemkin_react(f(i)%conc, ns, dt, sendode, i)

      enddo
   else
      ! Do nothing for now
   endif

end subroutine pasr_react



subroutine pasr_op(step)

   implicit none
   integer :: step


   write(*,'(A,2X,I5,2(2X,E10.4))') ' Mean concentration', step,cmean(1),cmean(2),cmean(3)

end subroutine

subroutine pasr_dump(istep)


   implicit none
   integer :: i,istep, j
   character(len=str_long) :: filename!, filename1
   character(len=str_short)  :: a
   real(WP) :: c(4), d(4), dens1,T
   character(len=40), parameter :: filename1='Particle.dat'

   open(unit=30,file=filename1,form='formatted')

   write(25,'(150(E12.6,2X))') istep, cmean(:)
   write(35,'(150(E12.6,2X))') istep, cvar(:)
   do i = 1,n

      write(30,'(150(E12.6,2X))') f(i)%conc(:)

   enddo

  close(30)

end subroutine pasr_dump
```

BIBLIOGRAPHY

[1] Akhtar, M., Xiong, Y., and Pratsinis, S. (1991). Vapor synthesis of titania powder by titanium tetrachloride oxidation. *AIChE J.*, 37:1561–1570.

[2] Akhtar, M. K., Pratsinis, S., and Mastrangelo, S. (1994a). Vapor-phase synthesis of Al-doped titania powders. *J. Mater. Res.*, 9:12411249.

[3] Akroyd, J., Smith, A. J., Shirley, R., McGlashan, L. R., and Kraft, M. (2011). A coupled cfd-population balance approach for nanoparticle synthesis in turbulent reacting flows. *Chem. Eng. Sci.*, 66:3792–3805.

[4] Bankmann, M., Brand, R., Engler, B., and Ohmer, J. (1992). Forming of high surface area TiO2 to catalyst supports. *Catal. Today*, 14:225–242.

[5] Benson, S. (1976). *Thermochemical Kinetics*, volume 2. Wiley, New York, USA.

[Bowman et al.] Bowman, C. T., Hanson, R. K., Davidson, D. F., Gardiner, W. C., Jr., Lissianski, V., Smith, G. P., Golden, D. M., Frenklach, M., and Goldenberg, M.

[6] Cheng, J. C. and Fox, R. O. (2010). Kinetic modeling of nanoprecipitation using CFD coupled with a population balance. *Ind. Eng. Chem. Res.*, 49(21):10651–10662.

[7] Consulting, S. (2001). *Chemical economics handbook*. SRI Consulting.

[8] Deberry, J., Robinson, M., Pomponi, M., Beach, A., Xiong, Y., and Akhtar, K. (May 14, 2002). Controlled vapor phase oxidation of titanium tetrachloride to manufacture titanium dioxide,US Patent 6,387,347.

[9] Diemer, R. J. and Olson, J. (2005). Bivariate moment methods for simultaneous coalgulation, coalescence and breakup. *Aerosol Science*, 37:363–385.

[10] Ehrman, S., Friedlander, S., and Zachariah, M. (1998). Characteristics of SiO2/TiO2 nanocomposite particles formed in a premixed flat flame. *J. Aerosol Sci.*, 29:687706.

[11] Fox, R. O. (2003). *Computational Models for Turbulent Reacting Flows*. Cambridge Series in Chemical Engineering. Cambridge University Press.

[12] Friedlander, S. and Wu, M. (1994). Linear rate law for the decay of excess surface area of a coalescing solid particle. *Phys. Rev. B*, 49:347.

[13] Friedlander, S. K. (2000). *Smoke, Dust, and Haze - Fundamentals of Aerosol Dynamics*. Oxford University Press.

[14] Fujishima, A. (2005). Discovery and applications of photocatalysis - creating a comfortable future by making use of light energy. *Japan Nanonet Bulletin*, 44.

[15] Geohegan, D. B., Puretzky, A. A., Duscher, G., and Pennycook, S. J. (1998). Time-resolved imaging of gas phase nanoparticle synthesis by laser ablation. *Applied Physics Letters*, 72(23):2987–2989.

[16] Ghoshtagore, R. N. (1970). Mechanism of heterogeneous deposition of thin film rutile. *J. Electrochem. Soc.: Solid State Sci.*, 117(4):529–534.

[17] Gonzalez, R., Musick, C., and Tilton, J. (April 16, 1996). Process for controlling agglomeration in the manufacture of tio2, US Patent 5,508,015.

[18] Gupta, A. K. and Gupta, M. (2005). Synthesis and surface engineering of iron oxide nanoparticles for biomedical applications. *Biomaterials*, 26(18):3995–4021.

[19] Heine, M. C., Mädler, L., Jossen, R., and Pratsinis, S. E. (2006). Direct measurement of entrainment during nanoparticle synthesis in spray flames. *Combust. Flame*, 144:809–820.

[20] Heine, M. C. and Pratsinis, S. E. (2007a). Agglomerate TiO_2 aersol dynamics at high concentrations. *Part. Part. Syst. Charact.*, 24:56–65.

[21] Heine, M. C. and Pratsinis, S. E. (2007b). Polydispersity of primary particles in agglomerates made by coagulation and sintering. *J. Aerosol Sci.*, 38:17–38.

[22] Hindmarsh, A. C. (1983). ODEPACK, A Systematized Collection of ODE Solvers , R. S. Stepleman et al. (eds.), North-Holland, Amsterdam, (vol. 1 of), pp. 55-64. *IMACS Transactions on Scientific Computation*, 1:55–64.

[23] Ho, T. and R., A. (1987). On apparent second-order kinetics. *AIChE J.*, 33:1050.

[24] Inc., F. M. (Dec, 2011). The World Market for Titanium Dioxide Nanopowders, http://www.marketresearch.com/future-markets-inc-v3760/titanium-dioxide-nanopowders-6235980/.

[25] Inderwildi, O. and Kraft, M. (2007). Adsorption, Diffusion and Desorption of Chlorine on and from Rutile TiO_2(110): A Theoretical Investigation. *ChemPhysChem*, 8:444–451.

[26] Jang, H. and Jeong, J. (1995). The effects of temperature on particle size in the gas-phase production of tio_2. *Aerosol Sci. Technol.*, 23:553–560.

[27] Jeong, J. I. and Choi, M. (2003). Analysis of non-spherical polydisperse particle growth in a two-dimensional tubular reactor. *Journal of Aerosol Science*, 34(6):713–732.

[28] Johannessen, T., Pratsinis, S. E., and Livbjerg, H. (2001). Computational analysis of coagulation and coalescence in the flame synthesis of titania particles. *Powd. Tech.*, 118:242–250.

[29] Kammler, H., Pratsinis, S., Morrison, Jr, P., and Hemmerling, B. (2002). Flame temperature measurements during electrically assisted aerosol synthesis of nanoparticles. *Combust. Flame*, 128:369–381.

[30] Kammler, H. K., Jossen, R., Morrison, P. W., Pratsinis, S. E., and Beaucage, G. (2003). The effect of external electric fields during flame synthesis of titania. *Powder Technology*, 135-136:310–320.

[31] Kammler, H. K., Mädler, L., and Pratsinis, S. E. (2001). Flame synthesis of nanoparticles. *Chem. Eng. Technol.*, 24(6):583–596.

[32] Karlemo, B., Koukkari, P., and Paloniemi, J. (1996). Formation of gaseous intermediates in titanium(IV) chloride oxidation. *Plasma Chem. Plasma Process.*, 16:59–77.

[33] Kempf, A., Lindstedt, R. P., and Janicka, J. (2006). Large-eddy simulation of bluff-body stabilized nonpremixed flame. *Combust. Flame*, 144(1-2):170–189.

[34] Kitahara, A. (1984). *Electric phenomena at interfaces*. Dekker.

[35] Kobata, A., Kusakabe, K., and Morooka, S. (1991). Growth and transformation of tio2 crystallites in aerosol reactor. *AIChE Journal*, 37:347.

[36] Koch, W. and Friedlander, S. (1990). The effect of particle coalescence on the surface area of a coagulating aerosol. *J. Colloid Interface Sci.*, 140:419–427.

[37] Kruis, F., Kusters, K., Pratsinis, S., and Scarlett, B. (1993). A simple model for the characteristics of aggregate particles undergoing coagulation and sintering. *Aerosol Sci. Technol.*, 19:514–526.

[38] Kumar, S. and Ramkrishna, D. (1996a). On the solution of population balance equations by discretization - II. A moving pivot technique. *Chemical Engineering Science*, 51:1333–1342.

[39] Kumar, S. and Ramkrishna, D. (1996b). On the solution of population balance equations by discretization - III. Nucleation, growth and aggregation of particles. *Chem. Eng. Sci.*, 52:4659–4679.

[40] Law, C. K. (2007). Combustion at a crossroads: Status and prospects. *Proc. Combust. Inst.*, 31:1–29.

[41] Lehtinen, K., Windeler, R., and Friedlander, S. (1996). A note on the growth of primary particles in agglomerate structures by coalescence. *J. Colloid Interface Sci.*, 182:606–608.

[42] Lu, T. and Law, C. K. (2005). A directed relation graph method for mechanism reduction. *Proc. Combust. Inst.*, 30:1333–1341.

[43] Lu, T. and Law, C. K. (2006a). An efficient error-propagation-based reduction method for large chemical kinetic mechanisms. *J. Phys. Chem. A*, 110:13202–13208.

[44] Lu, T. and Law, C. K. (2006b). Linear time reduction of large kinetic mechanisms with directed relation graph: n-heptane and iso-octane. *Combust. Flame*, 144:24–36.

[45] Marchisio, D. L., Vigil, R. D., and Fox, R. O. (2003a). Implementation of the quadrature method of moments in CFD codes for aggregation-breakage problems. *Chem. Eng. Sci.*, 58(15):3337–3351.

[46] Marchisio, D. L., Vigil, R. D., and Fox, R. O. (2003b). Quadrature method of moments for aggregation-breakage processes. *J. Colloid Interface Sci.*, 258:322–334.

[47] McGraw, R. (1997). Description of aerosol dynamics by the quadrature method of moments. *Aerosol Sci. Tech.*, 27:255–265.

[48] Mehta, M., Raman, V., and Fox, R. O. (2010a). Effect of reaction mechanism on the multiscale modeling of titanium dioxide nanoparticles. In *AIChE Annual Meeting*, Salt Lake City, UT, USA.

[49] Mehta, M., Raman, V., and Fox, R. O. (2012a). On the role of gas-phase and surface chemistry in the production of titania nanoparticles in turbulent flames.

[50] Mehta, M., Raman, V., and Fox, R. O. (2012b). On the role of gas-phase chemistry in the production of titania nanoparticles in turbulent flames.

[51] Mehta, M., Sung, Y., Raman, V., and Fox, R. O. (2010b). Multiscale modeling of TiO_2 nanoparticle production in flame reactors: Effect of chemical mechanism. *Ind. Eng. Chem. Res.*, 49(21):10663–10673.

[52] Mingzhou, Y., Jianzhong, L., and Hongbing, X. (2007). Quadrature method of moments for nanoparticle coagulation and diffusion in the planar impinging jet flow. *Chin. J. Chem. Eng.*, 15:828–836.

[53] Moody, E. G. and Collins, L. R. (2003). Effect of mixing on the nucleation and growth of titania particles. *Aerosol Science and Technology*, 37:403–424.

[54] Morgan, N., Wells, C., Kraft, M., and Wagner, W. (2005). Modelling nanoparticle dynamics: coagulation, sintering, particle inception and surface growth. *Combustion Theory and Modeling*, 9:449–461.

[55] Morgan, N. M., Wells, C. G., Goodson, M. J., Kraft, M., and Wagner, W. (2006). A new numerical approach for the simulation of the growth of inorganic nanoparticles. *J. Comput. Phys.*, 211:638–658.

[56] Mühlenweg, H., Gutsch, A., Schild, A., and Pratsinis, S. (2002). Process simulation of gas-to-particle-synthesis via population balances: Investigation of three models. *Chem. Eng. Sci.*, 57:2305–2322.

[57] Nakaso, K., Fujimoto, T., Seto, T., Shimada, M., Okuyama, K., and Lunden, M. (2001). Size distribution change of titania nano-particle agglomerates generated by gas phase reaction, agglomeration, and sintering. *AIChE J.*, 35:929–947.

[58] Park, S. and Rogak, S. (2003). A one-dimensional model for coagulation, sintering, and surface growth of aerosol agglomerates. *Aerosol Sci. Technol.*, 37:947–960.

[59] Pattersin, R. I. and Kraft, M. (2007). Models for the aggregate structure of soot particles. *Combust. Flame*, 151:160–172.

[60] Pepiot, P. (2008). *Automatic Strategies to Model Transportation Fuel Surrogates*. PhD dissertation, Stanford University, Stanford, California.

[61] Pepiot-Desjardins, P. and Pitsch, H. (2008). An efficient error-propagation-based reduction method for large chemical kinetic mechanisms. *Combust. Flame*, 154:67–81.

[62] Peters, N. (1992). *Fifteen Lectures on Laminar and Turbulent Combustion*. RWTH Aachen, Germany.

[63] Peters, N. (2000). *Turbulent Combustion*. Cambridge University Press.

[64] Peters, N. and Rogg, B. (1993). *Reduced Kinetic Mechanisms for Applications in Combustion Systems*. Springer-Verlag, New York, USA.

[65] Pitsch, H. (1998). A C++ computer program for 0-d and 1-d laminar flame calculations. Technical report. RWTH Aachen.

[66] Pitsch, H. (2006). Large-eddy simulation of turbulent combustion. *Annu. Rev. Fluid Mech.*, 38:453–482.

[67] Pope, S. B. (2000). *Turbulent flows*. Cambridge University Press.

[68] Pratsinis, S., Bai, H., Biswas, P., Frenklach, M., and Mastrangelo, S. (1990). Kinetics of titanium(iv) chloride oxidation. *J. Am. Ceram. Soc.*, 73:2158–2162.

[69] Pratsinis, S. E. and Spicer, P. T. (1998). Competition between gas phase and surface oxidation of $TiCl_4$ during synthesis of TiO_2. *Chem. Eng. Sci.*, 53(10):1861–1868.

[70] Pratsinis, S. E., Zhu, W., and Vemury, S. (1996). The role of gas mixing in flame synthesis of titania powders. *Powder Technol.*, 86(1):87–93.

[71] Raghavan, R. (2001). *Measurement of the High-Temperature Kinetics of Titanium Tetrachloride (TiCl4) Reactions in a Rapid Compression Machine*. PhD dissertation, Case Western Reserve University.

[72] Raman, V. and Pitsch, H. (2006). A consistent LES/filtered-density function formulation for the simulation of turbulent flames with detailed chemistry. *Proc. Combust. Inst.*, 31:1711–1719.

[73] Ren, Z. and Pope, S. B. (2004). An investigation of the performance of turbulent mixing models. *Combust. Flame*, 136:208–216.

[74] Roco, M. C. (1999). Flame temperature measurements during electrically assisted aerosol synthesis of nanoparticles. *Journal of Nanoparticle Research*, 1:1–6.

[75] Rosner, D. E. (2005). Flame synthesis of valuable nanoparticles: recent progress/current needs in areas of rate laws, population dynamics, and characterization. *Industrial & Engineering Chemistry Research*, 44:6045–6055.

[76] Roth, P. (2007). Particle synthesis in flames. *Proceedings of the Combustion Institute*, 31:1773–1788.

[77] Sabel'Nikov, V. and Silva, L. D. (2002). Partially stirred reactor: Study of the sensitivity of the Monte-Carlo simulation to the number of stochastic particles with the use of a semi-analytic, steady-state, solution to the pdf equation. *Combust. Flame*, 129:164–178.

[78] Santos, P. (April 7, 1970). Production of titanium dioxide,US Patent 3,505,091.

[79] Shah, J. J. and Fox, R. O. (1999). Computational fluid dynamics simulation of chemical reactors: Application of in situ adaptive tabulation to methane thermochlorination chemistry. *Ind. Eng. Chem. Res.*, 38:4200–4212.

[80] Shirley, R., Akroyd, J., Miller, L. A., Inderwildi, O. R., Riedel, U., and Kraft, M. (2011). Theoretical insights into the surface growth of rutile TiO2. *Combustion and Flame*, 158:1868–1876.

[81] Smith, R., Bennett, R., and Bowker, M. (2002). Measurement of the surface growth kinetics of reduced $TiO_2(110)$ during reoxidation using time-resolved scanning tunneling microscopy. *Phys. Rev. B: Condens. Matter Mater. Phys.*, 66:66.

[82] Spicer, P. T., Chaoul, O., Tsantilis, S., and Pratsinis, S. E. (2002). Titania formation by $TiCl_4$ gas phase oxidation, surface growth and coagulation. *J. Aerosol Sci.*, 33:17–34.

[83] Sung, Y., Mehta, M., Raman, V., and Fox, R. O. (2012). Large-eddy-simulation based computational modeling of flame synthesis of titania nanoparticles in a turbulent reactor using bivariate particle number distribution.

[84] Sung, Y., Raman, V., and Fox, R. O. (2011). Large-eddy-simulation-based multiscale modeling of TiO_2 nanoparticle synthesis in a turbulent flame reactor using detailed nucleation chemistry. *Chem. Eng. Sci.*, 66(19):4370–4381.

[85] T., T. (1990). Reduction of large reaction mechanism. *New J. Chem.*, 14:795–803.

[86] Teleki, A. and Pratsinis, S. E. (2009). Blue nano titania made in diffusion flames. *Physical Chemistry Chemical Physics*, 11:3742–3747.

[87] TNF (2002). *Sixth International Workshop on Measurement and Computation of Turbulent Non-premixed Flames*, Sapporo, Japan.

[88] Tsantilis, S., Kammler, H. K., and Pratsinis, S. E. (2002). Population balance modeling of flame synthesis of titania nanoparticles. *Chemical Engineering Science*, 57(12):2139–2156.

[89] Tsantilis, S. and Pratsinis, S. (2000). Evolution of primary and aggregate particle-size distributions by coagulation and sintering. *AIChE J.*, 46:407–415.

[90] Tsantilis, S. and Pratsinis, S. E. (2004). Narrowing the size distribution of aerosol-made titania by surface growth and coagulation. *J. Aerosol. Sci.*, 35:405–420.

[91] Ukaji, E., Furusawa, T., Sato, M., and Suzuki, N. (2007). The effect of surface modification with silane coupling agent on suppressing the photo-catalytic activity of fine TiO_2 particles as inorganic UV filter. *Applied Surface Science*, 254(2):563–569.

[92] Ulrich, G. and Subramanian, N. (1977). Particle growth in flames. *Combust. Sci. Technol.*, 17:119.

[93] Vajda, S., Valko, P., and T., T. (1985). Principal component analysis of kinetic models. *Int. J. Chem. Kinet.*, 17:55.

[94] Wang, H., Wu, Z., Zhao, W., and Guan, B. (2007). Photocatalytic oxidation of nitrogen oxides using TiO2 loading on woven glass fabric. *Chemosphere*, 66:185–190.

[95] Wegner, K. and Pratsinis, S. E. (2003). Scale-up of nanoparticle synthesis in diffusion flame reactors. *Chem. Eng. Sci.*, 58:4581–4589.

[96] Wegner, K., Stark, W. J., and Pratsinis, S. E. (2002a). Flame-nozzle synthesis of nanoparticles with closely controlled size, morphology and crystallinity. *Material Letters*, 55:318–321.

[97] Wegner, K., Walker, B., Tsantilis, S., and Pratsinis, S. E. (2002b). Design of metal nanoparticle synthesis by vapor flow condensation. *Chemical Engineering Science*, 57(10):1753–1762.

[98] West, R. H., Beran, G. J. O., Green, W. H., and Kraft, M. (2007a). First-principles thermochemistry for the production of TiO_2 from $TiCl_4$. *J. Phys. Chem. A*, 111(18):3560–3565.

[99] West, R. H., Celnik, M. S., Inderwildi, O. R., Kraft, M., Beran, G. J. O., and Green, W. H. (2007b). Toward a comprehensive model of the synthesis of TiO_2 particles from $TiCl_4$. *Ind. Eng. Chem. Res.*, 46:6147–6156.

[100] West, R. H., Shirley, R. A., Kraft, M., Goldsmith, C. F., and Green, W. H. (2009). A detailed kinetic model for combustion synthesis of titania from $TiCl_4$. *Combust. Flame*, 156(9):1764–1770.

[101] Wheeler, J. C. (1974). Modified moments and gaussian quadratures. *Rocky Mountain Journal of Mathematics*, 4(2):287–296.

[102] Willcox, O. (May 7, 1957). Method and means for commingling and reacting fluid substances. US Patent 2,791,490.

[103] Wright, D. L. (2007). Numerical advection of moments of the particle size distribution in eulerian models. *Aerosol Science*, 38(21):352–269.

[104] Xiong, Y., Akhtar, M., and Pratsinis, S. (1993). Formation of agglomerate particles by coagulation and sintering–part ii. the evolution of the morphology of aerosol-made titania, silica and silica-doped titania powders. *J. Aerosol Sci.,*, 24:301–313.

[105] Xiong, Y. and Pratsinis, S. E. (1991). Gas phase production of particles in reactive turbulent flows. *Journal of Aerosol Science*, 22(5):637–655.

[106] Xiong, Y. and Pratsinis, S. E. (1993). Formation of agglomerate particles by coagulation and sintering-part I: A two-dimensional solution of the population balance equation. *J. Aerosol Sci.*, 3:283–300.

[107] Xiong, Y., Pratsinis, S. E., and Mastrangelo, S. (1992). The effect of ionic additives on aerosol coagulation. *Journal of Colloid and Interface Science*, 153:106–117.

[108] Yu, M.-Z., Lin, J.-Z., and Chan, T.-L. (2001). Computational analysis of coagulation and coalescence in the flame synthesis of titania particles. *Chem. Eng. Sci.*, 118:242–250.